IMPROVEMENT OF THE EFFICIENCY AND BEAM QUALITY OF THE TRIUMF CHARGE STATE BOOSTER

by

Adedapo Joseph Adegun
MSc, University of Saskatchewan, Saskatoon, Canada, 2017
BSc, Ekiti State University, Ado Ekiti, Nigeria, 2012

A Dissertation Submitted in Partial Fulfillment
of the Requirements for the Degree of

DOCTOR OF PHILOSOPHY

in the Department of Physics and Astronomy

University of Victoria

Supervisory Committee

IMPROVEMENT OF THE EFFICIENCY AND BEAM QUALITY OF THE TRIUMF CHARGE STATE BOOSTER

by

Adedapo Joseph Adegun
MSc, University of Saskatchewan, Saskatoon, Canada, 2017
BSc, Ekiti State University, Ado Ekiti, Nigeria, 2012

Supervisory Committee

Dr. Oliver Kester, Co-Supervisor
Department of Physics and Astronomy

Dr. Dean Karlen, Co-Supervisor
Department of Physics and Astronomy

Dr. Tobias Junginger, Departmental Member
Department of Physics and Astronomy

Dr. Scott McIndoe, Outside Member
Department of Chemistry

Abstract

At the Isotope Separator and Accelerator (ISAC) facility of TRIUMF, charge state breeding of radioactive isotopes with an atomic mass greater than 30 is required before they are injected into the linear accelerator (LINAC) for post-acceleration to provide the required mass-to-charge ratio (A/Q). A 14.5 GHz Electron Cyclotron Resonance Ion Source (ECRIS) PHOENIX booster developed by Pantechnik is employed for the charge breeding process. On the Charge State Booster (CSB), the two-frequency heating technique was implemented using only a single waveguide, contrary to the conventional implementation using two separate waveguides. In addition, the injection and extraction optics and the injection and extraction systems of the CSB were optimized for the first time.

The optimization of the CSB injection optics performed in TRANSOPTR (TRIUMF's in-house beam transport code) involved modelling of the magnetic field and electric field at the injection of the CSB ECRIS to determine tune settings for the injection of singly charged ions. Moreover, the magnetic field distribution of the source was mapped and the measurement results, when compared with the OPERA© simulation, revealed a discrepancy in the control settings of the power supply of the electron cyclotron resonance ion source's solenoid coils. The measured magnetic field distribution was finally used to model the beam extraction system using the code IGUN©, which allowed the optimization of the extraction of highly charged ions and the reduction of the beam emittance. The implementation of the two-frequency heating technique provides an additional knob to condition the plasma of the CSB for the production of highly charged ions, while the optimization of the injection and extraction systems as well as the associated beam optics, were necessary to ensure that singly charged ions are efficiently injected into the charge state booster and highly charged ions with higher intensity and best emittance are extracted and delivered to the experiments in the TRIUMF ISAC Facility.

The systematic optimizations of the CSB injection and extraction optics and the extraction system along with the implementation of the two-frequency heating resulted in a significant increase in the maximum charge state of cesium that can be produced, shifting it from 28+ to 32+. The global efficiency between 20+ and 32+ also increased to 41.1%, while the peak of the efficiency distribution shifted to 26+ with an efficiency of 9.1%. Additionally, the emittance of the total current extracted from the CSB decreased by a factor of 2.

Table of Contents

List of Tables

List of Figures

Acknowledgments

I would like to express my sincere gratitude to Dr. Oliver Kester, my research supervisor, for his invaluable guidance and unwavering support throughout the completion of this research project. Additionally, I extend my special appreciation to Marco Lovera, Brian Minato, Dr. Keerthi Jayamanna, Dr. Friedhelm Ames, Dr. Dean Karlen, and all the members of the beam physics group at TRIUMF for their constant availability and willingness to answer my questions.

Furthermore, I would like to acknowledge TRIUMF, the Natural Sciences and Engineering Research Council of Canada, and the University of Victoria for providing the funding necessary to support my thesis. I am also deeply grateful to my friends and family for their unwavering encouragement and emotional support throughout this journey.

Finally, I give all glory to God for granting me the strength, wisdom, and perseverance to overcome the challenges I faced halfway through my Ph.D. program and ultimately complete it.

Dedication

I dedicate this dissertation to all those who believed in and supported me, and to myself for persevering through the challenges and completing this achievement.

Chapter 1 – Why Charge Breeding?

1.1 Overview of Charge Breeding

One of the most exciting and foremost frontiers in nuclear physics today is the physics of radioactive ion beams (RIBs) near or above the Coulomb barrier and the study of nuclear reactions in a stellar environment. Nuclear physics focuses on exploring nucleonic matter under extreme conditions, the limits of nuclear structure, and understanding the origin of elements in the universe. The opportunities exotic nuclei beams offer for research in nuclear structure physics and nuclear astrophysics are exciting. The worldwide activity in the operation and construction of different types of RIB facilities bears witness to the strong scientific interest in physics that can be probed with such beams. For example, intense radioactive beams from isotopes like ${}^{11}_{6}C$ or ${}^{15}_{8}O$ can be used to study critical CNO cycle reactions. Further details on how the nuclear properties of these isotopes are crucial for our understanding of the CNO cycle reactions can be found here [1].

To perform experiments with radioactive isotopes at the Coulomb barrier at an isotopes separation on-line (ISOL) facility, post-acceleration of radioactive ions in a low-velocity ($v \ll c$) heavy ion accelerator is required. The least sophisticated and somehow expensive way is the continuous acceleration of the singly charged radioactive ions in a low-frequency linear accelerator (LINAC) to stripping energies in the range of several keV. The beam then passes through a stripping section where its charge-to-mass ratio increases. The resultant highly charged ions are subsequently post-accelerated in an additional LINAC section. However, this method is well-tested and used in several facilities (ISAC I, SPIRAL) but is limited in the mass range of the isotopes. A more economical scheme uses charge multiplication of the radioactive ions to $Q+$ in a high charge states ion source like the Electron Beam Ion Source (EBIS) [2], [3] and the Electron Cyclotron Resonance Ion Source (ECRIS) [3] to use the accelerating electrical field Q-times better.

Charge state breeding or charge state boosting is an important process in a rare isotope production facility such as TRIUMF. With charge state breeding, the cavities of the linear accelerators (LINAC) used for post-acceleration can operate on a higher frequency and be made more compact and smaller, reducing the cost of designing such a facility. The final energy that a rare isotope beam can be accelerated to is directly proportional to the charge state of the beam, as given in Equation 1.1.

$$E(keV) = QeU_a \tag{1.1}$$

where Q is the charge state of the beam, e is the electron charge, and U_a is the accelerating voltage in $kilovolts$.

Moreover, with charge state breeding, the injection energy of the linear accelerator as well as its mass to charge (A/Q) ratio acceptance can be properly matched to avoid or limit beam loss. Besides, with charge state breeding, molecular ions can be extracted from the target ion source station and injected into the CSB, where they break up and then extract part of the constituents of the molecule to form a useful beam for experiments. For example, carbon dioxide ions (CO_2^+) can be extracted from the target ion source station and injected into a CSB, where it breaks up into carbon and oxygen isotopes, and either carbon or oxygen beam can be extracted afterwards. Charge breeding of rare isotope beams (RIBs) using EBIS or ECRIS involves electron impact ionization of the injected singly charged ions and extraction of highly-charged ions (HCIs) $(1+\rightarrow Q+)$, where Q is the charge state of the extracted ion beam. Detailed atomic processes involved with charge breeding will be discussed later in the dissertation.

At TRIUMF, all the charge breeding techniques and the stripping method are in operation. For example, the stripping foil technique is used with the TRIUMF $500\ MeV$ cyclotron to extract the proton beam with H^- as the primary driver beam accelerated. It is also used in the ISAC I facility of TRIUMF after the Radiofrequency Quadrupole (RFQ) for charge stripping of light elements. The EBIS is part of the newly constructed TRIUMF's Advanced Rare Isotope Laboratory (ARIEL) and the newest charge state breeder. However, at the TRIUMF's Isotope Separation and Acceleration (ISAC) facility, the Electron Cyclotron Resonance Ion Source is used as a charge state booster (CSB) because, unlike an EBIS, it supports a continuous mode of operation (CW) which is well adapted to the target ion source and linear accelerator of the ISAC facility. Besides, unlike the EBIS, there is no limit on the intensity and emittance of a singly charged ion beam that can be injected into the source for charge breeding.

The Electron Cyclotron Resonance Ion Source of TRIUMF, which has been in operation since 2010, is a 14.5 GHz PHOENIX developed by Pantechnik in France. This charge state breeder was originally designed as a conventional single-frequency heating source. Extraction of highly charged ions (HCIs) is achieved by the three-electrode extraction system. The injection and extraction electrodes, as well as the plasma chamber wall, have been replaced with aluminum to reduce the intensity of background ions liberated by plasma-wall interaction. The minimum magnetic field configuration for plasma confinement and stability is achieved by combining the fields of three solenoids and a hexapole field generated by permanent magnets. The CSB has been used in user beam delivery to charge breed rare isotopes ranging from Potassium to uranium. The efficiency of the breeder depends on the rare isotope that is being charge-bred. However, single-charge state efficiency $(1+\rightarrow Q+)$ has been measured up to 8.5 % operating the CSB at the designed single RF frequency of 14.5 GHz.

1.2 TRIUMF Isotopes Separation and Acceleration (ISAC) Facility

The TRIUMF Isotopes Separation and Acceleration (ISAC) facility was designed to produce rare isotopes for experiments in nuclear physics, nuclear astrophysics, fundamental symmetries and material science using the Isotope Separator On-Line (ISOL) method. In the TRIUMF ISAC facility, thick target materials such as Ta, UO_2, ThO, TaC, NiO, Nb, SiC, TiC, ZrC and UC_2 are irradiated with an energetic proton beam of energy up to $480\ MeV$ extracted from the TRIUMF cyclotron. Proton with energy up to $520\ MeV$ could be extracted from the cyclotron but because of unwanted electromagnetic stripping that occurs at high energy which reduces the efficiency of the beam, the proton beam is extracted at $480\ MeV$ The irradiation process produces exotic isotopes of different atomic masses. The exotic isotopes are allowed to diffuse to the surface of the target material and then effuse into the closely coupled Forced Electron Beam Induced Arc Discharge (FEBIAD) ion source [4] where they are ionized (singly charged ions are mostly produced). A Resonant Ionization Laser Ion Source is also used at TRIUMF to ionize short-lived isotopes [5]. The singly charged ions are extracted and accelerated to a maximum energy of $60\ keV$ (the target ion source extraction voltage is up to $60\ kV$). The accelerated isotopes are separated using a high-resolution analyzing sector magnet with a mass resolution $M/\Delta M$ of 2000 to select the desired isotope before injection into the linear accelerator (LINAC) for post-acceleration.

There are two areas in the ISAC facility: ISAC I and ISAC II. The layout of the facility is shown in Figure 1.1. The ISAC I facility was designed to address various questions about energy production and nucleosynthesis in various astrophysical environments. The nuclear astrophysics program at ISAC is best known for directly measuring hydrogen and helium radiative capture reactions with the Detector of Recoil and Gammas Of Nuclear Reaction (DRAGON) recoil separator. The ISAC II superconducting accelerator complex provides beams, depending on the A/Q ratio of up to a final energy of 16 MeV/u. This allows reaction experiments at energies below and above the Coulomb barrier and excitation measurements. Another area of interest is the Equation of State (EOS) for asymmetric nuclei, such as very N-rich isotopes [6].

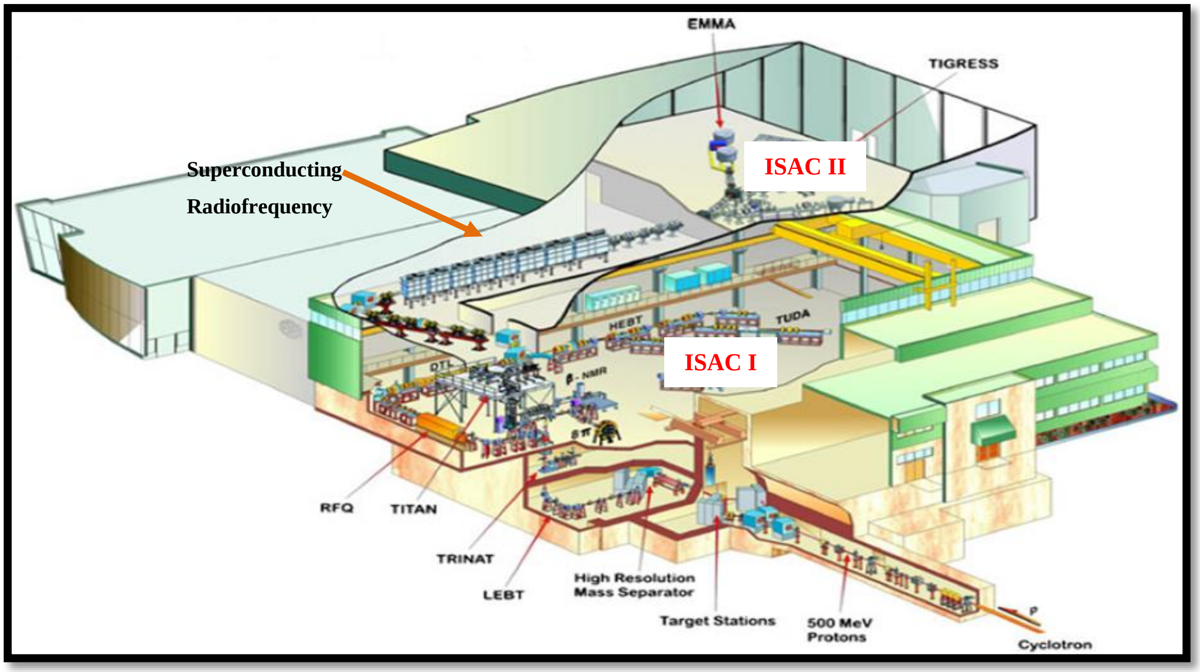

Figure 1.1: Overview of TRIUMF isotope separator and accelerator facility showing the linear accelerators and some of the experimental stations [7].

In the ISAC I area of the TRIUMF facility, a Radiofrequency Quadrupole (RFQ) and a Drift Tube Linear accelerator (DTL), designed for nuclear astrophysics experiments, are used to post-accelerate rare isotope beams to final energies of 153 keV/u and 1.53 MeV/u respectively with the initial energy of 2.0 keV/u for RFQ and 153 keV/u for DTL. In the ISAC II area, the Superconducting Radiofrequency linear accelerator (SRF), designed for experiments in nuclear physics, is used to raise the energy of isotopes to the energy above the Coulomb barrier ($>$ 10 MeV/u) from the initial energy of 1.53 MeV/u. The RFQ, which is the first section of the linear accelerator, was designed to accept rare isotope beams at the mass-to-charge ratio (A/Q) less than or equal to 30 ($A/Q \leq 30$) at the injection energy of 2.0 keV/u while the DTL, the next section and SRF, the last section were designed to accept rare isotope beams at the $A/Q \leq$

6. Thus, to match the A/Q acceptance of the DTL and SRF, it is preferable to inject isotopes with $A/Q \leq 6$ into the RFQ.

The energy gained per nucleon by an isotope of atomic mass A and a charge Q through an accelerating voltage U_{acc} is defined as:

$$W(keV/u) = \frac{QeU_{acc}}{A} \qquad 1.2$$

where W = energy per nucleon in keV/u, Q = charge state of the ion beam, U_{acc} = extraction voltage in kilovolt (kV) and A = atomic mass of the ion beam.

Using Equation 1.2, the accelerating voltage required to inject isotopes with A/Q $(Q = 1)$, say between 1 and 60, to match the injection energy of TRIUMF RFQ at 2.0 keV/u is plotted in Figure 1.2.

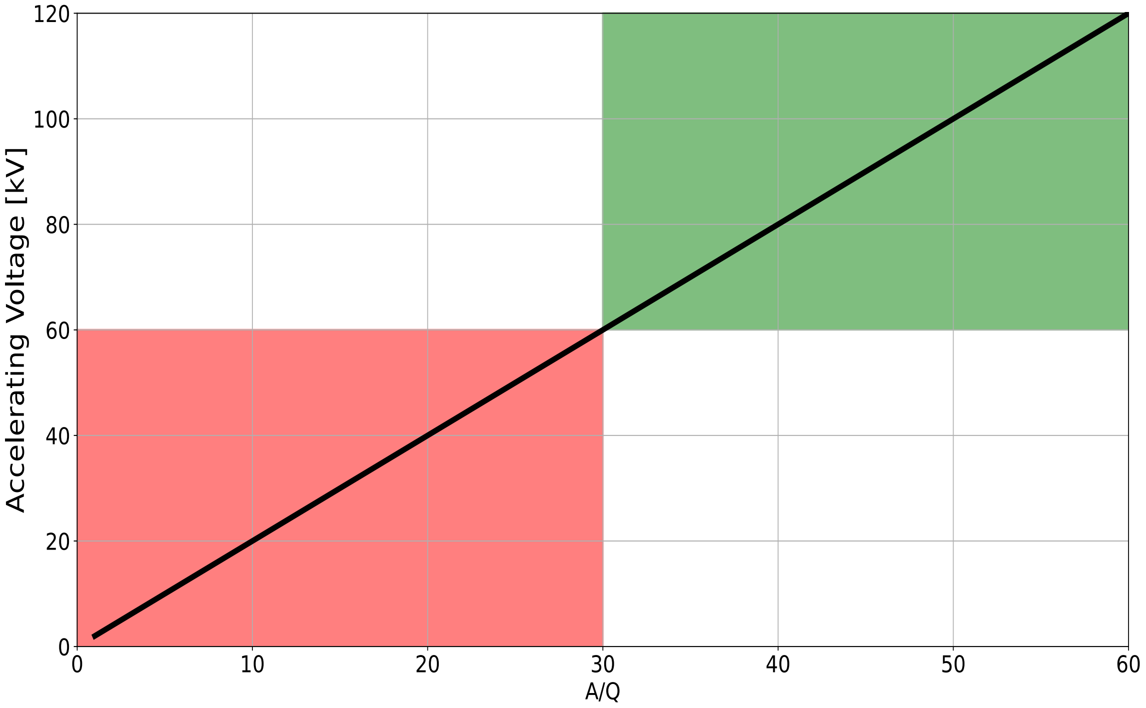

Figure 1.2: Plot of the required accelerating voltage for beam injection into the ISAC RadioFrequency Quadrupole linear accelerator vs. A/Q value.

As shown in Figure 1.2, the area shaded in red is the limit of the TRIUMF target ion source extraction/accelerating voltage. The plot shows that isotopes with $A/Q \leq 30$ require accelerating voltage $U_{acc} \leq 60\ kV$ while the isotopes with $A/Q > 30$ require accelerating voltage $U_{acc} > 60\ kV$ (area shaded in green), which suggests that charge breeding is required for RIBs with a mass greater than 30 u.

At the TRIUMF ISAC facility, to charge breed isotopes with the $A/Q > 30$, electrostatic benders are inserted into the path of the ions selected with the analyzing sector magnet and are directed into the charge state booster (CSB), where their charge state is boosted (see Figure 1.3). The chamber of the CSB is biased to an electrical potential close to the potential of the target ion source station to allow the ions to be decelerated and stopped in the plasma where charge breeding takes place. The highly charged ions (HCIs) are extracted on the other side of the booster and accelerated to the ground potential. From Equation 1.2, if the charge state of the extracted isotope ions from the CSB is boosted to say $Q = 10$, then the A/Q value of the isotopes considered in Figure 1.2 is reduced by a factor of 10 and the extraction/accelerating voltage required to match the injection energy of the RFQ at $2.0\ keV/u$ is also reduced by a factor of 10, allowing efficient injection and post-acceleration of the RIBs. The extraction voltage after the charge boosting is determined by the CSB bias voltage.

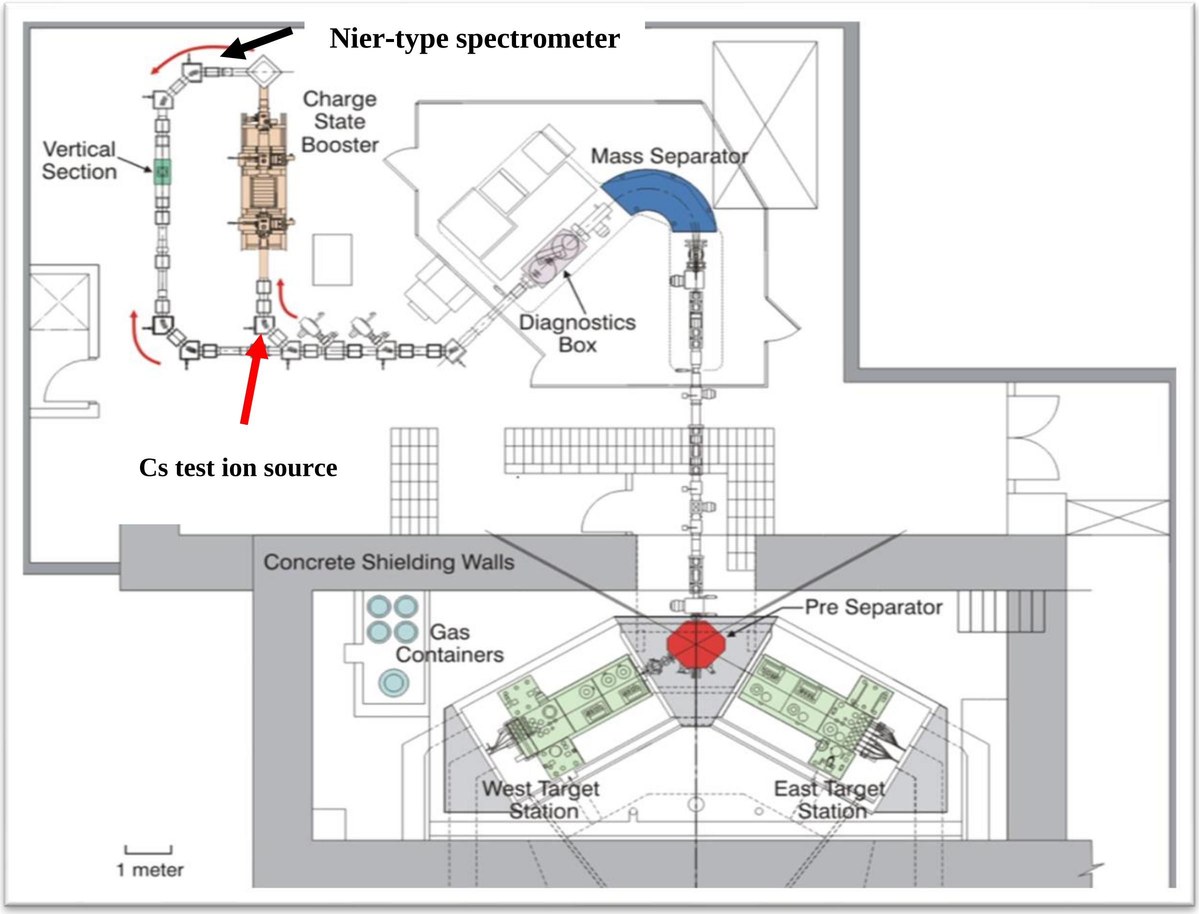

Figure 1.3: Layout of radioactive ion beam production and charge breeding facilities at TRIUMF ISAC facility [6].

The desired A/Q that matches the acceptance of the RFQ is selected using the Nier-type spectrometer [8], essentially a velocity filter combining a magnetic dipole and two electrostatic benders. The selected ions with the right injection energy are injected into the LINAC for post-acceleration. The layout of the mass separator room where the charge state booster (CSB) is located is shown in Figure 1.3. To mention a few, the layout contains the target stations (located at the bottom of the picture), the mass separator, the cesium test ion source (CTIS), the CSB, the Nier-type spectrometer and beam optics (mostly drifts and electrostatic quadrupoles).

1.3 Thesis Goal

This research project aims to improve the efficiency and beam quality of the TRIUMF Electron Cyclotron Resonance Ion Source Charge State Booster.

1.4 Thesis Objectives

There are five main objectives to achieve the thesis goal. They are:

- Development of an alternative method for Emittance measurement of the CSB
- A proper definition of the injection and extraction optics of the CSB in TRANSOPTR, TRIUMF's beam optics design code.
- Systematic investigation of the beam formation and extraction from the CSB
- Implementation of the two-frequency heating of the ECRIS CSB plasma
- Study of the effect of the Two-Frequency Heating on the efficiency and Emittance of the TRIUMF CSB

Several numerical codes will be used in this thesis to model and simulate the components of the charge state booster. IGUN© [9], [10] will be used for the extraction system simulation. For magnetic field modelling of the CSB, OPERA simulation software [11] will be used. The TRANSOPTR code [12]–[14] will be used for beam transport modelling and simulation. Python will be used for curve fitting, data analysis and data processing. This report will not present the operation of these modelling and simulation tools. However, it is worth noting that I developed and defined the input files of the CSB modelled and simulated geometry and developed the Python scripts for data processing and analysis.

A brief introduction to Physics and the atomic processes involved with the operation of the Electron Cyclotron Resonance Ion Source (ECRIS) are presented in Chapter 2. In Chapter 3, a review of Beam transport and transverse beam dynamics, as well as the alternative method of emittance measurement that I developed, are presented and discussed. Chapter 4 introduces the TRIUMF ECRIS CSB, cesium test ion source, injection and extraction systems, and their corresponding beamlines. The chapter also presents the results of properly defining the injection and extraction optics of the CSB in the beam optics code TRANSOPTR. Chapter 5 presents the results of the operation of the CSB in a single-frequency heating mode after I properly optimized the plasma and the adjacent optics. Results of the systematic investigation of the CSB extraction system are also presented and discussed. In Chapter 6, the results of the operation of the CSB, after I implemented the two-frequency heating, are presented and compared with the results of the single-frequency heating regime. Chapter 7 concludes and presents the further work to be carried out on the CSB to improve its operational performance further.

Finally, a brief description of the Python codes, IGUN files, TRANSOPTR files, OPERA files and results of the mapped magnetic field of the CSB and where all these files are securely kept are presented in the Appendix.

Chapter 2 - The Physics of Electron Cyclotron Resonance Ion Source

2.1 Introduction

The physics of the Electron Cyclotron Resonance Ion Source (ECRIS) is entirely plasma physics. According to [15], plasma is a quasi-neutral gas of charged and neutral particles exhibiting collective behaviour. Plasma, following the solid, liquid, and gaseous states, is sometimes considered the fourth state of matter. This consideration refers to the temperature of the state of the matter. As the gaseous state's temperature increases, the matter transitions into the plasma state, where one or more of the orbital electrons of the atoms of the matter have been stripped from the nucleus. Some basic plasma parameters that are required to describe the plasma physics of ECRIS are plasma density, plasma temperature, Debye length, and plasma frequency. While these parameters are briefly described in this chapter, for a more extensive and comprehensive explanation, refer to textbooks on plasma physics, such as the one cited above.

2.1.1 Plasma Density

Depending on the degree of ionization, which is determined by the plasma temperature, plasma can either be fully or partially ionized. In the case of fully ionized plasma, which requires significant heating such that the ionization rate is much higher than the recombination rate, the degree of ionization is 1, and the plasma comprises only ions and electrons. Meanwhile, in the case of partially ionized plasma, such as ECR plasma, the degree of ionization is less than 1; thus, the constituents of the plasma are ions, electrons and neutrals. The degree of ionization is defined as:

$$\alpha_{DOI} = \frac{n_i}{n_i + n_n} \qquad 2.1$$

where n_i is the ion density and n_n is the neutral density.

However, electrons respond faster to both internal and external fields because of their high mobility (and low mass) compared to ions. So, in the partially ionized plasma, the electron density is usually referred to as the plasma density, which is denoted as n_e, and it is usually expressed in particles per cm^3. Most laboratory-produced plasmas have densities in the range between $10^8 - 10^{16}\ cm^{-3}$.

2.1.2 Plasma Temperature

The thermal energy of the plasma is generally described by temperature. Thermal energy is related to temperature by $\bar{E} = 3/2\, kT$, where $\bar{E}$ is the average thermal energy. Meanwhile, the temperature in plasma is not a single particle parameter but describes a Maxwellian distribution of the particle kinetic energy, so the temperature is an average over the distribution function. There are different temperatures in the ECR plasma since the plasma is non-equilibrium and not fully ionized. They are electron temperature T_e, ion temperature T_i, and neutral temperature T_n. In the ECR plasma, where an electromagnetic wave is applied, the energy transfer only heats the electrons, while the ions are significantly cooler due to their larger mass compared to the electrons. Since the electron temperature is always larger than the ion and neutral temperature, the electron temperature is usually regarded as the plasma temperature T_e most especially in nonthermal plasmas. The plasma temperature is usually expressed in units of electron Volts (eV), where $11{,}600\ K = 1\ eV = 1.6 \times 10^{-19}\ J$. Temperature T given in Kelvin $[K]$ is converted to energy by multiplication by Boltzmann's constant $k = 1.38 \times 10^{-23}\ JK^{-1}$.

2.1.3 Debye Shielding and Debye Length

Debye shielding, first investigated by Peter Debye in the 1920s [16], is a physical phenomenon that preserves charge neutrality in the plasma. The preservation of charge neutrality is a consequence of the collective behaviour of the plasma particles. However, charge neutrality is not fulfilled at the plasma's edge because electrons, due to their large thermal speed, leave the plasma much faster than the ions, thus reducing the plasma density and leaving the plasma positively charged. The positive potential that plasma acquires in this process is called the plasma potential, and the extraction of ions from the plasma must take the plasma potential into account. In the ECR ion source, the plasma potential has been measured to be between $10 - 40\ V$ [17]. The expression for plasma potential is given as:

$$V_p = \frac{T_e}{e} \ln \sqrt{\frac{m_i}{2\pi m_e}} \qquad 2.2$$

Where T_e is the plasma temperature in eV, m_i is the mass of the ion, m_e is the mass of the electron, and e is the charge. If the plasma consists of protons and electrons only, $m_i = 1.67 \times 10^{-27}\ kg$, then Equation 2.2 becomes $V_p = \frac{2.84 T_e}{e}$ and for an average plasma electron of $5\ eV$, the plasma potential is approximately $14\ V$.

Meanwhile, the external injection of electrons into the ECR plasma has been demonstrated in [17] to reduce the plasma potential. With the injection of secondary electrons, the product of plasma density and ion confinement time ($n_e \tau_i$) is increased, and the plasma potential is reduced, resulting in the enhanced production of highly charged ions. The plasma sheath is the edge of the plasma (plasma boundary) where the charge neutrality does not hold. In the plasma sheath, the ions build an equilibrium electrostatic potential to reduce the electron loss so that charge neutrality is preserved. In other words, if there is a charge separation in the plasma due to the high mobility of electrons, the particles of the plasma undergo a rearrangement to shield the electric fields that arise within the order of length so that the particles that are farther than the length do not experience the fields. The length over which this screening occurs is called the Debye length, usually denoted as λ_D. The Debye length equation is given in Equation 2.3, where T_e is plasma temperature in kelvin, k is Boltzmann constant and n_e is plasma density in m^{-3}, ϵ_0 is the permittivity of free space, and e is the electron's charge. In an ECR ion source plasma, with an average plasma density of $1 \times 10^{18}\ m^{-3}$ and average plasma temperature of $5\ eV$, the Debye length is about $17\ \mu m$.

$$\lambda_D = \sqrt{\frac{\epsilon_0 k T_e}{e^2 n_e}} \qquad 2.3$$

2.1.4 Plasma Frequency

Charge neutrality is very important in bulk plasma, and if there is a departure from charge neutrality, electric fields are created, and the particles of the plasma shield the electric fields that arise from it. However, the plasma is instantaneously disturbed when there is a departure from charge neutrality. A restoring force in terms of the internally generated electric field by the ions sets in to restore the charge neutrality of the plasma by pulling the electrons back to their original positions. However, the electrons will overshoot and oscillate around their original positions leading to a periodic oscillation. The frequency of the oscillation is fundamental, and it is referred to as plasma frequency, denoted as f_p. Also, since the oscillation is due to electrons' inertia, plasma frequency is usually referred to as the electron plasma frequency. The plasma frequency is given by:

$$f_p = \frac{1}{2\pi} \sqrt{\frac{e^2 n_e}{\epsilon_0 m_e}} \qquad 2.4$$

where ϵ_0 is the permittivity of free space, n_e is the plasma density, m_e is the mass of electrons, and e is the electron's charge. The plasma with an average density of $1 \times 10^{18}\ m^{-3}$ has a fundamental frequency of about 9 GHz.

2.1.5 Magnetic Field Effects: Cyclotron Frequency and Larmor Radius

In the ECR plasma, magnetic fields are used to confine the plasma. The applied magnetic field lines are parallel to the axis of the plasma chamber so that particles of the plasma, mostly electrons, are confined in the direction perpendicular to the magnetic lines (radial direction). The motion of charged particles is circular in a magnetic field if the particles have entire velocities perpendicular to the magnetic field lines, but if the motion of the particles is parallel to the magnetic field lines, then the motion of the particles is unaffected. Without collisions, the resultant particle motion is helical if the velocity is not entirely perpendicular but has a longitudinal component. The radius of the circular motion is called Larmor radius or gyro-radius, and the frequency of the circular motion is called cyclotron frequency.

Meanwhile, for the plasma electron to be properly confined by the magnetic field, the cyclotron frequency must be higher than the plasma frequency. The radius and the cyclotron frequency are different for ions and electrons. The Larmor radius and cyclotron frequency equations are derived from centripetal motion. The force experienced by an object exhibiting a circular motion is given as,

$$F = \frac{mv_{\perp}^2}{r} \qquad 2.5$$

While the force that a charged particle experiences in a magnetic field is given by the Lorentz force as,

$$F = Qev \times B = Qev_{\perp}B \qquad 2.6$$

By equating Equation 2.5 to 2.6, the radius of the particle around the magnetic field, which is called the Larmor radius, is defined as,

$$r = \frac{mv_{\perp}}{QeB} \qquad 2.7$$

The Larmor radius varies with the particles' mass and charge state. For example, in an ECR plasma, if the resonance field is 0.5 T with helium as a support gas, assume the average electron temperature is 5 eV, and the average ion temperature is 0.5 eV, the electron Larmor radius is about 18 μm, while the He^{2+} Larmor radius is about 240 μm (480 μm for $Q = 1+$), which shows that the He^{2+} Larmor radius is about 13 times larger than the electron Larmor radius. Furthermore, by rewriting Equation 2.7, and equating it to $v = r\omega$, as given in Equation 2.8,

$$v_{\perp} = \frac{QeBr}{m} = \omega r = 2\pi f r \qquad 2.8$$

The frequency of the circular motion, which is called the cyclotron frequency, is given as,

$$f_{cyc} = \frac{QeB}{2\pi m} \qquad 2.9$$

where m is the mass of the particle, $v_{\perp}$ is the transverse velocity component of the particle, B is the magnitude of the magnetic field and e electron charge, Q is the absolute value of the charge state of the particle. The cyclotron frequency depends on the particle's charge state, the magnetic field's magnitude and the particle's mass. For example, if the magnitude of the field in the plasma is 0.5 T, the electron cyclotron frequency is about 14.5 GHz, and for He^{2+}, the cyclotron frequency is about 0.004 GHz (0.002 GHz for $Q = 1+$). This indicates that for a He ion with a charge state of 2, the electron cyclotron frequency is more than 3000 times higher than the helium ion cyclotron frequency; this suggests that electrons are more magnetically confined compared with He^{2+} (and He^{+}), meanwhile, for protons, the cyclotron frequency is 7.6 MHz, which is about 2000 times small than the electron cyclotron frequency.

2.2 Atomic Processes in ECR Plasma

The main atomic processes that significantly influence the production of HCIs in ECR plasma are electron impact ionization and charge exchange.

2.2.1 Electron Impact Ionization

In ECR ion sources, highly charged ions (HCIs) are produced by either a single electron-neutral/ion encounter where many electrons are removed in a single collision or through a step-by-step electron-neutral/ion encounter in which one or two electrons are removed per collision and HCIs are produced by a sequence of many collisions. Both encounters depend on the energy of the plasma electrons. In the ECR plasma, there is a distribution of electron energy, although the Maxwellian distribution cannot overall describe the energy distribution because ECR plasma electrons cannot reach thermal equilibrium because of the applied magnetic field. However, a reasonable description is to assume two electron populations, although, in some articles, three electron populations are assumed, cold, warm and hot populations [18]. However, in this thesis work, especially in this section, the electron population will be categorized as low and high-energy.

- **Low-Energy Electrons Population (LEEP)**

  The low-energy electrons, otherwise known as the cold electrons, are most of the plasma electrons. They are not well confined because they are highly collisional; that is, their collision frequency is far greater than their cyclotron frequency $\left(f_{col} \gg f_{cyc}\right)$. Their loss rate is higher than the ions leaving behind a positively charged plasma, generally called a plasma potential. The plasma with a high plasma potential is unstable. The LEEPs have energies ranging from $0.026\ to\ 100\ eV$. They are responsible for the ionization of low-charge state ions and medium-charge state ions.

- **High-Energy Electrons Population (HEEP)**

  The high-energy electrons of the ECR plasma, known as warm and hot, are responsible for producing highly charged ions. They are well-confined and almost collisionless. They are located in the core of the plasma, thus creating a negative potential for ion confinement. Because of their high energy, they are the main source of Bremsstrahlung radiation. The HEEPs have energy greater than 100 eV. Measurements of the plasma densities in ECRIS have shown that HEEP makes up about 10% of the total plasma electrons, representing the tail of the overall electron energy distribution [19].

However, regardless of the energy population of the plasma electrons, minimum energy is required for charge breeding or ionization to occur during the electron–neutral/ion encounter. The impinging electron's energy must exceed the electron's ionization or binding energy to remove. The electron impact ionization model proposed by Lotz [20] for a step-by-step ionization, in which only one electron is removed per collision, is given by:

$$\sigma_{q \rightarrow q+1}(cm^2) = \frac{4.5\times10^{-14}}{E_e} \sum_{j=1}^{N} \frac{Z_{qj}}{\phi_{qj}} \ln \frac{E_e}{\phi_{qj}} \qquad 2.10$$

where E_e is the electron energy in eV and ϕ_{q1} is the ionization energy of the electrons in the outermost shell of the atom to ionize in eV, ϕ_{q2} is the atomic binding energy for the first inner subshell, etc, Z_q is the number of electrons in the respective shells, and N is the number of shells. Meanwhile, the number of shells needed depends on how rapidly the atomic binding energy increases with the number of shells. According to [20], $N = 2$ is sufficient for low atomic number atoms. Figure 2.1 shows the cross-section of electron impact ionization for ionizing all the charge states of oxygen using Equation 2.10 as a function of electron energy. From Equation 2.10, with $N = 2$ (oxygen has two shells with two electrons in the innermost shell, K and 6 electrons in the outermost shell, shell L), we have, where q is the charge state of the oxygen atom to ionize.

$$\sigma_{q\rightarrow q+1} = \frac{4.5\times10^{-14}}{E_e}\left(\frac{2}{\phi_{q1}}\ln\frac{E_e}{\phi_{q1}} + \frac{6}{\phi_{q2}}\ln\frac{E_e}{\phi_{q2}}\right) \quad 2.11$$

As is seen in Figure 2.1, the cross-section for producing each charge state increases with the electron energy until a maximum is reached. Further increase in the electron energy leads to a gradual decrease of the cross-section. Moreover, the cross-section for ionizing to higher charge states decreases with charge state, as shown in Figure 2.1. The cross-section for producing O$^+$ is about $5.290 \times 10^{-16} cm^2$ while the cross-section for ionizing oxygen from 7+ to 8+ is about $6.440 \times 10^{-20} cm^2$, which is over 8000 lower than the cross-section for ionizing oxygen to 1+. It is worth noting that the cross-section for all charge states which is energy dependent is maximum at electron energy about 3 to 4 times the ionization energy.

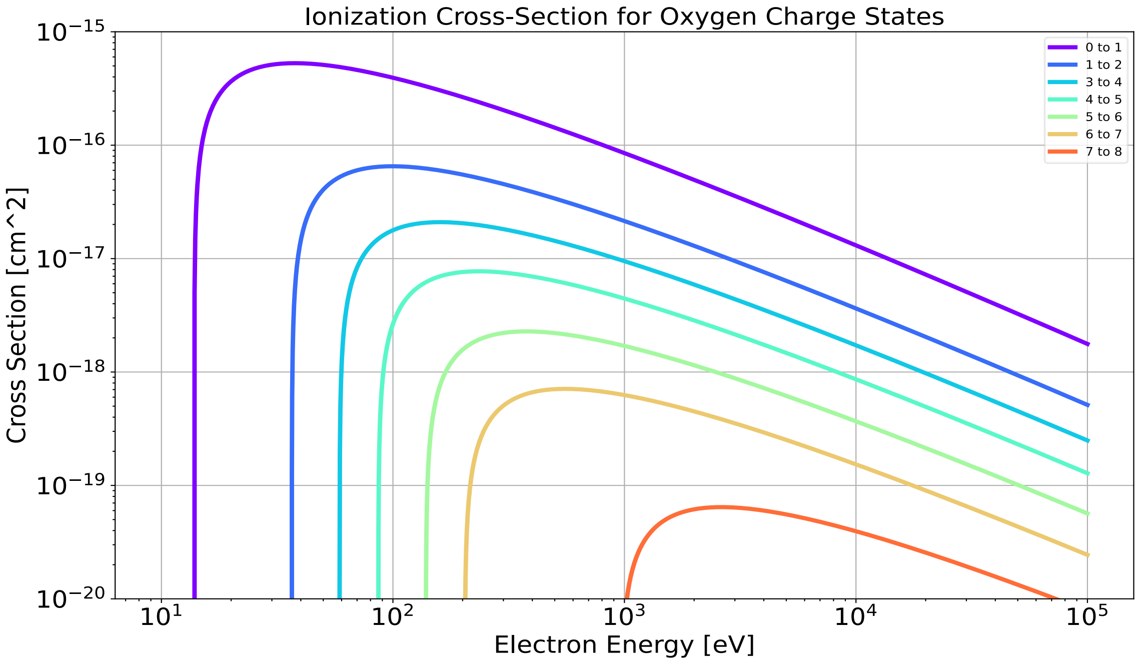

Figure 2.1: Cross-section of electron impact ionization for all the oxygen charge states using Lotz Equation for K and L shells.

For example, to ionize oxygen to 1+, the cross-section peaked at $E_e = 37.70\ eV$, and ionization energy to that charge state is $13.62\ eV$, which suggests that it requires about 2.72 times ionization energy to produce O^+. Meanwhile, since electron impact ionization cross-section decreases with charge states and electron energy, thus, to reach a higher charge state in the ECR plasma, the density of hot electrons must be increased. The process of increasing the plasma density will be discussed later in this report. The rate at which ions of charge state $q + 1$ are produced by electron impact ionization of neutrals/ions with charge state q is given by [21],

$$Rate_{production,q} = n_e \langle \sigma_{q,q+1} v_e \rangle \tag{2.12}$$

where n_e is the density of electrons, $\langle \sigma_{q,q+1} v_e \rangle$ is the product of the electron impact ionization cross-section from charge state q to $q + 1$ and electron thermal velocity averaged over the electron energy distribution. Increasing the electron density, even though the electron energy is high, highly charged ions can still be produced at the required rate.

2.2.2 Charge Exchange

In the ECR ion source, the high charge state of ions can be lost to charge exchange with neutral atoms. The density of the neutral atoms in the ECRIS is determined by the operating pressure (connected vacuum pumps). The cross-section for charge exchange from initial charge state q to final charge state $q - 1$ is given by [22],

$$\sigma_{q \to q-1} = 1.43 \times 10^{-12} q^{1.17} \phi_{0,1}^{-2.76} \tag{2.13}$$

where $\phi_{0,1}$ is the first ionization energy of the neutral atom or molecule in eV.

The cross-section of ion charge exchange with neutral atoms increases with the charge state, as shown in Equation 2.13. The cross-section equation was plotted for oxygen charge states (1+ to 8+) in Helium neutral atoms with the first ionization energy of $24.59\ eV$. The plot of the cross-section against the oxygen charge state from 1+ to 8+ is shown in Figure 2.2.

As seen in Figure 2.2, the cross-section of O^{8+} charge exchange with Helium atom and then decay to O^{7+} is higher than the cross-section of O^{7+} recombining to O^{6+} and so on. Moreover, comparing Figure 2.2 with Figure 2.1, the charge exchange cross-section is larger than the corresponding electron impact ionization. For example, to produce O^{8+}, the electron impact ionization cross-section, according to Figure 2.1, is $6.440 \times 10^{-20}\ cm^2$ while the charge exchange cross-section for O^{8+} decaying to O^{7+} is $2.364 \times 10^{-15}\ cm^2$ which is more than 10000 higher than the electron impact ionization cross-section. This shows that the rate at which highly charged ions are lost to charge exchange with neutral atoms is higher, and therefore the rest gas pressure must be kept as low as possible.

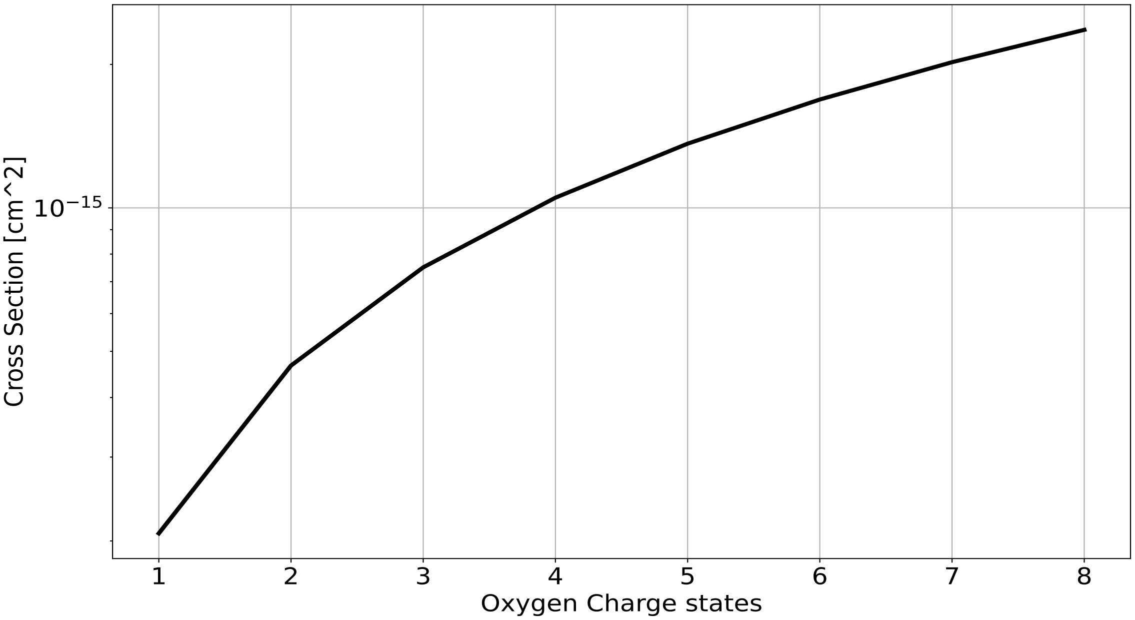

Figure 2.2: Charge exchange cross-section of oxygen charge state (1+ to 8+) in helium-neutral atoms.

According to Equation 2.12, the rate of reaction is proportional to the projectile velocities (that is, electrons and neutral atoms) and the electron density, and since neutral atoms are much slower than hot electrons and have a lower density, the rate of electron impact ionization is greater than the rate of ions charge exchange with neutral atoms. However, the rate of production of highly charged ions by electron impact ionization can be balanced with the rate of loss by charge exchange by operating the ECR plasma at low pressure (high vacuum pressure), typically at $10^{-7}\ Torr$ or less to reduce the density of neutral atoms.

2.3 Plasma Confinement

Plasma confinement is crucial in the ECR ion source to produce highly charged ions. The plasma electrons must be well confined to be efficiently heated by the applied electromagnetic field. On the other hand, ions must also be well confined to reach a higher charge state before being extracted. Since electrons and ions of ECR plasma are not at thermal equilibrium, their confinement times vary. Moreover, the electron energy distribution consists of two populations, as discussed in Section 2.2.1. They are usually described as low and high-energy electron populations. The total time needed for an ion to be stripped to a certain charge state by successive electron-impact ionization is proportional to the electron energy as given by Equation 2.14, and they are different for each electron population.

$$\tau_{confinement} \propto \frac{1}{n_e\langle E_e\sigma_{q\to q+1}\rangle} \tag{2.14}$$

where n_e is the density of electrons, $\langle\sigma_{q\to q+1}E_e\rangle$ is the product of the electron impact ionization cross-section from charge state q to $q+1$ and electron energy averaged over the electron energy distribution. In ECRIS, the ion confinement time cannot be arbitrarily interrupted like EBIS to extract the confined highly charged ions. The extracted ions from ECRIS are the ions that have lost confinement. The confinement time of ions must not be too short or too long. If it is too short, the ions do not have time to reach a high charge state, and if it is too long, the high charge state can be lost to charge exchange with neutral atoms.

In the ECR ion source, a magnetic mirror structure is employed to confine the plasma electrons, while the ions are confined by the electrostatic potential established by the electrons. The magnetic mirror is achieved using two or three sets of solenoid coils generating a magnetic field in the direction parallel to the axis of the plasma chamber with the minimum field existing at the center of the plasma chamber, which confines the plasma radially. Longitudinally, plasma confinement is achieved through the magnetic fields produced by a hexapole magnet in the radial direction. Combining these fields forms a minimum magnetic configuration that confines and stabilizes the plasma against magnetohydrodynamic (MHD) instabilities [23]. The magnetic field is minimum at the center of the plasma chamber and increases in every direction radially and longitudinally.

In a magnetic mirror structure, electrons are confined in the plasma in the direction transverse to the magnetic field. They are tied in their orbital motion to the magnetic field lines providing the means to confine the electrons. The electron confinement (if the velocity is entirely perpendicular to the applied magnetic field) is achieved due to the conservation of the magnetic moment given by,

$$\mu = \frac{mv_{\perp}^2}{2B} \tag{2.15}$$

But if there is an angle θ between the velocity of the electron and the magnetic field, Equation 2.15 is then written as $\mu = \frac{mv_{\perp}{}^2 sin^2\theta}{2B}$

Where m is the mass of electrons, $v_{\perp}$ is the velocity component transverse to the magnetic field lines, B is the magnetic flux density.

Consider the magnetic mirror structure in Figure 2.3 in which the magnetic field is produced by two solenoid coils, 1 and 2, a charged particle with a velocity $v = v_t + v_p$ is confined within the structure when the particle has a velocity component perpendicular to the magnetic field lines, where v_t is the velocity component transverse to the magnetic lines, and v_p is the velocity component that is parallel to the magnetic field lines.

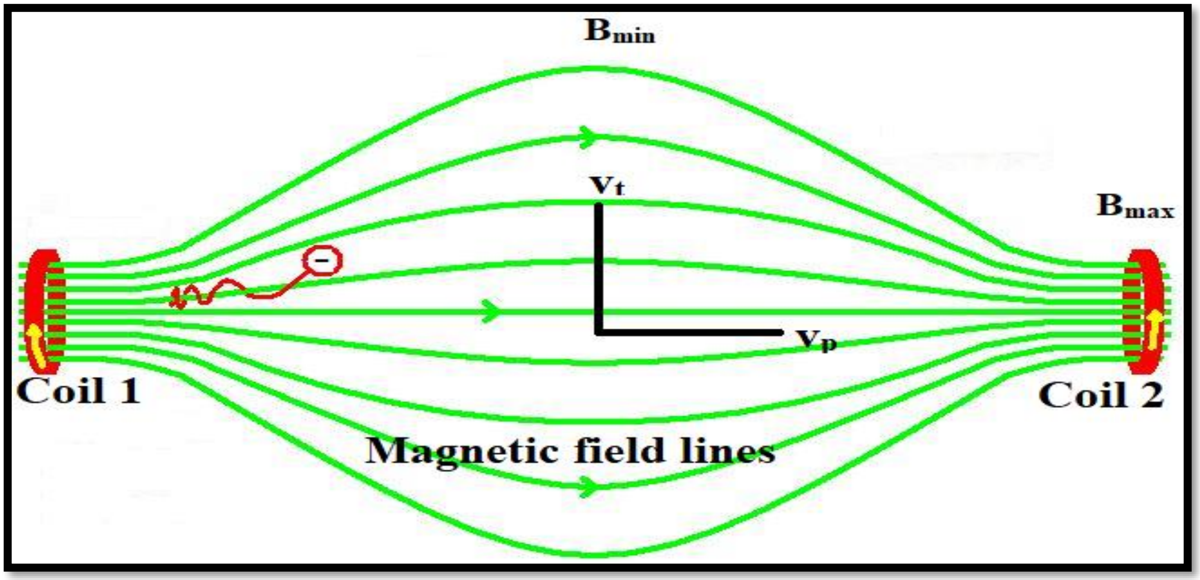

Figure 2.3: Schematic of the Structure of Magnetic Mirror Fields [24]. The Vt and Vp are the transverse and longitudinal velocity components of a charged particle with respect to the magnetic field lines.

Generally, a charged particle experiences a magnetic force called Lorentz force when placed in a magnetic field. The particle's motion is circular if there is an angle between the velocity of the particle and the magnetic field, where the field is the guiding center of the motion. The Lorentz force is given by,

$$F = Qev \times B \tag{2.16}$$

where Q is the charge of the particle, e is the electron charge, $v \times B = vBsin\theta$ where v is the total velocity of the particle, B is the magnetic field, and θ is the angle between the velocity of the particle and the magnetic field. If v is entirely perpendicular to the magnetic field, then $\theta = 90^0$ and $v \times B = v_{\perp}B$.

For conservation, the magnetic moment at the center of the magnetic mirror structure where the magnetic field is minimum must be equal to the magnetic moment where the magnetic field is maximum, which is at the coil locations,

$$\mu = \frac{mv^2 sin^2\theta}{2B_{min}} = \frac{mv^2}{2B_{max}} \qquad 2.17$$

The transverse velocity of the particle at the center of the magnetic mirror is $v_t = vsin\theta$, as the particle moves in the direction of increasing magnetic field, its transverse velocity increases so that conservation of magnetic moment is fulfilled while the longitudinal or parallel velocity component, v_p decreases. However, at the location of the maximum magnetic field, B_{max}, the parallel velocity component is zero ($v_p = 0$), and $v_t = v$, and the particle is reflected into the region of a low magnetic field. Substituting for v_t and cancelling out the like terms in Equation 2.17, we have,

$$\sin\theta = \sqrt{\frac{B_{min}}{B_{max}}} = \sqrt{\frac{1}{R_m}} \qquad 2.18$$

Where $R_m = \frac{B_{max}}{B_{min}}$ is called the mirror ratio. The angle θ determines if the particles are confined or lost. The particles with $\theta = \theta_{min} = 90^{\circ}$ are well confined at the maximum magnetic field location, while particles with $\theta_{min} > \sin^{-1}\sqrt{\frac{B_{min}}{B_{max}}}$ are trapped between B_{min} and B_{max}. The particles will continue to oscillate back and forth in the magnetic mirror provided that $\theta < 90^{\circ}$. The particles with $\theta_{min} < \sin^{-1}\sqrt{\frac{B_{min}}{B_{max}}}$ are lost into the loss cone and not confined. However, beam extraction from the ECRIS is possible because of the imperfection of the magnetic structure.

2.4 Particles Collisions in ECR Plasma

Plasma particle collisions can lead to loss of particle confinement. The temperature of the particles involved dictates collision rates in the ECR plasma, and since electrons and ions are involved and have different temperatures, there are different collision rates for electron-electron collisions, electron-ion collisions, and ion-ion collisions. There is also the collision between charged particles (electrons and ions) and neutral atoms, but collisions between charged particles dominate in ECR plasma because the density of neutral atoms is kept as low as possible by operating the ECR at low pressure (high vacuum pressure); thus, the degree of ionization is relatively high. As discussed in Section 2.2.1, the low-energy electrons and the cold ions are mostly affected by collisions. Particle collisions occur mainly at the plasma's edge since the plasma's core is hot (comprised of energetic electrons). At the plasma's edge, near the plasma chamber wall, charge neutrality is not fulfilled; thus, low-energy electrons and ions suffer collisions within the Debye length of the plasma. However, beyond the Debye length, the coulomb potential that arises from non-charge neutrality is shielded from the bulk plasma due to the collective behaviour characteristic of the plasma. At the atomic level, collision is not physical contact between two particles, and it is an interaction between the fields associated with the interacting particles. When the particles are scattered or deflected, their initial momentum is mostly lost; thus, particle collision leads to a loss of energy and momentum.

The cross-section of the collision between charged particles of the plasma has been derived in [25]. Assuming the scattered particle with mass m_1 is in motion, and the other particle with mass m_2 is at rest, the cross-section of the collision between the particles is defined as:

$$\sigma = \frac{\pi}{Mm_1}\left(\frac{Ze^2}{2\pi\epsilon_0 v^2}\right)^2 \ln\Lambda \qquad 2.19$$

where $\Lambda = \frac{\lambda_D}{b_{min}}$, Z is the charge of the ion, v is the velocity of the scattered particle, λ_D is the Debye length, b_{min} is the impact parameter, and M is the reduced mass of the particles exhibiting collision, given in Equation 2.20. $\ln\Lambda$ is called the Coulomb logarithm, and for most laboratory plasma, its value lies between 10 and 20 [26].

$$M = \frac{m_1 m_2}{m_1 + m_2} \qquad 2.20$$

For the distribution of particles, the speed of the particle in m/s is the average over the distribution given by

$$\langle v \rangle = \sqrt{\frac{3kT}{m}} \qquad 2.21$$

And mean energy in $Joule(J)$ of the distribution is given by,

$$\langle E \rangle = \frac{3}{2}kT \qquad 2.22$$

where $k = 1.38 \times 10^{-23}\, JK^{-1}$, the Boltzmann's constant, T is the temperature in $kelvin(K)$, and m is the mass of the particle.

The collision frequency between the charged particles is given by,

$$f = n\langle \sigma v \rangle \qquad 2.23$$

Substituting Equation 2.19, 2.20 and 2.21 into Equation 2.23, the collision frequency for electron-electron, electron-ion and ion-ion is defined as follows,

- **Electron-Electron Collision Frequency**

  The collision frequency for electron-electron collision is given as,

$$\langle f_{ee} \rangle = \frac{n_e e^4}{2\pi\varepsilon_0^2 \sqrt{m_e} (3kT_e)^{3/2}} ln\,\Lambda \qquad 2.24$$

- **Electron-Ion Collision Frequency**

  The electron-ion collision frequency is given as,

$$\langle f_{ei} \rangle = \frac{Z^2 e^4 n_i}{4\pi\varepsilon_0^2 (3kT_e)^{3/2} \sqrt{m_e}} ln\,\Lambda = \frac{n_i Z^2 \langle f_{ee} \rangle}{2n_e} \qquad 2.25$$

- **Ion-Ion Collision Frequency**

  The ion-ion collision frequency is given as,

$$\langle f_{ii} \rangle = \frac{Z_1^2 Z_2^2 e^4 \sqrt{A_1} n_{i2}}{4\pi\varepsilon_0^2 A_r \sqrt{m_u} (3kT_i)^{3/2}} ln\,\Lambda \qquad 2.26$$

where T_e is electron temperature, T_i is ion temperature, n_e is the density of the electron n_i is the density of ions, Z is the charge of ions, m_u is the atomic mass unit, $A_r = \text{reduced mass between the interacting ions}$, $n_{i2} = \text{density of target ions}$, and A is the atomic mass of the ion. Equations 2.24 – 2.26 show that the collision frequency depends on the electron and ion temperature and density. In particular, the electron-ion and ion-ion collisions directly vary with the square of the charge state of ions involved in the collision process.

The types of collision frequencies are plotted and compared with the ion and electron cyclotron frequencies in Figure 2.4. The collisions between $e - O^{5+}$, $e - e$, and $He^{2+} - O^{5+}$ interactions are considered, although ECR plasma comprises many ion species. The electron and ion densities were assumed to be the same so that $n_e = n_i = 2 \times 10^{18}\ m^{-3}$. Assuming $ln\Lambda = 15$, the collision frequency was plotted against the particle temperature ranging from $0.026\ eV$ to $100\ keV$, and compared with ion and electron cyclotron frequencies. For calculating electron and ion cyclotron frequencies, a magnetic field with a magnitude of $0.5\ T$ was assumed.

As shown, the collision rate between $e - O^{5+}$ is plotted in dashed black colour, the collision rates for $e - e$ interaction is plotted in dashed blue colour, while the collision rate for $He^{2+} - O^{5+}$ interaction is plotted in solid red colour.

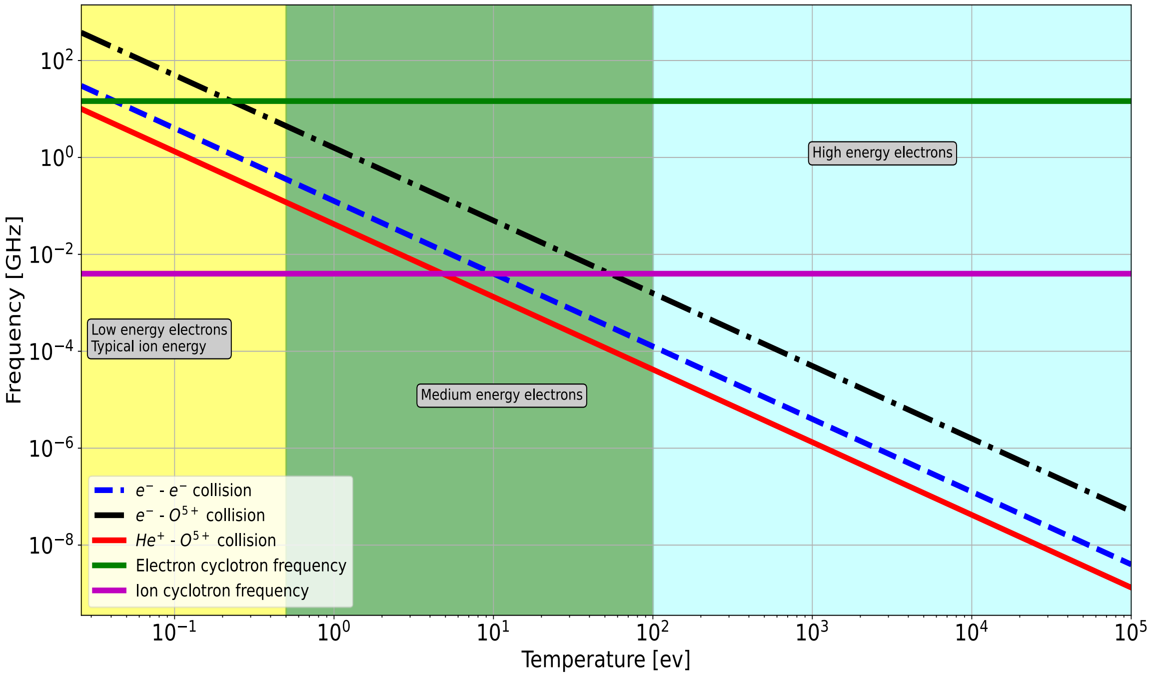

Figure 2.4: Collision frequency vs. temperature compared with cyclotron frequency for electron temperature ranging from 0.026 to 100 keV. The ion and electron cyclotron frequencies were calculated at 0.5 T.

The electron cyclotron frequency at $B = 0.5\,T$, which is $14.5\,GHz$ and independent of temperature, is plotted in solid green. The ion cyclotron frequency depends on the atomic mass and the charge state of the interacting ions. For 4He^{2+} at $B = 0.5\,T$, is about $4\,MHz$. The ion cyclotron frequency is plotted in solid magenta colour. Furthermore, as discussed in Sub-section 2.2.1, low-energy electrons have temperatures ranging from $0.026 - 100\,eV$, and high-energy electrons have a temperature greater than $100\,eV$. For simplicity, the low energy can be further categorized into low and medium temperatures, with the low temperature assumed to be between $0.026 - 0.5\,eV$ and medium temperature assumed between $0.5 - 100\,eV$ and high temperature greater than $100\,eV$. In Figure 2.4, the area shaded in yellow corresponds to the temperature of low-energy electrons, the area shaded in green corresponds to the temperature of medium-energy electrons, and the area shaded in blue corresponds to the temperature of high-energy electrons. In the ECR plasma, ion temperatures are a few electron volts, so the temperature is assumed to be the same as the low-temperature electrons.

For the $e - O^{5+}$ interactions, and for the ion and electron temperature lower than $0.2\,eV$, the collision frequency is between about $16 - 400\,GHz$, which is several factors greater than the electron and ion cyclotron frequencies, $14.5\ GHz$ and $4\ MHz,$ respectively. This suggests that electrons and ions in that temperature range are not confined magnetically but are highly collisional. For the $e-e$ interactions at the electron temperature lower than $0.04\ eV$, the collision frequency is between 16 and $30\ GHz$, a few factors higher than the electron cyclotron frequency. This indicates that electrons in this temperature range suffer more collisions than confinement by the magnetic field. For the $He^{+}-O^{5+}$ interactions, the collision frequency is between $123\ MHz$ and $10\ GHz$ which is several factors greater than the ion cyclotron frequency, and this means that the ions are not magnetically confined but suffer many collisions, and since the collision frequency depends on the mass and the charge states of the interacting ions, it varies depending on the charge states of the ions.

For the medium energy electrons, for the $e-e$ interactions, the collision frequency ranges between about $0.12\ MHz$ and $0.4\ GHz$. The collision frequency is several factors lower than the electron cyclotron frequency, and this suggests that the electrons in this temperature range are less collisional and more confined by the magnetic field. For the medium energy electrons, for the $e-O^{5+}$ interactions, the collision frequency ranges between about $1.7\ MHz$ and $5\ GHz$, and since ions are not found in this temperature range, the collision frequency depends solely on the electron temperature, and the electromagnetic field more likely confines the electrons than interacting with the ions.

At a temperature greater than $100\ keV$, the electrons are considered to have high energy and the collision frequency for both the $e-e$ and $e-O^{5+}$ interactions decrease with the increase in the electron temperature. At the temperature range, for both interactions, the collision frequency ranges from about $4\ Hz$ – $1.6\ MHz$. These collision frequencies are several orders of magnitude smaller than the electron cyclotron frequency of $14.5\ GHz$. It shows that at electron temperature greater than $100\ keV$, the electrons are almost collisionless and well confined and gyro-motions around the magnetic field largely dominate the collisions with other charged particles.

2.5 Ion Extraction from Plasmas and Extraction System

Extraction of ions from the plasma relies on the loss of ion confinement while the extraction system creates the electric fields that provide the path from the plasma to pull ions for formation and extraction. The extracted ions are not well-confined and flow to the point where they are extracted and formed into a useful beam. In other words, electrodes are required to form and extract ions from the plasma. There are many different configurations for the extraction system. The extraction system, consisting of a minimum of two electrodes, can either be a two-electrode system or a three- and more-electrode system. The configuration applicable to this thesis is the three-electrode extraction system (Figure 2.5 shows a typical example). It has the advantage over the two-electrode extraction system because the electric field in the extraction gap can be chosen so that the extracted ions' energy is not affected.

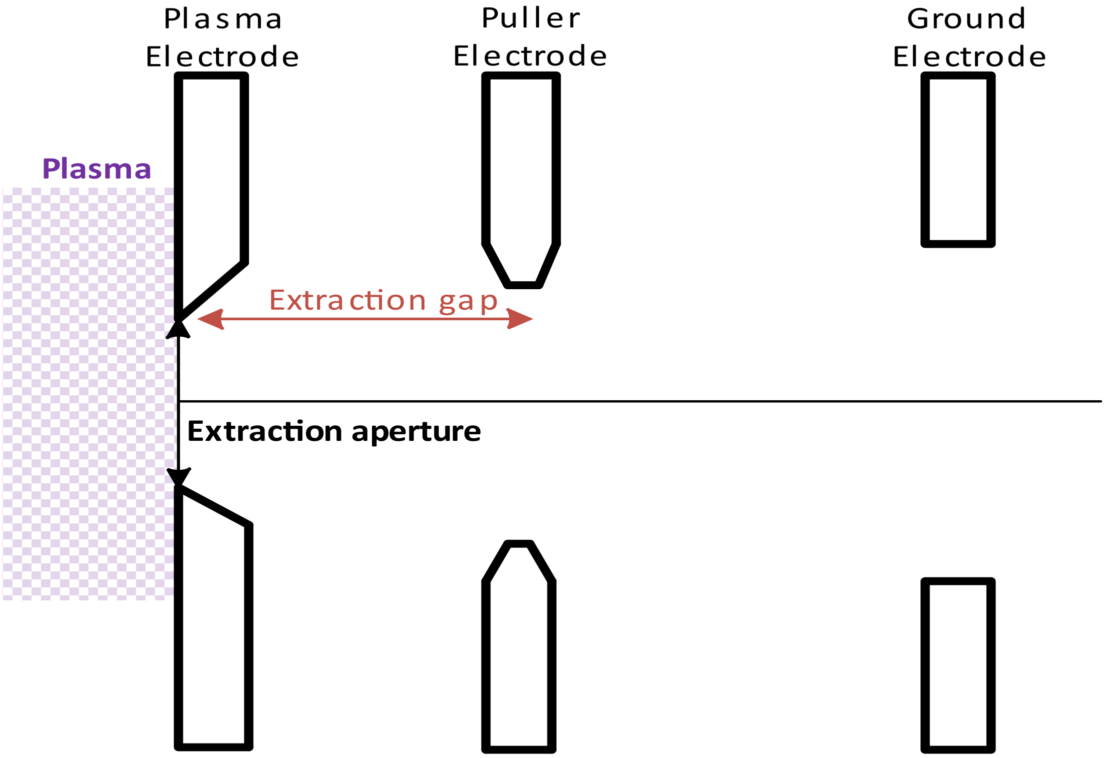

Figure 2.5: Schematic of a typical three-electrode extraction system. The system comprises the plasma electrode, the puller electrode and the ground electrode. The beam energy is determined by the potential difference between the plasma electrode and the ground electrode while the optimized extraction system is achieved based on the potential difference between the plasma electrode and the puller electrode.

In that order, it consists of the plasma electrode, the puller electrode, and the ground electrode. In any case, the first electrode, which bears the aperture where ions are emitted, is called the plasma electrode, while the last electrode is always on ground potential. Furthermore, the plasma electrode is always on the highest electrical potential (positive for ions), accelerating ions out of the plasma. In the three-electrode extraction system, the electric field that accelerates ions from the plasma is created by the potential difference between the puller electrode and the plasma electrode; thus, the extraction gap is between these electrodes.

Ion beam extraction from the plasma is quite different from the ion and electron beams extraction from the surface of a cathode because the location where the ions are emitted from called the plasma meniscus, is not fixed with respect to the puller electrode, unlike the beam emission from a cathode surface. The plasma meniscus moves in and out of the plasma boundary depending on the plasma density and the extraction fields. The Child-Langmuir law [27], [28] which describes the total and maximum extractable current from either ion source (both plasma and cathode source), is given by,

$$I_{CL}[A] = \frac{4r^2}{9d^2}\pi\varepsilon_0 U^{3/2}\sqrt{\frac{2Qe}{m}} \qquad 2.27$$

Where ε_0 is the permittivity of vacuum, e is the electron charge, Q is the ion charge state, m is the mass in kg, d is the extraction gap in $meters$, r is the extraction aperture in $meters$, and U is the potential drop in $Volts$. For example, using the geometrical parameters of the TRIUMF ECRIS CSB extraction system, the maximum extractable current from a pure Helium-4 plasma with $Q = 2+$ at a potential drop of $2.5\ kV$ for an extraction aperture radius of $3\ mm$ and extraction gap of $25\ mm$ is about $220\ \mu A$.

For a given extraction system, the extraction gap is fixed during the design, and for a given potential drop between the plasma electrode and puller electrode and a fixed emitting surface, Equation 2.27 determines the total theoretical achievable ion beam current. Since the plasma meniscus is not fixed with respect to the puller electrode, the total current varies. The shape of the meniscus can either be concave (plasma boundary shifts inward, long extraction gap), planar (boundary maintains the designed extraction gap, plane) or convex (boundary shifts outward, shorter extraction gap), as shown in Figure 2.6. However, the optimum extraction field can be determined by systematically varying the potential drop between the plasma electrode and the puller electrode. The effect of the plasma meniscus on the beam emittance will be discussed later in Chapter 5.

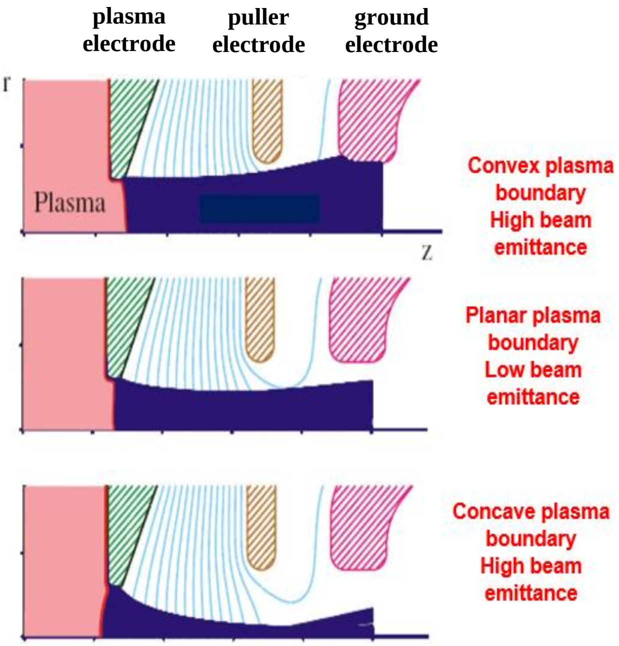

Plasma density too high or applied extraction field too low

Plasma density matched the applied extraction field

Plasma density too low or applied extraction field too high

Figure 2.6: Schematic of plasma meniscus in a three-electrode extraction system. The schematic describes the plasma boundary depending on the plasma density, space density and applied extraction field between the plasma electrode and the puller electrode.

2.6 Electromagnetic Waves Propagation in Magnetized Plasma

In the ECR ion source, plasma is ignited when an electromagnetic wave of a defined frequency is introduced. The electromagnetic wave selectively heats the plasma's electron (most electrons with a reasonable temperature) on a small surface in the plasma where the applied wave's frequency equals the electrons' cyclotron frequency due to the magnetic field. When the frequency of the electromagnetic wave is equal to the electron cyclotron frequency, there is an efficient transfer of energy between the wave and the electrons. The method of selectively heating the electrons in the plasma is called Electron Cyclotron Resonance Heating (ECRH). The equation that describes ECRH is given by,

$$f_{rf} = f_{cyc} = \frac{eB}{2\pi m_e} \tag{2.28}$$

where f_{rf} is the frequency of the electromagnetic wave, e is the electron charge, m_e is the mass of the electron, and B is the magnitude of the applied magnetic field at the resonance surface.

Plasma, generally, is a conducting medium with dielectric, conductivity and refractive index; however, in an ECR plasma, where a magnetic field is applied for particle confinement, the electrical properties of such plasma become highly anisotropic because of different components of motions (parallel and perpendicular) that arise due to the applied magnetic field. The anisotropic feature in magnetized plasmas makes electromagnetic wave propagation a complicated process. To simplify the complexity, the cold plasma approximation has been adopted. In this approximation, the wave propagating in the plasma is assumed to be travelling at the phase velocity close to the speed of light, and the thermal velocity of the particles is far lower than the speed of light, so the electrons of the plasma that will be selectively heated are considered to be at rest except for motions created by the electromagnetic wave.

In [29], the properties of the electromagnetic wave in a magnetized, cold and collisionless plasma have been derived from Maxwell's and Lorentz's force equations. The refractive index of the wave in the plasma is called the Appleton-Hartree equation given as:

$$N = \sqrt{1 - \frac{X(1-X)}{1-X-\frac{1}{2}Y^2\sin^2\theta \pm \left[\left(\frac{1}{2}Y^2\sin^2\theta\right)^2 + (1-X)^2Y^2\cos^2\theta\right]^{1/2}}} \qquad 2.29$$

where $X = \frac{f_p^2}{f_{rf}^2}$, $Y = \frac{f_{cyc}}{f_{rf}}$, f_p is the plasma frequency, f_{cyc} is the electron cyclotron frequency f_{rf} is the frequency of the propagating electromagnetic wave, and θ is the angle between the propagation vector of the wave and the applied magnetic field. The refractive index, N is related to the phase velocity of the wave by $N = \frac{c}{v_{rf}}$, where c is the speed of light and v_{rf} is the phase velocity of the wave in plasma.

There are four possible solutions to Equation 2.28 depending on the orientation of the propagating wave with respect to the applied magnetic field. The wave can either be oriented parallel to the magnetic field, $\theta = 0^{\circ}$ or perpendicular to the magnetic field, $\theta = 90^{\circ}$.

- For $\theta = 0^{\circ}$, the wave propagates parallel to the magnetic field; these waves are called Right-hand (R) and Left-hand (L) polarized waves, respectively.
- For $\theta = 90^{\circ}$, the wave propagates perpendicular to the magnetic field; these waves are called Ordinary (O) and Extraordinary (X) waves, respectively.

The equations for the conditions above are referred to as the dispersion relations, which are summarized in Table 2.1

Table 2.1: Dispersion Relations of Electromagnetic Wave Propagation in Magnetized Cold Plasmas

Conditions	Dispersion Relations	Wave Type	
$\boldsymbol{\theta} = \mathbf{0}^{\circ}$ $(\vec{\boldsymbol{k}} \parallel \vec{\boldsymbol{B}})$	$N = \sqrt{1 - \frac{f_p^2/f_{rf}^2}{1 - f_{cyc}/f_{rf}}}$	Right-hand (R) Polarized Wave	2.30
$\boldsymbol{\theta} = \mathbf{0}^{\circ}$ $(\vec{\boldsymbol{k}} \parallel \vec{\boldsymbol{B}})$	$N = \sqrt{1 - \frac{f_p^2/f_{rf}^2}{1 + f_{cyc}/f_{rf}}}$	Left-hand (L) Polarized Wave	2.31
$\boldsymbol{\theta} = \mathbf{90}^{\circ}$ $(\vec{\boldsymbol{k}} \perp \vec{\boldsymbol{B}})$	$N = \sqrt{1 - \frac{f_p^2}{f_{rf}^2}}$	Ordinary (O) Wave	2.32
$\boldsymbol{\theta} = \mathbf{90}^{\circ}$ $(\vec{\boldsymbol{k}} \perp \vec{\boldsymbol{B}})$	$N = \sqrt{1 - \frac{f_p^2}{f_{rf}^2}\left(\frac{f_{rf}^2 - f_p^2}{f_{rf}^2 - f_p^2 - f_{cyc}^2}\right)}$	Extraordinary (X) Wave	2.33

$\vec{k}$ is electromagnetic wave propagation vector and $\vec{B}$ is a magnetic field vector.

According to Table 2.1, all the waves except O-wave (2.32) depend on the electron cyclotron frequency. The O-wave behaves like the plasma is unmagnetized and has a refractive index equal to zero only when the wave's frequency equals that of the plasma frequency. Besides, the O-wave does not propagate at an electromagnetic wave frequency less than the plasma frequency. Furthermore, if there was no plasma oscillation, that is if $f_p = 0$, then the refractive indexes of all the waves equal one, and plasma behaves like a medium made of vacuum, and there is no change in the wave's phase velocity.

The applied wave must first penetrate the plasma for electron heating to occur in the ECR plasma. The plasma frequency defines the wave frequency that can propagate in the plasma. If the frequency of the applied electromagnetic wave is smaller than the frequency of the plasma electrons oscillating around their equilibrium positions, the electrons are not influenced by the wave; thus, the plasma acts as an opaque body to the wave, and the wave is reflected at the plasma boundary. However, at the electromagnetic wave frequency greater than or equal to the plasma frequency, the plasma electrons appear stationary to the wave, and the wave penetrates the plasma. In addition, the ECR plasma requires a magnetic field to confine the electrons, so it is also important that the electron cyclotron frequency is also greater than the plasma frequency.

In Figure 2.7, the phase velocities of the propagating waves in a magnetized plasma are plotted against the frequency of electromagnetic waves ranging from 1 GHz to 20 GHz with the y-axis plotted in logarithmic scale. The right-hand polarized wave is plotted in red, the left-hand polarized wave is plotted in cyan, the O-wave in green, and the X-wave in blue. The solid magenta line is the electron cyclotron frequency determined at the magnetic field $B = 0.52\ T$. The black dashed line is the plasma frequency at $n_e = 1.79 \times 10^{18}\ m^{-3}$. The magenta dashed line is the upper hybrid frequency $f_{rf}^2 = f_p^2 + f_{cyc}^2$. The region shaded in blue are the frequencies less than the plasma frequency, and the region shaded in red are the frequencies greater than the plasma frequency.

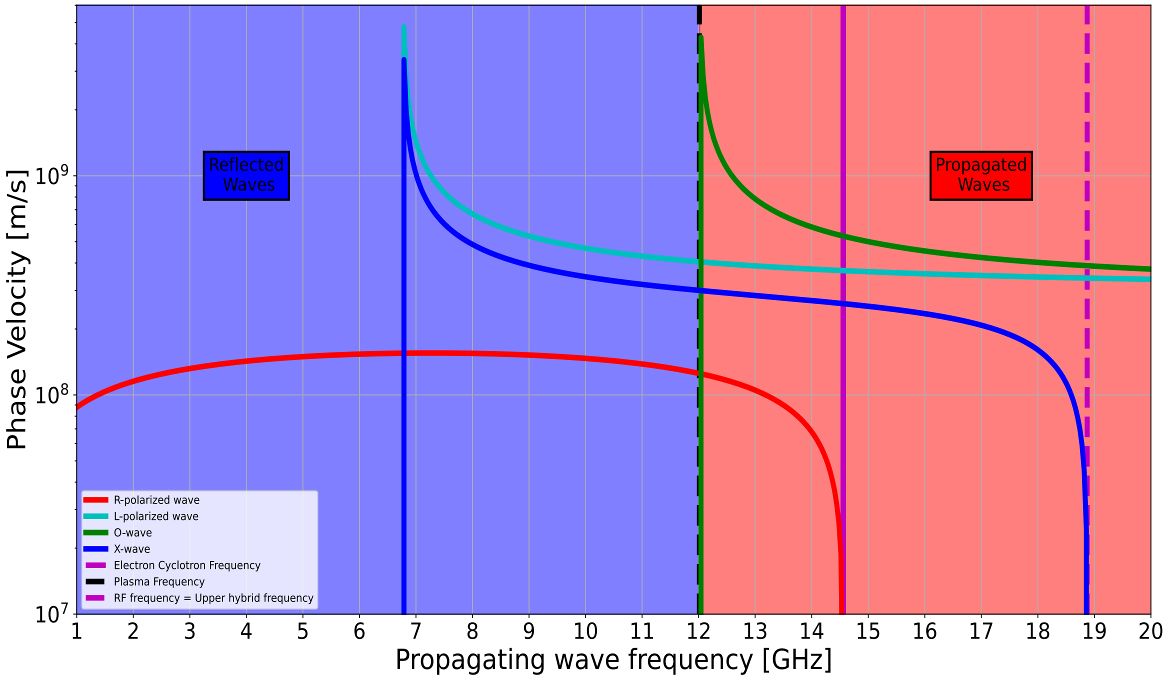

Figure 2.7: Phase velocity of R-polarized wave, L-polarized wave, O-wave and X-wave in a magnetized cold plasma compared with electron cyclotron frequency, plasma frequency and upper hybrid frequency. An electromagnetic wave with a frequency less than 12 GHz is reflected at the plasma boundary while a frequency greater than 12 GHz propagates through the plasma boundary.

As seen in the Figure, the O-wave does not propagate at the frequency below the plasma frequency; it is cut off at the plasma frequency. The phase velocity of the X-wave strongly depends on the plasma density. Increasing the plasma density increases the wave's velocity until the cut-off is reached. Further increase in the plasma density leads to an evanescent wave until it attains resonance at the upper hybrid frequency and then propagates until it is cut off again [30]. The L-wave does not have resonance, while the R-wave has a resonance at a frequency equal to the electron cyclotron frequency. The ECRIS operates based on the R-wave. The wave's phase velocity drops to zero, and the wave's energy is dissipated and absorbed by the electrons exhibiting gyration motion around the magnetic field at the said frequency. This process of energy absorption by the electrons is called electron cyclotron resonance heating (ECRH).

Chapter 3 - Beam Transport System and Transverse Beam Dynamics

3.1 Introduction

In this chapter, a brief review of the optics of the charge state booster that I worked on is presented. This includes the transfer matrices of drifts, electrostatic quadrupoles, magnetic dipoles, and electrostatic benders. An introduction to emittance and Liouville's theorem is also provided, followed by a discussion of the quadrupole scan technique (QST) for the emittance measurement of the CSB that I developed. The method of error analysis in the QST measurement is presented, along with a simple description of the space charge effect. Finally, a summary of the magnetic emittance in the electron cyclotron resonance Ion Source is discussed. Refer to [31] for further reading on linear beam optics.

3.2 Hill's Equation and Linear Beam Optics

In a rare isotope separation and acceleration facility like TRIUMF's, low-energy beam transports (LEBT) are usually used to transport beams (up to a few tens of keV) to experimental areas. The most efficient and cost-effective way to transport the beams at this energy is by using electrostatic focusing and bending elements. The reason can be deduced from the Lorentz force, Equation 3.1. If the velocity, v of a beam, is much less than the speed of light ($v \ll c$), then the force that a beam experiences due to the first term of Lorentz force is much larger than the second term. Besides, electric fields up to 1 MV/m are far more economical to produce than magnetic fields up to 1 T. Furthermore, with an electrostatic field, unlike a magnetostatic field, each specie of an ion beam accelerated from rest by the same potential will have the same trajectory.

$$F = Qe(E + v \times B) \tag{3.1}$$

where Q is the charge state of a beam, e is the charge of the electron, E is the electric field, v is the beam's velocity, and B is the magnetic field. Since at low energy, electrostatic focusing is employed, Equation 3.1 reduces to

$$F = QeE \tag{3.2}$$

As the ions have the same charge, they experience intra-repelling Coulomb force that leads to transverse or radial beam divergence. Transverse focusing is important in beam transport; otherwise, the transported beam will grow unnecessarily in the directions perpendicular to the main direction of the beam. Transverse focusing involves providing restoring forces, usually linear, created by an electric and /or magnetic field to reduce the divergence of the transported beam. The term “emittance” describes beam divergence in accelerator physics. Thus, for a useful beam, it is important to keep the beam emittance as low as possible otherwise, the exotic isotopes being transported will be lost to the walls of the transport system. The transverse directions are usually taken as x and y, while the main direction of the beam is usually taken as s. During beam transport, quadrupoles (quads) are used to provide focusing for accelerated beams and dipoles are used to bend the beam around corners. However, depending on their energy as previously stated in the introduction, electrostatic quads and electrostatic benders are used to focus and bend beams with a velocity much less than the speed of light, while magnetostatic quads and dipoles are used to focus and bend beams with a velocity closer to the speed of light. To describe the effects of electrostatic quadrupoles and bender on a beam, let us consider the motion of a single particle of mass m with charge Q whose velocity is solely in the direction of travel (that is $v = (0,0, v_s)$ where s is the direction of particle travel) in an electric field that has components perpendicular to the direction of travelling of the particle so that the electric field has the form $\vec{E} = \left(E_x, E_y, 0\right)$. The particle will be deflected and have a circular trajectory of radius ρ. Taking $x - s$ as the horizontal plane, then there is a balance between the x component of Equation 3.2 and the centrifugal force $F_r = mv_s^2/\rho$ where ρ is the radius of curvature of the beam trajectory given as

$$F_x = QeE_x(x, y, s) = \frac{mv_s^2}{\rho(x,y,s)} \tag{3.3}$$

Because the overall transverse dimensions of the particle are small compared to the radius of curvature of the particle trajectory, then the electric field can be expanded in the vicinity of the nominal particle trajectory, say x direction, so that;

$$E_x(x) = E_{x0} + \frac{dE_x}{dx}x + \cdots \tag{3.4}$$

The electric field around the particle may be regarded as a sum of many terms in which each term affects the particle's path differently. For linearity, we will only consider the first-order terms. The first term is the bending or deflection effect (electrostatic bender), and the second is the focusing effect (electrostatic quadrupole). So that by equating Equation 3.3 to 3.4, we have,

Table 3.1: Bending and Focusing Effects of Transverse Electric Field

Effects	**Field term (x direction only)**
Bending effect	$\frac{1}{\rho} = \frac{E_{x0}}{2U_{acc}}$
Focusing/Defocusing effect	$K = \frac{1}{2U_{acc}}\frac{dE_x}{dx}$

Where K is the strength of the quadrupole, $mv_s^2 = 2QeU_{acc}$, U_{acc} is the beam acceleration voltage. The equations of motion that describe the motion of charged particles in a series of quadrupoles and benders transporting the particles from one location to another have been derived in [32] these fundamental equations are referred to as Hill's equation. For a constant quadrupole strength and bending radius, Hill's equation in the transverse direction (both x and y directions) is given as,

$$x''(s) + \left(\frac{1}{\rho^2} - K\right)x(s) = \frac{1}{\rho}\frac{\Delta P}{P},\ y''(s) + Ky(s) = 0 \qquad 3.5$$

Where x'' and y'' are the second derivative of x and y with respect to s, ρ is the radius of curvature of the beam trajectory in benders, K is the quadrupole strength which is the gradient of either the magnetic field or electric field, and $\Delta P/P$ is the relative momentum deviation. The expressions for both ρ and K are given in Table 3.1. As seen in Equation 3.5, there is no coupling between the $x - s$ plane and $y - s$ plane; hence it is sufficient to consider only one plane while solving Hill's equation. Hill's equation is used to describe the motion of a beam through a series of optics. The beam optics are a drift region usually denoted as O (a region where this no restoring forces), a quadrupole usually denoted as F and D (where F means focusing and D means defocusing). A transport system, for example, may consist of a focusing quadrupole (F), a drift region (O), a defocusing quadrupole (D) and finally, a drift region (O). This type of transport system is called a FODO lattice transport system. There can be many FODO lattices in a single transport system, and the overall effect of these latices is to provide an overall focus for the beam that is being transported. In the following sections, we will consider the effect of each optic on the motion of a single particle after the particle has travelled a certain distance through the optics.

3.3 Drift Region

In the drift region, there is no bending of the particle and no focusing or defocusing effect on the particle. So $1/\rho = 0$, $K = 0$ and Equation 3.5 reduces to

$$x''(s) = 0, y''(s) = 0 \qquad 3.6$$

Consider a particle travelling through a drift region of length d, the final coordinate, considering only $x - s$ plane – horizontal direction, (x, x') of the particle is the solution to Equation 3.6, which is given as (similarly in $y - s$ plane – vertical direction),

$$x = x_0 + x_0' d,\ x' = x_0' \qquad 3.7$$

Where d is the length of the drift space, x_0 is the initial position of the beam, x_0' is the initial beam divergence (angle), and x and x' are the final position and angle of the beam. As can be seen in Equation 3.7, the particle's final position increased by $x_0' d$.

Equation 3.7 can be transformed into a 2×2 matrix as $\begin{pmatrix} x \\ x' \end{pmatrix} = \begin{pmatrix} 1 & d \\ 0 & 1 \end{pmatrix} \begin{pmatrix} x_0 \\ x_0' \end{pmatrix}$.

Similarly, in y direction, we have $\begin{pmatrix} y \\ y' \end{pmatrix} = \begin{pmatrix} 1 & d \\ 0 & 1 \end{pmatrix} \begin{pmatrix} y_0 \\ y_0' \end{pmatrix}$, where $\begin{pmatrix} x_0 \\ x_0' \end{pmatrix}$ and $\begin{pmatrix} y_0 \\ y_0' \end{pmatrix}$ are the starting coordinates of the particle, $\begin{pmatrix} x \\ x' \end{pmatrix}$ and $\begin{pmatrix} y \\ y' \end{pmatrix}$ are the final position of the beam. The 2×2 matrix $\begin{pmatrix} 1 & d \\ 0 & 1 \end{pmatrix}$ is called the transfer matrix of the drift region. However, to determine the final position of a particle through a drift length region of length d, the transfer matrix is multiplied by the beam's initial position.

$$\begin{pmatrix} x \\ x' \\ y \\ y' \end{pmatrix} = \begin{pmatrix} 1 & d & 0 & 0 \\ 0 & 1 & 0 & 0 \\ 0 & 0 & 1 & d \\ 0 & 0 & 0 & 1 \end{pmatrix} \begin{pmatrix} x_0 \\ x_0' \\ y_0 \\ y_0' \end{pmatrix} \qquad 3.8$$

Generally, for a drift space of length d in both $x\ and\ y$ directions, the transfer matrix is given as

$$M_O = \begin{pmatrix} 1 & d & 0 & 0 \\ 0 & 1 & 0 & 0 \\ 0 & 0 & 1 & d \\ 0 & 0 & 0 & 1 \end{pmatrix} \qquad 3.9$$

3.4 Electrostatic Quadrupole

Quadrupoles are generally used to provide the overall focusing of transported beams. The schematic of an electrostatic quadrupole is shown in Figure 3.1, where a is the radius of the aperture of the quad, and the electrodes of the quad are defined by the parabolic curve with voltage $-V$ and $+V$. However, the quadrupolar field geometry close to the beam axis can be very well approximated by circular-shaped electrodes, with an optimized radius.

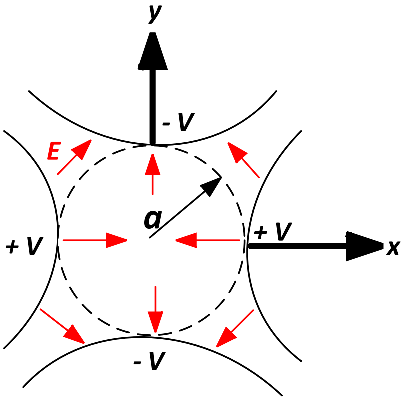

Figure 3.1: Schematic of electrostatic quadrupole and electric field lines of the quadrupole electrode. The electrode cross-section is circularly shaped for simplification of the geometry, while optimally approximating the fields of the optic.

The direction of beam travel is into the page. The red arrows are the electric field created by the electric potential V on the electrodes.

Consider the motion of a single particle travelling from one point to another through a quadrupole of length L and strength K; since the quadrupole focusing effect is created only by the second term of Equation 3.4 as given in Table 3.1, there is no bending effect, so $1/\rho = 0$ and assume $\Delta P = 0$, Equation 3.5 reduces to

$$x''(s) - Kx(s) = 0, \;\; y''(s) + Ky(s) = 0 \qquad 3.10$$

As seen in Equation 3.10, the quadrupole strength K is negative in x direction and positive in y direction because the quadrupole is focusing in one direction and defocusing in another direction simultaneously. The solutions to Equation 3.10 for a given quadrupole of length L are,

- For $K > 0$, Focusing

$$x = x_0 \cos(\sqrt{K}L) + \frac{x_0'}{\sqrt{K}} \sin(\sqrt{K}L)$$

$$x' = -x_0\sqrt{K} \sin(\sqrt{K}L) + x_0' \cos(\sqrt{K}L)$$

- For $K < 0$, Defocusing

$$y = y_0 \cos h(\sqrt{K}L) + \frac{y_0'}{\sqrt{K}} \sin h(\sqrt{K}L)$$

$$y' = y_0\sqrt{K}\,\sinh\left(\sqrt{K}L\right) + y_0'\cos h\left(\sqrt{K}L\right)$$

In general, a particle moving through a quadrupole experience a defocusing force in the vertical plane, say y direction and a focusing force in the horizontal plane, say x direction and vice versa. As a result, a 4×4 matrix is required to describe the motion of a particle through a quadrupole. So, for a quadrupole that is focusing in the horizontal direction, the four-dimensional trajectory vector is given by with, $\varphi = \sqrt{K}L$,

$$\begin{pmatrix} x \\ x' \\ y \\ y' \end{pmatrix} = \begin{pmatrix} cos\,\varphi & \frac{1}{\sqrt{K}}sin\,\varphi & 0 & 0 \\ -\sqrt{K}\,sin\,\varphi & cos\,\varphi & 0 & 0 \\ 0 & 0 & cosh\,\varphi & \frac{1}{\sqrt{K}}sinh\,\varphi \\ 0 & 0 & \sqrt{K}\,sinh\,\varphi & cosh\,\varphi \end{pmatrix} \begin{pmatrix} x_0 \\ x_0' \\ y_0 \\ y_0' \end{pmatrix} \quad 3.11$$

However, suppose the quadrupole is required to focus the particle in the vertical direction, then, the matrix elements are interchanged so that the hyperbolic functions are replaced with the normal trigonometric functions and vice versa. Equations 3.12 and 3.13 summarize the transfer matrices for the quadrupoles defocusing horizontally (focusing vertically) and focusing horizontally (defocusing vertically), respectively.

$$M_{DQ} = \begin{pmatrix} cosh\,\varphi & \frac{1}{\sqrt{K}}sinh\,\varphi & 0 & 0 \\ \sqrt{K}\,sinh\,\varphi & cosh\,\varphi & 0 & 0 \\ 0 & 0 & cos\,\varphi & \frac{1}{\sqrt{K}}sin\,\varphi \\ 0 & 0 & -\sqrt{K}\,sin\,\varphi & cos\,\varphi \end{pmatrix} \quad 3.12$$

$$M_{FQ} = \begin{pmatrix} cos\,\varphi & \frac{1}{\sqrt{K}}sin\,\varphi & 0 & 0 \\ -\sqrt{K}\,sin\,\varphi & cos\,\varphi & 0 & 0 \\ 0 & 0 & cosh\,\varphi & \frac{1}{\sqrt{K}}sinh\,\varphi \\ 0 & 0 & \sqrt{K}\,sinh\,\varphi & cosh\,\varphi \end{pmatrix} \quad 3.13$$

In a beam transport system, the focusing strength of the quadrupole is often localized to a point usually referred to in light optics as the focal point. The localized focusing quadrupoles are referred to as thin lens quadrupoles. With a thin lens, a quadrupole is designed with a focal length much greater than the length of the quadrupole. Assume that as the length of the quadrupole approaches zero ($L \rightarrow 0$), which is a thin lens approximation, the focal power of the quadrupole is constant. From Equation 3.13 (similarly in Equation 3.12), after finding the series expansion of the trigonometric functions, then $\cosh\varphi = \cos\varphi = 1, \frac{1}{\sqrt{K}}sinh\,\varphi = \frac{1}{\sqrt{K}}sin\,\varphi = 0$

and $\sqrt{K}\, sinh\, \varphi \approx \sqrt{K}\, sin\, \varphi \approx KL$. Thus, the thin lens approximation results in the focal length of the quadrupole as $f = \frac{1}{KL}$ and Equation 3.13 reduces to

$$M_{FQ} = \begin{pmatrix} 1 & 0 & 0 & 0 \\ -KL & 1 & 0 & 0 \\ 0 & 0 & 1 & 0 \\ 0 & 0 & KL & 1 \end{pmatrix} \qquad 3.14$$

For electrostatic quadrupole, the potential on the electrodes is defined as $V = \frac{V_0}{a^2}(y^2 - x^2)$. Using the quadrupole strength defined in Table 3.1, where $E = -\nabla V,$ the strength of the quadrupole is defined as $K = \frac{|V_0|}{a^2 U_{acc}}$, where V_0 is the electric potential, a is the radius of the aperture of the quadrupole and U_{acc} is the beam acceleration voltage.

3.5 Magnetic Dipole

A magnetic dipole is used as the mass separator in an accelerator facility. It is used to separate ion beams into their respective mass depending on the momentum of the ions.

Consider a beam of a non-relativistic particle entering a magnetic dipole of an effective length l, if the particle's motion is perpendicular to the magnetic field of the dipole, the ions travel in a circular motion around the magnetic field. The radius of curvature of the beam trajectory in a constant magnetic field as derived from centrifugal and the Lorentz forces in meters is:

$$\rho_B = \frac{1.44\times10^{-4}}{B}\sqrt{\left(\frac{A}{Q}\right) U_{acc}} \qquad 3.15$$

where B is the magnitude of the magnetic field in Tesla of the dipole, U_{acc} is the beam acceleration voltage, A is the atomic mass of the beam, and Q is the charge state.

Equation 3.15 shows that at a constant magnetic field and acceleration voltage, the ions entering perpendicularly into the magnetic dipole follow a radius defined by their $A/_{Q}$ ratio.

Hill's Equation can be written as

$$x''(s) + \left(\frac{1}{\rho_B{}^2} - K\right) x(s) = \frac{1}{\rho_B}\frac{\Delta P}{P},\ y''(s) + Ky(s) = 0 \qquad 3.16$$

The transfer matrix extracted from the inhomogeneous solution of Equation 3.16 where $K = n/\rho_B^2$ and $\varphi = 1 - n$ such that $0 < n < 1$ is given as

$$M_d = \begin{pmatrix} cos\frac{\sqrt{\varphi}l}{\rho_B} & \frac{\rho_B}{\sqrt{\varphi}}sin\frac{\sqrt{\varphi}l}{\rho_B} & 0 & 0 & \frac{\rho_B}{\varphi}(1-cos\frac{\sqrt{\varphi}l}{\rho_B}) \\ -\frac{\sqrt{\varphi}}{\rho_B}sin\frac{\sqrt{\varphi}l}{\rho_B} & cos\frac{\sqrt{\varphi}l}{\rho_B} & 0 & 0 & \frac{1}{\sqrt{n}}sin\frac{\sqrt{\varphi}l}{\rho_B} \\ 0 & 0 & cos\frac{\sqrt{n}l}{\rho_B} & \frac{\rho_B}{\sqrt{n}}sin\frac{\sqrt{n}l}{\rho_B} & 0 \\ 0 & 0 & -\frac{\sqrt{n}}{\rho_B}sin\frac{\sqrt{n}l}{\rho_B} & cos\frac{\sqrt{n}l}{\rho_B} & 0 \\ 0 & 0 & 0 & 0 & 1 \end{pmatrix}$$

3.17

The transfer matrix of the dipole is a 5×5 matrix, unlike the solution of the quadrupole and drift region. The added term to the x- direction motion where the beam is deflected is the dispersion created by the dipole due to the change in the momentum of the deflected beam. There is no dispersion in the y −direction because the ions are undeflected since this direction is the same as the direction of the dipole magnetic field. Furthermore, by comparing the transfer matrix with the solution of the quadrupole, we immediately realize that the beam through the dipole is weakly focused in both directions because of the negative sign as they exit the dipole. The focusing effect is due to the field index n included in Equation 3.16. In other words, by introducing a slight gradient in the dipole's magnetic field, weak focusing is distributed between the vertical and horizontal planes where the beam is travelling.

From Equation 3.17, if the field gradient $n = 0$, then $K = 0$, and we have,

$$M_d = \begin{pmatrix} cos\frac{l}{\rho_B} & \rho_B\, sin\frac{l}{\rho_B} & 0 & 0 & \rho_B\left(1-cos\frac{l}{\rho_B}\right) \\ -\frac{1}{\rho_B}sin\frac{l}{\rho_B} & cos\frac{l}{\rho_B} & 0 & 0 & sin\frac{l}{\rho_B} \\ 0 & 0 & 1 & l & 0 \\ 0 & 0 & 0 & 1 & 0 \\ 0 & 0 & 0 & 0 & 1 \end{pmatrix} \qquad 3.18$$

Equation 3.18 is the general transfer matrix of a dipole magnet with a uniform magnetic field. When a particle enters such a dipole, the particle follows a trajectory with a curvature radius defined by the magnetic field and the mass-to-charge ratio of the said particle; it then exits the dipole with a larger size due to the change in transverse momentum in one direction, usually referred to as momentum dispersion which is accounted for by the term in the last column of the transfer matrix; meanwhile, the trajectory of the particle is unaffected in the other direction.

3.6 Electrostatic Bender

Electrostatic benders are used to bend beams with low kinetic energy around corners in accelerator facilities. Unlike magnetic dipole, the radius ρ_E that the deflected beam follows depends only on the kinetic energy of the beam which is defined by the accelerating voltage U_{acc}, thus making the optics energy-dispersive. The electric field lines of the bender are perpendicular to the beam's velocity. Figure 3.2 shows the schematic of an electrostatic bender.

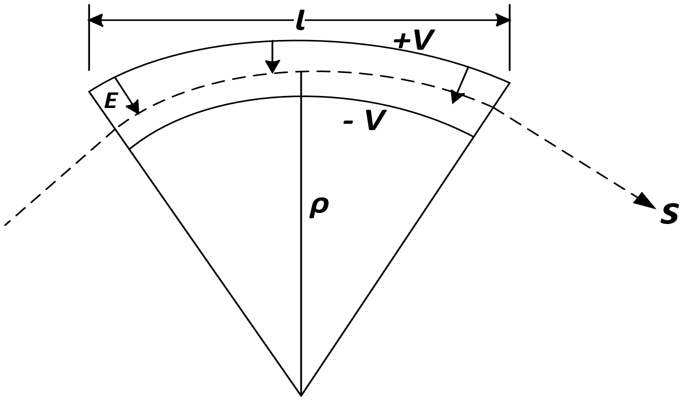

Figure 3.2: Schematic of the side view of an electrostatic bender showing the electric field lines and curvature radius of the electrodes.

Meanwhile, because an electric field is used to bend the beam, the solution for the electrostatic bender is not as straightforward as the magnetic bender. However, a detailed explanation and solution have been presented in [33], [34]. The first-order transfer matrix derived from the general Hamiltonian for electrostatics for a non-relativistic beam is given as

$$M_E = \begin{pmatrix} \cos\vartheta & \rho_E \sin\vartheta & 0 & 0 & 0 & 2\rho_E(1-\cos\vartheta) \\ \frac{-1}{\rho_E}\sin\vartheta & \cos\vartheta & 0 & 0 & 0 & 2\sin\vartheta \\ 0 & 0 & \cos\vartheta & \rho_E \sin\vartheta & 0 & 0 \\ 0 & 0 & \frac{-1}{\rho_E}\sin\vartheta & \cos\vartheta & 0 & 0 \\ -2\sin\vartheta & -2\rho_E(1-\cos\vartheta) & 0 & 0 & 1 & \rho_E\vartheta[1-4\left(1-\frac{\sin\vartheta}{\vartheta}\right)] \\ 0 & 0 & 0 & 0 & 0 & 1 \end{pmatrix} \quad 3.19$$

Where $\rho_E = 2U_{acc}/E$, $\vartheta = l/\rho_E$, U_{acc} is the accelerating voltage, and E is the electric field between the spherical plates of the bender. The solution of the Hamiltonian, as presented in Equation 3.19, includes the particle's longitudinal motion, which is why the transfer matrix is a 6×6 matrix. Comparing the electrostatic bender transfer matrix with the magnetic dipole, it can be seen that the bender focuses in both the x and y directions, as is the case with magnetic dipole with a field gradient. Furthermore, the bender creates dispersion in both x and longitudinal directions, unlike the magnetic dipole, which only creates dispersion in the x direction.

3.7 Transverse Beam Dynamics of Particle Ensembles

During the acceleration of a beam of particles through the optics discussed above, it is expected that an ensemble of particles would follow the ideally designed trajectory, but because of many deteriorating factors such as intrinsic thermal velocity spread due to ion sources, nonlinear forces due to external fields, and space-charge forces due to similar charge of the particles, the particles diverge from the ideal trajectory and significantly impacts the beam quality. However, the area occupied by the beam of particles in phase space is described by emittance, which according to Liouville's theorem, is invariant at every point in a beam transport system for conservative forces. The particle's transverse positions and momentum components define the phase space area. At a given time t, a beam of particles can be described by the sum of the coordinates of each particle in six-dimensional phase space.

The dimension of the phase space is defined by the three space coordinates and their corresponding momenta: $x, y, s, P_x, P_y,$ and P_s.The coordinates of the particles can be divided into two sub-spaces (transverse phase space and longitudinal phase space) and treated separately. The transverse phase spaces are (x, P_x) and $\left(y, P_y\right)$, and the longitudinal phase is (s, P_s) where s is the direction of the main momentum of the particles, and since the momentum in this direction is usually much larger than the momenta in the transverse directions, the coordinate of the transverse phase spaces can be rewritten as (x, x') and (y, y'), where $x' = \frac{P_x}{P_s} = \frac{mdx/dt}{mds/dt} = \frac{dx}{ds}$, and $y' = \frac{P_y}{P_s} = \frac{mdy/dt}{mds/dt} = \frac{dy}{ds}$. The x' and y' are the transverse angles of the particle defined with respect to the longitudinal direction s. For a continuous wave (CW) beam, such as the extracted beam from the ECRIS, the longitudinal phase space can be neglected as long as the momentum deviation, $\Delta P/P = 0$.

In the preceding sections of this chapter, only the motion of a single particle has been considered through the transport optics discussed. However, this consideration does not represent the property of a beam of many particles. To define the area occupied by an ensemble of particles, Hill's Equation is solved considering that the transverse directions of the particles vary with the longitudinal direction, and in the area, every particle represents a point in the phase space.

Considering only the motion of a beam of particles in the x direction (similar in the y direction), and assume that $1/\rho = 0$ and $\Delta P/P = 0$, at any given distance s along the direction of beam propagation, the x coordinates of the beam are given by,

$$x(s) = X_0(s)cos(\psi(s) + \psi_0) \qquad 3.20$$

$$x'(s) = -\sqrt{\frac{\varepsilon}{\beta(s)}}\left[\alpha(s)cos(\psi(s) + \psi_0) + si\,n(\psi(s) + \psi_0)\right] \qquad 3.21$$

Where $X_0(s) = \sqrt{\varepsilon\beta(s)}$, $\psi(s) = \int_0^s \frac{ds}{\beta(s)}$, $\alpha(s) = -\frac{\beta'(s)}{2}$, ε is the emittance, $\beta(s)$ is the amplitude function, also known as the beta function, and it depends on the beam focusing/ defocusing, which varies with position along the beam's path. Equations 3.20 and 3.21 describe the evolution of the transverse position of all the particles along the beam propagation direction. The amplitudes of the functions describe the maximum position and angle of the beam. The evolution of the beam envelope that contains all the rest of the particles is shown in Figure 3.3 below. The top plot shows the evolution of the outermost particle and the trajectory of a single particle performing sinusoidal motion inside the envelope, while the bottom plot shows the evolution of a typical beam of particles.

However, Equations 3.20 and 3.21 can be combined to define an expression that describes the particle motion in the $x - x'$ phase space (similar in the $y - s\ plane$) by eliminating the terms that depend on ψ, this gives Equation 3.22, plotted in Figure 3.4.

$$\varepsilon = \gamma x^2 + 2\alpha x x' + \beta {x'}^2 \qquad 3.22$$

Where $\gamma = \frac{1+\alpha^2}{\beta}$. The $\alpha, \beta,$ and γ are referred to as the Twiss parameters.

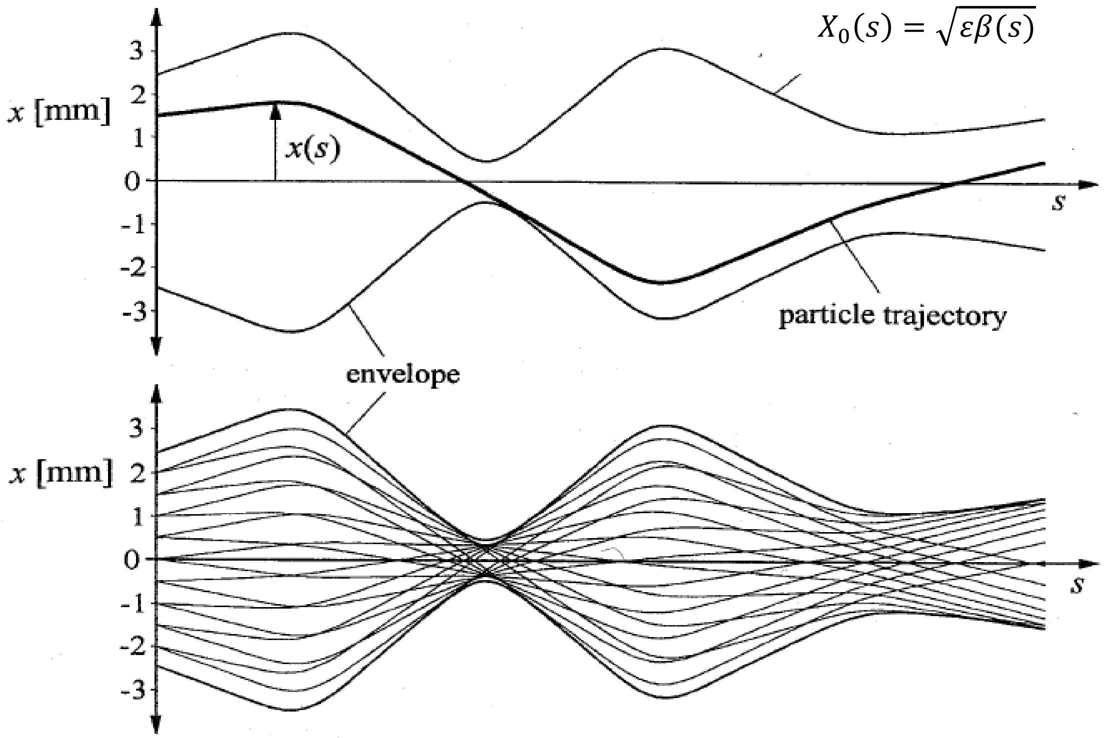

Figure 3.3: Schematic of a beam envelope of a beam of particles in $\boldsymbol{x}$ direction [32]. The top figure shows the trajectory of a single particle within a beam envelope, while the bottom figure shows the trajectories of exaggerated many particles.

As shown in Figure 3.4, Equation 3.22 is the general solution of the ellipse in the $x - x'$ Phase space, while the emittance ε is the area of the ellipse, given as $\varepsilon = A/\pi$. Moreover, Equation 3.22 also obeys Liouville's theorem, which states that the emittance is conserved in the presence of conservative forces. In other words, the area under the ellipse can neither be increased by defocusing nor reduced by focusing. If the beam size is reduced, for example, due to focusing, the corresponding beam angle increases and vice versa, thus conserving the emittance. The commonly used units of emittance are $cm - rad$, $cm - mrad$, $mm - mrad$ and μm. Moreover, as shown in Figure 3.4, the maximum beam radius and angle are given as, $x_{max} = \sqrt{\varepsilon\beta}$ and $x'_{max} = \sqrt{\varepsilon\gamma}$. The intercepts of x and x' are given as $x_{int} = \sqrt{\varepsilon/\gamma}$ and $x'_{int} = \sqrt{\varepsilon/\beta}$, respectively where $\alpha\sqrt{\varepsilon/\gamma}$ and $-\alpha\sqrt{\varepsilon/\beta}$ are the slopes of the ellipse, and the area of the ellipse is given as $A = \pi\varepsilon$. The orientation and the shape of the ellipse are defined by the Twiss parameters $\alpha, \beta,$ and γ. For a beam that is converging, α is greater than zero $(\alpha > 0)$, for diverging beam, α is less than zero $(\alpha < 0)$ while at the beam minimum size, $\alpha = 0$, and this is referred to as beam waist, and the ellipse is upright at that given position.

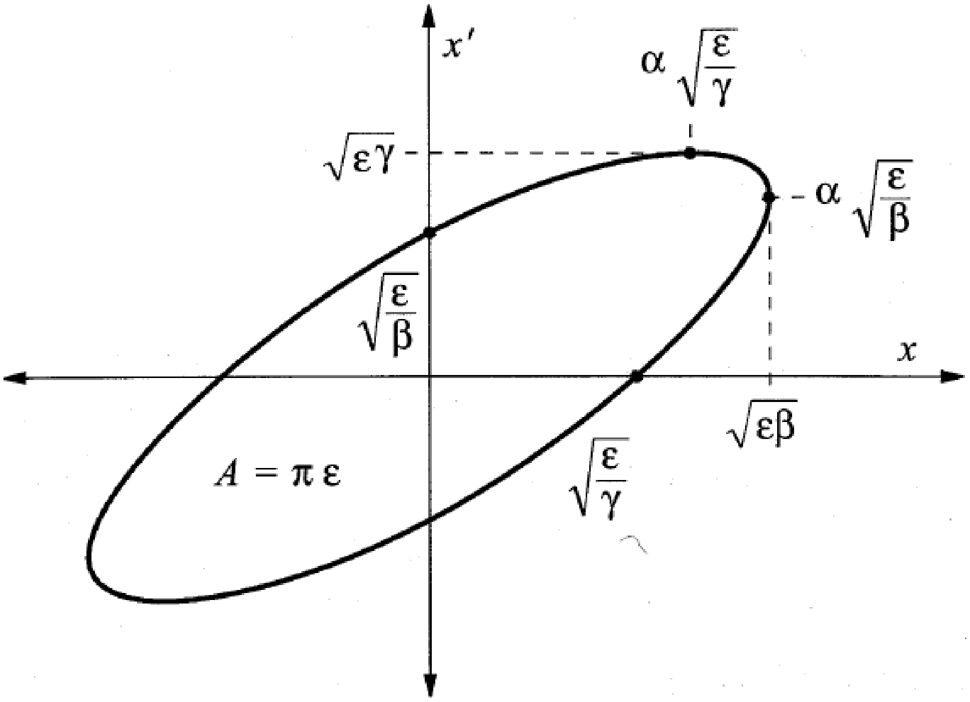

Figure 3.4: The phase space ellipse in the $\boldsymbol{x - x'}$ plane [32]. The Twiss parameters $\alpha, \beta,$ and γ and the emittance ε describe the shape and the orientation of the ellipse at a given location along the beamline. The area under the ellipse is given by $\pi\varepsilon$.

Meanwhile, for this special case that is $\alpha = 0$, the emittance of the beam can be defined as the product of the maximum beam radius and maximum divergence given as $\varepsilon_{\alpha=0} = x_{max}x'_{max}$. The emittance defined above also referred to as geometrical emittance, will shrink during beam acceleration with increasing P_s, therefore, it is important to normalize the emittance to the beam's energy. This type of emittance is called normalized emittance, and it is defined by, (tilde has been introduced to differentiate them from the Twiss parameters),

$$\varepsilon_N = \tilde{\beta}\tilde{\gamma}\varepsilon \qquad 3.23$$

Where $\tilde{\beta} = v/c$ is the velocity in terms of speed of light c, and $\tilde{\gamma}$ is the Lorentz factor defined as $\tilde{\gamma} = 1/\sqrt{1-\tilde{\beta}^2}$. The normalized emittance allows the comparison of beams of different energy.

The emittance of the beam extracted from the electron cyclotron resonance ion source charge state booster is influenced by electron energy, extraction field, and unavoidably fast-decreasing axial magnetic field in the extraction region of the charge breeder. All these parameters are optimized in this thesis to achieve the best beam quality.

3.8 Root-Mean-Square (RMS) Emittance

The root-mean-square emittance developed by Sacherer [35] is the statistical analysis of the emittance of a beam distribution without a defined shape. The profile distribution of beams can be of different shapes, such as normal Gaussian distribution, and coincidentally, in this thesis work, the shape of the beam distribution considered is Gaussian. In a Gaussian distribution *f(x)* of *N* number of particles, the RMS emittance, corresponding to one standard deviation of the Gaussian distribution, in $x - x'$ phase space is given by,

$$\varepsilon_{RMS} = \sqrt{\langle x^2\rangle\langle x'^2\rangle - \langle xx'\rangle^2} \qquad 3.24$$

Where,

$$\langle x^2\rangle = \frac{\iint (x-\bar{x})^2 f(x,x')dxdx'}{\iint f(x,x')dxdx'}, \qquad \langle x'^2\rangle = \frac{\iint \left(x'-\overline{x'}\right)^2 f(x,x')dxdx'}{\iint f(x,x')dxdx'}, \qquad \langle x\rangle = \frac{\iint x f(x,x')dxdx'}{\iint f(x,\ x')dxdx'}$$

$$\langle x'\rangle = \frac{\iint x' f(x,x')dxdx'}{\iint f(x,x')dxdx'}, \qquad \langle xx'\rangle = \frac{\iint (x-\bar{x})\left(x'-\overline{x'}\right) f(x,x')dxdx'}{\iint f(x,x')dxdx'}$$

Also, the RMS Twiss parameters are defined as, $\alpha_{RMS} = \frac{-\langle xx'\rangle}{\varepsilon_{RMS}}$, $\beta_{RMS} = \frac{\langle x^2\rangle}{\varepsilon_{RMS}}$, $\gamma_{RMS} = \frac{\langle x'^2\rangle}{\varepsilon_{RMS}}$. For the case of cylindrical coordinates, that is, in $r - r'$ phase space, the RMS emittance is given as such that $\langle x^2\rangle = \langle r^2\rangle/2$, $\langle x'^2\rangle = \langle r'^2 + (r\theta')^2\rangle/2$, $\langle xx'\rangle = \langle rr'\rangle/2$

$$\varepsilon_{RMS} = \frac{1}{2}\sqrt{\langle r^2\rangle\langle r'^2 + (r\theta')^2\rangle - \langle rr'\rangle^2} \qquad 3.25$$

For the 2-standard deviation, which corresponds to the RMS emittance, we have $\varepsilon_{2RMS} = 4\varepsilon_{RMS}$. This definition will be used throughout this research to describe the emittance of the reported beams. In the presence of an axial magnetic field, as in the ECR ion source, beam rotation is induced at the extraction region, which leads to an additional term in the emittance definition in the cylindrical coordinate. The beam rotation is accounted for by including the θ' term in Equation 3.25. However, to describe the motion of a beam of particles through any of the beam optics described above in $x - x'$ phase space, for example, if the initial x_0 and x_0' are known, then the final position can be determined through the transfer matrix of the optics, as presented in sections 3.2 to 3.5.

3.9 Emittance Measurement: Quadrupole Scan Technique (QST)

The Quadrupole scan technique is an approximate technique employed in an accelerator facility to determine the beam emittance. The technique involves scanning through a range of focusing strengths of a quadrupole and measuring the beam size at a given drift length downstream of the quadrupole. The technique is well understood and widely used in accelerator facilities [36]–[38] as a good approximation for beam emittance measurement. The measurement setup involves a focusing quadrupole, a field-free region (drift) and a profile monitor arranged in a series with the quadrupole located before the profile monitor along the beam transport system. The product of the beam matrix, and transfer matrix of the focusing quadrupole, and the drift length are solved to determine the beam size at the profile monitor. The schematic of the measurement set-up is shown in 3.5, where a is the quad aperture radius, d is the length of the drift length, and L is the quad length. The emittance and the Twiss parameters are determined at the entrance of the quadrupole at point P.

The electrostatic quadrupole strength k is defined as $k = V/a^2U_a$, where V is the voltage on the quadrupole electrodes, a is the quadrupole aperture radius, and U_a is the beam accelerating voltage. So, when the voltage V on the quadrupole electrodes is changed, the quadrupole strength is directly changed, and the beam size (width of the beam distribution) at the profile monitor is equally changed. Meanwhile, during the scanning of the quadrupole voltage, the minimum beam size must be achieved for the technique to work. Thus, plotting the square of the beam size against the quadrupole strength results in a parabolic curve; the beam size is determined from the beam distribution width measured on a profile monitor.

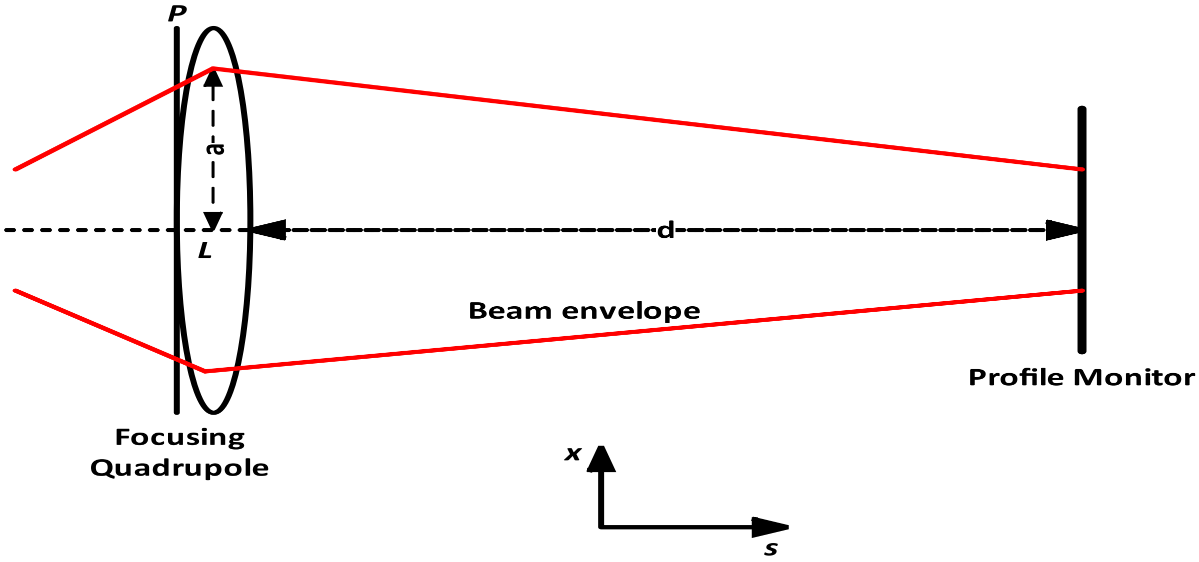

Figure 3.5: Schematic of the principle of the quadrupole scan technique for emittance measurement. Point P is the location along the beamline where beam emittance and the Twiss parameters are determined.

The beam radius can either be calculated as 1 standard deviation of the beam distribution, which contains 68 % of the particles or 2 standard deviations, which contains 95 % of the particles in the case of a Gaussian distribution. In this research, the beam radius is taken as 2 standard deviations for a Gaussian-like beam profile. Figure 3.6 shows an ideal Gaussian beam profile distribution. The width of the profile could be determined either by Gaussian curve fitting or RMS.

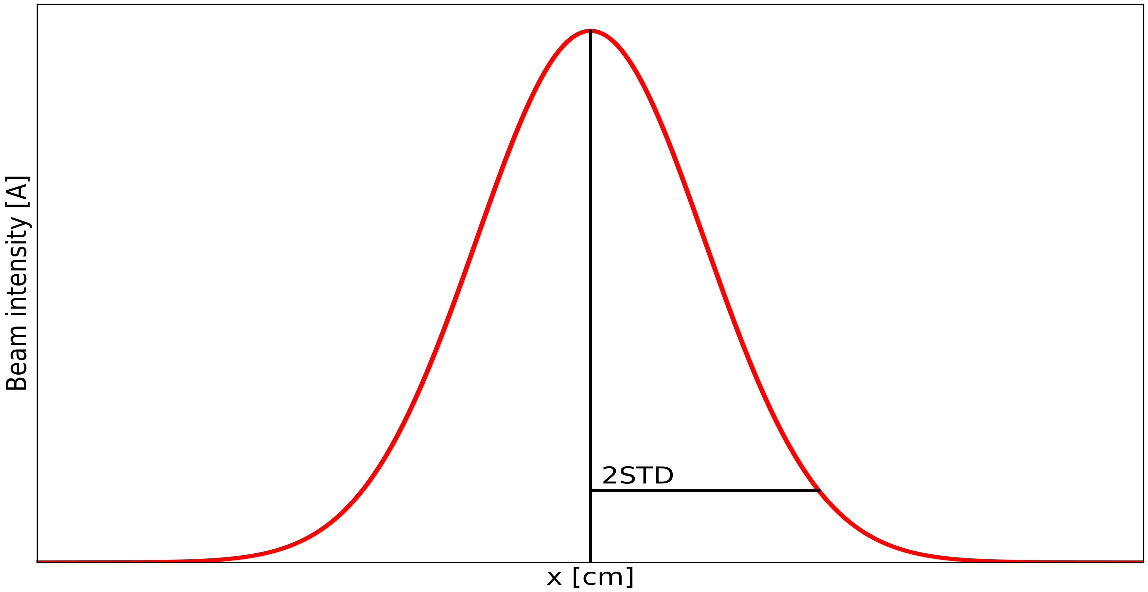

Figure 3.6: An ideal beam distribution on a profile monitor. The width of the beam is determined by either fitting the Gaussian distribution on the recorded profile to extract the 2-standard deviation or by using the root-mean-square method.

A 2 × 2 matrix can also describe the area occupied by a beam of particles, generally referred to as the beam matrix, given as

$$\sigma = \begin{bmatrix} \sigma 11 & \sigma 12 \\ \sigma 21 & \sigma 22 \end{bmatrix} \qquad 3.26$$

Where $x_{max} = \sqrt{\sigma 11} = \sqrt{\beta\varepsilon}$, the maximum beam radius, $x'_{max} = \sqrt{\sigma 22} = \sqrt{\gamma\varepsilon}$, the maximum beam angle, $\sigma 12 = \sigma 21 = r_c\sqrt{\sigma 11 \sigma 22} = -\alpha\varepsilon$, which can also be written as $r_c = \frac{-\alpha\varepsilon}{x_{max}x'_{max}}$, r_c is the cross-correlation coefficient of the $x - x'$ phase space, whose absolute value is between 0 and 1. From Equation 3.26, the emittance can then be defined as, where $|\sigma|$ is the determinant of Equation 3.26.

$$\varepsilon = \sqrt{|\sigma|} = \sqrt{\sigma 11 \sigma 22 - \sigma 12^2} \qquad 3.27$$

Moreover, using the beam matrix, the Twiss parameters can also be defined as $\alpha = -\sigma 12/\varepsilon$, $\beta = \sigma 11/\varepsilon$ and $\gamma = \sigma 22/\varepsilon$. Meanwhile, the beam matrix elements, in $x - x'$ phase space (similar in $y - y'$ phase space), can be defined statistically as root-mean-square, which is given as,

$$\sigma 11 = \langle x^2 \rangle = \frac{\iint (x - \bar{x})^2 f(x, x') dx dx'}{\iint f(x, x') dx dx'}$$

$$\sigma 22 = \langle x'^2 \rangle = \frac{\iint (x' - \overline{x'})^2 f(x, x') dx dx'}{\iint f(x, x') dx dx'}$$

$$\sigma 12 = \sigma 21 = \langle x x' \rangle = \frac{\iint (x - \bar{x})(x' - \overline{x'}) f(x, x') dx dx'}{\iint f(x, x') dx dx'}$$

By substituting these expressions into Equation 3.27, we have RMS emittance in $x - x'$ phase space is given as

$$\varepsilon_{RMS} = \sqrt{\langle x^2 \rangle \langle x'^2 \rangle - \langle x x' \rangle^2} \tag{3.28}$$

Where the 4RMS equivalence of Equation 3.28 contains about 86 % of the particles.

From Figure 3.5, the equation of beam transformation [39] between the quadrupole and the profile monitor is defined as

$$\sigma_{PM} = M \sigma_{Quad} M^T \tag{3.29}$$

Where σ_{PM} is the beam matrix at the profile monitor, M is the transfer matrix from the quadrupole to the profile monitor, σ_{Quad} is the beam matrix at the quadrupole entrance and M^T is the transpose of the transfer matrix M, which in general can be defined as $M = \begin{bmatrix} m11 & m12 \\ m21 & m22 \end{bmatrix}$. For example, the transfer matrix for a drift region of length d is defined as $M_{drift} = \begin{bmatrix} 1 & d \\ 0 & 1 \end{bmatrix}$, and the transfer matrix for a thick quadrupole lens of length L and strength k that is focussing in x direction is defined as $M_{Quad} = \begin{bmatrix} \cos(\sqrt{k}L) & \frac{1}{\sqrt{k}} \sin(\sqrt{k}L) \\ -\sqrt{k} \sin(\sqrt{k}L) & \cos(\sqrt{k}L) \end{bmatrix}$, thus the transfer matrix M, after the drift length d, is defined as the product of the transfer matrix of the drift length and the quadrupole, which is given as $M = M_{drift} M_{Quad}$

$$M = \begin{bmatrix} \cos(\sqrt{k}L) - d\sqrt{k} \sin(\sqrt{k}L) & d\cos(\sqrt{k}L) + \frac{\sin(\sqrt{k}L)}{\sqrt{k}} \\ -\sqrt{k} \sin(\sqrt{k}L) & \cos(\sqrt{k}L) \end{bmatrix} \tag{3.30}$$

by defining M, σ_{PM} and σ_{Quad} as $\begin{bmatrix} m11 & m12 \\ m21 & m22 \end{bmatrix}$, $\begin{bmatrix} x11 & x12 \\ x21 & x22 \end{bmatrix}$ and $\begin{bmatrix} \sigma 11 & \sigma 12 \\ \sigma 12 & \sigma 22 \end{bmatrix}$, respectively, Equation 3.29 can be rewritten as,

$$\begin{bmatrix} x11 & x12 \\ x21 & x22 \end{bmatrix} = \begin{bmatrix} m11 & m12 \\ m21 & m22 \end{bmatrix} \times \begin{bmatrix} \sigma 11 & \sigma 12 \\ \sigma 12 & \sigma 22 \end{bmatrix} \times \begin{bmatrix} m11 & m21 \\ m12 & m22 \end{bmatrix} \qquad 3.31$$

After the multiplication of Equation 3.31, the element of the resultant matrix corresponding to $x11$, which is the square of the beam radius at the profile monitor, is given as

$$x11 = x^2 = (d^2\sigma 22 + 2d\sigma 12 + \sigma 11)cos^2\left(\sqrt{k}L\right) + \left(d^2k\sigma 11 - 2d\sigma 12 + \frac{\sigma 22}{k}\right) sin^2\left(\sqrt{k}L\right) + \left(\frac{2d\sigma 22}{\sqrt{k}} + \frac{2\sigma 12}{\sqrt{k}} - 2\sigma 12 d^2\sqrt{k} - 2d\sigma 11\sqrt{k}\right)\cos\left(\sqrt{k}L\right)\sin\left(\sqrt{k}L\right) \qquad 3.32$$

For a given drift length d and quadrupole length L, Equation 3.32 can be fitted to experimental data to determine $\sigma 11, \sigma 12,$ and $\sigma 22$ that correspond to $\langle x^2\rangle, \langle xx'\rangle,$ and $\langle x'^2\rangle$, respectively, and the beam emittance and the Twiss parameters can be calculated in Equations 3.26 to 3.28. To validate the accuracy of the quadrupole scan technique, the CSB extraction beamline was modelled in TRANSOPTR (the CSB beamlines will be presented in Chapter 4). TRANSOPTR, a beam transport design code, is used at TRIUMF to calculate the evolution of the beam envelope and the Twiss parameters along the beam direction of travel to optimize the transport system. The schematic of the triplet optics after the CSB extraction system is shown in Figure 3.7. The QST was performed on the result of TRANSOPTR to determine beam emittance; the emittance evaluated using the QST is then compared with the emittance calculated by the TRANSOPTR code to determine the accuracy of the QST. The beam parameters defined by the TRANSOPTR were calculated from the IGUN simulation of the CSB extraction system. The initial parameters of the beam used in TRANSOPTR at point O in Figure 3.7 are $x_{max} = 0.54\ cm, x'_{max} = 3.90\ mrad$, and emittance $\varepsilon_{rms} = 11.88\ cm - mrad$ and the corresponding Twiss parameters are $\alpha = -0.18, \beta = 24.72\ cm, \gamma = 0.042\ 1/cm$. The phase space ellipse of the beam is shown in Figure 3.8. The extracted beam propagates from left to right.

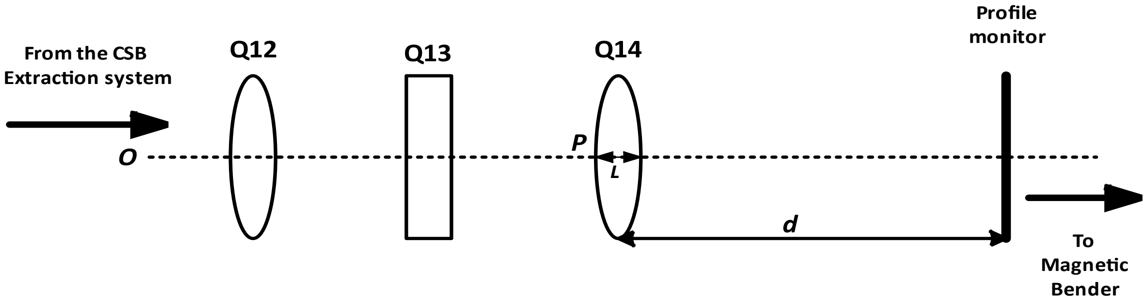

Figure 3.7: Schematic of the triplet quadrupole optics after the CSB extraction system and profile monitor RPM14. The emittance and the Twiss parameters are determined at point P using QST, while the Twiss parameters transformation is used to determine the shape and the orientation of the beam at point O.

As an example, the triplet optics were modelled in the TRANSOPTR, and the beam envelope of the extracted beam from the CSB was simulated. The first quad, Q12, focuses in x direction (defocusing in y direction), Q13 defocuses in x direction (focuses in y direction), and finally, Q14 focuses in x direction (defocuses in y direction). The quadrupole scan technique was performed using Q14, and the beam size was recorded on the profile monitor located downstream of Q14, as shown in Figure 3.7. The beam emittance and the Twiss parameters at the entrance of Q14 (point P) were compared with the parameters calculated in TRANSOPTR. The length of Q14 is $8.64\ cm$ with an aperture radius of $2.54\ cm$. The drift length between Q14 and the profile monitor is $7.42\ cm$. The voltage of Q14 was scanned from 50 V to 2000 V with a step size of 50 V. The strength of the quadrupole was calculated using $k = V/a^2U_a$, where V is the voltage of the quad, a is the aperture radius of the quadrupole, U_a is the beam accelerating voltage which is $10\ kV$ for the beam extracted from the CSB. The corresponding beam size to each voltage value was evaluated at the profile monitor.

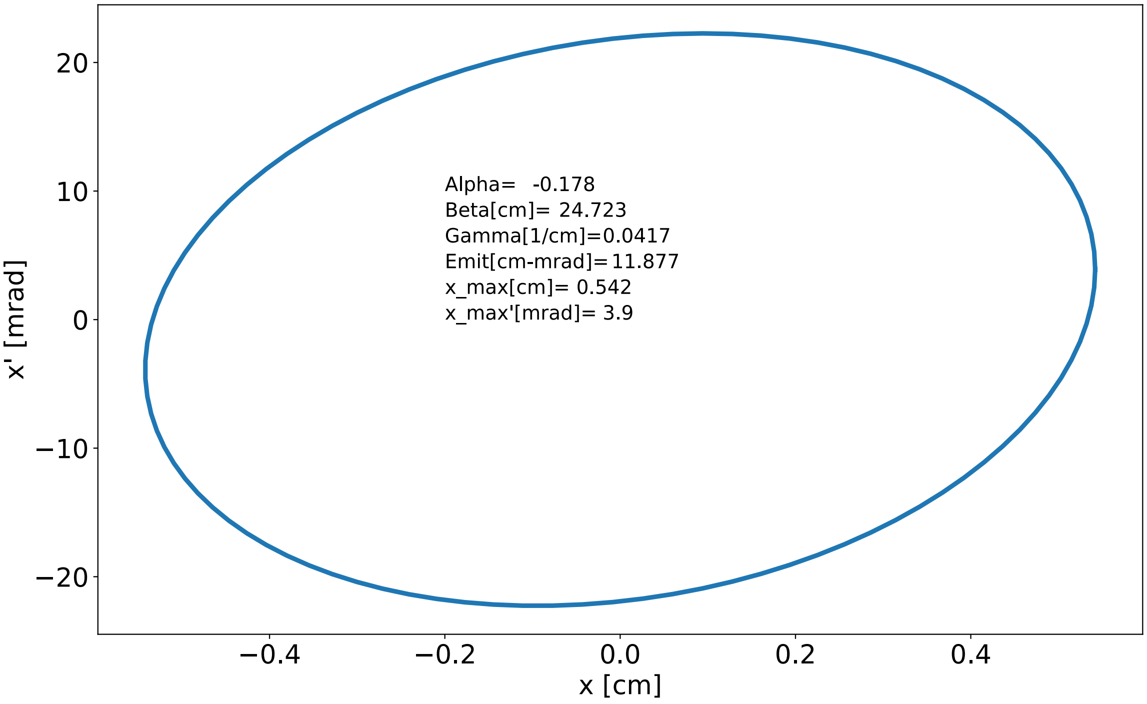

Figure 3.8: Reconstructed phase space ellipse of the simulated TRANSOPTR beam in $x - x'$ plane.

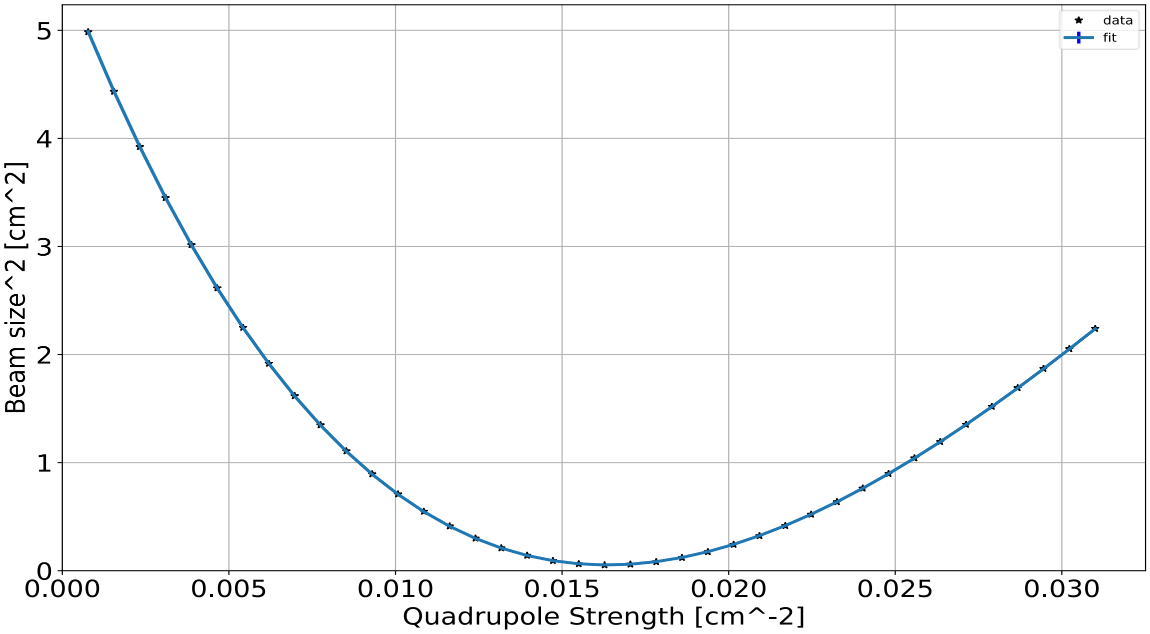

Figure 3.9: Parabolic curve produced as a result of scanning the strength of quadrupole Q14 with a range.

Figure 3.9 shows the plot of the square of the beam size against the quadrupole strength, and Equation 3.32 is fitted to the data. As seen in Figure 3.9, Equation 3.32 fits the data perfectly;

the R-square of the goodness of fit was 0.999. The coefficients $\sigma 11, \sigma 12,$ and $\sigma 22$ of Equation 3.32 deduced from the curve fitting are $\sigma 11 = 0.54$, $\sigma 12 = 0.049$, and $\sigma 22 = 0.0048$. However, using Equation 3.28, the RMS emittance is $\varepsilon_{RMS} = 12.18\ cm - mrad$ and the Twiss parameters are $\alpha = -4.02$, $\beta = 43.93\ cm$ $\gamma = 0.39\ \ 1/cm$.

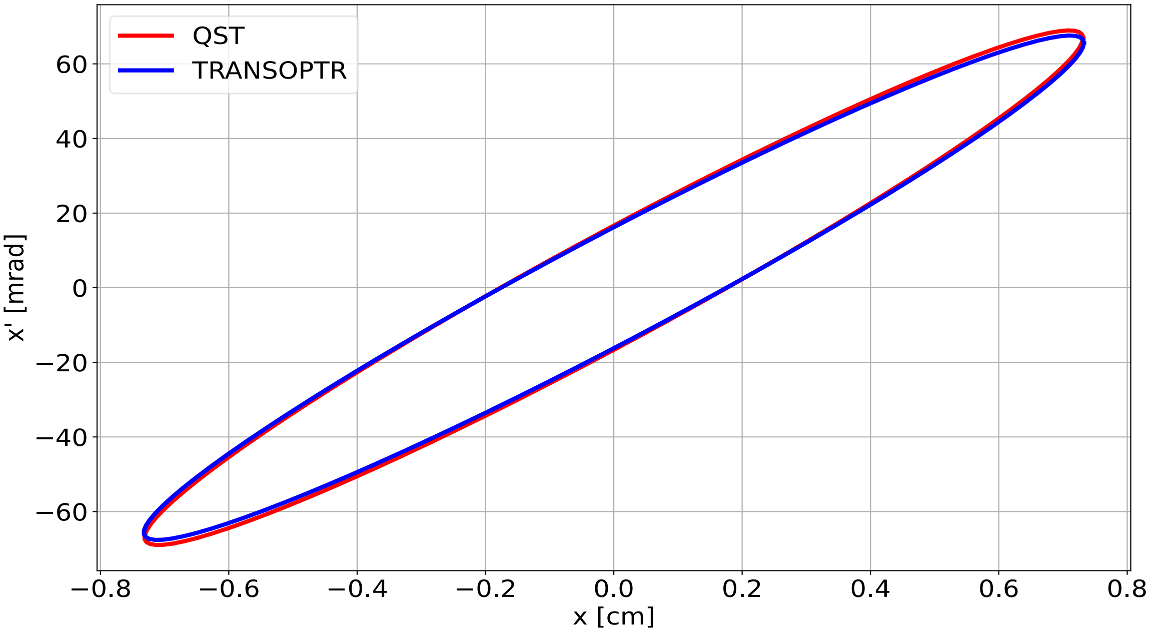

Figure 3.10: Comparison between the reconstructed phase space ellipse of the beam simulated in TRANSOPTR using QST and the actual phase space ellipse of the beam simulated and calculated in TRANSOPTR in $\boldsymbol{x - x'}$ plane at point *P*.

Figure 3.10 compares the phase space ellipse benchmarking with QST with the TRANSOPTR calculation. The red plot ellipse was generated using the Twiss parameters calculated with the quadrupole scan technique, while the blue plot ellipse was generated using the Twiss parameters calculated with TRANSOPTR. As can be seen, the two ellipse plots matched very well, indicating that the quadrupole scan technique can be used for the emittance measurement of beams from the CSB. Table 3.2 summarizes and compares the result of QST with TRANSOPTR calculations. Meanwhile, comparing the beam size, the beam angle, the emittance and the Twiss parameters evaluated using the QST with the TRANSOPTR calculation shown in Table 3.2, it can be seen that all the values deduced from the QST have a percentage error of less than 3 % which indicates that the technique is more than 97 % accurate for emittance measurement.

Moreover, to determine the Twiss parameter of the beam at any other location on the beamline, since they change as the beam moves through the transport system, and only the beam emittance is the conserved parameter, the Twiss parameter transformation can be used because these parameters define the shape and the orientation of the emittance phase ellipse.

Table 3.2: Comparison of Quadrupole Scan Technique results with TRANSOPTR results.

Parameters	**TRANSOPTR**	**Quad Scan Technique**	**Percentage error**
$\boldsymbol{\varepsilon}$ **[cm-mrad]**	11.88	12.18	2.5 %
$\boldsymbol{\alpha}$	-4.05	-4.02	0.7 %
$\boldsymbol{\beta}[\boldsymbol{cm}]$	45.16	43.93	2.7 %
$\boldsymbol{\gamma}[\boldsymbol{1/cm}]$	0.39	0.39	0 %
$\boldsymbol{x_{max}}[\boldsymbol{cm}]$	0.73	0.73	0 %
$\boldsymbol{x'_{max}}[\boldsymbol{mrad}]$	67.60	68.96	2 %

If the Twiss parameters $\alpha, \beta,$ and γ are known at a location, the parameters at any other location can be determined through the action of each optical element along the path of the beam. The effect of the optical elements is described by a 3×3 matrix, defined as

$$T = \begin{bmatrix} m_{11}^2 & -2m_{11}m_{12} & m_{12}^2 \\ -m_{11}m_{21} & m_{11}m_{22} + m_{12}m_{21} & -m_{22}m_{12} \\ m_{21}^2 & -2m_{22}m_{21} & m_{22}^2 \end{bmatrix} \quad 3.33$$

where the elements of the matrix T are defined in the 2×2 transfer matrix of the optical elements $M = \begin{bmatrix} m_{11} & m_{12} \\ m_{21} & m_{22} \end{bmatrix}$. For example, if the Twiss parameters at a location with index 0 are known, the Twiss parameters at another location with index n on the beam transport system can be determined using Equation 3.33, given as

$$\begin{pmatrix} \beta \\ \alpha \\ \gamma \end{pmatrix}_n = \begin{bmatrix} m_{11}^2 & -2m_{11}m_{12} & m_{12}^2 \\ -m_{11}m_{21} & m_{11}m_{22} + m_{12}m_{21} & -m_{22}m_{12} \\ m_{21}^2 & -2m_{22}m_{21} & m_{22}^2 \end{bmatrix} \begin{pmatrix} \beta \\ \alpha \\ \gamma \end{pmatrix}_0 \quad 3.34$$

For a drift length of length d, the transfer matrix is $M_d = \begin{bmatrix} 1 & d \\ 0 & 1 \end{bmatrix}$ and 3×3 matrix, according to Equation 3.33, is

$$T_d = \begin{bmatrix} 1 & -2d & d^2 \\ 0 & 1 & -d \\ 0 & 0 & 1 \end{bmatrix} \quad 3.35$$

From Equation 3.34, the Twiss parameter after a drift of length d is given as

$$\begin{pmatrix}\beta\\ \alpha\\ \gamma\end{pmatrix}_d = \begin{bmatrix}1 & -2d & d^2\\ 0 & 1 & -d\\ 0 & 0 & 1\end{bmatrix}\begin{pmatrix}\beta\\ \alpha\\ \gamma\end{pmatrix}_0 \tag{3.36}$$

Similarly, the Twiss parameters transformation matrix can be derived for quadrupoles (focusing and defocusing), magnetic dipoles and electrostatic benders provided either or all of the optics are between the initial and final locations where the Twiss parameters are required to be determined. However, from Figure 3.7, the Twiss parameters at point P (β_P, α_P and γ_P) are known, so using the Twiss parameter transformation, the Twiss parameters at point O (β_O, α_O and γ_O) can be determined. Between points O and P, there is one focusing quad (Q12), one defocusing quad (Q13) and three drift regions. From Equation 3.36, the Twiss parameters transformation is given as, where T_{OP} is the 3×3 Twiss parameter matrix derived from the transfer matrix M_{OP} between points O and P.

$$\begin{pmatrix}\beta\\ \alpha\\ \gamma\end{pmatrix}_P = T_{OP}\begin{pmatrix}\beta\\ \alpha\\ \gamma\end{pmatrix}_O \tag{3.37}$$

Equation 3.37 is a system of equations, and it can be solved using the Python NumPy linalg module to determine unknown β_O, α_O and γ_O. After solving the system of equations, the Twiss parameters at point O are $\alpha = -0.38, \beta = 21.28\ cm$ and $\gamma = 0.054\ 1/cm$. The phase space ellipse of the beam at point O is shown in Figure 3.11.

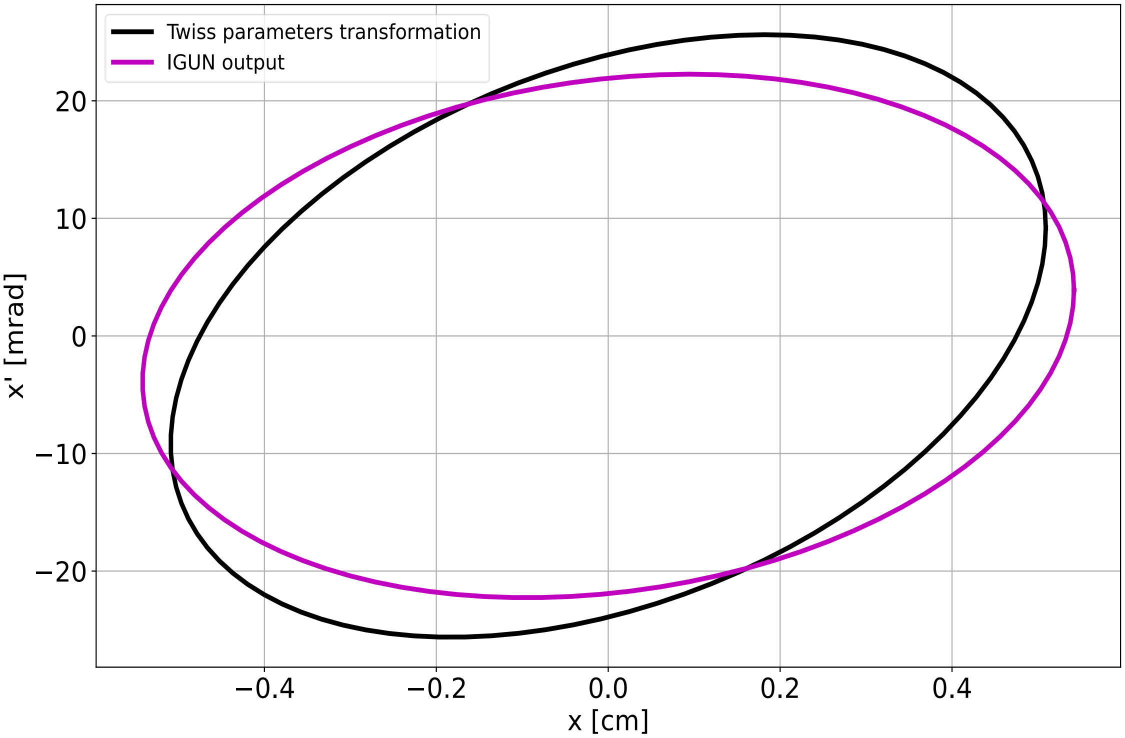

Figure 3.11: The phase space ellipse of the beam in $\boldsymbol{x} - \boldsymbol{x}'$ plane determined using the Twiss parameters transformation at Point *O*. The purple plot represents the initial phase space ellipse imported from the IGUN simulation of the CSB extraction system into the TRANSOPTR.

3.10 Error Analysis in the Emittance Measurement

To quantify the errors in the emittance measurements, random errors are assumed to be negligible, and the physical properties of the beam optics, such as drift lengths, quadrupole lengths and apertures, are assumed to be exact. So, the error in the emittance is determined through error propagation in the fitted parameters $x11, x12, x22$ ($x12 = x21$). The error propagation is derived from the resultant matrix after minimizing the chi-square of the least-square fitting [40]. That is, if H is the $n \times 3$ curvature matrix which contains the product of the experimental data and the transfer matrix elements of the optics used for the quadrupole scans, then the square of the errors in $x11, x12, x22$, ($x12 = x21$) is defined mathematically as

$$\delta x11 = \left(\sqrt{covariance * (H^T H)^{-1}}\right)_{11} \tag{3.38}$$

$$\delta x12 = \delta 21 = \left(\sqrt{covariance * (H^T H)^{-1}}\right)_{22} \tag{3.39}$$

$$\delta x22 = \left(\sqrt{covariance * (H^T H)^{-1}}\right)_{33} \tag{3.40}$$

$$covariance = \frac{\sum_i^n (measurement - model)^2}{n-2} \tag{3.41}$$

Where n is the number of scans, and subscript numbers are diagonal matrix elements.

3.11 Space Charge Effect

Space charge is a critical factor contributing to emittance growth in the accelerator system, especially highly charged-high intensity beams. Refer to [41] for further reading on the effects of space charge on the beam and the associated linear optics. External forces from the electric and magnetic fields are used for acceleration and manipulation (steering) of charged particles in the transport system.

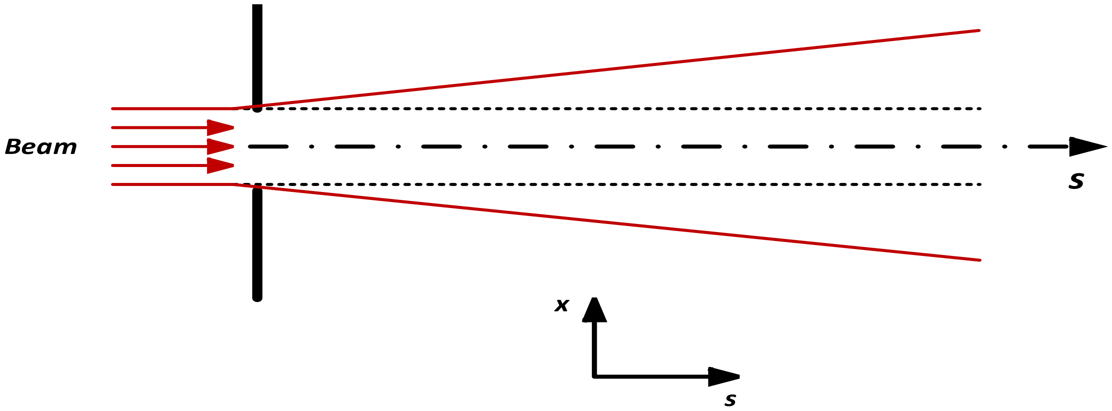

Figure 3.12: Schematic of the envelope of a low-energy beam under space charge effect. The envelope starts from a waist and diverges due to self defocusing electric field.

However, because of the similar charge of the ions (or electrons) being transported, they experience a repelling force known as space charge force so that in the transverse directions, the trajectories of the ions become divergent during transport, as shown in Figure 3.12. The space charge force can be large, in extreme cases dominating the external forces for beam focusing. Assume non-relativistic, consider a particle with charge Q embedded in a beam of particles with a constant charge density ρ_0 travelling with velocity v in a cylindrical beam pipe of radius R shown in Figure 3.13. The charged particle whose charge is similar to the charge of the beam will experience the Coulomb force and moves the particle radially towards the beam edge leading to defocusing of the particle. The Coulomb force arises from the radial electric field E_r acting on the particle, as shown in Figure 3.13.

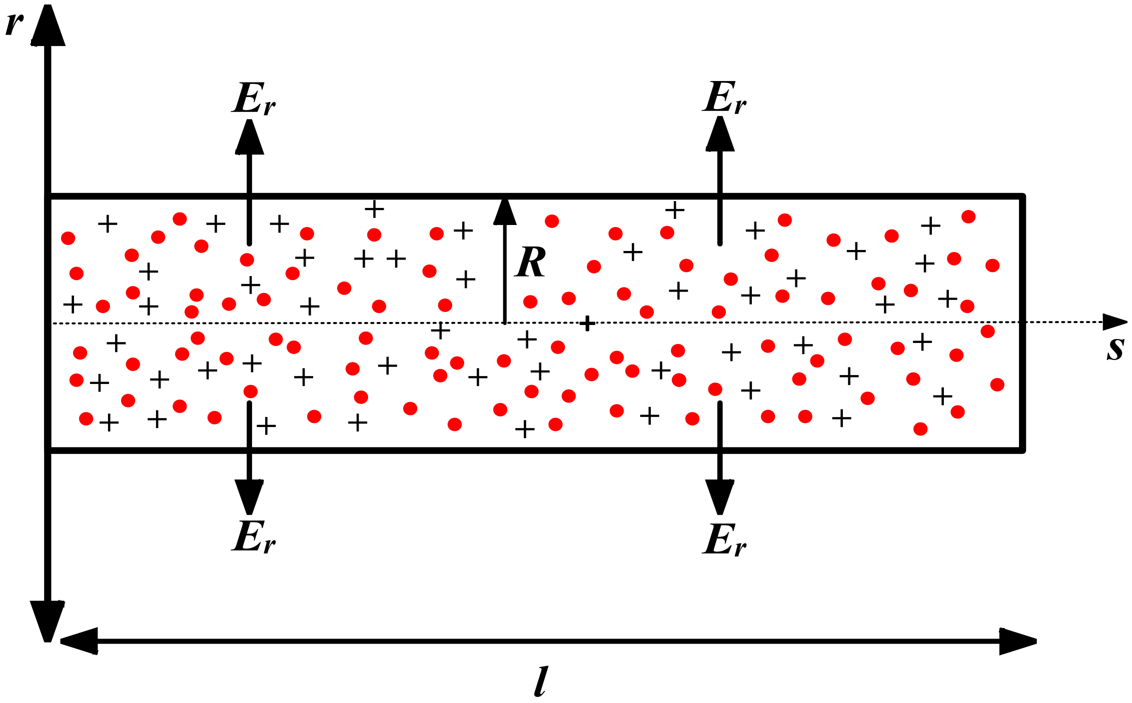

Figure 3.13: Schematic of a low-energy beam of particles propagating to the right in a cylindrical beamline and the self-produced electric field creating a defocusing effect on the particles.

However, for a complete description of the transverse motion of the beam, the space charge force must be included in Hill's Equation presented in Section 3.1. The space charge field can be calculated using Gauss's law of Maxwell's Equation, which states that:

$$\int_A \vec{E} \cdot dA = E_r(2\pi rl) = \int_V \frac{\rho_0}{\epsilon_0} dV = \int_0^r \frac{\rho_0}{\epsilon_0}(2\pi rl)dr \qquad 3.42$$

Where A is the lateral surface area of the cylindrical beam pipe and V is the corresponding volume.

Carrying out the integration, the electric field is given as

$$E_r = \begin{cases} \frac{\rho_0 r}{2\epsilon_0} \; when\, r < R \\ \frac{\rho_0 R^2}{2\epsilon_0 r} \; when\, r > R \end{cases} \qquad 3.43$$

where ϵ_0 is the permittivity of free space, l is the finite length of the pipe, r is the beam radius, and R is the radius of the beam pipe. As seen in Equation 3.43, the electric field has two unique solutions, and it is linear inside the beam, that is when $r < R$ and decreases when $r > R$.

Moreover, a charged particle travelling with a velocity v in a certain direction has a magnetic field associated with it which can be calculated using the Ampere circuital law of Maxwell's equation. Considering Figure 3.13, if the current density of the beam in the transport system is given as J, and the area of the beam pipe is given as $A = \pi r^2$, the azimuthal magnetic field created by the beam is given by Equation 3.44:

$$\int_C \vec{B} \cdot dl = \mu_0 \int_S J dA \qquad 3.44$$

After computing the integration, we have $B_\phi l = \mu_0 JA$, where $l = 2\pi r, J = \rho_0 v$ and the beam's self-generated magnetic field is given as

$$B_\phi = \frac{\mu_0 \rho_0 v}{2} r \qquad 3.45$$

The force due to the space charge experienced by a particle of charge Q embedded in a beam of particles is radial, and from Equations 3.43a and 3.45, is given as

$$F_r = Qe(E_r - vB_\emptyset) = \frac{Qe\rho_0}{2}\left(\frac{1}{\epsilon_0} - \mu_0 v^2\right) r \qquad 3.46$$

Equation 3.46 is the space charge force experienced by a particle of charge Q embedded in a beam of particles with a uniform charge density of ρ_0. However, for relativistic beams, putting $v = \tilde{\beta} c$, where $\tilde{\beta}$ is the relativistic speed parameter, c is the speed of light and $1/\epsilon_0 = \mu_0 c^2$ Equation 3.46 becomes,

$$F_r = \frac{Qe\rho_0}{2\epsilon_0}\left(1 - \tilde{\beta}^2\right) r \qquad 3.47$$

As it is seen in Equation 3.47, the 1 in the bracket represents the force due to the electric field, and $-\tilde{\beta}^2$ represents the magnetic force. The electric field is defocusing while the magnetic field is focusing. For relativistic beams $\tilde{\beta} \cong 1$, $F_r \cong 0$, which suggests that the magnetic force balances the electric force and the particle in the beam is unaffected by the space charge. However, for non-relativistic beams $\tilde{\beta} \cong 0$, the space charge force due to the magnetic field is negligible, and the force has a defocusing effect.

Thus, the extracted beams from ion sources such as Electron Cyclotron Resonance Ion Source Charge State Booster (ECRIS CSB) are non-relativistic (beam energy up to $35\ keV * Q$ for TRIUMF CSB), thus $\tilde{\beta} \ll 1$ and Equation 3.47 reduces to,

$$F_r^{sc} = \frac{QeI}{2\pi\epsilon_0 v b^2} r \qquad 3.48$$

where $\rho_0 = I/\pi v b^2$ where b is the beam radius, I is the beam current, and ϵ_0 is the permittivity of free space. The transverse motion of the beam of particles is given as,

$$F_r^{sc} = mv^2 \frac{d^2r}{ds^2} = \frac{QeI}{2\pi\epsilon_0 vb^2} r \qquad 3.49$$

where $F_r^{sc} = \frac{mdv_r}{dt} = m\frac{d}{ds}\cdot\frac{dr}{ds}\cdot\frac{ds}{dt}\cdot\frac{ds}{dt} = \frac{mv^2d^2r}{ds^2}$, $v = \frac{ds}{dt}$, the velocity of the beam along the direction of travel s. Equation 3.49 can be written as, where r'' is the second derivative of r with respect to s:

$$r'' = \frac{QeI}{2\pi\epsilon_0 mb^2v^3} r \qquad 3.50$$

where $r = \sqrt{x^2 + y^2}$, $x = r\cos\theta$ and $y = r\sin\theta$. In Cartesian coordinate at $\theta = 0°$ in $x - s$ plane, $r = x$, (similarly in $y - s$ plane at $\theta = 90°, r = y$) then we have,

$$x'' = K_{sc}x \qquad 3.51$$

$$K_{sc} = \frac{QeI}{2\pi\epsilon_0 mb^2v^3} \qquad 3.52$$

where K_{sc} is the strength of space charge effects which must be included in Hill's Equation which is given as

$$x''(s) + \left(\frac{1}{\rho^2} - K - K_{sc}\right)x(s) = \frac{1}{\rho}\frac{\Delta P}{P},\ y''(s) + (K - K_{sc})y(s) = 0 \qquad 3.53$$

For $mv^2/2 = QeU_a$ and $m = Am_u$ where U_a is accelerating voltage, Equation 3.53 becomes,

$$K_{sc} = \frac{I}{4\pi\epsilon_0 b^2 U_a^{3/2}}\sqrt{\frac{Am_u}{2Qe}} \qquad 3.54$$

where A is the atomic mass of ions in a.m.u, m_u is the atomic mass unit.

The strength of the space charge effect, as seen in Equation 3.54, shows that the higher the beam current, the higher the space charge effect, provided that the beam is not relativistic.

In Figure 3.13, the product of the space charge strength and square of the beam radius is plotted against beam current ranging from 0 to $500\ \mu A$ for a $10\ kV$ $^{16}O^{5+}$ beam. As seen, for a given beam radius, the space charge strength is linear with increasing beam current, and its effect becomes stronger at a higher current but negligible at a low current.

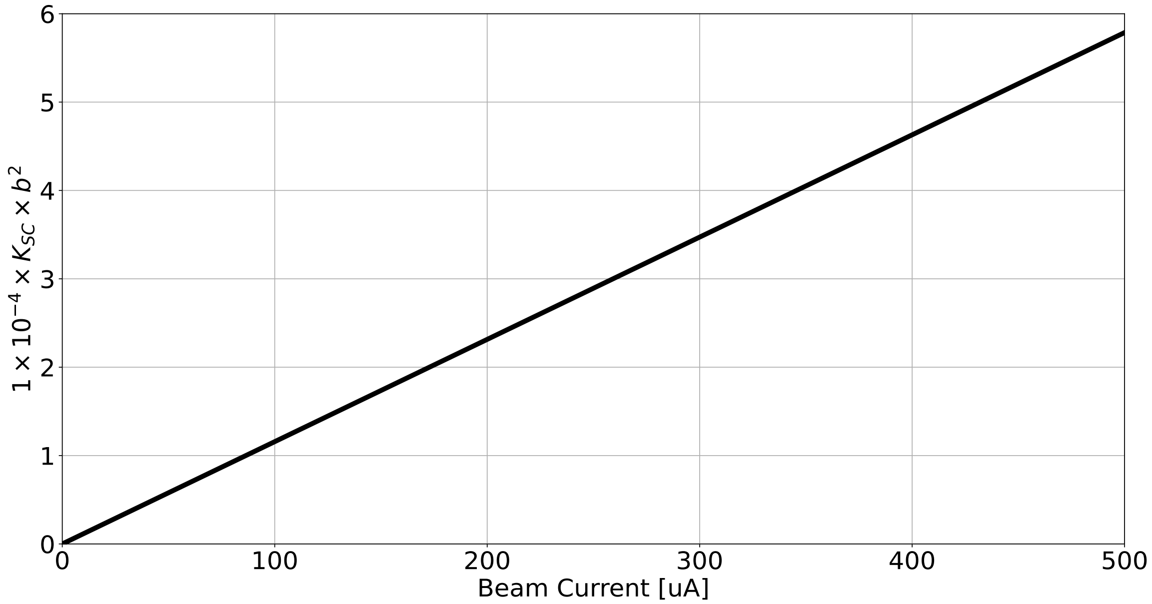

Figure 3.13: Product of space charge strength and square of beam radius for $^{16}O^{5+}$ beam at an energy of Q*10 keV vs the beam current up to 500 uA.

For example, in a drift region of length d, in $x - s$ plane, the solution to Hill's Equation with space charge effect included in the transfer matrix is given as, where K_{sc} is given by Equation 3.54 for non-relativistic velocity,

$$\begin{pmatrix} x \\ x_0 \end{pmatrix} = \begin{pmatrix} cosh\left(\sqrt{K_{sc}}d\right) & \frac{1}{\sqrt{K_{sc}}} sin\,h\left(\sqrt{K_{sc}}d\right) \\ \sqrt{K_{sc}}\, sinh\left(\sqrt{K_{sc}}d\right) & cosh\left(\sqrt{K_{sc}}d\right) \end{pmatrix} \begin{pmatrix} x_0 \\ x_0' \end{pmatrix} \quad 3.55$$

Where the 2×2 transfer matrix is given as

$$M_d^{SC} = \begin{pmatrix} cosh\left(\sqrt{K_{sc}}d\right) & \frac{1}{\sqrt{K_{sc}}} sin\,h\left(\sqrt{K_{sc}}d\right) \\ \sqrt{K_{sc}}\, sinh\left(\sqrt{K_{sc}}d\right) & cosh\left(\sqrt{K_{sc}}d\right) \end{pmatrix} \quad 3.56$$

If the length of the drift region is small, and $\sqrt{K_{sc}}d \ll 1$, then the effect of space charge in the drift region is negligible, and Equation 3.56 reduces to drift length transfer matrix without space charge,

$$M_{drift} = M_{drift}^{SC} = \begin{pmatrix} 1 & d \\ 0 & 1 \end{pmatrix} \quad 3.57$$

Furthermore, in the electrostatic quadrupole with strength K_Q and length L, the solution to Hill's Equation with space charge strength K_{sc} is given as:

$$\begin{pmatrix} x \\ x' \\ y \\ y' \end{pmatrix} = \begin{pmatrix} cosh\, \varphi_T & \frac{1}{\sqrt{K_T}} sinh\, \varphi_T & 0 & 0 \\ \sqrt{K_T}\, sinh\, \varphi_T & cosh\, \varphi_T & 0 & 0 \\ 0 & 0 & cos\, \varphi_T & \frac{1}{\sqrt{K_T}} sin\, \varphi_T \\ 0 & 0 & -\sqrt{K_T}\, sin\, \varphi_T & cos\, \varphi_T \end{pmatrix} \begin{pmatrix} x_0 \\ x'_0 \\ y_0 \\ y'_0 \end{pmatrix} \qquad 3.58$$

the transfer matrix is given as

$$M_Q^{SC} = \begin{pmatrix} cosh\, \varphi_T & \frac{1}{\sqrt{K_T}} sinh\, \varphi_T & 0 & 0 \\ \sqrt{K_T}\, sinh\, \varphi_T & cosh\, \varphi_T & 0 & 0 \\ 0 & 0 & cos\, \varphi_T & \frac{1}{\sqrt{K_T}} sin\, \varphi_T \\ 0 & 0 & -\sqrt{K_T}\, sin\, \varphi_T & cos\, \varphi_T \end{pmatrix} \qquad 3.59$$

where $K_T = K_Q - K_{sc}$, $\varphi_T = \left(\sqrt{K_Q - K_{SC}}\right)L$, $K_Q = V/U_a a^2$ and $K_{sc} = \frac{I}{4\pi\epsilon_0 b^2 U_a^{3/2}} \sqrt{\frac{Am_u}{2Qe}}$

As seen in Equation 3.59, the magnitude of the quadrupole strength is decreased by the space charge strength in both the focusing and defocusing plane. Also, the quadrupole and space charge strength depends on the beam energy. Figure 3.14 compares the magnitude of space charge strength with quadrupole strength for accelerating voltage ranging from $5 - 50\ kV$ for a ^{16}O^{5+} beam with a maximum beam size of $5.5\ mm$ and an intensity of $50\ \mu A$ (typical current from the TRIUMF CSB) with the quad electrode voltage $V = 800\ V$, and quad aperture radius, $a = 25.4\ mm$. The blue curve is the strength of an electrostatic quadrupole, while the red plot is the strength of the space charge. As seen, both strengths decrease with beam accelerating voltage; however, in the case of the beam current considered, ^{16}O^{5+} at an intensity of 50 μA, the quadrupole strength dominates the space charge strength across the accelerating voltage, although quadrupole strength does not depend on beam intensity.

The TRIUMF CSB is usually operated at the accelerating voltage of 10 kV; the quad strength at this voltage is 77.5 m^{-2} while the space charge strength is 1.9 m^{-2} which is about 40 times smaller than the quadrupole strength; thus, the space charge effect in the further measurement and analysis of the CSB results can be neglected as the ECRIS is not operated in a high current regime.

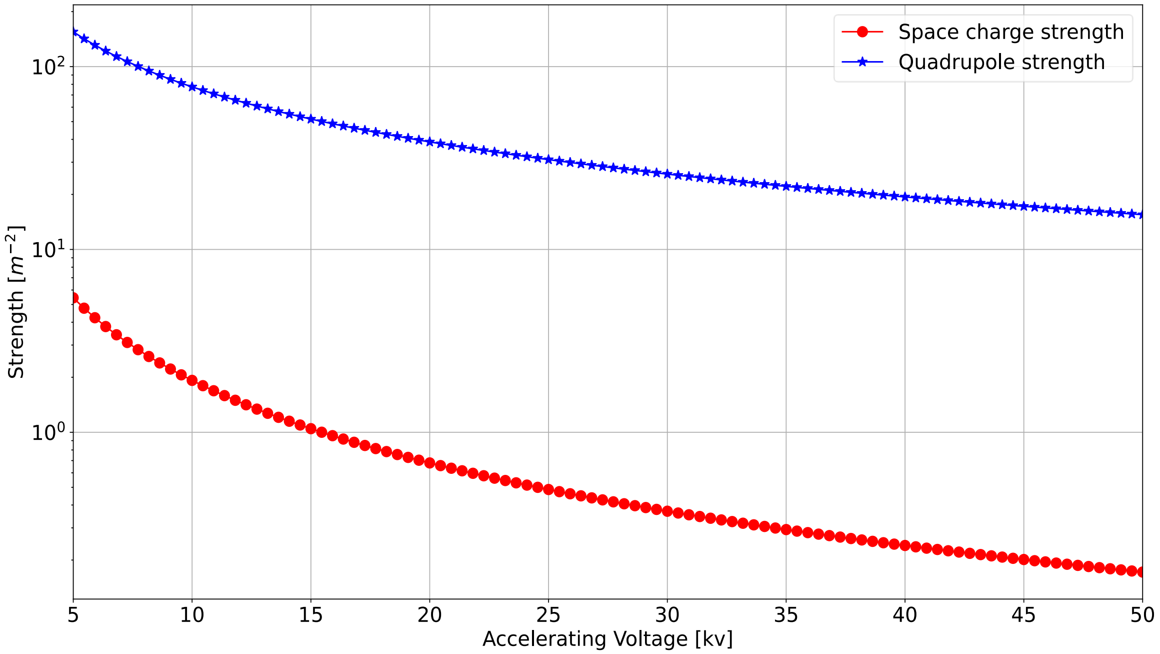

Figure 3.14: Comparison between space charge and quadrupole strengths on $^{16}O^{5+}$ beam at an energy of Q*10 keV plotted against accelerating voltage between 5 and 50 kV. The size of $^{16}O^{5+}$ was assumed to be 5.5 *mm* while the voltage on the quadrupole electrode is 800 V.

3.12 Magnetic Field Emittance Due to Beam Rotation in the Electron Cyclotron Resonance Ion Source

The formation and extraction of ion beams from the ECRIS occur in the source's strong solenoid magnetic field. The magnetic field's magnitude in the source's extraction region decreases rapidly as the extracted beams propagate into the beam transport lines. The decreasing magnetic field induces a beam rotation that significantly affects the emittance of the extracted beam.

The contribution of the magnetic field to the ion beam emittance in the ECR ion source can be derived from Gauss's law of Maxwell's equation and the Lorentz force law. In cylindrical coordinate (r, θ, s), Gauss's law of Maxwell's equation is given as, where $\vec{B} = (B_r, 0, B_s)$

$$\nabla \cdot \vec{B} = \frac{1}{r}\frac{\partial (rB_r)}{\partial r} + \frac{\partial B_s}{\partial s} = 0 \qquad 3.60$$

Where B_r is the radial field due to the solenoid coil and B_s is the main field on the beam axis in the *s* direction. The radial field, which is derivable to the first order from the on-axis magnetic field component B_s is given as, from Equation 3.60:

$$B_r = -\frac{r}{2}\frac{\partial B_s}{\partial s} \qquad 3.61$$

From the Lorentz force law, the force experienced by the ions due to the radial field of the ECRIS solenoid coil is given as:

$$m\frac{dv_\theta}{dt} = Qev_sB_r \qquad 3.62$$

From $v_s = \frac{ds}{dt}$, $dt = \frac{ds}{v_s}$, substitute for dt and B_r in Equation 3.62, and cancel out v_s, we have,

$$m\frac{dv_\theta}{ds} = \frac{dp_\theta}{ds} = -Qe\frac{r}{2}\frac{\partial B_s}{\partial s} \qquad 3.63$$

The magnitude of the angular momentum kick due to the radial magnetic field is given as

$$p_\theta = \frac{QerB_s}{2} \qquad 3.64$$

Normalizing Equation 3.64 to the longitudinal momentum p_s we have the beam angle given as

$$\theta' = \frac{p_\theta}{p_s} = \frac{QerB_s}{p_s} \qquad 3.65$$

In $r - \theta'$ phase space, the geometrical magnetic emittance is then defined as the product of r and θ'

$$\varepsilon_{mag} = \frac{QeB_0r^2}{2p_0} = \frac{QeB_0r^2}{2mv_s} \qquad 3.66$$

Where B_0 is the magnitude of the magnetic field at the extraction aperture with radius r, Q is the charge of the ion, e is the electron charge and p_0 is the beam's momentum defined as the product of the mass and velocity of the extracted beam. In terms of the atomic mass and charge, $\mathrm{m} = \mathrm{Am_u}$, Equation 3.66 becomes,

$$\varepsilon_{mag} = \frac{QeB_0r^2}{2Am_uv_s} \qquad 3.67$$

Where m_u is the atomic mass unit.

Equation 3.67 is the geometrical magnetic emittance due to the magnetic field in the extraction region of the electron cyclotron resonance ion source. Furthermore, by multiplying Equation 3.67 with the relativistic beta and Lorentz factor, substituting $v_s = \tilde{\beta}c$, where c is the speed of light, the normalized magnetic emittance is given as:

$$\varepsilon_{normalize}^{mag} = \frac{QeB_0r^2}{2Am_uc}\tilde{\gamma} \qquad 3.68$$

For non-relativistic beam, $\tilde{\gamma} = 1$, the normalized magnetic emittance in $m - rad$ can then be expressed as

$$\varepsilon_{normalize}^{mag} = 0.161\frac{B_0r^2}{A/Q} \qquad 3.69$$

As seen from Equation 3.69, the normalized magnetic emittance depends on the magnitude of the magnetic field, B_0, at the extraction aperture location, the radius of the extraction aperture, r, and most importantly, the mass-to-charge ratio, A/Q of the beam that is being extracted.

The magnitude of the magnetic field at the location of the extraction aperture of the TRIUMF ECR ion source charge state booster is about $0.7\ T$ while the radius of the extraction aperture is 3 mm. Figure 3.16 shows the theoretical normalized RMS magnetic emittance of the beam with A/Q between 1 and 16.

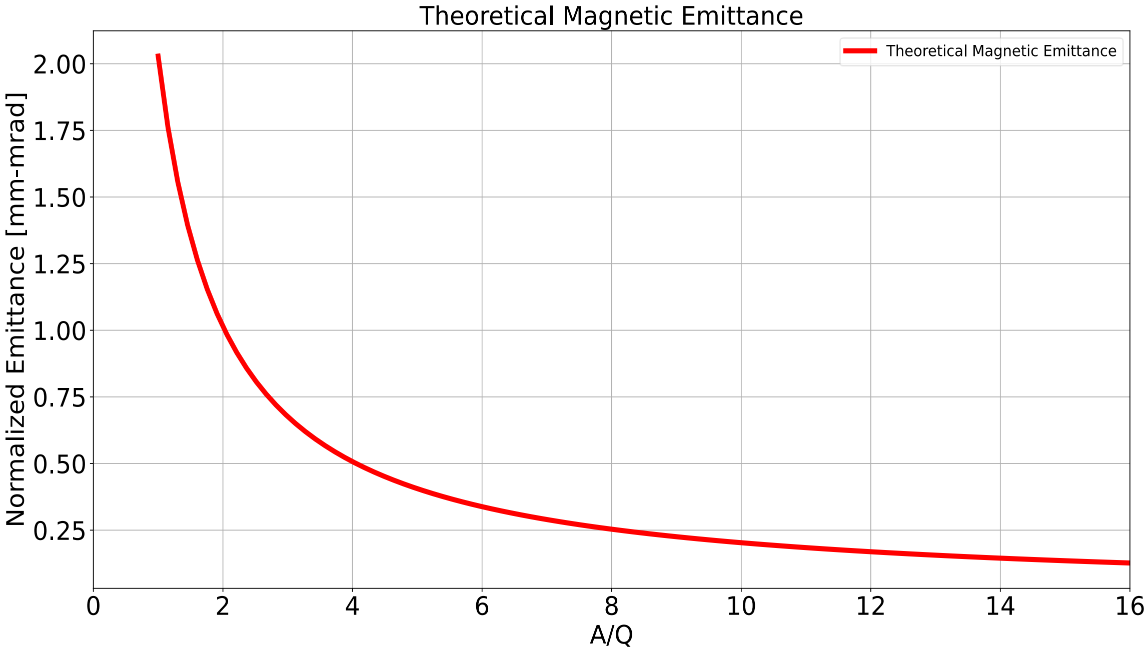

Figure 3.16: Theoretical magnetic field emittance plotted against A/Q between 1 and 16 calculated at an extraction aperture radius of 3 mm and magnetic field of 0.7 T.

Chapter 4 - The TRIUMF Electron Cyclotron Resonance Ion Source Charge State Booster (ECRIS CSB)

4.1 Introduction

The TRIUMF ECRIS CSB is a modified 14.5 GHz PHOENIX booster developed by Pantechnik, France. It was originally designed to be operated as a single-frequency plasma-heating source. The booster was installed and commissioned in 2010 [42]. The CSB is installed adjacent to the main mass separator in a radiation-shielded room in the basement of the TRIUMF ISAC facility. As presented in Chapter 1, an ECRIS is used at the TRIUMF ISAC facility as a charge state booster to increase the charge state of rare isotope beams before injection into the LINAC for post-acceleration. The schematic drawing of the TRIUMF ECRIS CSB is shown in Figure 4.1.

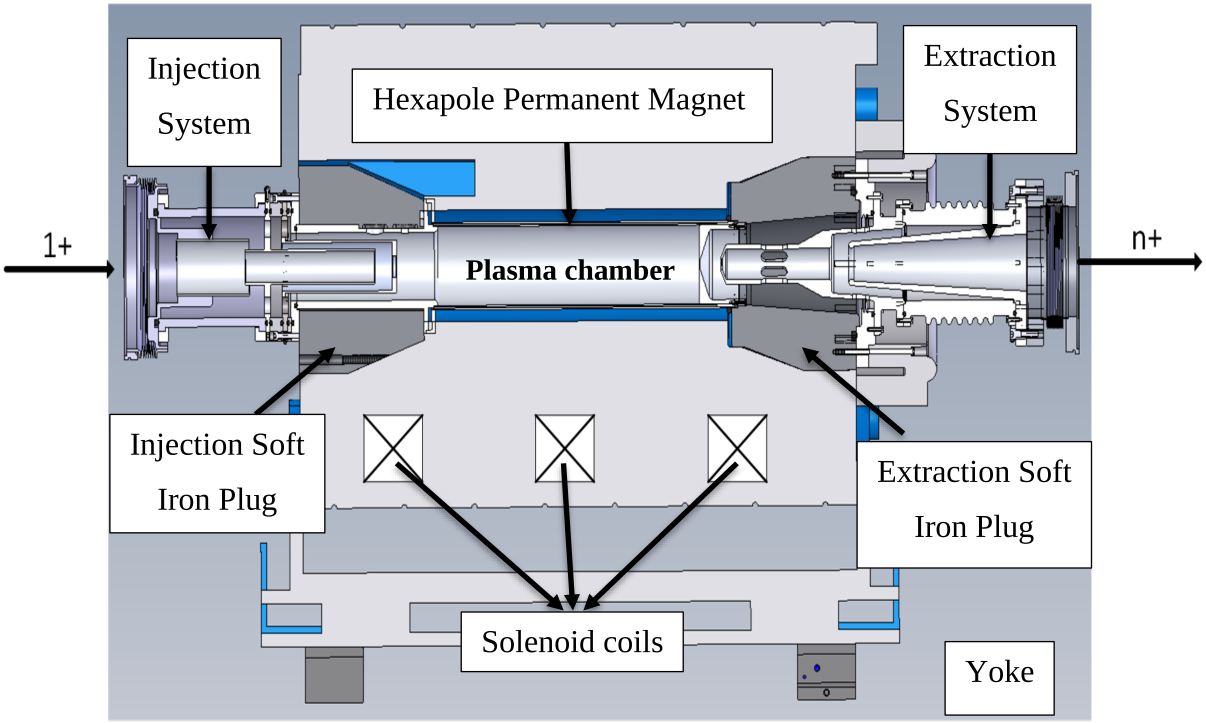

Figure 4.1: Schematic diagram of the TRIUMF ECRIS CSB showing the solenoid coils, iron yoke, hexapole permanent magnet, iron plugs, injection system and extraction system [43].

Singly charged ions are injected into the booster from the left, and highly charged ions (HCIs) are extracted from the right. The solenoid coils are indicated with the rectangular boxes with the crosses, while the hexapole permanent magnet (not shown completely) is located around the plasma chamber. For clarity, the model of the CSB designed in OPERA is shown in Figure 4.2.

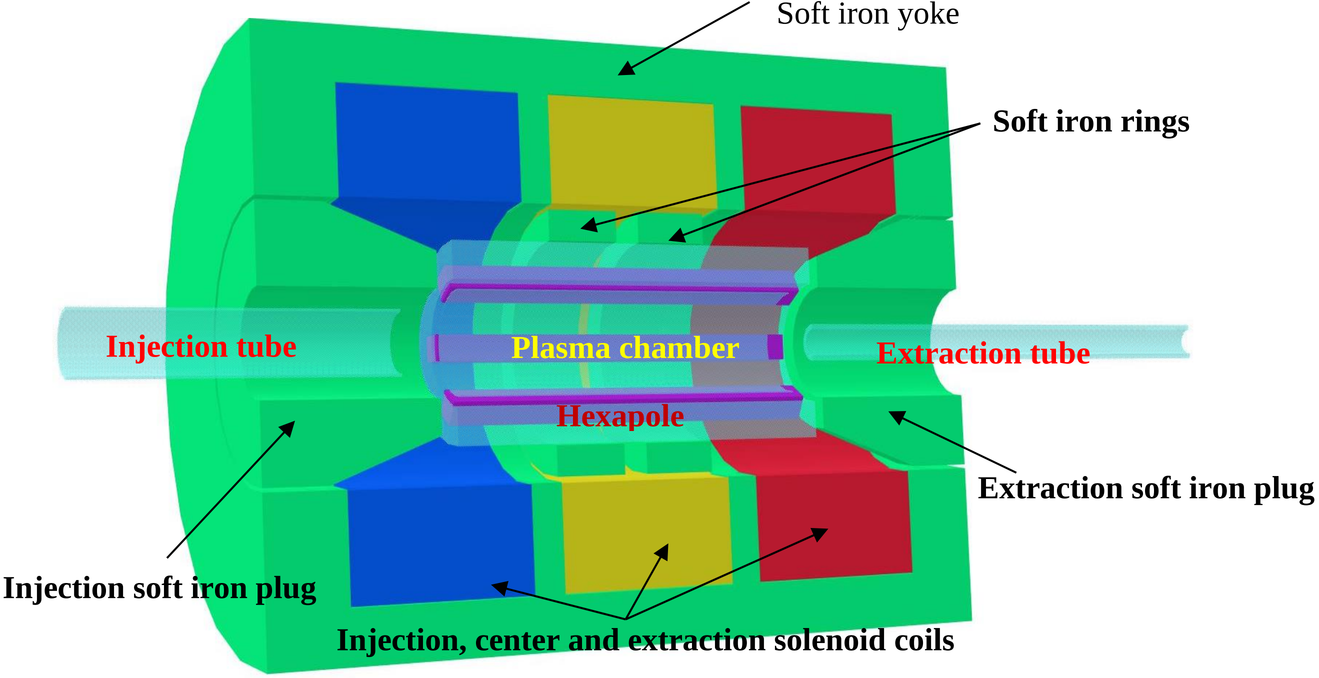

Figure 4.2: TRIUMF ECRIS CSB system modelled in OPERA© to simulate the magnetic field (both radial and axial) distribution of the CSB.

The plasma chamber of the booster is about 300 mm long and 74 mm inner diameter. A singly charged ion beam selected from the mass separator is injected into the booster through a two-step deceleration injection system, and extraction of highly charged ions is achieved through a three-electrode extraction system, otherwise known as the accel-decel extraction system. The extraction system comprises the plasma electrode, the puller electrode (extraction electrode) and the ground electrode. The CSB is installed on a high-voltage platform with an electrical voltage close to the voltage source of the target ion source station so that injected ions can be decelerated and stopped in the plasma. The booster is equipped with two axial slots at the injection region, one of these slots is used to introduce support gases into the plasma chamber, and the other is used to launch electromagnetic waves through the WR-62 water-cooled waveguide into the plasma. The booster is routinely operated with helium gas as a support gas. To achieve a low-pressure vacuum as low as $10^{-8}\ Torr$, two cryo pumps are connected to the booster at the injection and extraction regions because they are not sensitive to the stray fields of the CSB. Cryo pumps achieve high vacuum by using cold helium-cooled surfaces to trap gas molecules.

For axial plasma confinement, magnetic fields are generated axially by a set of three solenoid coils, one at the injection, one at the center, and the last at the extraction region, while radial confinement is achieved using magnetic fields generated by hexapole permanent magnets. Each solenoid coil has 128 turns and comprises four pancakes of copper coils. The solenoid coils and the hexapole are encapsulated in an ARMCO soft iron core to increase and concentrate the flux of the magnetic field. The soft iron plugs at the injection and extraction are in place to shield stray magnetic fields. The axial slot for gas and electromagnetic injection into the CSB is located in the injection iron plug, making the magnetic field in the region to be asymmetric. The center coil of the solenoids produces the minimum magnetic field required to meet the resonance condition of the booster. Besides, the CSB is equipped with two soft iron rings in the center around the hexapole to adjust the minimum and the resonance magnetic field of the CSB. The combination of the solenoid fields and the hexapole fields form the minimum magnetic field configuration that stabilizes the plasma against Magnetohydrodynamic (MHD) instabilities. In the minimum-B field configuration, the minimum magnetic field occurs at the center and increases in every direction towards the wall of the plasma chamber. The typical operating parameters of the CSB are summarized in Table 4.1.

Table 4.1: Typical Operating Parameters of the TRIUMF CSB

Parameters	Values
B_{inj}(I = 1050 A)	$\sim 1.0\ T$
B_{min}(I = 200 A)	$\sim 0.3\ T$
B_{ext}(I = 762 A)	$\sim 0.7\ T$
B_{ecr} ($f_{rf} = 14.5\ GHz$)	$\sim 0.5\ T$
$B_r(r = 32\ mm)$	$\sim 0.7\ T$
High voltage bias	$10 - 15\ kV$

The magnetic field distributions, both axial and radial of the CSB, were recently mapped using a robotic Hall probe that was assembled and calibrated at TRIUMF. The magnetic field mapping of the CSB was necessary to accurately describe the CSB injection and extraction systems and to also have up-to-date information about the booster.

The hall probe can map up to 1000 mm longitudinally and radius at different angles ($0-360°$). The maximum radius that the probe can map is limited by the system's radius to be mapped. For the CSB, it was only possible to map the radius up to $24\,mm$. As part of this thesis, the field distributions, transverse (Bx and By) and longitudinal (Bz), were mapped from the injection region to the extraction region of the CSB, one measurement after the other. The magnetic field was mapped from $123\,mm$ away from the injection soft iron plug for longitudinal field measurements and $144.5\,mm$ away from the injection iron plug for transverse field measurements. The measurement covers $1000\,mm$ through the CSB geometrical center up to the extraction region. The magnetic field distribution of the CSB was also simulated in OPERA and compared with the measurements. Figure 4.3 shows the measured B_x and B_y field distribution resulting from the hexapole at $r = 24\,mm$ and $z = 10.5\,mm$ from the geometrical center of the CSB as a function of theta. The measured radial field distribution up to $r = 24\,mm$ due to the hexapole is compared with the OPERA simulation in Figure 4.4.

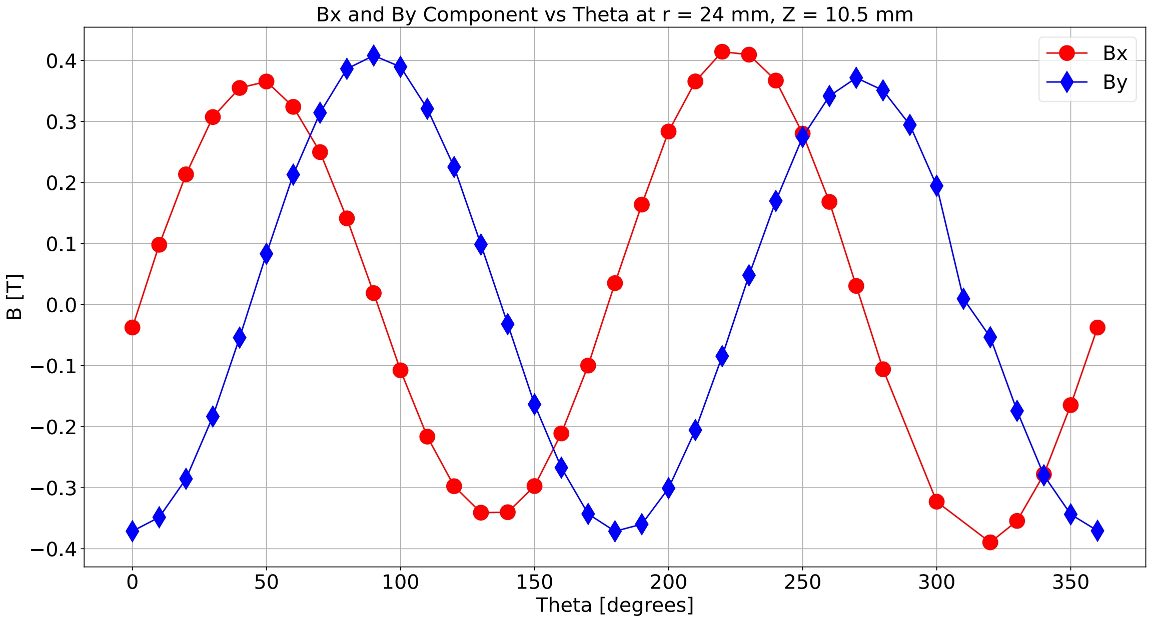

Figure 4.3: B_x and B_y field distributions of the CSB mapped inside the CSB at the radius of 24 *mm* and longitudinal position of 10.5 *mm*.

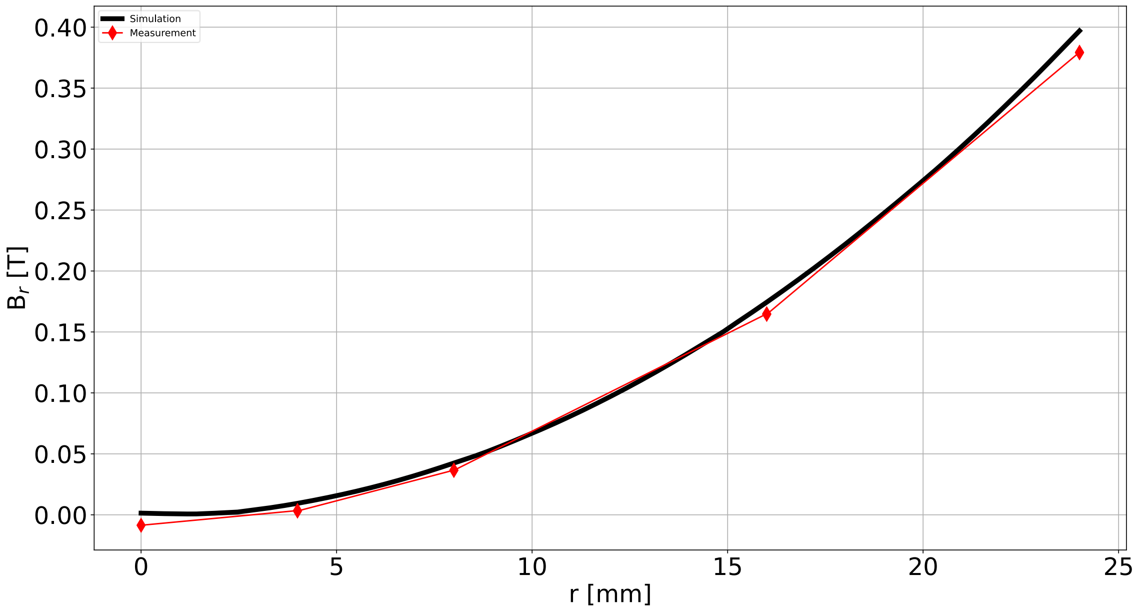

Figure 4.4: Comparison between mapped radial magnetic field distribution and OPERA simulated radial magnetic field distribution at the geometrical center of the CSB.

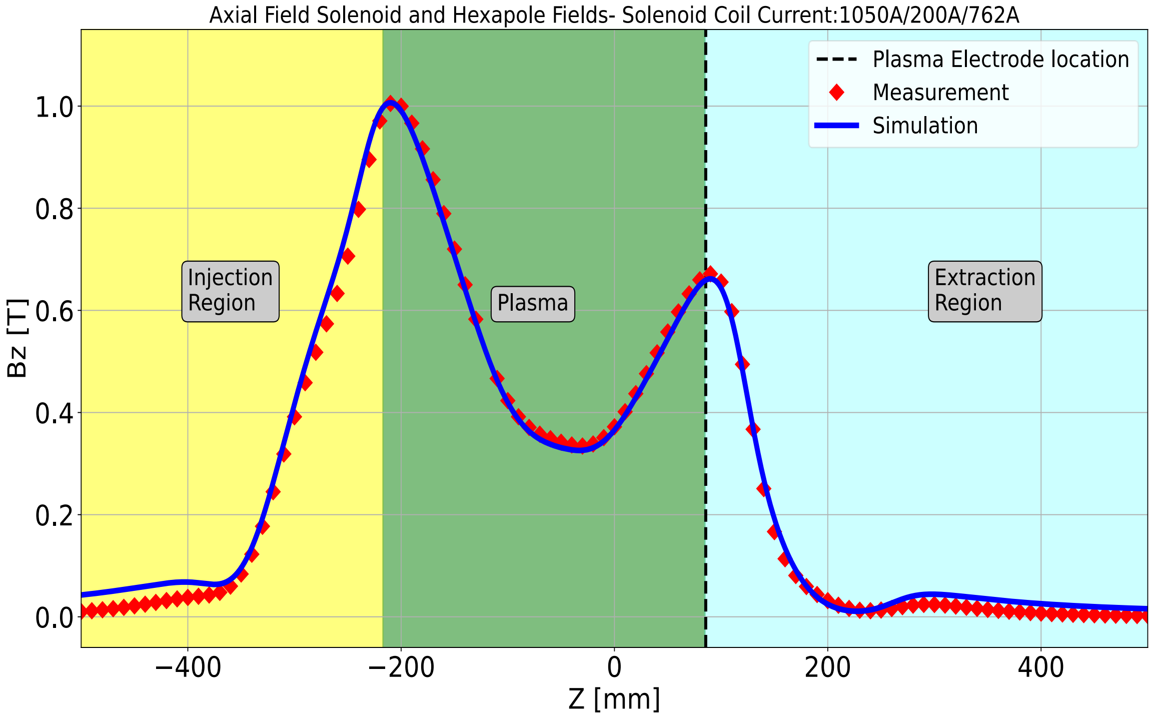

Figure 4.5: Measured axial magnetic field distribution of the CSB compared with the axial magnetic field distribution modelled in OPERA simulation. The yellow region is where the injection system of the CSB is installed while the blue region is where the extraction system of the CSB is installed.

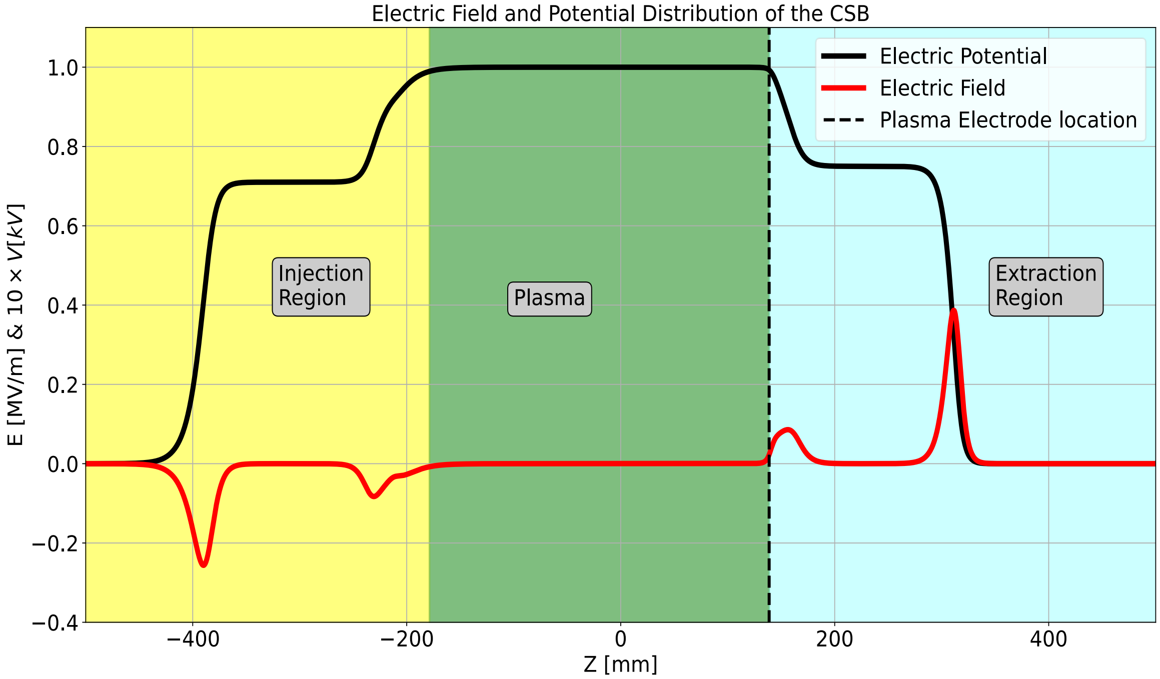

Figure 4.6: Electric field and potential distribution of the CSB simulated in OPERA including the voltage and electric fields from the injection and the extraction systems. The negative electric field in the injection region indicates that the injected ions are decelerated in two stages while the positive electric field in the extraction region indicates that highly charged ions are accelerated in two steps.

The longitudinal magnetic field distribution of the CSB is compared with the OPERA simulation in Figure 4.5. The vertical black dash line indicates the location of the extraction aperture along the magnetic field. The area shaded in yellow is the injection region, while the shaded in blue is the extraction region. As seen, both regions are in a strong magnetic field.

Figure 4.6 shows the electric potential distribution (black plot) and the corresponding electric field distribution (red plot) of the CSB calculated and plotted from the injection ground to the extraction potential in OPERA. The distributions consist of the potential and the corresponding electric fields created by the injection system, the plasma chamber and the extraction system. The first and the second injection electrodes (IE1 and IE2) are biased to 7.1 kV and 9.2 kV, respectively, and the CSB plasma chamber and the plasma electrode are both biased to 10 kV, and finally, the puller electrode is biased to 7.5 kV. These are the typical operating parameters for the CSB. As seen in Figure 4.6, the two negative peaks of the electric fields (two steps in the electric potential) in the injection region indicate that the injected ions are decelerated in two stages. In the plasma, the ions are completely stopped, provided that the energy of the injected ions is equal to the plasma chamber bias voltage. The highly charged ions are extracted and accelerated in two stages, as shown by the positive two peaks in the electric field in the extraction region.

The CSB has been used to charge breed rare isotopes ranging from Potassium to uranium. For injection optics, extraction optics and beam transport system tunning, the CSB is equipped with a cesium test ion source (CTIS) located behind the injection system of the CSB. Injection of rare isotope beams into the CSB from the target ion source station is achieved by inserting a set of electrostatic benders into the beam's path. Overall beam focusing into the booster is achieved using three FODO lattices (more details in Section 4.4, Figure 4.11), while beam focusing of extracted highly charged ions before A/Q selection is achieved by OFODOFO lattice (Section 4.5). The injection and the extraction beamlines of the CSB are equipped with several Faraday cups at specifically defined locations to measure the beam current with sensitivities down to a few picoamperes. The Faraday cups are inserted into the beam's path and stop the beam's ions to determine the beam current.

Furthermore, several profile monitors are installed on the beamlines to monitor the shape and position of the beam vertically (y-direction) and horizontally (x-direction). Also, several vertical and horizontal steerers are installed to correct the beam angles and compensate for the misalignment of the beamline optics. Due to the restricted space in the installation area of the CSB, there was no room to install emittance meters, so profile monitors are usually relied on to monitor the beam quality. The combination of a magnetic dipole, which has the resolving power $(M/\Delta M)$ of about 200, two electrostatic benders act as a Nier-type spectrometer [8] to select the desired charged-bred rare isotope beams.

4.2 The Electromagnetic Wave Heating Setup

The radio-frequency heating of the ECRIS plasma was originally configured for single-frequency heating. The setup consists of a BNC signal generator (model 845) with a frequency range between $100\,kHz - 26.5\,GHz$, and a CPI travelling wave tube amplifier (TWTA) (model VZM6993J4) with a frequency range between $13.75 - 14.5\,GHz$ with a maximum output power of $600\,W$. Figure 4.7 shows the not-drawn-to-scale schematic of the single-frequency heating setup of the TRIUMF ECRIS CSB.

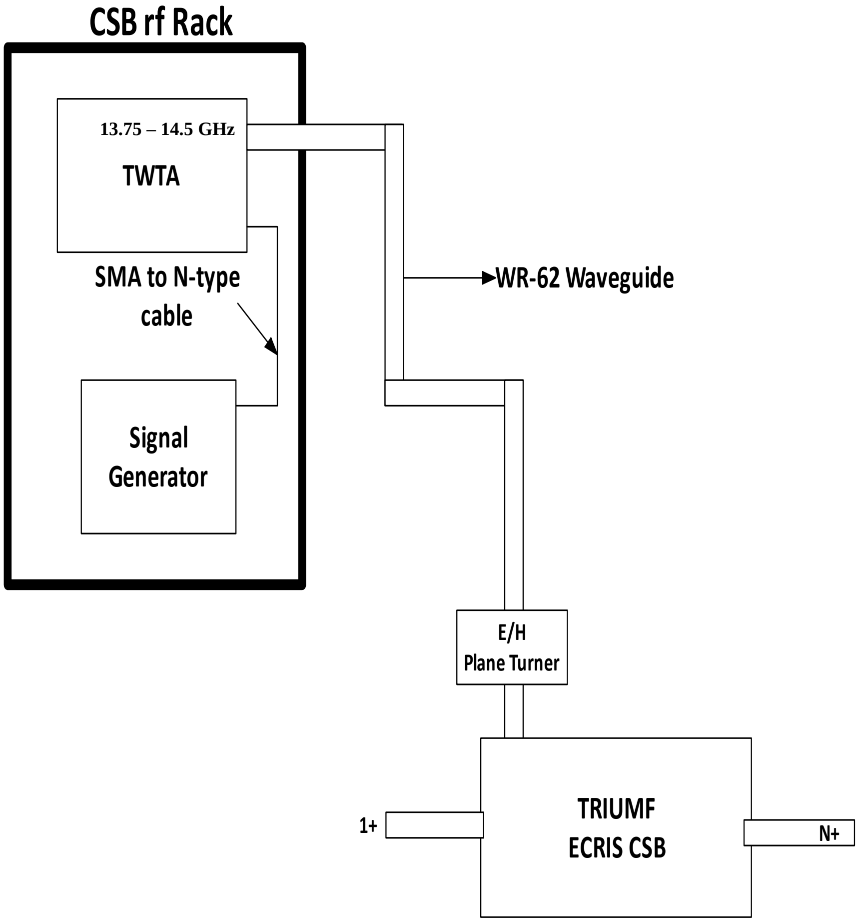

Figure 4.7: Schematic of the rf system for the TRIUMF ECRIS CSB under single-frequency heating.

The signal generator and the amplifier are located in the ISAC 1 experimental station in a rack behind the ISAC yield station. The amplified electromagnetic wave is coupled to the ECR plasma via a WR-62 waveguide with a frequency range between $12.4 - 18\,GHz$. The waveguide, which is about $16\ m$ long, has four E-bends between the amplifier and the ECRIS. A CERNEX© E/H plane turner (model CPT62EH-01, S/N:7513) is connected to the other end of the waveguide before transitioning the waveguide into the high-voltage section of the ECR.

4.3 Cesium Test Ion Source (CTIS)

For the tuning of the ECRIS CSB (including the injection beam optics, CSB injection system, extraction system and the extraction beam optics) for preparation for charge breeding of radioactive isotope beam (RIB), a cesium test ion source (CTIS) is used. The ion source is adjacent to the electrostatic bender switchyard for injecting the RIBs produced from the online station into the booster (see Figure 4.12). The CTIS is a surface ion source designed and developed by HeatWave Labs, Inc, with model number 101500 HWIG-250. The ion source assembly consists of a heater to heat up and surface ionize the cesium evaporated from the pellet (singly charged $133Cs^+$ ions are mostly produced) and an extraction system that consists of an extraction electrode (EE), an Einzel lens (EL) (for beam focusing) and the ground electrode (GE). Meanwhile, the extraction system of the ion source has been modified to adapt the surface ion source to the injection beamline of the TRIUMF ECRIS CSB. The ground electrode in the original design was replaced with another extraction electrode followed by another ground electrode. The total length of the extraction system is about 40 mm (shown in the simulation in Figure 4.8). The CTIS is biased with the same high voltage as the CSB so that Cs$^+$ ions can be injected and decelerated in the center of the plasma of the CSB.

Meanwhile, to overcome the positive plasma potential of the CSB, the CTIS is equipped with a delta-V (ΔV) power supply to slightly increase the energy of the injected ion to account for the plasma potential. During normal operation, ΔV is usually between $8 - 20\ V$, depending on the plasma conditions. The CTIS extraction system was simulated in IGUN for the extraction of a singly charged cesium ion beam with a current of 10 nA at the energy of 10 kV. The result of the simulation of the extracted beam is shown in Figure 4.8.

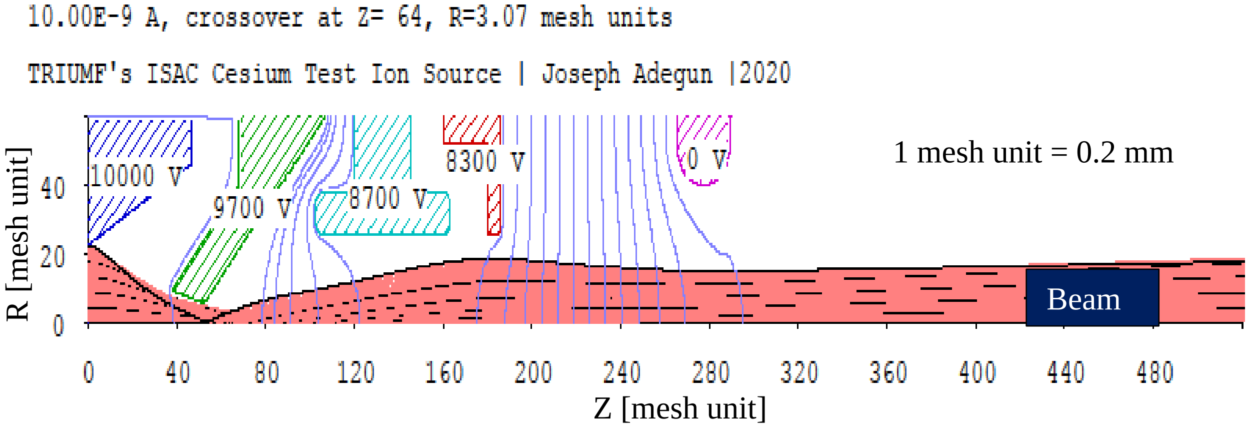

Figure 4.8: IGUN simulation of singly charged cesium ion beam at 10 kV from the optimized extraction system of the test ion source. The extraction system is optimized at the voltage values printed on the electrodes of the extraction systems. The current of the extracted ions is printed at the top of the figure.

The heater that houses and ionizes the cesium pellets is embedded in the electrode, biased to $10000\,V$ (blue), which defines the beam energy. The extraction electrode that creates the electric field that extracts the ion beam is biased to $9700\ V$ (green), while the Einzel lens, which focuses the extracted beam, is biased to $8700\ V$. The added electrode that adapts the extraction system to the beamline is biased to $8300\ V$ (red). The singly charged cesium beam (red plot) is extracted from the left to the right, as shown in Figure 4.8.

The values of the voltage set on the electrodes were defined by systematically varying the voltage on the extraction electrode (CTIS: EE), Einzel lens (CTIS: EL) and second extraction electrode (CTIS: EE2) one after the other while monitoring the Faraday Cup (FC5) for the highest intensity of Cs^{+} which is around $10\ nA$, and also monitoring the spatial distribution of the beam on profile monitor, CSB: RPM5 located in the front of quadrupole Q5, to ensure that the beam distribution is not distorted. The electrostatic steerers and the quadrupole (Q5) directly in front of the CTIS extraction system were switched off during this systematic investigation. Meanwhile, the emittance and the Twiss parameter of the Cs+ ions extracted at the settings above were measured using the quadrupole scan technique by scanning the strength of quadrupole Q5 and measuring the beam size at profile monitor RPM5.

The RMS emittance and the Twiss parameters of the beam at the entrance of Q5 are $\varepsilon = (8.78 \pm 0.58)\ mm - mrad, \quad \alpha = (-2.78 \pm 0.20),\ \beta = (116.2 \pm 7.3)\ cm, \gamma = (0.0752 \pm 0.0045)\ cm^{-1}$. And by using the Twiss parameters transformation, the shape and the orientation of the Cs ions can be determined at the exit of the test ion source extraction system. The RMS emittance and the Twiss parameters of the beam at the entrance of Q5 are $\varepsilon = (8.78 \pm 0.58)\ mm - mrad, \quad \alpha = (0.21 \pm 0.02),\ \beta = (13.91 \pm 0.02)\ cm,\ \gamma = (0.075 \pm 0.005)\ cm^{-1}$. Figure 4.9 compares the phase space ellipse at the entrance of Q5 (red plot) with the phase space at the exit of the CTIS (blue plot). As seen, the phase space ellipse at the exit of the test ion source appears almost upright, which suggests that the extracted ions from the CTIS are approximately parallel ($\alpha \cong 0$), while at the entrance of the Q5, the beam is diverging ($\alpha < 0$) because of the large drift length.

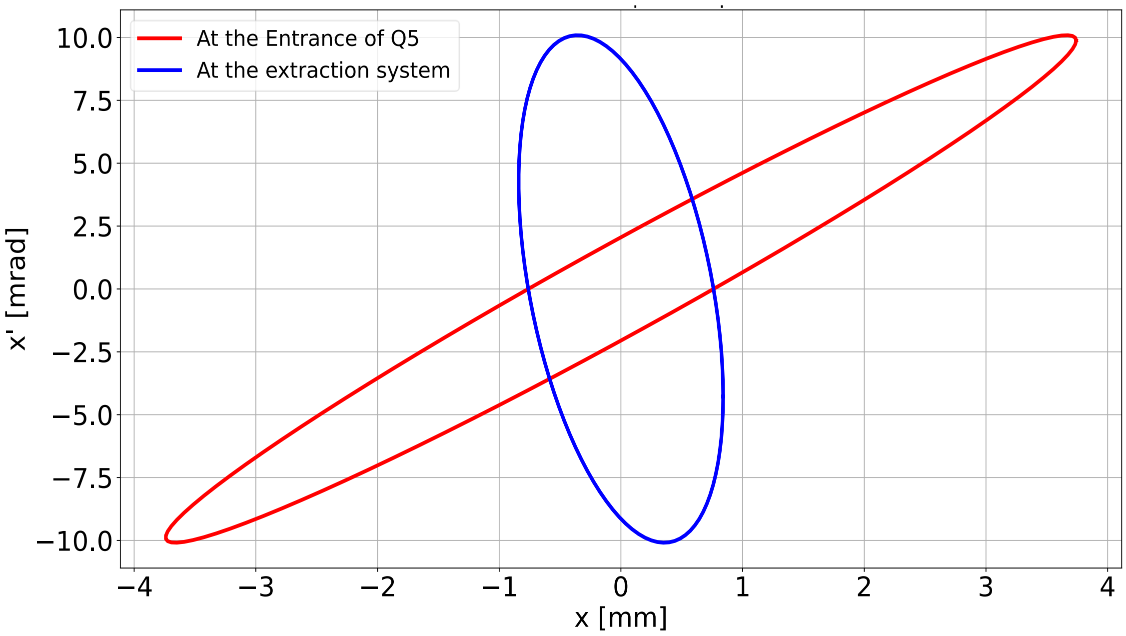

Figure 4.9: Phase space ellipses of singly charge cesium ion beam. The red ellipse was determined using the quadrupole scan technique at the entrance of quadrupole Q5 (see Figure 4.10), while the blue plot was determined using the Twiss parameters transformation at the extraction region of the cesium test ion source.

4.4 CSB Injection Beamline and Injection System

The schematic of the CSB injection beamline shown in Figure 4.10 from the CTIS to the CSB consists of 4 x-direction focusing quadrupoles (Q5, Q7, Q9, Q11), 3 y-direction defocusing quadrupoles (Q6, Q8, Q10), drift regions, 2 Faraday cups (FC5 and FC9), 2 profile monitors (RPM5 and RPM8), 2 vertical steerers, 2 horizontal steerers and an electrostatic switchyard for radioactive beam injection.

Singly charged ions from the test ion source or deflected rare isotopes through the electrostatic benders propagate from the left through the beam optics and the injection system into the CSB. The beam optics are arranged in cells, with each cell consisting of one focusing quadrupole (F), one defocusing quadrupole (D) and two drift regions (O) that are usually referred to as FODO lattice.

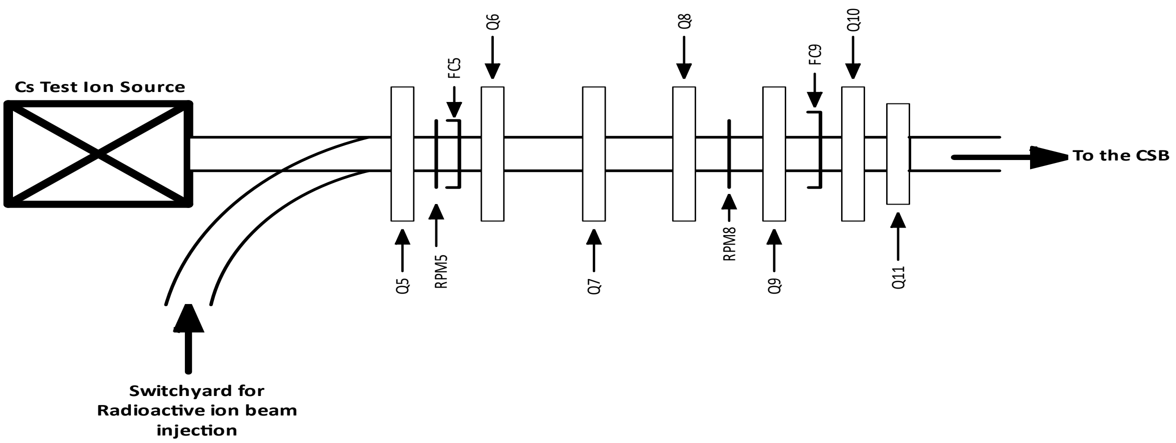

Figure 4.10: Schematic of the CSB injection beamline elements including the cesium test ion source and the switchyard for radioactive ion beam injection into the CSB. The right side of the beamline is coupled to the injection system of the CSB.

The injection beamline consists of three FODO lattices with an additional focusing quadrupole at the entrance of the CSB. The optics arrangement provides the beam's overall focus from CTIS or the target ion station into the CSB. To visualize the envelope and optimize the beam from the CTIS into the CSB, the TRANSOPTR beamline code was used to simulate the injection beamline. The objective of the modelling was to utilize the fitting routine of TRANSOPTR to optimize the strengths of all the quadrupoles to achieve an overall focusing beam with a size less than the aperture radii of the CSB injection system for efficient injection into the ECRIS plasma. The first Injection electrode (IE1) has a radius of $28\,mm$, and the second injection electrode (IE2) is $20\,mm$, respectively. A converging beam is required to prevent beam loss to the electrodes of the injection system. The CSB injection system is discussed later in this section. As presented above, the emittance and the Twiss parameters of the beam at the entrance of Q5 were imported into the TRANSOPTR for modelling the injected ions beam envelope. Figure 4.11 shows the optimized beam envelope of the singly charged cesium beam from the entrance of Q5 up to the booster. The TRANSOPTR calculation includes the injection magnetic field of the CSB and the electric field of the injection electrodes in this region.

In Figure 4.11, the blue curve is the horizontal beam envelope, while the vertical envelope is the curve in red. The black horizontal dashed line is the aperture radius of the quadrupoles, which is $2.54\ cm$. The green vertical dashed lines are the geometrical center of the quadrupoles. The magenta plot is the scaled energy of the beam as a function of longitudinal position. The solid green plot is the axial magnetic field distribution of the CSB at the injection site of the ECR.

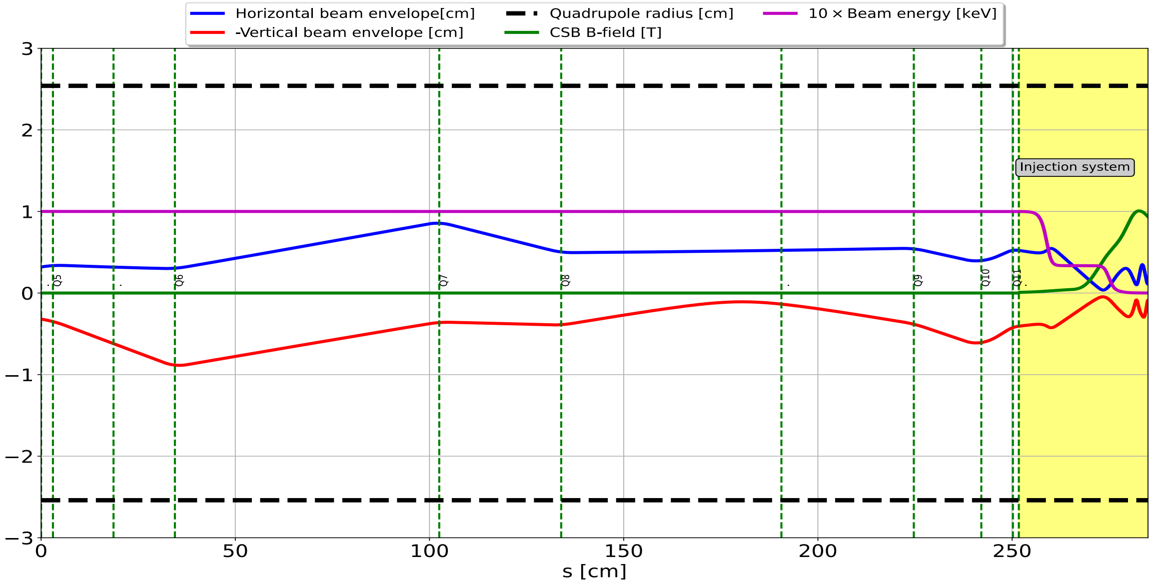

Figure 4.11: Optimized beam envelope of singly charge cesium ion beam modelled in TRANSOPTR from the entrance of quadrupole Q5 to the plasma edge. The envelope was modelled by including the magnetic and electric fields of the CSB in the injection region up to the edge of the plasma (area shaded in yellow). The space charge from the plasma is not included. The black dash lines depict the aperture of the quadrupole, while the green dash lines denote the location of the quadrupoles. The sign of the vertical envelope (red plot) is reversed for visualization.

The yellow-shaded region of the plot shows the injection system and part of the CSB plasma vacuum chamber. As is seen in the beam envelope plot, the beam's energy from the CTIS is constant until the ions reach the injection system of the CSB, where they are decelerated in two stages and simultaneously experience a fast-increasing strong magnetic field before entering the ECR plasma. The beam, in both directions, is overall focused into the CSB through the combined actions of all the quadrupoles depending on the beam parameters at the entrance of Q5. The maximum beam size in both directions as the ions enter the plasma is around 0.1 cm, which is far smaller than the aperture of the injection electrodes.

Furthermore, the injection system of the CSB consists of two electrodes, and they are biased electrically so that injected ions are decelerated before entering the plasma. The injection system is designed to decelerate injected ions in two stages. (Figure 4.6). It is embedded in the strong magnetic field of the ECR ion source. The waveguide and support gas ports are located radially at the injection site of the CSB. The feedthrough for the waveguide and support requires an opening in the magnetic iron yoke, which makes the magnetic field at the injection region non-symmetric and thus affects the trajectories of the injected ions from the CTIS or target ion source station. The 2D cross-section drawing of the injection system is shown in Figure 4.12. Singly charged ions are injected in the drawing from right to left.

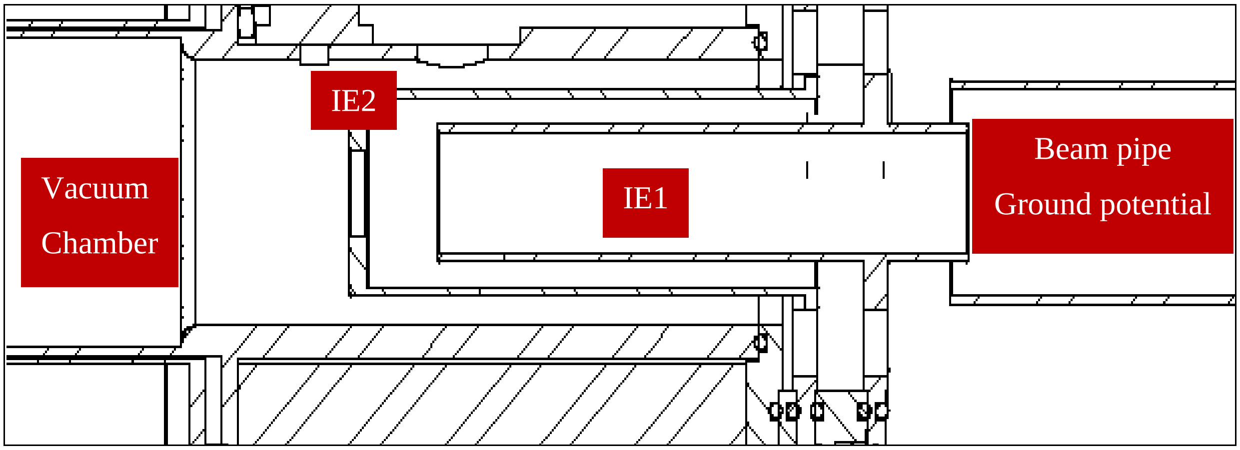

Figure 4.12: Geometry of the electrodes of the CSB injection system showing part of the plasma vacuum chamber [43].

During regular operation, the applied voltage to the first injection electrode (IE1) is about 66 % of the CSB-biased voltage, while the second injection electrode (IE2) voltage is about 96 % of the CSB-biased voltage. The injection system is coupled to the beam pipe that is grounded through an insulator.

4.5 CSB Extraction System and Extraction Beamline

Extraction of highly charged ion beams from the CSB is achieved using the configuration known as the accel-decel extraction system, which consists of three electrodes: the plasma electrode (PE), the puller electrode (EE), and the ground electrode (GE). The extraction system is about 378 mm long and is also embedded in the strong magnetic field of the ECR, just like the injection systems. During the operation of the CSB, the plasma electrode (PE) is biased to the same potential as the CSB, while the puller electrode (EE) is usually biased to about 70 % of the CSB high voltage bias so that ions are accelerated out of the CSB, and finally, and the last electrode is on the ground potential. The extraction aperture in the plasma electrode is 6 mm, the extraction gap, distance between the plasma electrode (PE) and the puller electrode (EE), is 25 mm, while the distance between the puller electrode (EE) and the ground electrode

(GE) is 26 mm. The aperture of the extraction electrode is 10 mm, while the aperture of the ground electrode is 32 mm. The 2D drawing of the extraction system is shown in Figure 4.12.

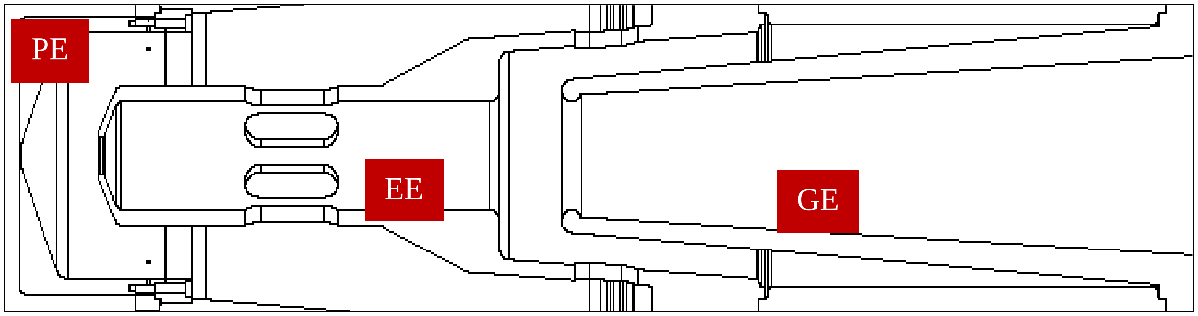

Figure 4.13: Geometry of the electrodes of the CSB extraction system [43]. The gaps in the puller electrode (EE) are for vacuum pumping.

Intrinsically, the electron cyclotron resonance ion sources produce ion beams of different mass-to-charge ratios, firstly, because support gas is needed to produce a plasma of energetic electrons and secondly because ECRIS is usually operated at a pressure (operating pressure $\sim 10^{-8}\ Torr$ is usually above ultra-high vacuum pressure) where residual gases such as carbon, nitrogen, oxygen and argon are not completely pumped out. So, during beam extraction, all the residual ions are extracted alongside the injected radioactive isotopes (radioactive isotope ion intensities are usually low).

Meanwhile, emittance measurement performed on AECR-U [44], [45] showed that the magnetic field plays a significant role in the magnitude of the emittance of the ECR beam, and normalized emittance is strongly dependent on mass and charge state. Furthermore, the evolution of the normalized emittance showed that low-charged light mass ions are found on the edge of the beam pipe while highly charged heavier mass ions are concentrated in the center of the beam pipe during extraction. However, considering the spatial distribution of the different species of ions extracted from the ECR, it is essential to include the contribution of the residual ions while simulating the extraction system of the ECR ion source to describe better the plasma sheath where different ions are extracted. Meanwhile, IGUN code has the feature to model an ion beam of different masses and many charge states. However, considering the computer's computing power required and time, only six masses and seven charge states were modelled. They are from the support gas ions ($4He^{+}$ and $4He^{2+}$), some prominent and intense charge states of residual ions (H^{+}, $^{12}C^{5+}$, $^{14}N^{6+}$, and $^{16}O^{7+}$) and a single desired high charge state of cesium ($^{133}Cs^{27+}$). The measured magnetic field of the ECRIS CSB, as presented in Section 4.1, was imported into IGUN to describe the extraction system accurately. Figure 4.14 shows the graphics of the extraction system exported from IGUN with the radius and the longitudinal plot of the picture in mesh units [1 $mesh\ unit = 0.2\ mm$].

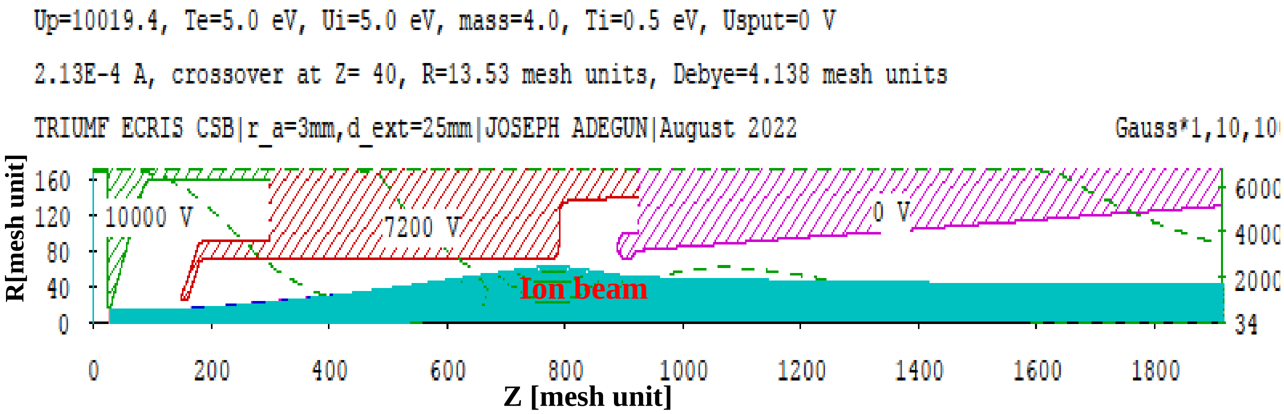

```
Up=10019.4, Te=5.0 eV, Ui=5.0 eV, mass=4.0, Ti=0.5 eV, Usput=0 V
2.13E-4 A, crossover at Z= 40, R=13.53 mesh units, Debye=4.138 mesh units
TRIUMF ECRIS CSB|r_a=3mm,d_ext=25mm|JOSEPH ADEGUN|August 2022
```

Figure 4.14: IGUN simulation of the CSB extraction system. Some selected intense residual ions from the CSB plasma and Cs^{27+} were modelled in the simulation. At a bias voltage of 10 kV, the extraction system is optimized with the puller electrode voltage of 7.2 kV. The plasma parameters and the extracted beam current are printed at the top of the figure.

The properties of the plasma where the defined ions are extracted, such as bias potential, plasma potential, electron temperature, ion initial energy, ion temperature, Debye length and extracted current, are displayed at the top of the Figure. The electrode in green colour is the plasma electrode which bears the aperture where ions are extracted. The plasma electrode is on the same electrical potential as the plasma chamber. The electrode in red colour is the puller electrode. The potential on the puller electrode creates an electric field with respect to the plasma electrode to extract ions. The last electrode on the right in magenta is on ground potential. The extracted ion beam flows from the left to the right in Figure 4.14. The green dash line is the axial magnetic field of the ECR in Gauss (G).

Figure 4.15 shows the phase space of all the ions modelled in IGUN but processed in Python. Different masses and charge states have different phase spaces, focal lengths and orientations because of the strong magnetic field at the extraction system of the ECR ion source, which acts as a magnetic solenoid lens.

The emittances of all seven ion species ranging from H^{+} to Cs^{28+} modelled in IGUN are presented in Table 4.1. In addition to the feature in IGUN that allows the modelling of several ions and computes individual emittance for each ion modelled, as presented in Table 4.1, IGUN can also compute an average emittance (a single value) for the modelled ions. So, for all the ions simulated in Figure 4.14, the average emittance is $136.19\ mm - mrad$. As would be presented in Chapter 5, the simulated emittance is within a typical ECR emittance.

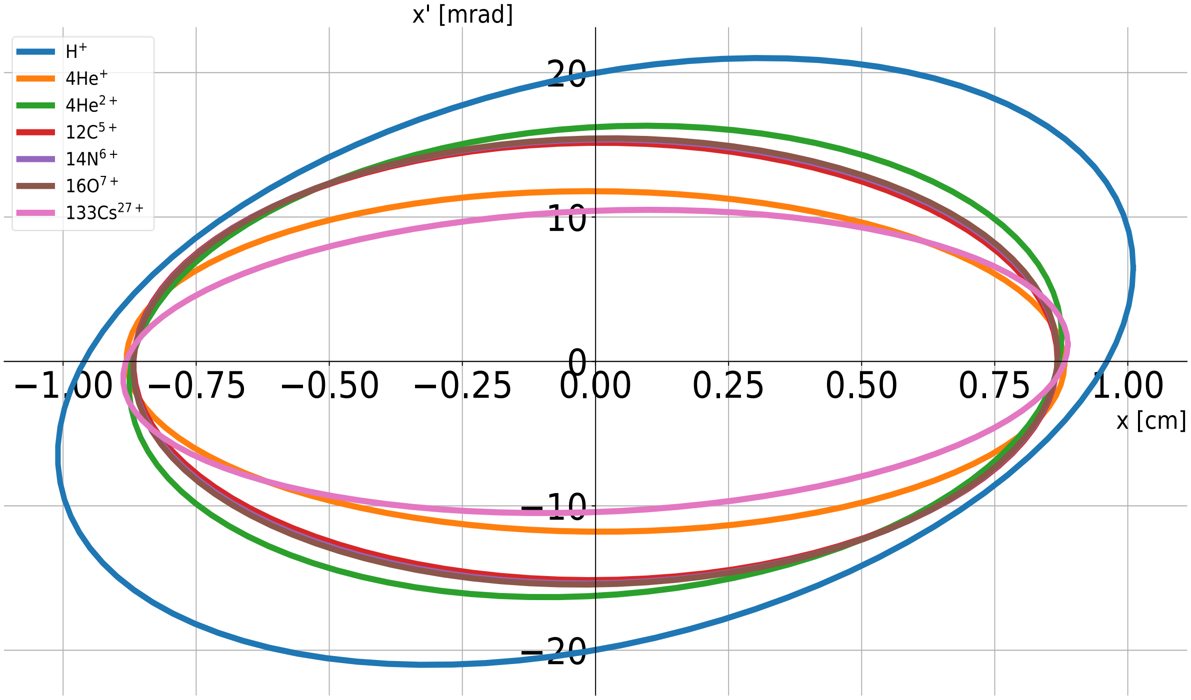

Figure 4.15: Phase space ellipses in $x - x'$ plane of some selected intense residual ions and $^{133}Cs^{27+}$ simulated in IGUN using the extraction system of the CSB. The magnetic field in the extraction region of the CSB is responsible for different phase space orientations.

Furthermore, as seen in Figure 4.15, the phase space of H^+ encapsulates the phase spaces of other ions, and the phase space of the desired cesium ion is averagely located in the center of the rest of the other phase spaces, thus if an emittance measurement is performed on the total extracted beam from the ECR, it can be then be assumed that the emittance of the desired cesium charge state lies within the measured value.

Table 4.1: Modelled Emittance of Some Selected Intense Residual Ions and Cs^{27+} Extracted from the TRIUMF ECRIS CSB.

Ion	A/Q	Emittance [mm-mrad]
H+	1	201.88
$^4He^+$	4	103.89
$^4He^{2+}$	2	142.17
$^{12}C^{5+}$	2.4	131.38
$^{14}N^{6+}$	2.33	133.43
$^{16}O^{7+}$	2.28	134.08
$^{133}Cs^{27+}$	4.93	92.59

Figure 4.15 can be further explained by comparing the emittance due to ion temperature with the emittance due to the magnetic field in the extraction region of the CSB. The normalized emittance as a result of the ion temperature in the plasma assuming a Maxwellian temperature distribution is given by [21]:

$$\varepsilon_{Temp}^{norm} = 0.016r\sqrt{\frac{KT_i}{A/Q}} \tag{4.1}$$

While the contribution from the magnetic field has been derived in Section 3.10, and it is given as follows:

$$\varepsilon_{Mag}^{norm} = 0.161\frac{B_0 r^2}{A/Q} \tag{4.2}$$

Where r is the radius of the extraction aperture, B_0 is the magnetic field at the location of the extraction aperture, KT_i is the ion temperature in eV and A/Q is the mass-to-charge ratio of the ion beam. Since equations 4.1 and 4.2 both depend on the mass-to-charge ratio, Figure 4.16 compares the magnetic emittance with the contribution from the ion temperature, assuming. $KT_i = 0.5\ eV$ with the magnetic field at the aperture radius $B_0 = 0.7\ T$ and aperture radius $r = 3\ mm$ for the A/Q modelled and plotted in Figure 4.15.

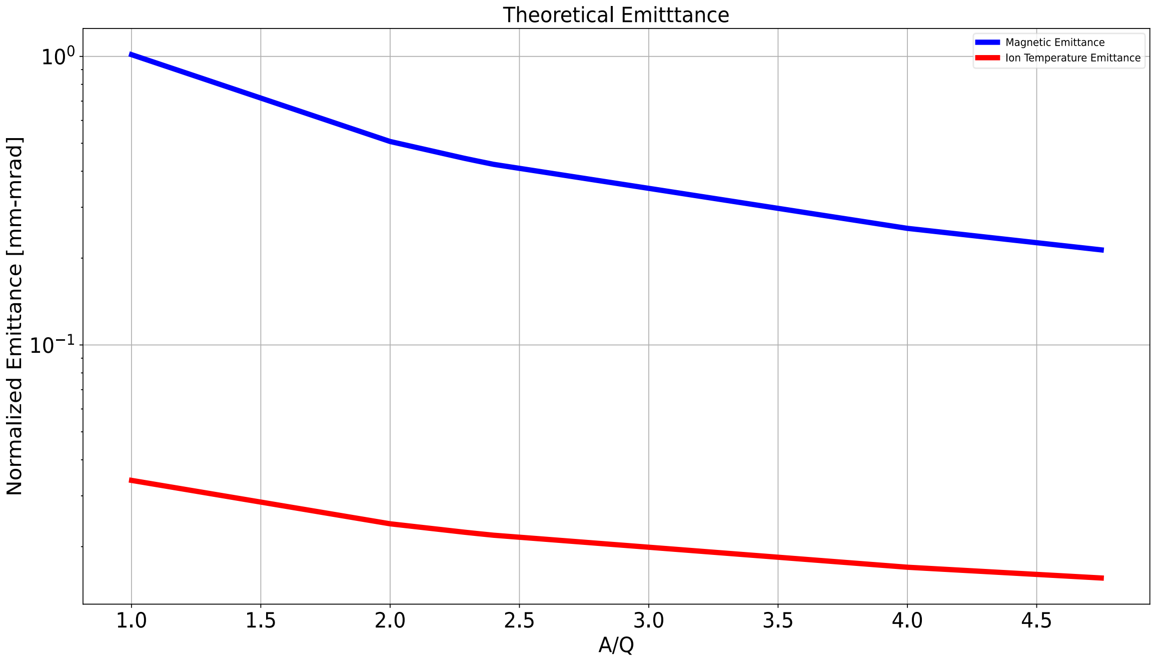

Figure 4.16: Comparison between magnetic and ion temperature emittances plotted against A/Q between 1 and 4.75 for ion temperature of 0.5 keV, an aperture radius of 3 mm and a magnetic field of 0.7 T.

As seen, both the magnetic emittance and the ion temperature emittance decreases with A/Q, however, the magnetic emittance is more prominent than the emittance due to the ion temperature; thus, the emittance resulting from the magnetic field in the ECR dominates the contribution from the ion temperature.

Furthermore, the schematic of the CSB extraction beamline is shown in Figure 4.17. The beamline will only be discussed until the Faraday cup 16A (FC16A). In this section, the beam optics consist of five quadrupoles, one 90° sector magnetic dipole, two 45° electrostatic benders, four profile monitors, drift regions, three Faraday cups, three mass slits that have a maximum opening width of $20\ mm$, three vertical steerers, and one horizontal steerer. As shown in the schematic, three quadrupoles (otherwise referred to as the triplet), Q12, Q13 and Q14, which are focusing beams in the $x-$direction (defocusing in the $\mathrm{y}-$direction), defocusing in the $x-$direction (focusing in the $y-$direction) and focusing in the $\mathrm{x}-$direction (defocusing in the $y-$direction), respectively, are designed to focus a high current beam (current up to $500\ \mu A$) into a waist horizontally before and after the magnetic dipole, while the optics after the magnetic dipole were designed for the transport of low current beam (about $10\ nA$).

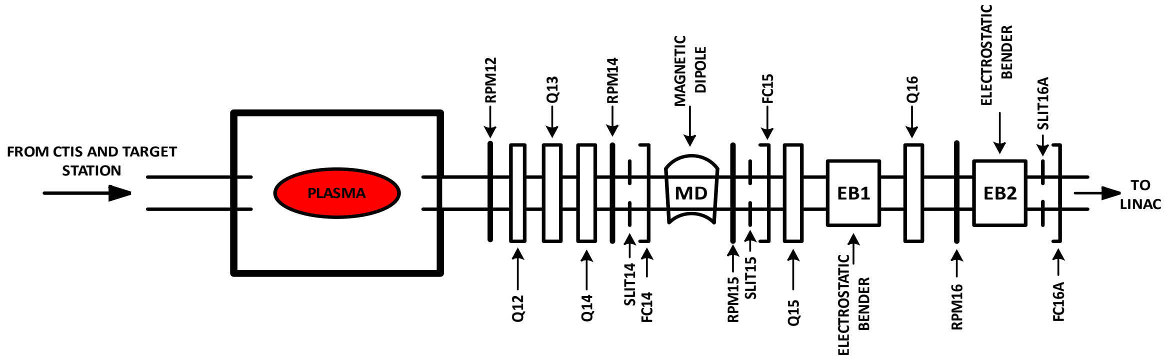

Figure 4.17: Schematic of the CSB extraction beamline elements with Nier-type spectrometer configuration. The left side of the schematic is connected to the injection beamline.

At the entrance and exit of the dipole are mass slits to trim the beam tail of the transverse particle distribution. The momentum dispersion created by the magnetic dipole is counteracted by the two quadrupoles (Q15 and Q16) and two 45° electrostatic benders (EB1 and EB2) located after the magnetic dipole. At the exit of the last electrostatic bender (EB2) is another slit placed to purify the selected beam further before it is sent to ISAC LINAC for post-acceleration.

As already demonstrated and presented, several ions are extracted alongside the charge state of interest from the ECRIS-based charge state booster, but in TRANSOPTR, only a single envelope can be modelled at once. So, the envelope of the $^{133}Cs^{27+}$ beam was modelled from the exit of the extraction system up to Faraday cup 16A (Figure 4.17). The objective of the TRANSOPTR modelling and optimization was to vary the strength of all the quadrupoles along the beam path to achieve an achromatic focussed beam (beam with zero dispersion) at the location of Faraday cup FC16A.

Using the quadrupole scan technique (QST), the total emittance of the CSB was determined by scanning quadrupole Q14 and measuring the beam size on RPM14, and since emittance is conserved, the Twiss parameters transformation was used to determine the beam size and shape at the exit of the CSB extraction system using the Python NumPy linear algebra module. For example, the emittance and the Twiss parameters of the CSB determined using this technique are given as $\varepsilon = (118.9 \pm 8.9)\, mm - mrad, \alpha = -0.67 \pm 0.01, \beta = (23.1 \pm 1.8)\, cm, \gamma = (0.06 \pm 0.01)\, 1/cm$ and for a given charge state, say $^{133}Cs^{24+}$, the envelope of the beam can be modelled from the exit of the CSB extraction system up to the final destination of the desired beam. Figure 4.18 below shows the beam envelope of $^{133}Cs^{24+}$ at $10 * Q\ keV$ energy from the CSB.

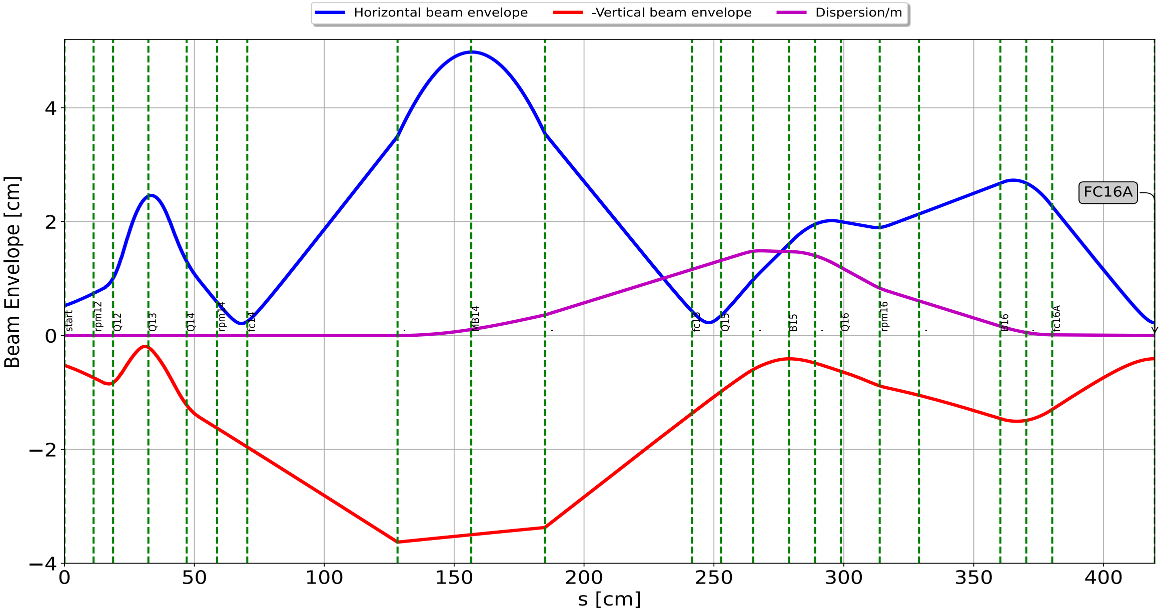

Figure 4.18: Optimized beam envelope of $^{133}Cs^{24+}$ from CSB extraction system to Faraday cup FC16A (see Figure 4.17) at an energy of 10*Q keV. The green dash lines indicate the locations of the optics along the CSB extraction beamline. The sign of the vertical envelope (red plot) is reversed for visualization. The elbow in the horizontal beam envelope (blue plot) around the horizontal axis at $s = 150\ cm$ indicates deflection in the magnetic dipole.

The blue plot is the envelope of the beam in the horizontal plane (affected and deflected by the magnetic field), while the red plot is the envelope in the vertical plane (unaffected by the dipole fields). The magenta plot is the dispersion created by the magnetic dipole. The dashed-green lines are plotted to indicate the diagnostics locations along the beam transport.

As seen, the extracted ions coming from the CSB diverge as they approach the entrance of Q12, but at the exit of the triplet (Q14), the beam is focused into a waist horizontally (blue curve) into the entrance and at the exit of the magnetic dipole (MB14) but drifts vertically (red curve) through the dipole. However, at the location of Faraday cup FC16A, the objective of the modelling was satisfied, which is a beam with a waist in both planes.

The magenta curve is the dispersion in meters created by the magnetic dipole. As seen in the plot, there was no dispersion before the magnetic dipole. However, due to the fundamental properties of a dipole, the deflected plane experienced dispersion at the center of the dipole and increased the size of the beam as the ion beam exited the dipole. However, it was cancelled out by the combined actions of the quadrupoles Q15 and Q16 and electrostatic benders B15 and B16. The combination of the magnetic dipole and electrostatic benders is called the Nier-type spectrometer [8].

4.6 Major Improvements of the TRIUMF ECR Ion Source CSB in the Past

The most critical problem in the operation of the ECR ion source is the issue of background and residual ions contamination. The ion source operating pressure, the composition of the chamber wall materials, and the injection and extraction electrodes define the type of these background ions. In the TRIUMF ECRIS CSB, the chamber wall, the injection and extraction electrodes were originally stainless steel, and the background ions that are encountered during regular operation are from residual gases, mainly carbon, oxygen, nitrogen and argon, and sputtered materials such as iron, manganese, and cobalt from the plasma chamber, the injection and extraction electrodes. The intensity, most especially of the residual ions, can be more than 10^{12} particles per second (pps) during regular operation. These impurity ions contaminate the A/Q regions of the desired radioactive ions, which usually have an intensity several orders of magnitude lower than the intensity of the background ions. The residual gases are generally abundant in the ECR ion sources because they are not usually operated at ultra-high vacuum since support gases such as helium and oxygen are required for ECRIS operation. Meanwhile, sputtered materials are introduced into the plasma from the chamber wall and the surrounding electrodes during plasma-wall interaction. The plasma-wall interaction is a phenomenon whereby energetic plasma particles that are unstable magnetically or not well-confined escape and interact with the surrounding materials releasing secondary particles, primarily neutrals, in the process. The released particles enter the plasma, get ionized, extracted, and obscure the mass-to-charge ratio (A/Q) of the desired exotic isotopes.

However, in 2012, the chamber wall, the injection and extraction electrodes, and other plasma-surrounding materials were either coated or replaced with pure aluminum materials. This modification reduced the intensity of some sputtered ions by about 2 orders of magnitude, and the intensities of the residual ions were enhanced [46], as shown in Figure 4.19. Furthermore, in 2014, the rf amplifier of the CSB, which was initially a fixed-frequency klystron amplifier [47], was replaced with a travelling wave tube amplifier (TWTA) that allows for frequency tuning for better optimization of the CSB. As reported in [48], the installation of the TWTA enabled frequency tuning between 13.75 and 14.5 GHz and helped in operating the CSB in stable conditions during beam delivery.

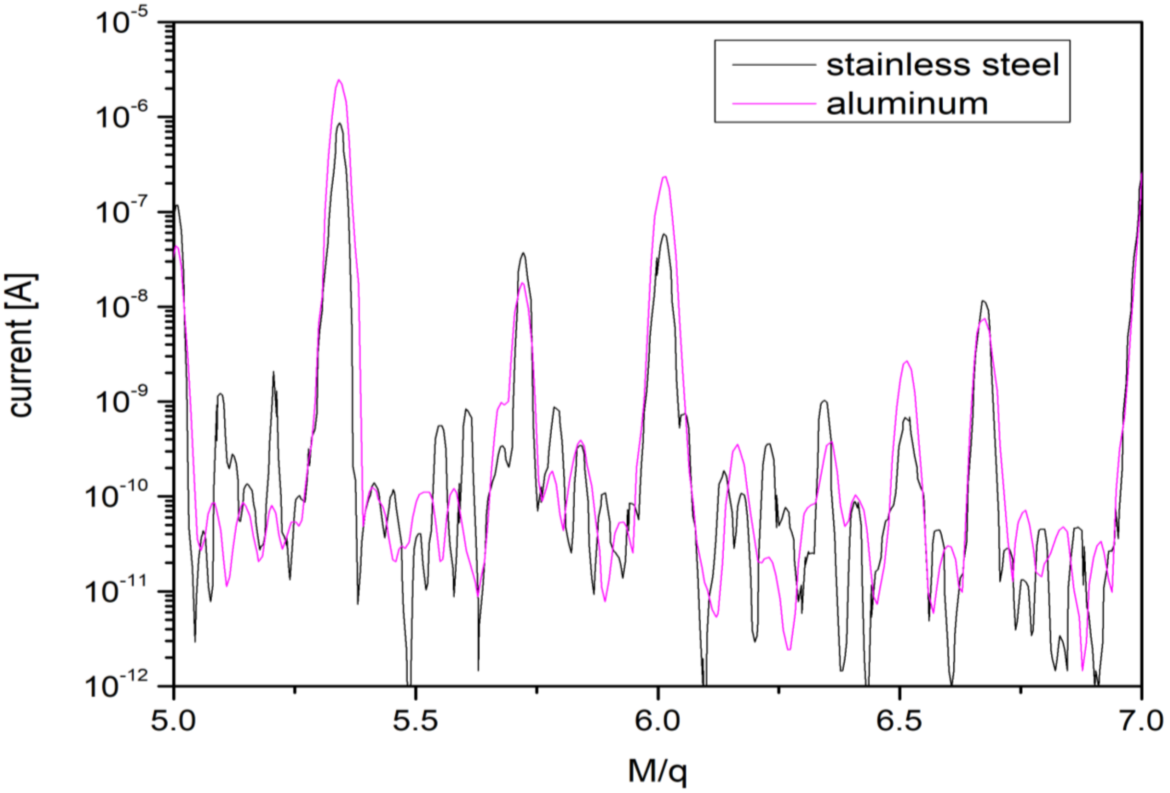

Figure 4.19: Comparison between the mass spectrum of the CSB between A/Q of 5.0 and 7.0 for bare stainless steel vacuum chamber and aluminum-coated vacuum chamber [46].

Chapter 5 - Operation of the TRIUMF Charge State Booster with the Single Frequency Heating

5.1 Introduction

This chapter will present and discuss the results of the TRIUMF CSB operation with single-frequency heating. The outputs of the CSB that are investigated are the beam current, emittance, plasma potential and charge breeding efficiency. Concerning the efficiency, one distinguishes between the charge breeding efficiency in a single charge state and the global efficiency by summing the extracted charge-bred ions over all the charge states in the spectrum. Although the TRIUMF ECRIS CSB is used for the charge breeding of radioactive ion beams, there is a cesium surface ion source, otherwise known as the cesium test ion source (CTIS) (described in section 4.3) installed upstream of the CSB for routine tuning and optimization of the injection and extraction system as well as the CSB using singly charged ions. The CTIS and the CSB are biased to the same electrical potential so that injected singly charged ions are decelerated and stopped in the CSB. The difference between the CSB bias voltage and the CTIS bias voltage is called the delta-V. This parameter is varied to adjust for the plasma potential, which can be determined via this parameter. For the emittance measurement using the quadrupole scan technique (QST), the quadrupole Q5 and RPM 5 (Figure 4.9) are used to measure the emittance of the injected beam, Q14 and RPM 14 (Figure 4.15) are used to measure the emittance of the total extracted beam from the CSB, and Q16 and RPM16 are used to measure the emittance of the separated beam. The total beam current of the singly charged cesium ions being injected into the CSB is monitored using the Faraday cup FC5, and the total beam current extracted from the CSB is monitored using FC14, while the current of the separated beam is monitored using FC16A. For the emittance measurement of the separated beam, the magnetic dipole is set to the A/q of the beam of interest. The CTIS and CSB were biased to the electrical potential of 10 kV, and a singly charged cesium ion beam of about $10\,nA$ with the RMS emittance of $\varepsilon = (7.6 \pm 0.3)\,mm - mrad$ was injected into the CSB. The magnetic dipole was set to $A/q = 5.54$ corresponding to $133\mathrm{Cs}^{24+}$.

5.2 Emittance of the Total Extractable Current versus Extraction Field

The RMS emittance of the total current extracted from the CSB as a function of the extraction field was measured via the QST and Twiss parameter transformation (TPT) by scanning the strength of quadrupole Q14 and recording the beam size on the profile monitor RPM14. The voltage on the puller electrode defines the electric field of the CSB in the extraction region, and by changing the voltage of the puller electrode, the extraction field is modified. The extraction field is defined as the difference between the CSB high voltage bias and the voltage on the puller electrode divided by the distance of the extraction gap. As previously stated, the CSB is biased to $10\ kV$ electrical potential, which defines the beam energy, and the extraction gap of the CSB is $25\ mm$. The voltage on the puller electrode varied between $6.5\ kV$ and $8.0\ kV$. Thus, the extraction field varies between $80\ kV/m$ and $140\ kV/m$. The beam emittance, as a function of the extraction field published in [49], is shown in Figure 5.1.

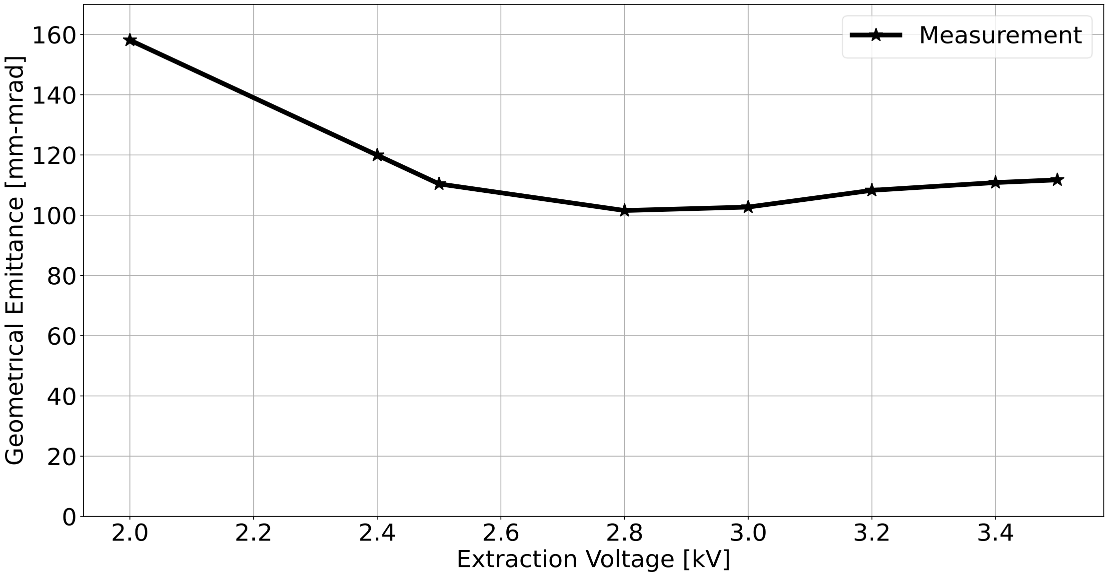

Figure 5.1: 4RMS total emittance of the CSB at a bias voltage of 10 kV versus puller electrode voltage between 2 and 3.5 kV. The total emittance was determined using the quadrupole scan technique discussed in section 3.9. The total current extracted from the CSB on the Faraday cup FC14 after the triplet is 30 μA.

As can be seen, the maximum emittance of the CSB, which is $158.1\ mm - mrad$, was measured at an extraction field of $80\ kV/m$. However, as the extraction field is increased, the emittance of the total extractable current decreases until it reaches $101.6\ mm - mrad$ at $112\ kV/m$. Further increase in the extraction field to $140\ kV/m$ leads to an increase in the emittance of the CSB to about $111.7\,mm - mrad$. The behaviour and the shape of the emittance indicate that the plasma boundary, the thin plasma sheath layer between the bulk plasma and the plasma electrode, was greatly affected by the variation of the extraction field, leading to the boundary changing shape from convex meniscus (high current density) at the lowest extraction field to the planar meniscus (optimum current density) at the lowest emittance and concave meniscus (low current density) at highest extraction field. The optimum extraction of ions from the ECR ion source plasma depends on the balance between the plasma density and the space charge density. So to further understand Figure 5.1 and the influence of the extraction field on the plasma boundary where the ions are extracted, the extraction system was simulated in IGUN code. Only the plasma electrode and about one-third of the puller electrode are simulated for clarity. As stated, the plasma boundary can assume either convex, planar or concave meniscus depending on the plasma density and extraction field in the ion beam formation region. In the simulation, the beam energy and the current density were fixed at $10\ kV$ and $155\ \mu A/cm^2$ respectively while the extraction field (puller electrode voltage) was varied. The puller electrode voltages that create the three meniscuses are $8\ kV, 7\ kV$ and $1\ kV$. The results of the simulation are presented in Figures 5.2 – 5.4. Since IGUN allows the simulation of more than one ion specie, the plasma was defined to consist of H^{+}, $4\mathrm{He}^{+}, 4\mathrm{He}^{2+}, 12\mathrm{C}^{5+}, 14\mathrm{N}^{5+}, 16\mathrm{O}^{6+}$ and $133\mathrm{Cs}^{24+}$. This definition approximates the plasma of an ECRIS, most especially the TRIUMF CSB being considered.

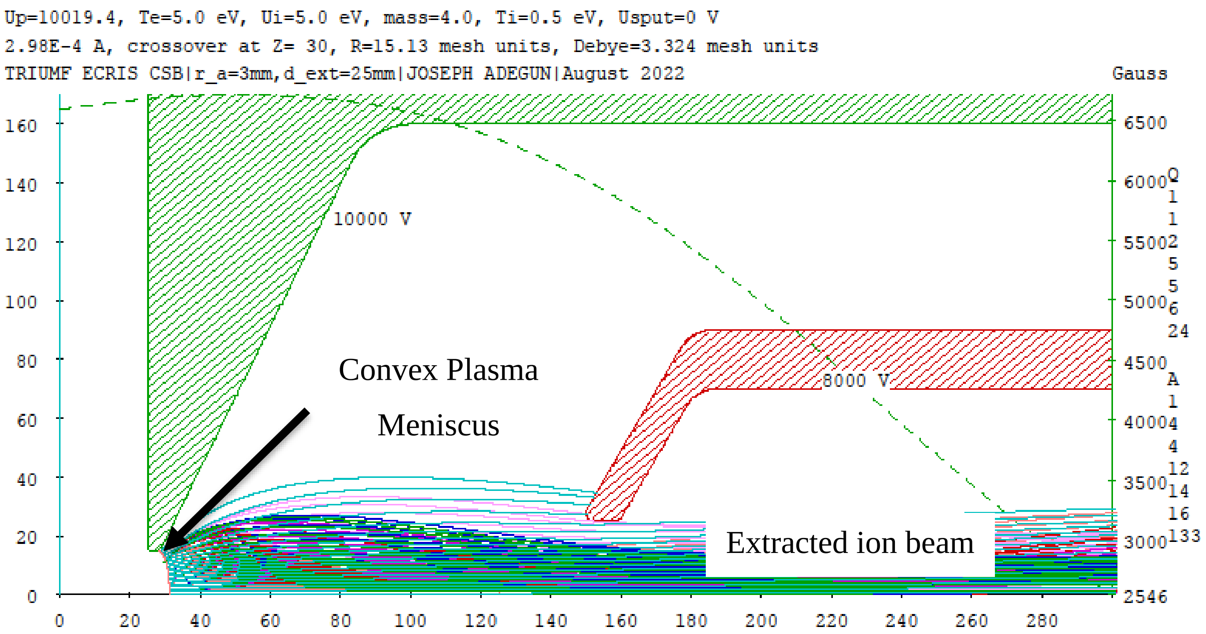

Figure 5.2: Simulation of convex plasma meniscus in IGUN at the puller electrode voltage of 8 kV. The plasma electrode is biased to 10 kV. The extracted ion beam consists of an intense current of some selected residual ions and Cs^{24+}. The atomic mass and the charge states of the ions are shown on the right-hand side of the figure, while the plasma parameters and the extracted beam current are printed at the top of the figure.

The convex meniscus forms a beam with a high divergence angle leading to the extracted ions being lost to the puller electrode, as shown in Figure 5.2. In this case, the plasma density in the extraction region is higher than the space charge current density and this results in the plasma extending beyond the plasma electrode aperture into the extraction gap leading to a significant emittance of the extracted beam, as shown in Figure 5.1, at the extraction field of $80\ kV/m$. On the other hand, the planar meniscus forms a parallel beam with a minimal divergence angle, as shown in Figure 5.3. In this case, the plasma density is equal to the space charge density, and the applied extraction field matched the plasma density in the extraction region resulting in the lowest beam emittance as shown in Figure 5.1 at the extraction field of $112\ kv/m$ which corresponds to an optimized extraction system. Finally, in the case of the concave meniscus, as shown in Figure 5.4, the plasma density in the extraction region is less than the space charge density.

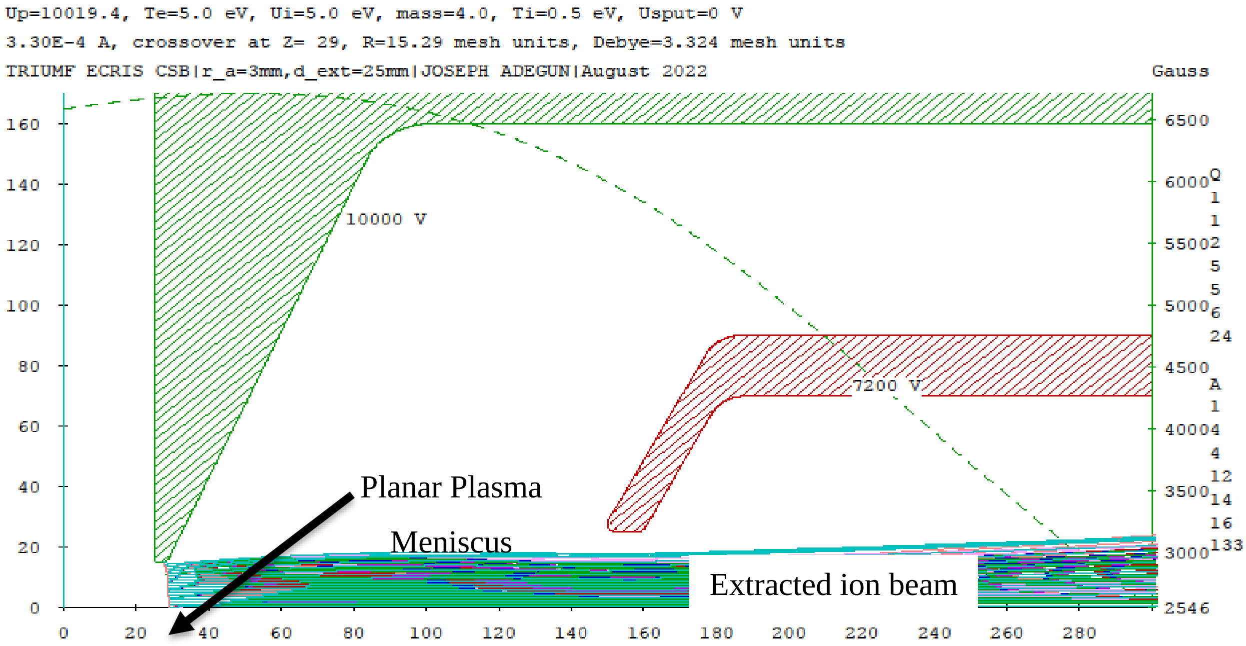

```
Up=10019.4, Te=5.0 eV, Ui=5.0 eV, mass=4.0, Ti=0.5 eV, Usput=0 V
3.30E-4 A, crossover at Z= 29, R=15.29 mesh units, Debye=3.324 mesh units
TRIUMF ECRIS CSB|r_a=3mm,d_ext=25mm|JOSEPH ADEGUN|August 2022
```

Figure 5.3: Simulation of planar plasma meniscus in IGUN at the puller electrode voltage of 7.2 kV. The plasma electrode is biased to 10 kV. The extracted ion beam consists of an intense current of some selected residual ions and Cs^{24+}. The atomic mass and the charge states of the ions are shown on the right-hand side of the figure, while the plasma parameters and the extracted beam current are printed at the top of the figure.

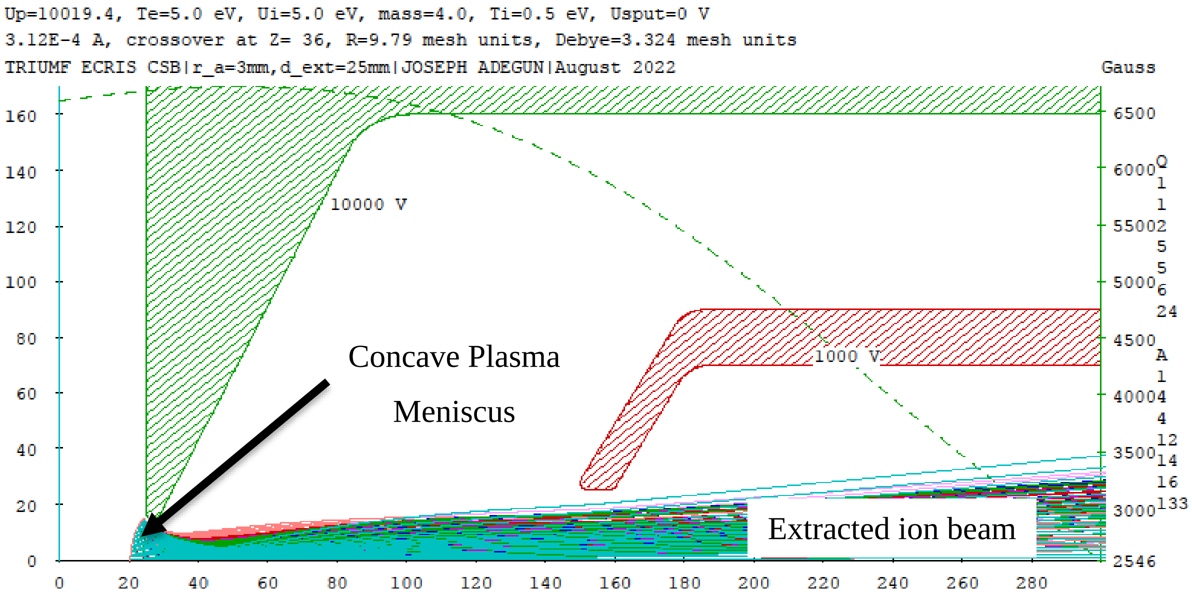

```
Up=10019.4, Te=5.0 eV, Ui=5.0 eV, mass=4.0, Ti=0.5 eV, Usput=0 V
3.12E-4 A, crossover at Z= 36, R=9.79 mesh units, Debye=3.324 mesh units
TRIUMF ECRIS CSB|r_a=3mm,d_ext=25mm|JOSEPH ADEGUN|August 2022
```

Figure 5.4: Simulation of the concave plasma meniscus in IGUN at the puller electrode voltage of 1 kV. The plasma electrode is biased to 10 kV. The extracted ion beam consists of an intense current of some selected residual ions and Cs^{24+}. The atomic mass and the charge states of the ions are shown on the right-hand side of the figure, while the plasma parameters and the extracted beam current are printed at the top of the figure.

The applied extraction field extends into the plasma for beam extraction leading to overfocussed extracted ions, thus, the ions leave the plasma boundary with high divergence and beam emittance. However, from Figure 5.1, it can be concluded that the plasma boundary of the TRIUMF ECRIS CSB is convex between the extraction field of 80 kV/m and 112 kV/m, planar at the field of 112 kV/m and concave between the extraction field of 112 kV/m and 140 kV/m. The effect of the extraction field on the total extractable current was also investigated by varying the puller electrode voltage between 1.0 kV and 4.5 kV, corresponding to the extraction field of 40 kV/m and 180 kV/m.

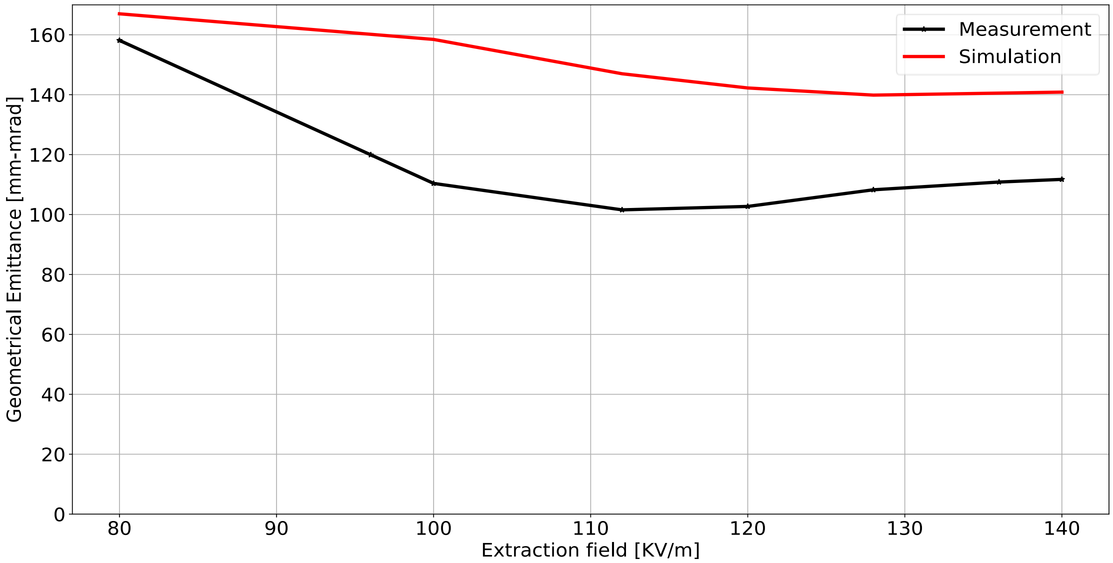

Figure 5.5: Comparison between the emittance of the total current extracted from the CSB modelled in IGUN and actual emittance of the total current extracted from the CSB using QST while the CSB is biased to 10 kV. The total current from the CSB varies with the extraction field.

Figure 5.5 compares the emittance of the CSB determined using the QST with the emittance simulated with IGUN. The disagreement between the measurement and IGUN simulation is because the total extracted current from the CSB was collimated by the quadrupole in front of the CSB extraction system, removing a fraction of the low-mass ions that significantly contribute to the large emittance of the CSB included in the IGUN simulation. However, the trend of the plots indicates that as the extraction field is varied, the total emittance of the CSB is changed as a result of the interplay between the plasma density and space charge density.

In addition to the emittance of the extracted beam from the CSB, the total extractable current is also influenced by the shape of the plasma boundary where ions are formed and extracted. For example, the intensities of the ions lost to the electrodes of the triplet quadrupole Q12, Q13 and Q14 in the front of the CSB were measured simultaneously with the beam's intensity that made it to the Faraday cup FC14. Figure 5.6 shows the plot of the ion current against the extraction field. The black plot is the current of the ions lost to the aperture of quadrupole Q12, the magenta plot is the current of the ions lost to the aperture of Q13, and the red plot is the current of the ions lost to the aperture Q14. The blue plot is the current of the ions not lost to the apertures of the quadrupoles, recorded on Faraday Cup FC14.

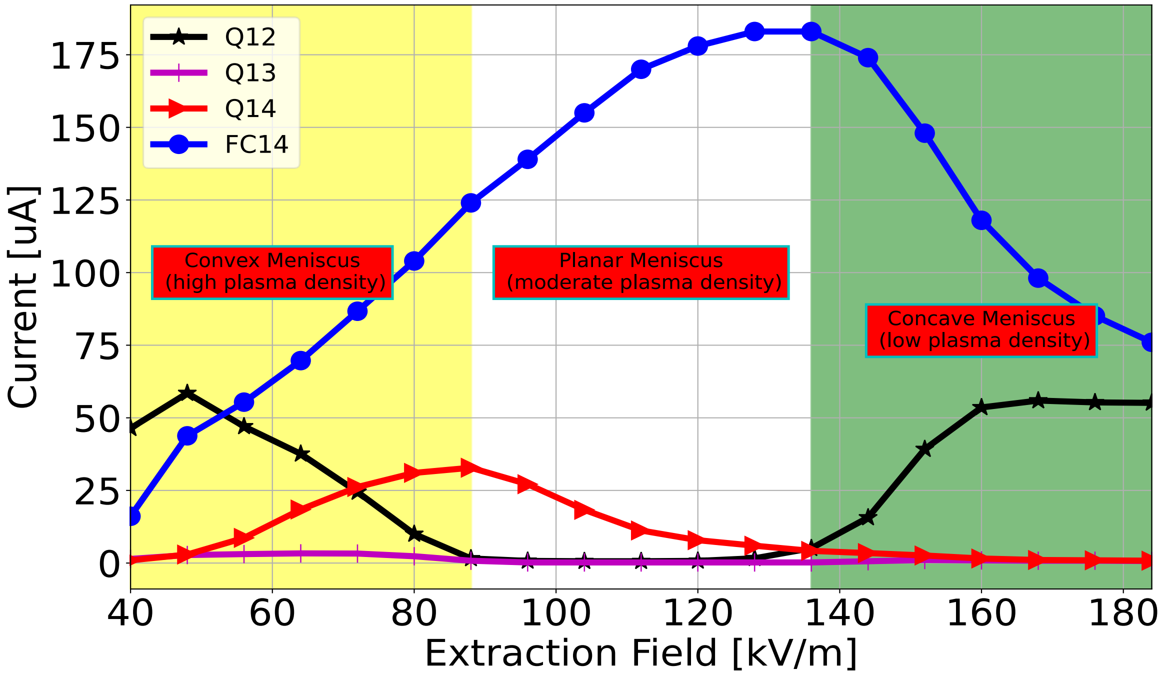

Figure 5.6: Extracted current losses on the quadrupole triplet after the extraction system of the CSB and the transmitted current of the ions measured using Faraday cup FC14 in front of the triplet vs. the field of the CSB extraction system.

As seen in Figure 5.6, at the extraction field between 40 kV/m and 88 kV/m, in addition to the ions lost to the extraction electrodes, the majority of the ions that made it to the end of the extraction system are lost to the aperture of the quadrupole Q12, and only a few ions made it to the Faraday cup FC14 downstream of the quadrupoles. The ion loss to the electrodes is due to the convex nature of the plasma boundary, which occurs between the extraction fields of 40 and 88 kV/m. The ions extracted in this regime are formed with large divergent angles because of the low extraction fields. As the extraction field is increased, the number of ions lost to the electrode of Q12 decreases while the current measured on Faraday cup FC14 increases according to Child-Langmuir's law, and by summing up all the currents around the peak of the FC14 plot, it equals to approximately $185\ \mu A$ which is close to the theoretical value calculated in Section 2.5.

The loss current on Q12 dropped to zero between the extraction field of $88\ kV/m$ and $136\ kV/m$, indicating that the plasma meniscus is close to the planar shape and the extracted ion trajectories are parallel. Furthermore, as shown in Figure 5.1, the lowest beam emittance was recorded within these extraction fields. The maximum extractable current from the CSB with the least divergence was achieved at the extraction fields of $128\ kV/m$. Further increase of the extraction field leads to a decrease in the current of ions that made it to FC14, and an increase of ions lost to the aperture of Q12 can be measured. The growth in the current of ions lost to the quadrupole occurs at the extraction field between $136\ kV/m$ and above. At these extraction fields, the plasma meniscus is concave with an overfocussed beam, leading again to significant divergence accompanied by large emittance.

5.3 Plasma Potential Measurement: Variation of Delta-V

With the lowest beam emittance of the CSB achieved at the extraction field of $112\ kV/m$ that corresponds to the extraction voltage $(\mathrm{CSB}_{\text{bias voltage}} - \text{Puller electrode}_{\text{bias voltage}})$ of $2.8\ kV$ at the $\mathrm{CSB}_{\text{bias voltage}} = 10\ kV$, the puller electrode voltage of the extraction system of the CSB was set to this value, and the plasma potential of the CSB was determined by varying delta-V. Figure 5.7 shows the normalized intensities of different Cs-charge states plotted against the delta-V values. As previously presented, a singly charged Cs+ ion beam of about $10\ nA$ was injected into the CSB and the intensities of Cs^{+}, Cs^{16+} and Cs^{24+} were monitored one after the other on Faraday cup FC16A (Figure 4.15). The delta-V was varied between 0 and $30\ V$.

As the delta-V increases, the intensities of Cs^{16+} and Cs^{24+} increase until the maximum value reaches around delta-V = $17\ V$. On the other hand, the intensity of Cs^{+} measured increased linearly between $15\ V$ and $25\ V$, while a further increase in delta-V led to a decrease in the intensities of Cs^{16+} and $Cs^{24+,}$ but the intensity of Cs^{+} remained constant. It can be concluded that with the delta-V between $0\ V$ and $15\ V$, most of the injected Cs^{+} ions are repelled by the positive potential of the plasma because the kinetic energy of the ions is less than the positive potential barrier generated by the plasma, and only a few of the injected ions are captured. At delta-V = 17 V, the injected ions are efficiently captured by the plasma via deceleration and thermalization due to collisions with the plasma ions. The optimum setting of delta-V indicates that the plasma potential is of the order of 17 V. However, between 25 V and 30 V, most of the injected ions were not effectively captured by the plasma, and they only passed through the plasma because their kinetic energy was higher than the plasma's positive potential.

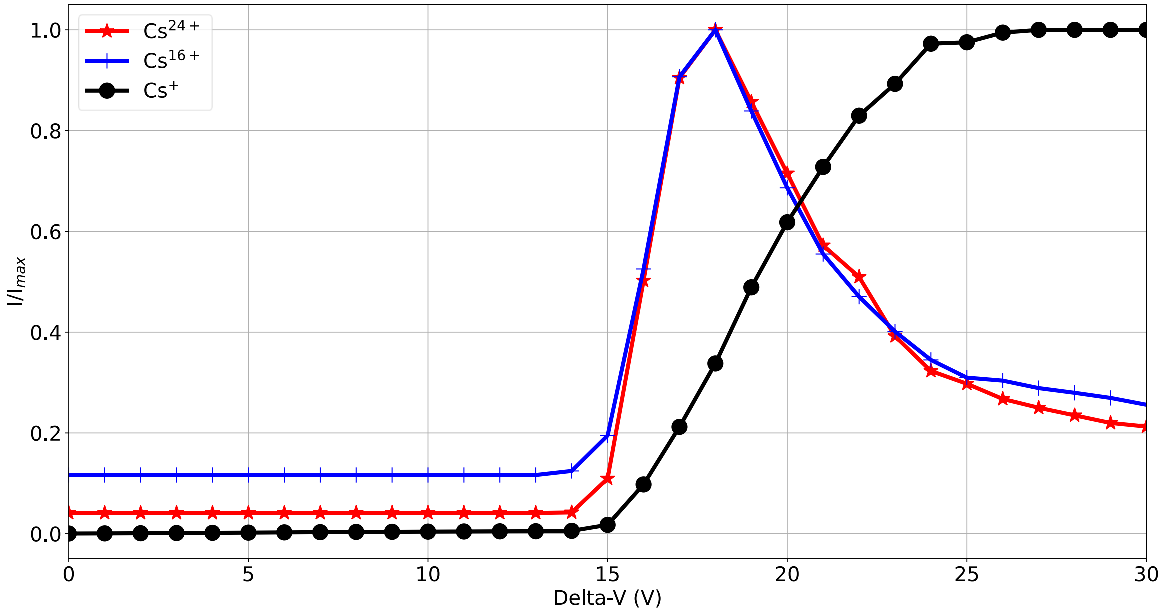

Figure 5.7: Normalized intensities of Cs^{+}, Cs^{16+} and Cs^{24+} versus delta-V. Variation of deltaV is an indirect method of plasma potential measurement.

5.4 Efficiency of the TRIUMF ECRIS CSB with cesium Beam Under Single Frequency Heating Regime

After the puller electrode voltage with the lowest extraction beam emittance has been identified at 7.2 kV, and the delta-V value at which ECR plasma efficiently captures the injected ions from CTIS has also been determined at 17 V, singly charged cesium ions of about 10 nA in intensity were injected into the CSB, and the efficiency of the charge breeding process using cesium was determined. Based on the experience of operating the TRIUMF ECRIS CSB, highly charged ions (HCIs) efficiency depends on how well the ECR plasma is conditioned. Electron energy and neutral density are the principal plasma parameters that influence the HCIs efficiency. As previously stated, the electron energy must be high enough to produce a higher charge state of interest, and the neutral density must be sufficient to produce the highly charged ions but low enough to prevent charge recombination. The ECRIS plasma and the extraction beamline optics of the CSB (from Q12 up to the Faraday cup FC16A (Figure 4.15)) were therefore optimized for the production and transport of the Cs^{24+} beam. This was done using the tune calculated and predicted by TRANSOPTR (see Figure 4.16 for a typical beam envelope). The ECR plasma was conditioned by carefully fine-tuning the TWTA output power, the center solenoid coil current and the flow of helium support gas while keeping the rf frequency constant at $14.5\ GHz$, the solenoid injection coil current fixed at $1050\ A$ and the extraction coil current fixed at $762\ A$. After systematic tuning, the combination of TWTA (model number VZU-6997AD) output power of $350\ W$, helium gas flow voltage of $6.0\ V$ (ion gauges at injection and extraction values are 6.18×10^{-8} Torr and 3.71×10^{-8} Torr respectively) and center solenoid coil current of $200\ A$ produced the maximum intensity of Cs^{24+} at Faraday cup FC16A while the total extractable current on the Faraday cup FC14 is $35\ \mu A$. Using Equations 5.1 and 5.2, the single charge state efficiency and the global efficiency of the CSB were calculated, respectively.

$$\mathrm{Efficiency}_Q = \frac{\mathrm{I_{Q+}}}{\mathrm{Q*I_+}} \times 100 \tag{5.1}$$

$$\text{Global Efficiency} = \sum\nolimits_{\mathrm{Q}=1} \mathrm{Efficiency_Q} \tag{5.2}$$

Where $\mathrm{I_{Q+}}[\mathrm{A}] = FC16A_{with\ Cesium} - FC16A_{without\ Cesium}$

$\mathrm{Q} = \text{charge state}$

$\mathrm{I_+}[\mathrm{A}] = \text{Current of the injected beam of singly charged Cs ions}$

According to Equation 5.2, global efficiency is the summation of the efficiency over all possible charge states that can be detected. The background ions in the A/q corresponding to the A/q of all the Cs charge states recorded on the Faraday cup FC16A were filtered out by subtracting the current value of the FC16A without cesium from the value with cesium injected into the CSB. Furthermore, as presented in Section 4.5 in the schematic of the CSB extraction beamline (Figure 4.15), there are three slits between the charge state booster and the Faraday cup FC16A. The slits were opened entirely for the CSB efficiency measurement, and the A/q of the mass separator along the CSB extraction beamline was scanned between 1 and 150 to record the mass spectrum with and without cesium injected. Figure 5.8 shows only the mass spectrum between $A/q = 1$ and 10.

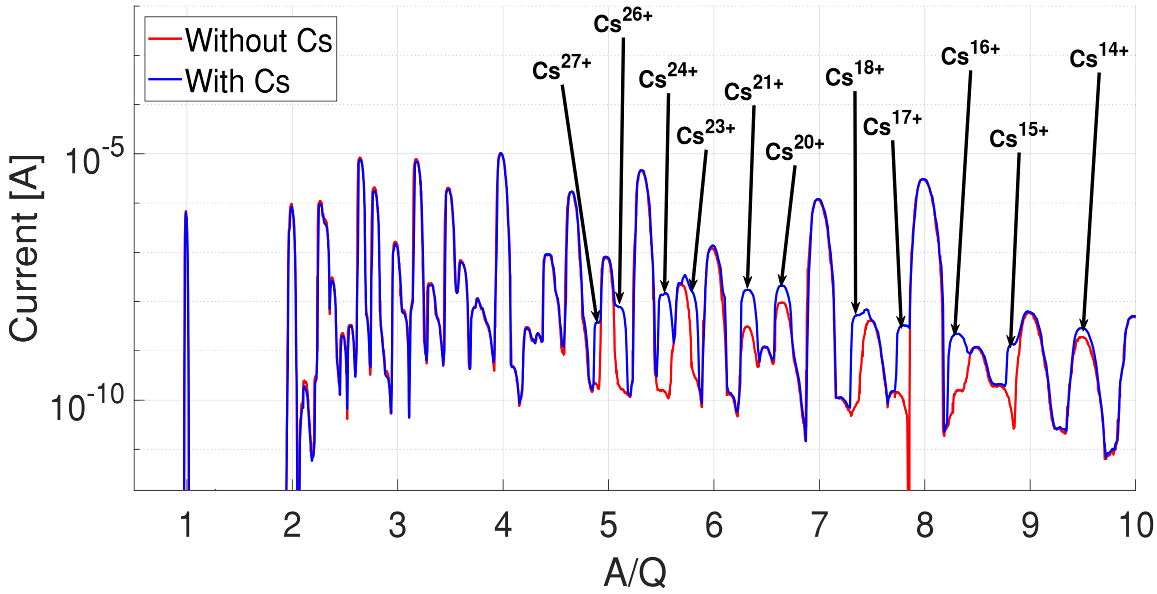

Figure 5.8: Mass spectrum of the CSB without magnetic dipole entrance and exit slits with and without cesium between A/Q of 1 and 10. The spectrum was taken by scanning the field of the magnetic dipole on the extraction beamline and recording the beam current on the Faraday cup FC16A.

In the plot, the black arrows show the cesium charge states that can be detected, while the rest of the peaks in the spectrum are from the residual gases such as carbon, nitrogen, oxygen, argon and so on. Although a mass scan was performed for A/Q up to 150, the mass spectrum is showing for A/Q between 1 and 10 because A/Q of interest for beam injection into the TRIUMF ISAC linear accelerator (LINAC) is less than or equal to 6. As it can be seen, cesium charge states between 14+ and 27+ can easily be identified, while some charge states in between, such as 19+, 22+ and 25+, are conspicuously dominated by higher residual ions intensity. Using Equation 5.1 and extracting the current of each charge state from the complete mass spectrum of Figure 5.8, the efficiency of all the charge states of the cesium was calculated and plotted against the respective charge state, as shown in Figure 5.9. The charge states such as 3+, 6+, 7+,10+, 11+, 19+, 22+ and 25+ with no information contain significant and very intense residual or background ions, and this will reduce the global efficiency of the cesium beam.

As seen in Figure 5.9, the maximum charge state of cesium that can be detected is 27+, with an efficiency of 1.4 %, while Cs^{23+} has a maximum efficiency of about 8.5 %. It is essential to know that because of the intense background ions that dominate the A/q region of charge 22+, there is a possibility that the efficiency distribution peaks on Cs^{22+} instead. Furthermore, using Equation 5.2, the minimum global efficiency of all the cesium charge states that can be measured is 53.6 %. The global efficiency would be higher than the determined value if it were possible to measure the current of Cs^{3+}, Cs^{6+}, Cs^{7+}, Cs^{10+}, Cs^{11+}, Cs^{19+}, Cs^{22+} and Cs^{25+}. From the efficiency of the cesium charge state distribution, as presented in Figure 5.9, it is evident that the plasma electrons have either not sufficient kinetic energy to produce the maximum charge state of 27+ or the Cs^{27+} ions are not well confined to reach the next charge states.

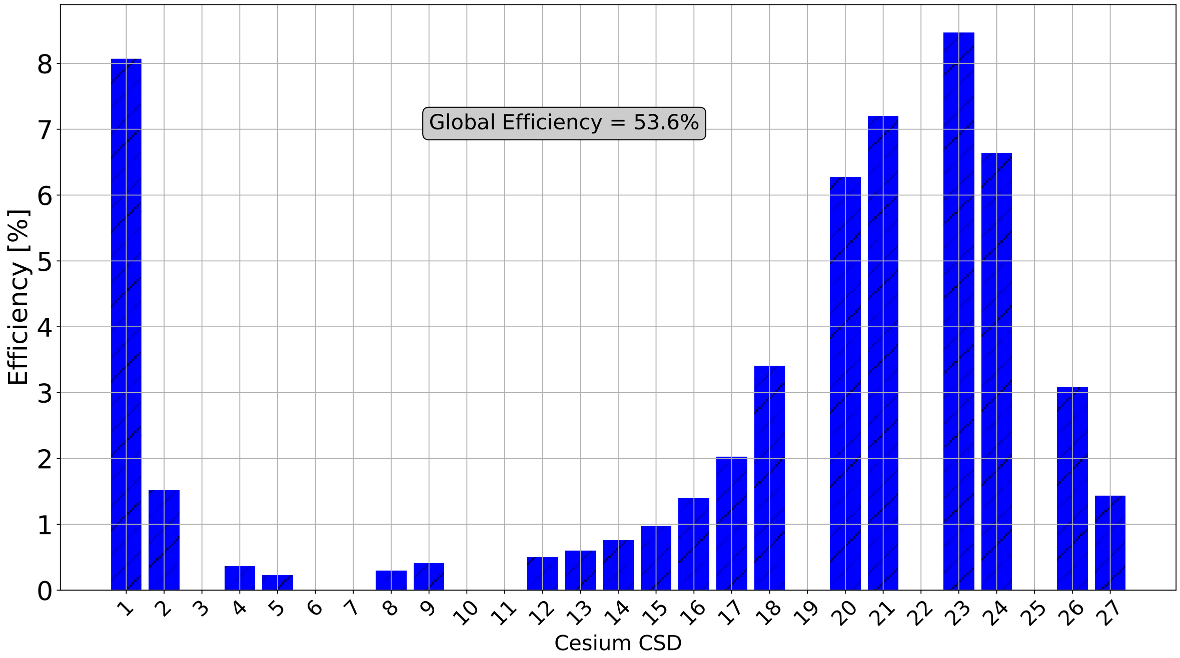

Figure 5.9: Efficiency of cesium charge states by operating the CSB with single frequency heating. The global efficiency is the summation of each efficiency of the cesium charge states.

It is also possible that the rate of recombination (with low energy electrons to produce lower charge states) for charge states greater than 27+ is higher than the rate of their production. Either way, by comparing the results of the TRIUMF PHOENIX ECR booster with the LPSC twin model, the global efficiency of the TRIUMF booster is generally lower than the efficiency of the LPSC booster. Recent efficiency measurements from the LPSC showed 14.1 % for Cs^{26+} and 91.8 % for global efficiency [50]. Although one needs to compare the results of the LPSC booster with the TRIUMF CSB under similar operation modes (both the single-frequency and two-frequency), however, these results are evidence that the TRIUMF booster is still being operated below its optimum potential, and further improvements can still be implemented to achieve improved and higher global efficiency.

5.5 Emittance of the Cesium Charge States and Some Selected Residual Ions

To quantify the beam quality of the highly charged ions extracted and selected from the charge state booster, the emittances of some cesium charge states and residual ions were measured after the magnetic dipole using the quadrupole scan technique (QST) by scanning the focusing strength of quadrupole Q16 with an aperture radius of $2.54\,cm$ and an effective length of $6.1\,cm$. The drift length between the quadrupole and rpm16, where the beam size was measured, is $12.1\,cm$. Since the optics used for the emittance measurement are located after the magnetic dipole in between the two-$45°$ electrostatic benders where the electrostatic benders have not compensated for the dispersion created by the dipole, the use of QST for emittance measurement at this location is quite tricky, and only the non-dispersive plane is suitable to gain information about the emittances. Furthermore, to transport a valuable beam to the entrance of the first section of the post-accelerator, the CSB extraction beamline was designed to overall focus highly charged ion beams at Faraday cup FC16A which makes the quadrupole scan technique for emittance measurement even more complicated. So, to perform the emittance measurement, the quadrupoles, the steerers and the electrostatic benders were tuned such that while scanning the strength of quadrupole Q16, a beam waist can always be achieved.

Furthermore, as previously discussed, impurities constitute a significant concern in the operation of ECRIS CSB; they are sometimes too intense that they obscure and mask the charge states of the charged-bred ions. So, to limit the intensity of these residual ions, the width of slit15 was systematically varied while keeping the width of slit14 constant at $15.0\,mm$, and the QST was performed to measure the emittance of Cs^{26+} as a function of the slit width. The Cs charge state of 26+ was selected because the corresponding A/Q contains less background intensity than the A/Q of Cs^{24+}. Figure 5.10 shows the plot of geometrical emittance of Cs^{26+} against the width of slit15. As seen, the emittance is approximately constant when the slit is completely opened until the slit is set to $10.0\,mm$. However, as the width of the slit is reduced, the geometrical emittance of Cs^{26+} decreases linearly. However, to avoid measuring the acceptance of the slit, the width of the slit was set to $2.65\,mm$. On the other hand, when the width of slit 14 was varied, it did not significantly affect the geometrical emittance of Cs^{26+}, so the width of slit14 was set to $3\,mm$, the minimum slit width without cutting into the beam.

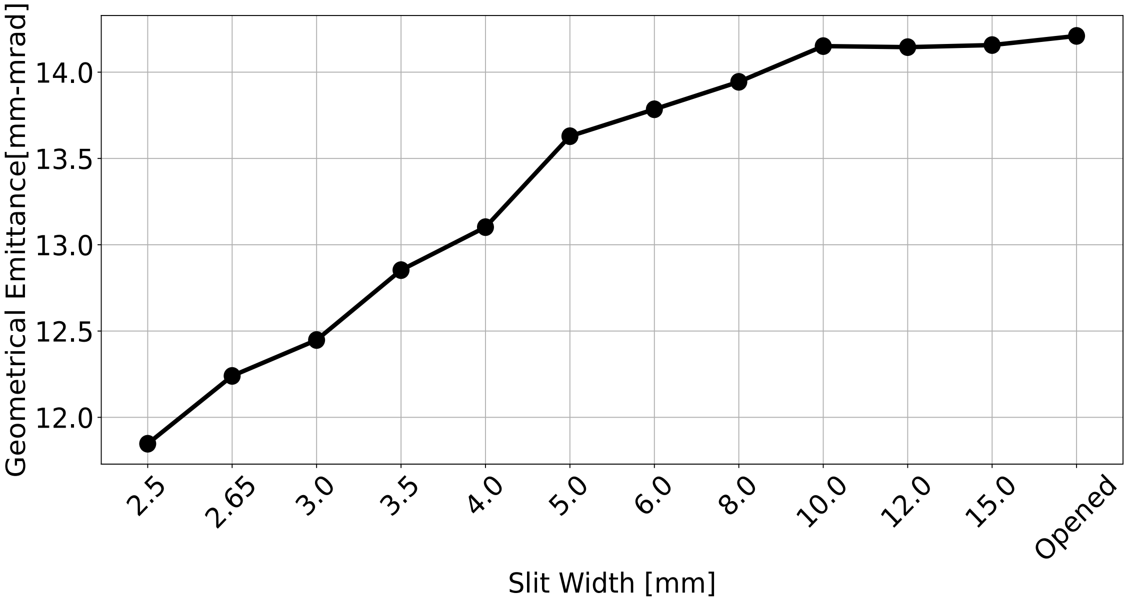

Figure 5.10: Geometrical 4RMS Emittance of Cs^{26+} vs Slit15 width. The width of the slit was varied between an opened position and 2.5 mm.

Also, because slit16A is located downstream of Q16 and RPM16, it was impossible to vary its width as a function of the separated emittance, so it was set to 3 mm to avoid cutting into the beam. With the slits14, 15 and 16A set to 3 mm, 2.65 mm and 3 mm, respectively, the mass spectrum of the CSB was measured between A/q = 4 and 8.5 as shown in Figure 5.11.

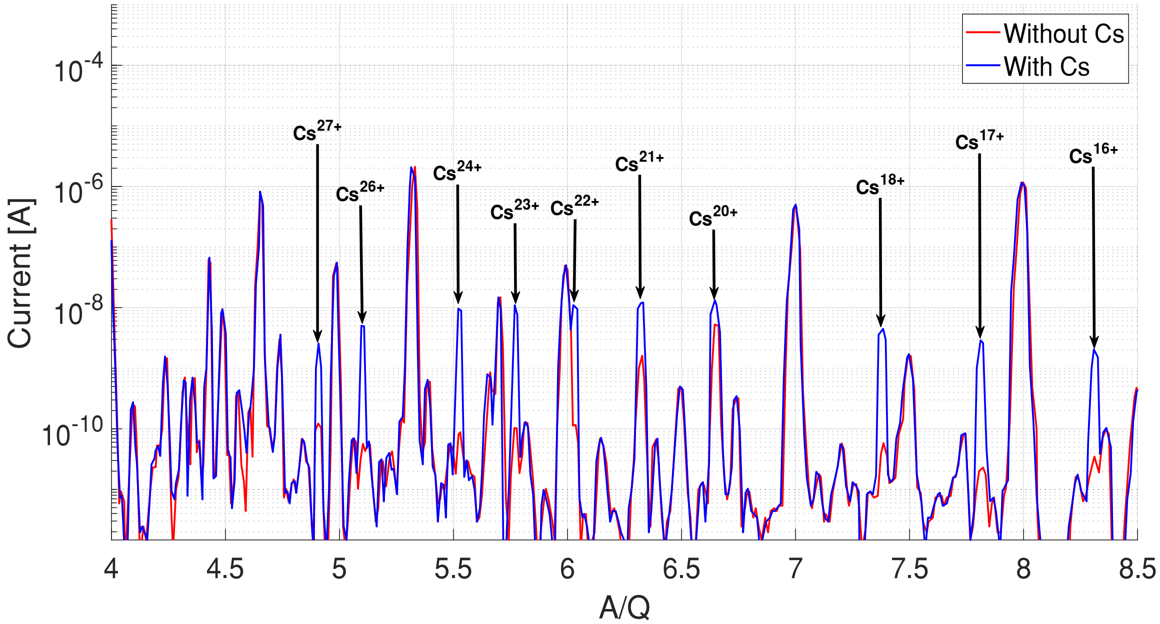

Figure 5.11: Mass spectrum of the CSB recorded by setting the entrance and exit slits of the magnetic dipole to 3 mm, 2.65 mm and 3 mm.

Similarly, the black arrow shows the charge states of cesium that are considered for the emittance measurements. Meanwhile, by comparing Figure 5.11 with Figure 5.8, it can be seen that by setting the slit widths to the above values, the peaks of each cesium charge state become narrower, and the peaks that were not previously shown are better separated due to the increased resolution of the A/Q separator.

The voltage of quadrupole Q16 was scanned between $400\ V$ and $1000\ V$ at a step of $50\ V$, and the emittances of higher charge states of cesium and some selected residual ions were measured. With the mass slits set to the above widths, the emittance of separated beams for A/Q between 1 and 16 was measured one after the other. The prominent ions between these A/Q ratios are residual ions from hydrogen, carbon, nitrogen, oxygen, argon and cesium charge states between 16+ and 33+. As shown in Figure 5.11, only Cs charge states of 16+, 17+, 18+, 20+, 21+, 22+, 23+, 24+, 26+, and 27+ are visible, as indicated by the arrows, while the high-intensity residual ions mask the missing charge states. Figure 5.12 shows the RMS geometrical emittance of the residual ions and the cesium charge states. As shown, the geometrical emittance depends on both mass and charge state.

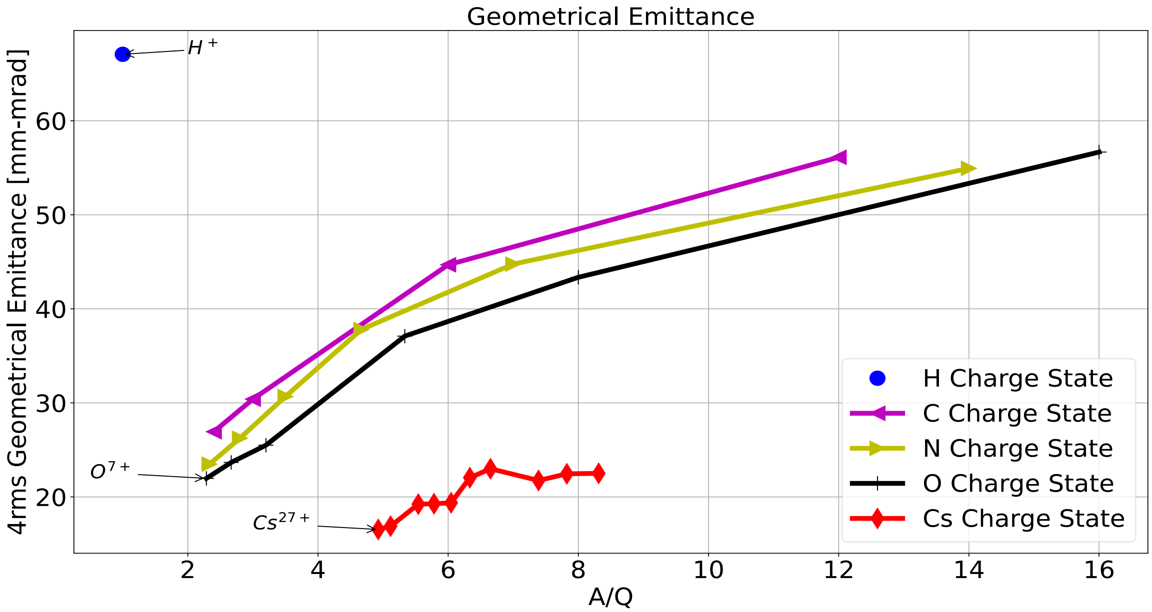

Figure 5.12: Geometrical 4RMS Emittance of cesium charge states and some selected intense residual ions from hydrogen, carbon, nitrogen and oxygen plotted against A/Q between 1 and 16.

The lightest mass of the measurements, hydrogen (H^{+}) has the highest geometrical emittance of $67.1\, mm - mrad$, while the heaviest mass, cesium, has the lowest. In addition, the geometrical emittance depends on the charge states, as shown. The higher charge state of each of the masses (smallest A/Q) has the lowest emittance, while the lowest charge state (higher A/Q) of each of the masses has the highest emittance. For example, $^{12}C^{+}$ has an emittance of $56.1\, mm - mrad$ while $^{12}C^{5+}$ has the lowest emittance of $26.9\, mm - mrad$ among the charge states of carbon. This trend is also observed among the charge states of nitrogen, oxygen and cesium.

The normalized emittance is plotted against A/Q for cesium charge states and residual ions charge states, as shown in Figure 5.13, to compare the beam emittances for different charge states and masses. As seen, the normalized emittance depends on the mass of the ions but is approximately constant for the charge states within a specified mass. Also, for the normalized emittance, Hydrogen ions with an atomic mass of $1\, u$ show the largest normalized emittance, while cesium ions with an atomic mass of $133\, u$ have the lowest normalized emittance. Meanwhile, the normalized emittance is approximately constant among the atom's charge state; this is expected as each charge state has been normalized to have the same energy.

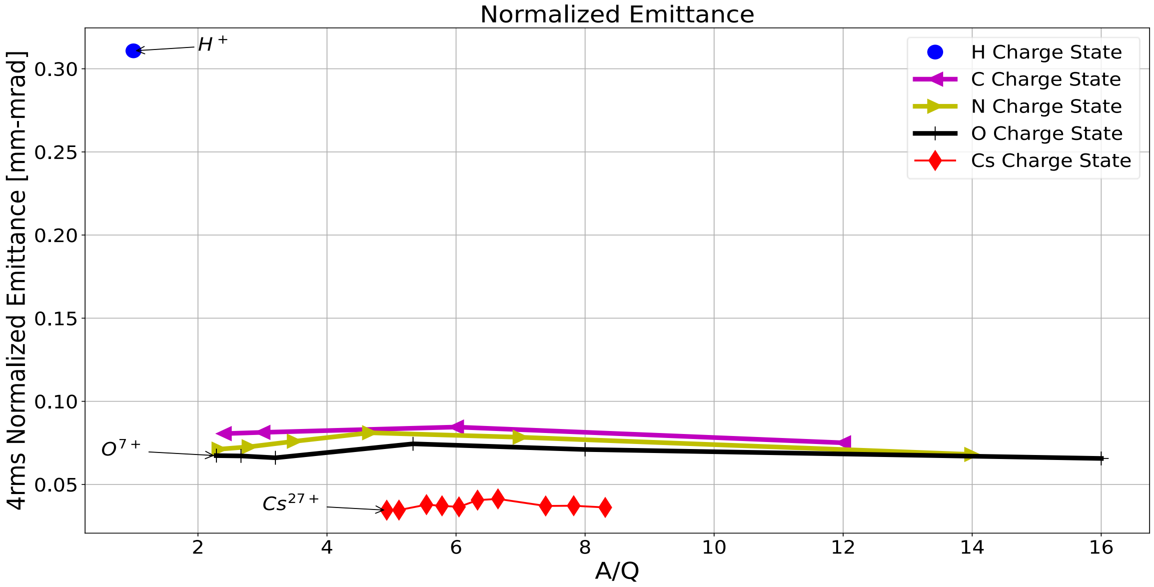

Figure 5.13: Normalized 4RMS Emittance of cesium charge states and some selected intense residual ions from hydrogen, carbon, nitrogen and oxygen plotted against A/Q between 1 and 16.

Furthermore, it can be concluded from Figure 5.13 that the lightest masses are extracted from a larger radius, while the heaviest masses are extracted from a smaller radius, and this is the only explanation for the different emittance values and corresponds to the physics of highly charged ions in an ECRIS. Figure 5.14 compares the magnetic emittance presented in Section 3.11 with the normalized measured emittance presented in Figure 5.13 at $B_0 = 0.7\,T$ (approximate magnetic field at the TRIUMF CSB plasma electrode) for extraction aperture radius ranging from $0.5 - 2.5\,mm$.

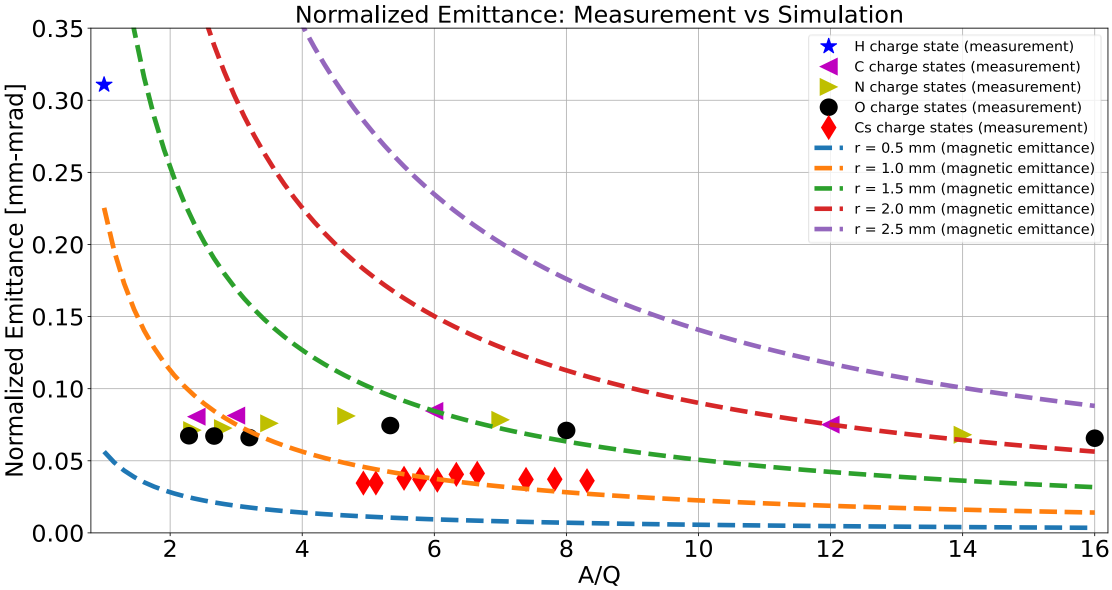

Figure 5.14: Normalized 4RMS Emittance of some selected intense residual ions from hydrogen, carbon, nitrogen and oxygen and cesium charge state between 16 and 27 compared with magnetic emittance for aperture radius between 0.5 mm and 2.5 mm at a magnetic field of 0.7 T for A/Q between 1 and 16.

From the comparison shown in Figure 5.14, it can be concluded that the residual ions (H to O charge states) were extracted at the aperture radius between $0.5\,mm$ and $2.5\,mm$ while the Cs charge states were extracted between $0.5\,mm$ and $1.5\,mm$. The measurements and the magnetic emittance model are consistent with the fact that there is a negative potential depression in the core of the ECR plasma where the hottest electrons are confined. The hot electrons attract and confine the highest charge state ions in the center, which migrate via ion-ion collisions, thus resulting in low beam radius and emittance after extraction. The low charge state ions and light masses are produced at the outer core of the electrostatic well and are less bound and therefore extracted with a larger beam radius and show higher emittance values. To further demonstrate the concentration of the higher charge state in the core of the ECR plasma, the phase spaces of the highest charge state of different masses measured from the CSB are plotted in Figure 5.15.

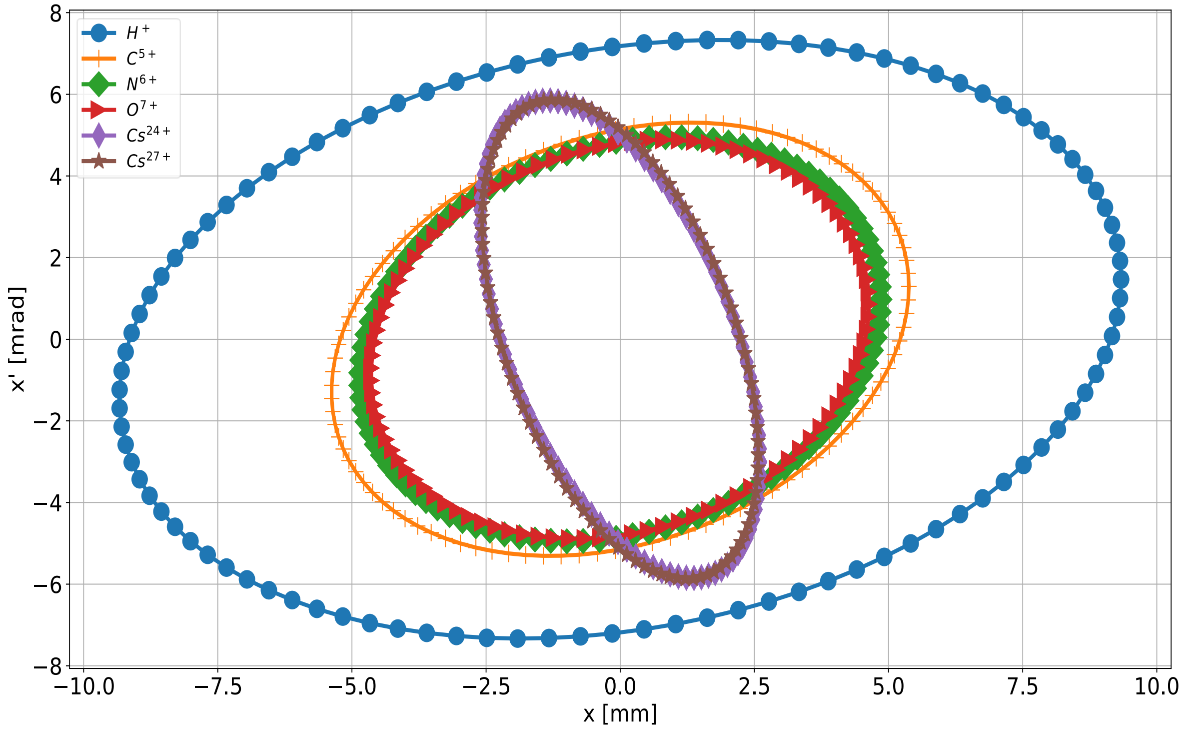

Figure 5.15: Phase space ellipses of some selected intense residual ions from hydrogen, carbon, nitrogen and oxygen and Cs47+ and Cs27+. The Twiss parameters for the plots were determined using the quadrupole scan technique.

As shown, the phase space ellipses for the highest charge states of Cs are compared with the phase space of the highest charge state of the residual ions. As can be seen, H^+, the lightest of the ions, has the largest phase space and Cs^{24+} and Cs^{27+} have the smallest phase space. Moreover, the phase space orientation and shape are different for different masses and charge states, as predicted by IGUN simulation and presented in Chapter 4 (Figure 4.15). It can also be seen that maximum beam size and angle are not only a function of the charge state but also the atomic mass of the constituent of the beam and different charge states have different focal lengths due to the influence of the strong magnetic solenoid field at the extraction system of the ECRIS charge state booster. However, the distribution of the phase space as shown can only be attributed to the ion-ion cooling effect [51] in which the lighter ions in the beam acquire more transverse energy due to the repulsive force they experience from the highly charged ions concentrated in the center while the lighter ions are extracted from the edge of the plasma. In other words, the highly charged ions experienced a deeper trapping potential due to their high charge state and repelled the low-charged lighter ions to the plasma edge.

5.6 Effect of Minimum Magnetic Field on the Total Emittance of the CSB

During the tuning of the CSB, it was observed that by changing the current of the center solenoid coil of the CSB at a fixed extraction field, the total current of the beam extracted from the CSB and recorded on the Faraday Cup FC14 is affected. To understand the behaviour, the emittance of the total current was systematically investigated as a function of the central solenoid coil current. The extraction system was optimized at the extraction voltage of 2.8 kV. The RMS emittance plotted against the solenoid coil current is shown in Figure 5.16, while the phase space corresponding to each emittance as a function of the coil current is shown in Figure 5.17.

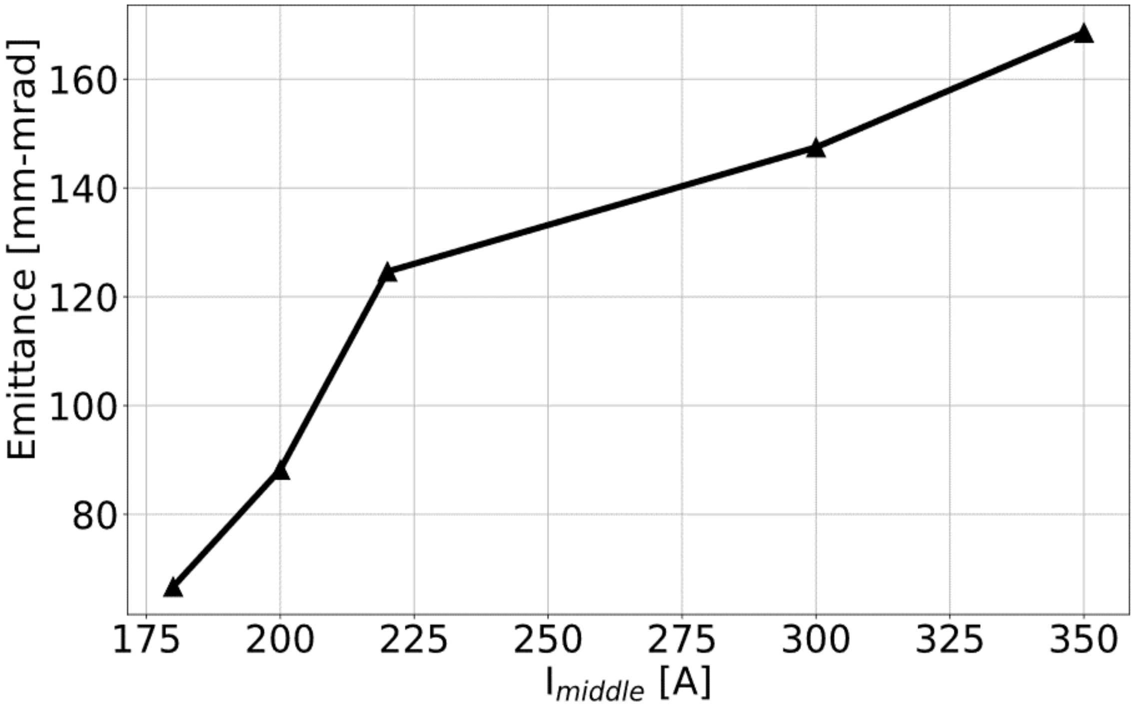

Figure 5.16: 4RMS Emittance of the total beam extracted from the CSB as a function of the coil current on the middle solenoid coil for the CSB magnetic field confinement. The coil current of the solenoid is varied between 180 A and 350 A.

As seen, the emittance of the extracted beam increases with the middle solenoid coil's current (magnetic field). The beam's phase space, as shown in Figure 5.17, gives further insight into the correlation. The only explanation for this behaviour is that the middle solenoid coil produces the minimum magnetic field of the CSB responsible for plasma confinement. So by changing the current of the center solenoid coil of the CSB, the magnitude of the minimum magnetic field of the source is changed, which directly changes the mirror ratio, $R_m = B_{max}/B_{min}$, and since the frequency of the coupled electromagnetic wave and the extraction field are kept constant, the resonance zone's size and shape are affected, leading to a reduced confinement of the core (hot) electrons and ions that are confined electrostatically by the potential dip. The release of the confined ions increases the ion density in the extraction region that no longer matches the set extraction electric field. So at $I_{mid} = 180\ A$, the phase space, as shown in Figure 5.17, indicates that the beam is parallel with a slightly small angle, but as the current of the middle solenoid increases, the beam changes from being parallel (waist) to divergent, which indicates that the extracted beam is either being overfocussed by the extracted electric field or under focus. It can then be concluded that the plasma meniscus at $I_{mid} = 180\ A$ is planar but either concave or convex as the I_{mid} is increased.

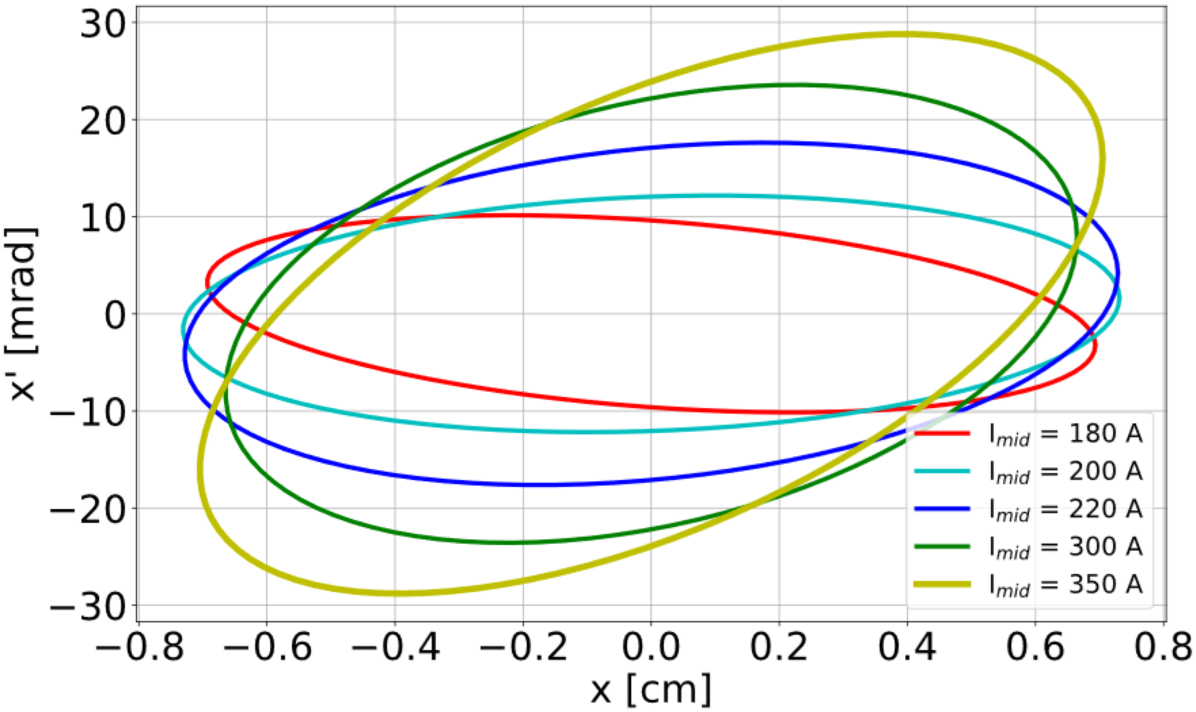

Figure 5.17: Phase space ellipses in $x - x'$ of the extracted beam as a function of the middle solenoid coil current.

Chapter 6 – Implementation of The Two-Frequency Heating Technique in the CSB

6.1 Introduction

Different techniques and methods have been explored and employed to improve the performance and the efficiency of the Electron Cyclotron Resonance Ion Source (ECRIS) since it was first used to produce highly charged ions in the 1970s [52]. Examples are plasma chamber wall coating, biased disks, gas mixing, the increase of the magnetic field strength, which allows for increasing the RF frequency, operation of the ECRIS in multiple frequencies heating mode and finally, frequency tuning of the applied electromagnetic waves. The operation of the ECRIS with these techniques mentioned has demonstrated increased performance of the ECRIS overall, and some are especially beneficial for the application as a charge state booster [53]–[58]. In addition, investigations of the $1+ \rightarrow Q+$ conversion processes by the community demonstrated that the efficiency of the process and quality of the highly charged ion beam produced by a charge state booster (CSB) could be significantly enhanced by also optimizing the plasma conditions and the beam formation in the extraction region [59]. Thus, the efficiency of the conversion of singly charged ions into highly charged ions in the ECR ion source depends on the following:

- Plasma conditioning – increased electron energy, moderate plasma potential, sufficient plasma density, and optimum ion confinement time.
- Beam transport – optimization of injection and extraction beam transport optics.
- Optimization of the injection and extraction systems.

Meanwhile, the last two bullet points are straightforward to accomplish. At TRIUMF, simulations using the codes IGUN© and TRANSOPTR followed by experimental campaigns have been employed to systematically optimize the ECRIS CSB injection system, extraction system, injection beamline and extraction beamline, respectively. These combined optimizations yielded an increase in the global efficiency of Cs CSD from $35\ \%$ to $44\ \%$ (a factor of about $26\ \%$ increase) for the Cs charge state between 12+ and 27+, and the charge state with the highest efficiency shifted from 21+ (5.6 %) to 23+ (8.8 %) [60] as shown in Figure 6.1 under the single frequency heating regime. The global efficiency reported represents the minimum global efficiency that can be determined, and it is expected to be higher if the efficiencies of Cs^{19+}, Cs^{22+} and Cs^{25+} are known.

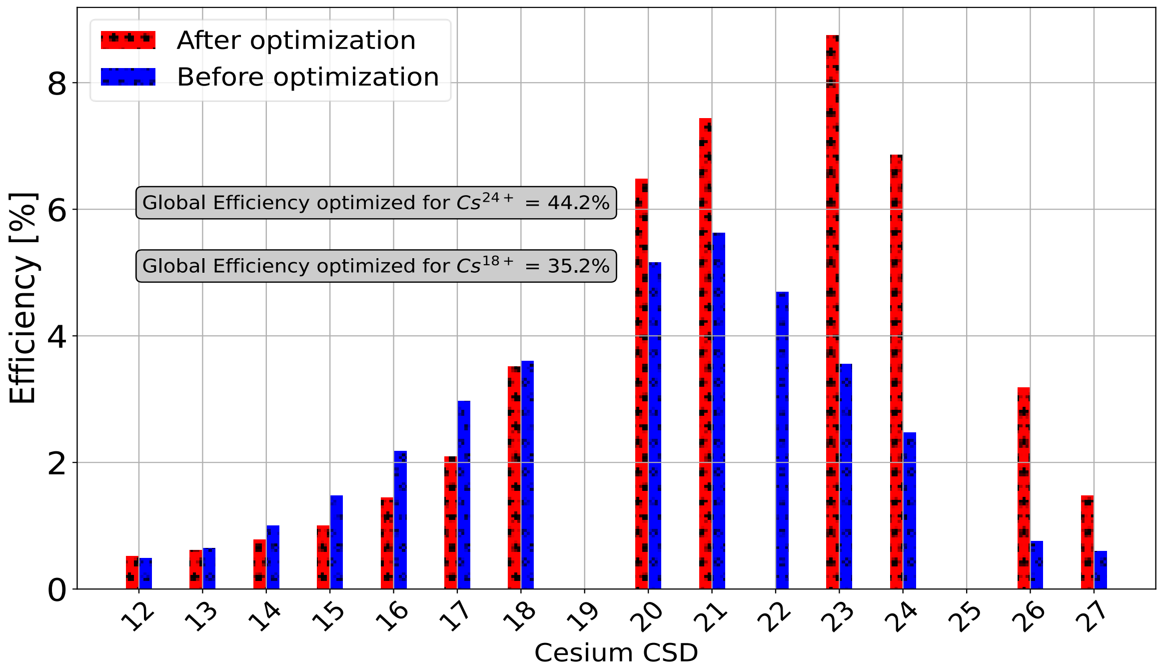

Figure 6.1: Efficiency of the CSB after optimization of the associated beamline optics, injection and extraction systems compared with efficiency without optimization of the optics, injection and extraction systems.

It is critical to know that no matter how well the injection and extraction systems of the CSB are optimized if the plasma is unstable (high plasma potential), the plasma density and the electron energy are insufficient to produce highly charged ions, or the ion confinement time is either too short or too long, the ECRIS will not be able to produce and deliver highly charged ions at the highest efficiency and the rate that is required. The two-frequency heating technique has been demonstrated in the ECRIS research community to stabilize the plasma, increase the intensity of charge states, decrease charge breeding time, and shift charge state distribution toward the higher charge state and, therefore, overall increases the global efficiency and improve the performance of the ECR ion source charge state booster [53], [55]. Therefore, this new method has been explored at the TRIUMF CSB as well.

6.2 The Two-Frequency Heating Technique of the Electron Cyclotron Resonance Ion Source (ECRIS) Plasma

The Two-Frequency Heating Technique (TFHT) of the ECRIS plasma involves operating the source at the two distinct electromagnetic wave frequencies to create two resonance surfaces where plasma electrons can be heated multiple times to produce highly charged ions. Traditionally, the electron cyclotron resonance ion source was designed to heat plasma electrons when the frequency of electromagnetic waves is equal to the electron cyclotron frequency as defined in Equation 6.1.

$$\omega_{rf} = \omega_{cyc} = \frac{eB_0}{m_e} \tag{6.1}$$

Where e is the electron charge, B_0 is the magnitude of the magnetic field in $Tesla$ that produces the electron cyclotron frequency that is equal to the electromagnetic waves' frequency, and m_e is the mass of the electron in kg. As discussed in Chapter 2, there is an efficient transfer of energy from the electromagnetic waves to the plasma electrons when the frequencies are equal. This usually occurs in a region inside the plasma chamber, generally known as the resonance zone or surface.

Considering the TRIUMF CSB, it was originally designed to be operated at the electromagnetic wave frequency of $14.5\ GHz$, and at this frequency, the magnetic field at the resonance zone of the source is $0.512\ T$. However, in this thesis, it will be demonstrated that it is possible to couple additional electromagnetic waves operating at another frequency other than $14.5\ GHz$ to the ECRIS CSB to create the expected additional resonance surface where the plasma electrons can be heated additionally to produce highly charged ions at higher intensities.

6.3 The Two-Frequency Heating Technique Implementation on the TRIUMF ECRIS CSB

Conventionally, the two-frequency heating technique (TFHT) is implemented in the ECR ion source using two separate signal generators, two separate amplifiers, and two separate waveguides, all operating at two different frequencies. The TRIUMF ECRIS CSB was not designed to accommodate two separate waveguides. Instead, the TFHT was implemented using the existing single waveguide of the ECRIS CSB. Before the implementation, the existing CSB RF waveguide was modelled and simulated in ANSYS HFSS [61] to study and investigate the properties of the electromagnetic waves at two different frequencies being injected into it. It was calculated that combined electromagnetic waves of different frequencies have a transmission of up to $70\ \%$ within the frequency region of interest for the CSB [62]. The simulation showed that the waveguide could be operated without significant reflected power.

6.3.1 First Approach: Two signal generators, One TWTA

The TFHT was initially set up using two separate BNC signal generators, a CPI travelling tube amplifier, and a low-power combiner (model ZX10-2-183-S+), as described in [63]. The waves from the signal generators were combined using the power combiner, and the output of the power combiner was fed to the CPI TWTA (frequency bandwidth between $8 - 18\ GHz$) for amplification through an SMA to N-type coaxial cable. The TWTA used in this setup is different from the SFHT setup. The amplified signal was injected into the plasma chamber via the existing waveguide. Figure 6.2 shows the schematic of the described setup. Furthermore, the software for controlling the signal generators and the amplifier was also changed to allow the automatic frequency tuning of the electromagnetic waves. After the complete upgrade of the CSB RF system, the first signal generator was set to $14.5\ GHz$, and the TWTA output power was set to $150\ W$. About $7\ nA$ of Cs^+ was injected into the CSB from the CTIS. The mass separator was set to select Cs^{29+} with $A/q = 4.59$. The frequency of the second signal generator was scanned between $13\ GHz$ and $15\ GHz$ while monitoring the intensity of Cs^{29+} ions on Faraday cup FC16A. At $13.65\ GHz$, the intensity of Cs^{29+} was at maximum value, the frequency of the second signal generator was set to that value, and a mass spectrum scan was conducted with and without cesium injected. However, during the operation of the CSB with the two-frequency heating, the travelling wave tube amplifier was damaged, and the reason for the damage could only be attributed to the high reflected power from the plasma.

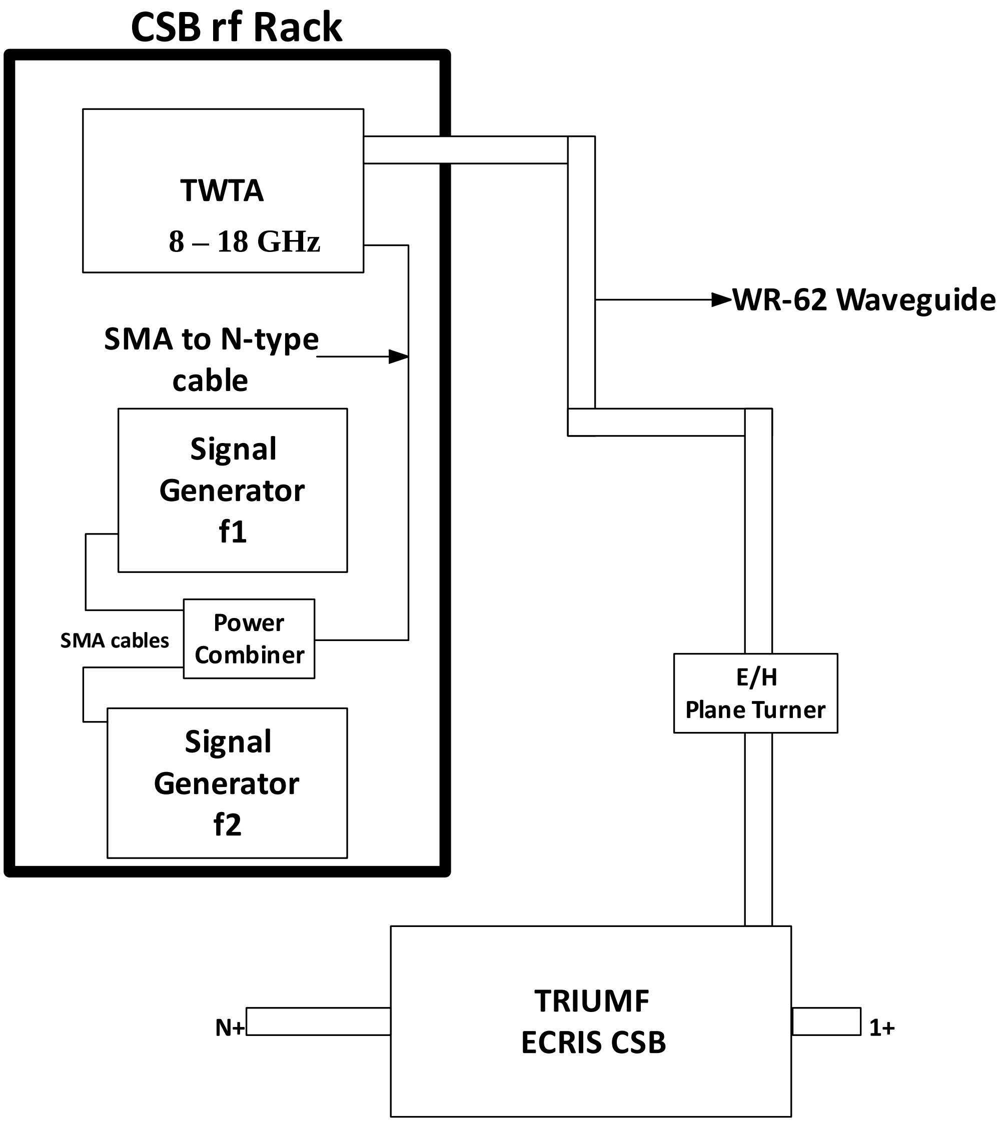

Figure 6.2: Schematic of the rf system setup for the two-frequency heating technique implemented on the charge state booster.

Figure 6.3 compares the efficiency of cesium with single-frequency heating with the efficiency of two-frequency heating for this approach. Unlike the single-frequency heating technique set up, the charge state booster, the injection and the extraction optics were not properly optimized for the two-frequency heating setup, but the maximum charge of cesium that can be detected shifted from $27+$ for single-frequency heating to $29+$ for the two-frequency heating set up. The result already showed the expected effect of the two-frequency heating on the ECR plasma.

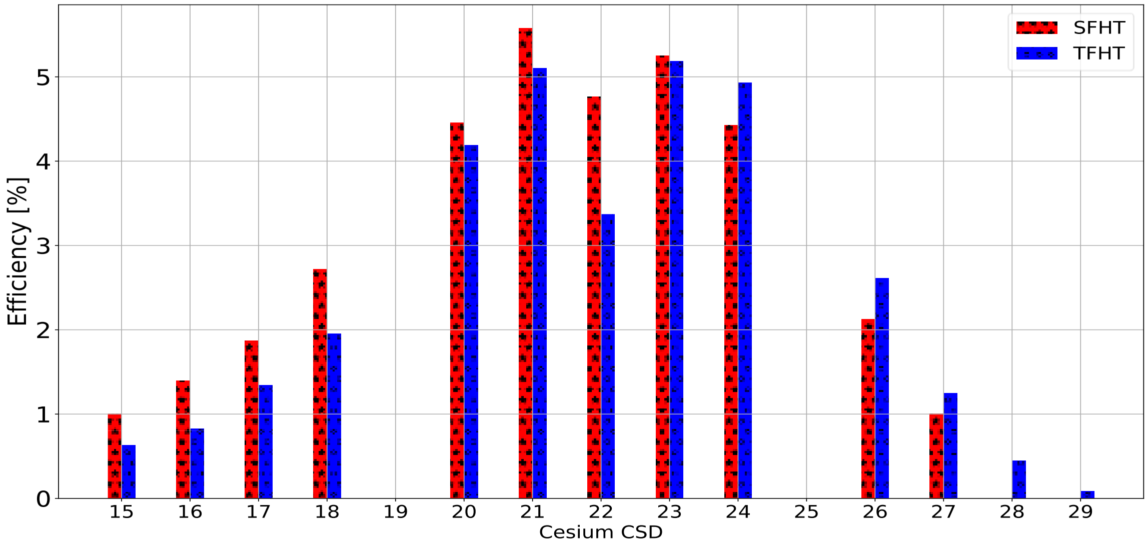

Figure 6.3: Efficiency of cesium in single and two-frequency heating modes. The CSB was well optimized under the single-frequency heating mode but not under the two-frequency heating mode.

6.3.2 Second Approach: Two Signal Generators, Two TWTA

The two signal generators and two travelling wave tube amplifier-approach of implementing the two-frequency heating were copied from [64]. The only difference is that two TWTAs and a power combiner are used to implement the TFHT on the TRIUMF CSB. The complete setup consists of a phase shifter (model 9428A), two BNC signal generators (model 845), two CPI travelling wave tube amplifiers (one of indoor rack mount and the other is designed for outdoor), a magic tee power combiner, a circulator, cross guide and E/H plane turner. Dummy loads are used to terminate the power combiner (frequency range of $14 - 14.5\ GHz$) and the circulator (frequency range of $12.8 - 18\ GHz$). Figure 6.4 shows the schematic of this specific TFHT setup. A major modification of the existing CSB RF rack was performed to accommodate the new setup. The phase shifter was added to have an additional knob to optimize further the electromagnetic wave composition properties injected into the CSB. The output of one of the signal generators is phase shifted while the other is not, as shown in Figure 6.4. The magic tee combines the outputs of the two TWTAs, and the combined amplified waves are fed to the circulator. The circulator is the major RF component missing from the first approach presented in Section 6.3.1. The circulator prevents the reflected power from reaching the amplifiers. It works so that reflected power from the plasma is diverted into the coupled dummy load, thus protecting the amplifiers. The cross guide provides a means to monitor the reflected powers.

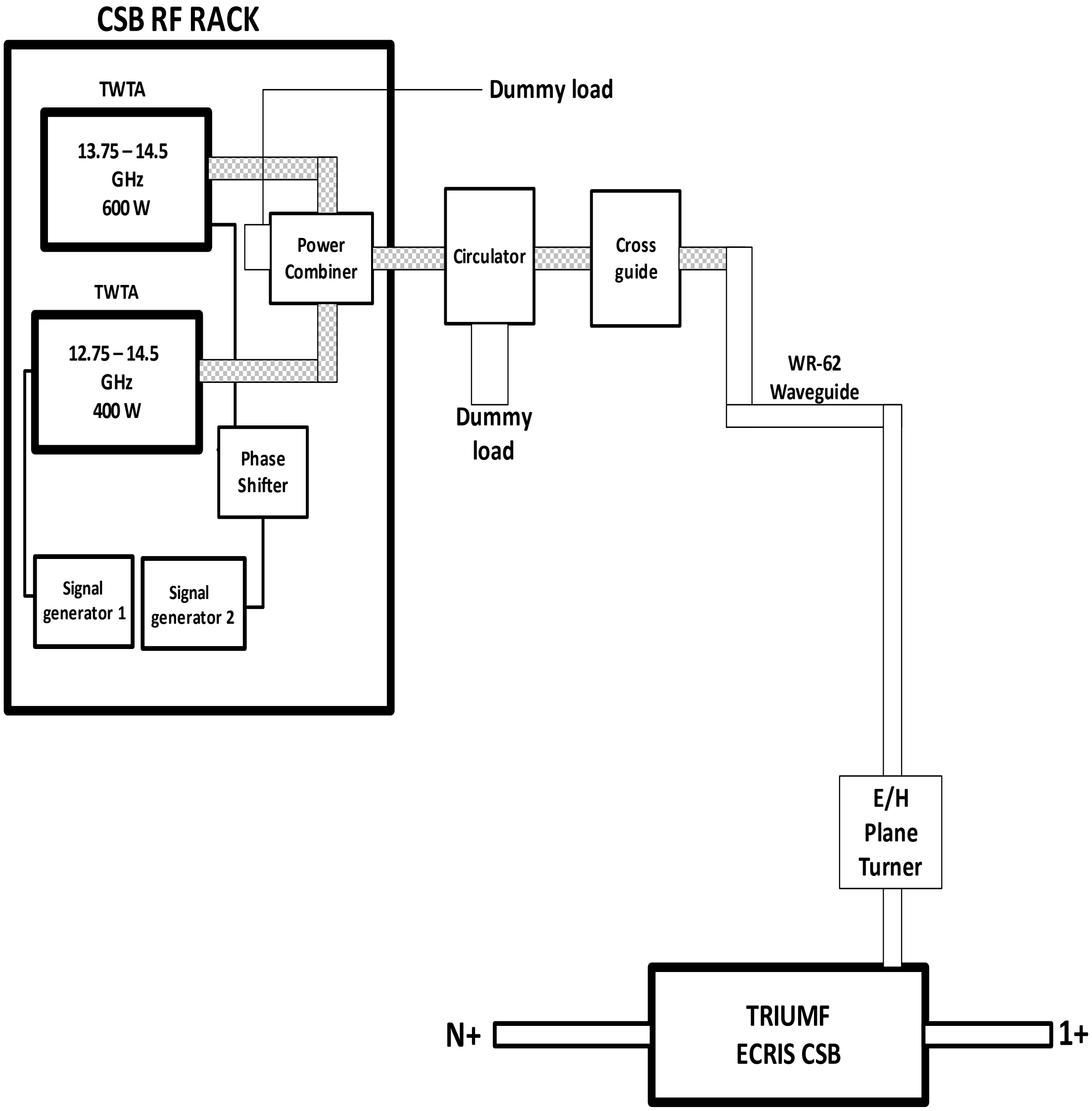

Figure 6.4: Schematic of the rf system for the implemented two-frequency heating technique using a single waveguide. The wave termination (dummy load) installed on the power combiner has a frequency bandwidth between 12.75 and 14.5 GHz.

6.4 The Two-Frequency Heating Experimental Setup

After the ECRIS CSB was opened for magnetic field measurement, the plasma condition and the total extracted current from the CSB changed significantly. The changes can be attributed to changing the location and the positions of the center soft iron rings and unavoidably misaligning the injection and the extractions optics during the assembly of the CSB. As a result, the optics settings and the ECR parameters, such as the solenoid coil settings that worked for the results reported in Chapter 5, no longer work. So, the CSB was systematically optimized, and a new set of settings for transport optics, plasma conditioning, injection and extraction systems, which will be presented later in this chapter, was determined.

The injection and extraction optics were optimized using the TRANSOPTR, and the tune calculated and predicted were loaded into the EPICS. The CSB high voltage bias, which defines the beam energy, was set to $10\ kV$, and the extraction voltage that forms a low beam emittance of $119.6\ mm-mrad$ at the extraction region was systematically found to be $2.8\ kV$, at this extraction voltage, the total beam current on Faraday cup FC14 was about $30\ \mu A$. After the extraction voltage has been determined, a singly charged cesium beam of about $8\ nA$ was injected into the CSB from the test ion source (CTIS) located upstream of the CSB, and the mass separator located downstream of the CSB was set to 4.75 corresponding to the Cs^{28+} A/q ratio while its intensity was monitored on Faraday cup FC16A downstream of the mass separator.

The ECR plasma was optimized and conditioned for the production of Cs^{28+} by scanning the frequencies of the signal generators one after the other, tuning the solenoid coil current, varying the voltage that controls the helium support gas valve, and systematically varying the RF travelling wave tube amplifiers (TWTAs) one after the other. While the plasma was being conditioned, the intensity of Cs^{28+} was monitored on the Faraday cup, FC16A. The plasma parameters that produced the maximum intensity of Cs^{28+} are solenoid coil settings: $I_{inj} = 1200\ A$, $I_{mid} = 263\ A$, and $I_{ext} = 801\ A$, RF frequencies: $f1 = 14.0631\ GHz$, $f2 = 14.3536\ GHz$, TWTA power1 = $300\ W$, TWTA power2 = $46\ W$ and gas valve voltage, $V_l = 6.5\ V$.

6.5 Plasma Potential Measurement under the Two-Frequency Heating Regime

The CSB was set to the parameters above, and deltaV was systematically varied between 0 and 30 V while monitoring the intensity of Cs^{28+} on Faraday Cup FC16A. Figure 6.5 shows the according result, the normalized intensities of Cs^{28+} plotted against the delta-V values.

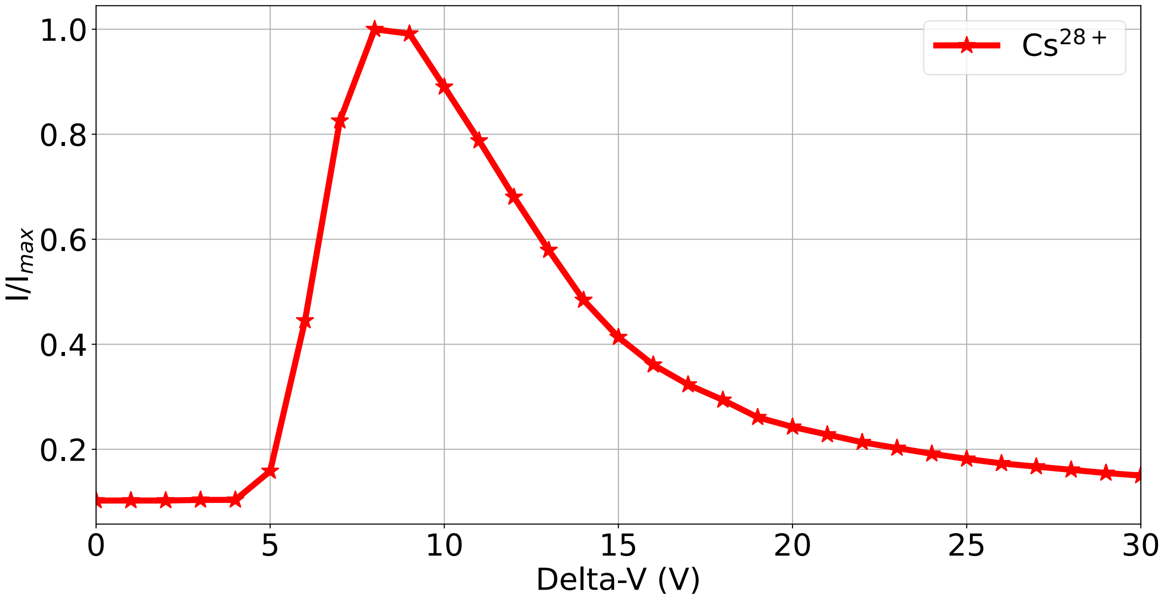

Figure 6.5: Normalized intensity of Cs^{28+} beam plotted against deltaV. The two frequencies launched into the plasma are 14.0631 GHz and 14.3536 GHz at TWTA powers of 300 W and 46 W.

As seen in Figure 6.5, the intensity of Cs^{28+} peaked at deltaV = 8 V. Below 8 V, that is, between 0 and 8 V, the kinetic energy of the injected singly charged Cs ions is too low to travel into and be captured by the plasma for the production of the Cs^{28+} ion beam, and above 8 V, that is between 8 and 30 V, the energy of the injected Cs^{+} ions is too high for the plasma to capture the singly charged ions efficiently, thus reducing the production of Cs^{28+} but at deltaV = 8 V, the injected singly charged Cs ions were efficiently captured by the plasma which led to the highest intensity of Cs^{28+}. The peak of the distribution, as shown in Figure 6.5, indicates that the plasma potential of the CSB is of the order of 8 V.

6.6 Efficiency of Cesium Charge State Distributions under the TFHT Regime

After the deltaV value had been determined, the efficiency of Cs charge states distribution was determined. To reduce the intensity of the background and residual ions, the widths of the slit before the mass separator and the two slits after the mass separator were set to 3 mm, 4 mm and 4 mm, respectively. Figure 6.6 shows the mass spectrum of the CSB between the A/q ratio of 3.0 and 6.0. The mass spectrum was recorded with and without injecting singly charged Cs ions.

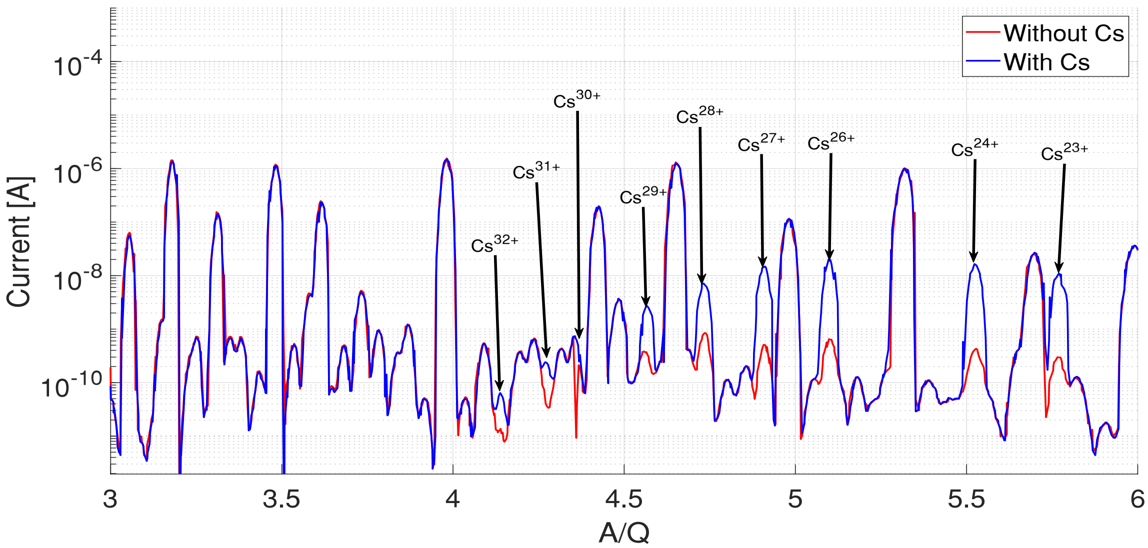

Figure 6.6: Mass spectrum of the CSB under the TFHT regime with and without cesium. The black arrows show the peaks of the cesium charge state between 23+ and 32+. The entrance and exit slits of the magnetic dipole were set to 3 mm, 4 mm and 4 mm. The two frequencies launched into the plasma are 14.0631 GHz and 14.3536 GHz at TWTA powers of 300 W and 46 W.

The red plot is the spectrum without injection of Cs, while the blue plot is with the Cs injection. The black arrows show the highly charged Cs charge states between 23+ and 32+, while the unlabeled peaks are from residual ions such as carbon, nitrogen and oxygen. To further reduce the influence of the background and the residual ions, the intensity of the background ions was subtracted from the total current with Cs, and the efficiency of each charge state and the global efficiency were calculated using Equations 5.1 and 5.2, respectively. Figure 6.7 shows the plot of the efficiency of the Cs against the charge state.

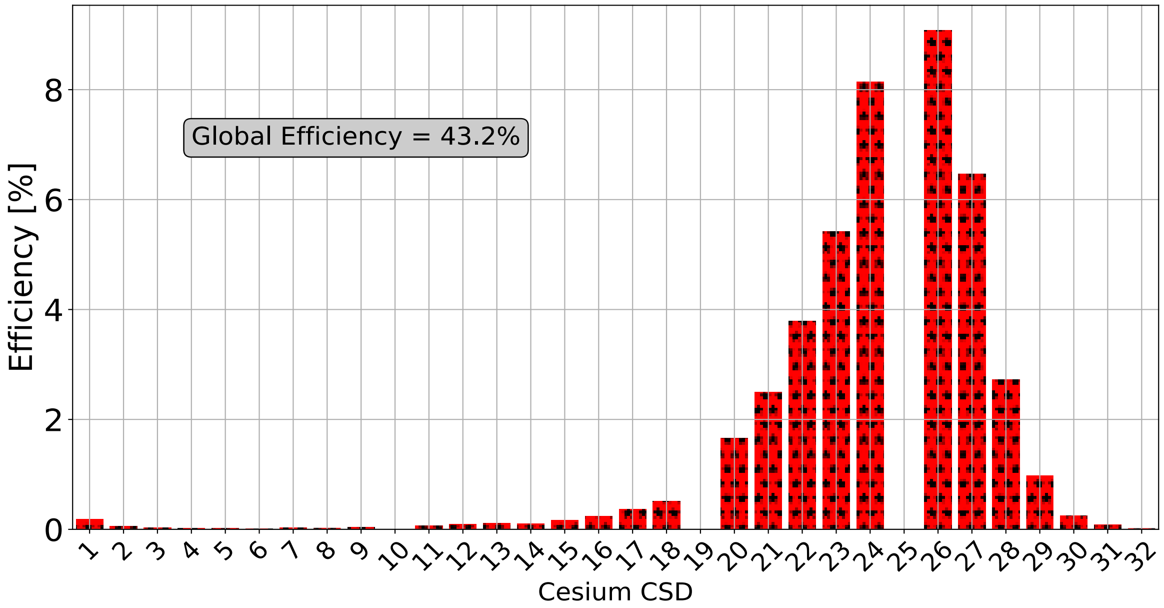

Figure 6.7: Efficiency of cesium charge states under the TFHT regime. The two frequencies launched into the plasma are 14.0631 GHz and 14.3536 GHz at TWTA powers of 300 W and 46 W.

As shown, the global efficiency of all the Cs charge states that can be detected was 43.2 %. It is important to know that the global efficiency would be higher than the shown value if the efficiencies of Cs^{10+}, Cs^{19+} and Cs^{25+} were known, but because of highly intense residual ions from argon, nitrogen and oxygen dominating corresponding A/Q for the charge states, it was difficult to detect their intensity as shown in Figure 6.6. Also, as seen in Figure 6.7, since the efficiency of Cs^{25+} is known, we will assume that the peak of the efficiency distribution falls on Cs^{26+} with an efficiency of 9.1 %. And finally, the maximum charge state of Cs that can be detected is 32+ with an efficiency of 0.02 %.

6.7 Effect of the Two-Frequency Heating on the Plasma Potential, total Emittance and the Efficiency of the TRIUMF ECRIS CSB

To determine the effect of the two-frequency heating on the plasma potential and the efficiency of the charge state booster compared with the single-frequency heating, one of the signal generators was switched off, and the frequency of the second signal generator was set to 14.5 GHz while the travelling wave tube amplifier power was also set $350\,W$. The injection, extraction optics, bias voltage ($10\,kV$), and extraction voltage ($2.8\,kV$) were kept constant. However, the plasma was systematically conditioned to produce and extract Cs^{24+}. So, in addition to the single-frequency heating at 14.5 GHz, the combination of magnetic coil settings that produced higher intensity of Cs^{24+} with $A/Q = 5.54$ was found to be $I_{inj} = 1200\ A$, $I_{mid} = 253\ A$ and $I_{ext} = 791\ A$. With these settings, the intensity of Cs^{24+} as a function of the deltaV value was measured, the total emittance of the CSB as a function of the extraction voltage was measured, and the efficiency of Cs charge states was also measured. The results were compared with the two-frequency heating of the charge state booster using the settings presented in Section 6.4. In addition, the parameters are also compared with the results of the CSB before the CSB was opened for the magnetic field measurements.

6.7.1 DeltaV Variation – Plasma Potential Measurement: SFHT vs. TFHT

Figure 6.8 compares the intensity of Cs^{24+} before the CSB was opened under the single-frequency heating regime with the intensity of Cs^{24+} after the CSB was opened, and the intensity of Cs^{28+} under the two-frequency heating regime with deltaV varied between 0 and 30 V.

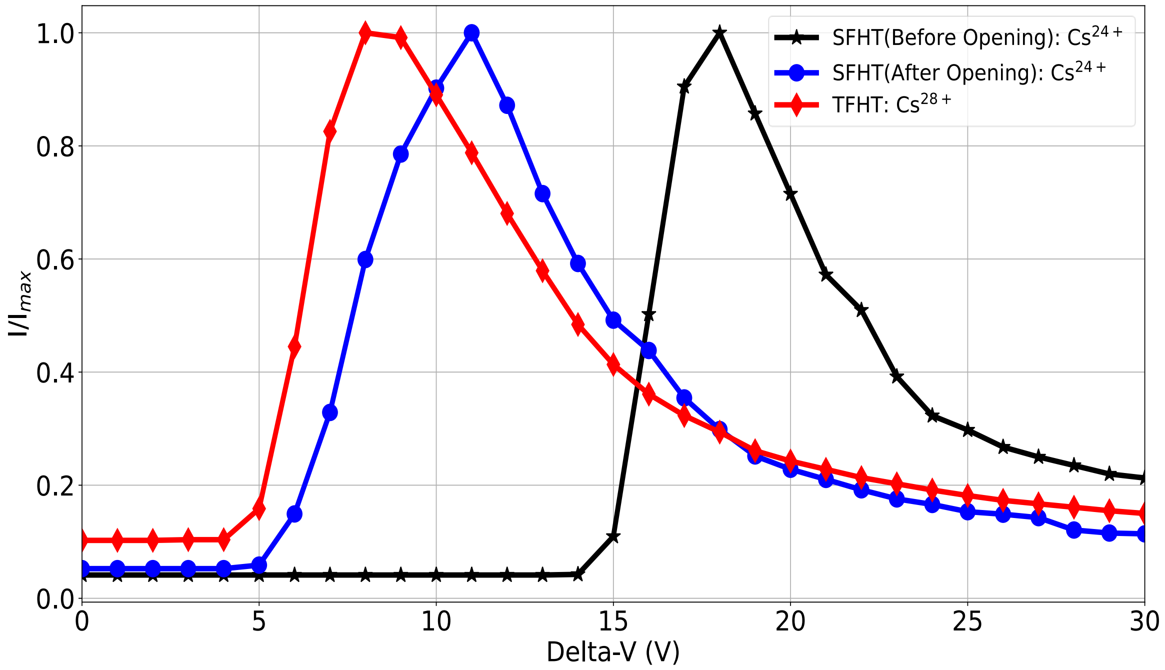

Figure 6.8: Variation of deltaV for plasma potential measurement under the SFHT and TFHT regimes. For the SFHT, the rf frequency was launched at 14.5 GHz at a TWTA power of 350 W, and for the TFHT, the rf frequencies were launched into the plasma at 14.0631 GHz and 14.3536 GHz at TWTA powers of 300 W and 46 W.

As previously discussed, the CSB and the extraction optics were tuned for the production and extraction of Cs^{24+} under the single-frequency heating regime and for Cs^{28+} under the two-frequency heating regime. As shown in the plot, the plasma potential seems to be an order of $17.0\ V$ before the was CSB (black plot) opened but decreased to $10.0\ V$ after opening the CSB (blue) under the single-frequency heating regime, then decreased further to $8.0\ V$. The difference between the plasma potential before and after the CSB was opened under the SFHT regime may be attributed to a difference in the plasma density. However, the decrease in the plasma potential under the TFHT regime can be attributed to the reduction in the density of the low-energy electrons escaping the plasma.

6.7.2 Total Emittance: SFHT vs. TFHT

Using the quadrupole scan technique (QST), the emittance of the total current extracted from the CSB was measured as a function of the extraction voltage between $2.0\ kV$ and $3.5\ kV$ for $10.0\ kV$ bias voltage. Figure 6.9 shows the plot of the total emittance as a function of the extraction voltage. The results are compared for the single-frequency (before and after opening) and two-frequency heating regimes.

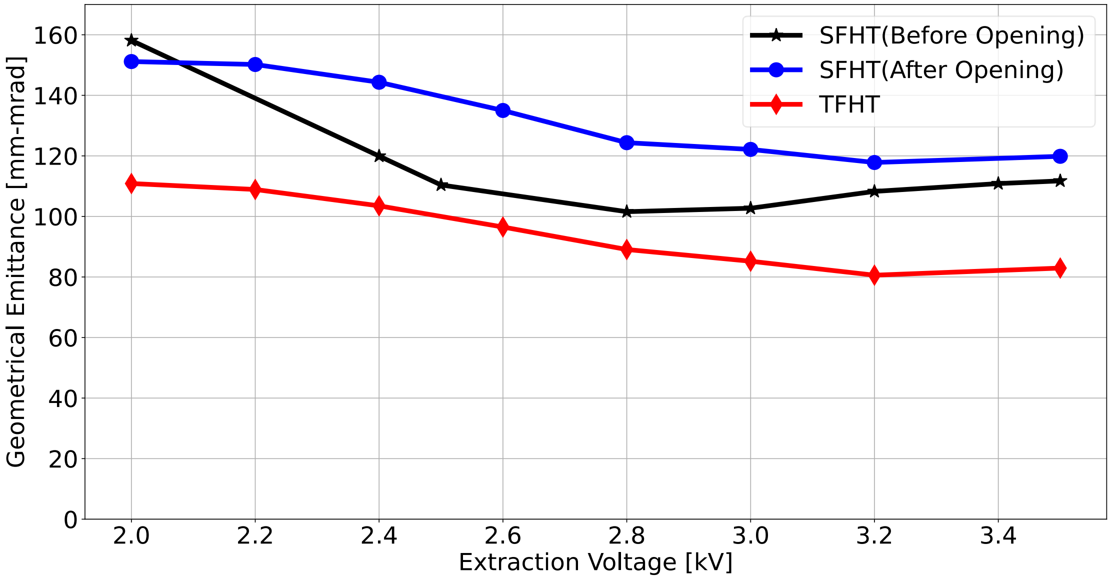

Figure 6.9: Comparison of the total 4RMS Emittance of the CSB under single-frequency heating and two-frequency regimes at a CSB bias voltage of 10 kV. For the SFHT, the rf frequency was launched at 14.5 GHz at a TWTA power of 350 W, and for the TFHT, the rf frequencies were launched into the plasma at 14.0631 GHz and 14.3536 GHz at TWTA powers of 300 W and 46 W.

The extraction voltage is the difference between the voltage on the puller electrode and the plasma chamber bias voltage of $10.0\,kV$. The combined power of the RF fed into the plasma under the two-frequency heating was $350\,W$, as in the single-frequency heating regime. The signal generator was set to $14.5\,GHz$ for single-frequency heating, while for two-frequency heating, the signal generators were set to $14\,GHz$ and $14.5\,GHz$. The black plot is the total emittance of the CSB (presented in section 5.2) under normal operation in single-frequency heating mode before the CSB was opened for the magnetic field measurement. The blue plot is the total emittance under the single-frequency heating regime after opening the CSB, and the red plot is the results under the two-frequency heating regime. At $2.0\,kV$, the emittances under all the cases considered are generally large. Before opening the CSB under the SFHT regime, the emittance is $158.1\,mm-mrad$; after opening the CSB, the emittance is $151.2\,mm-mrad$, while the emittance is $110.9\,mm-mrad$ under the TFHT. As the extraction voltage increases, the emittance of the CSB decreases to a minimum, $101.6\,mm-mrad$, $117.8\,mm-mrad$ and $80.6\,mm-mrad$, respectively. However, a further increase in the extraction voltage leads to an increase in the beam emittance. As already explained in Chapter 5, for a given plasma density at low extraction voltage (low extraction field), the emittance of the extracted beam is large because the plasma boundary (edge of the plasma electrode) where the extracted beam is formed is convex. The extracted field in the region does not match the ion density, and the extracted ions are created with a large angle producing a large emittance beam. Furthermore, as the extraction voltage or extraction field is increased, the protruded plasma boundary starts retracting into the bulk plasma until a planar plasma boundary is achieved where beams that are formed are extracted with small or no angle, producing the smallest emittance which was achieved at $2.8\,kV$ and $3.2\,kV$ respectively in Figure 6.9. The smallest emittance suggests that the applied extraction voltage or field matches the plasma density. However, when the extraction voltage or field is increased further from the point where the smallest emittance is achieved, the plasma boundary retracts further in the bulk plasma and creates a concave plasma interface where the beams formed are extracted with a large angle as a result of overfocusing due to the plasma density not matching the applied extraction voltage or field and producing a large emittance of $111.7\,mm-mrad$, $119.9\,mm-mrad$ and $82.9\,mm-mrad$ respectively at $3.5\,kV$. Moreover, by comparing the emittance of the CSB under the SFHT regimes before and after opening the CSB, as seen in Figure 6.9, the total emittance of the CSB across all the extraction voltages after the CSB was opened is larger compared to before opening the CSB, and in addition to that, the smallest emittance after the opening the CSB was achieved at the extraction voltage of $3.2\ kV$ and not $2.8\ kV$ as the case before opening the CSB. The discrepancy is due to the changes in the density of the bulk plasma of the ECR due to higher background pressure.

Furthermore, one of the first major significant effects of two-frequency heating on the ECR plasma can be seen in the plot in Figure 6.9. In addition to the plasma boundary (density and extraction field) determining the emittance of the extracted ions, the total emittance of the extracted ions is also determined by the electron energy of the plasma and the formation of the potential dip in the plasma. As previously discussed in this thesis, implementing the two-frequency heating creates an additional resonance zone where plasma electrons are additionally heated through the electromagnetic wave. With the additional energy gained by the electrons, their motions are directed toward the plasma center. Since the ions are confined electrostatically by the electrons due to the negative potential dip [18], the motions of the ions on an average are also directed to the plasma core where they are charged-bred, and upon extraction, the ions leave the plasma with small radii, thus the small emittances. So, by varying the extraction voltage (field), the angles at which the ions are extracted are further influenced by the shape of the plasma boundary (convex, plane, and concave) and smaller emittances can further be achieved which is an indication of an optimized extraction system of the ECR ion sources.

6.7.3 Efficiency of Cesium Charge States: Comparison between SFHT and TFHT

Figure 6.10 compares the efficiency of the charge state booster before the injection and extraction optics, injection and extraction systems were optimized and after optimization under the single-frequency heating regime with the two-frequency heating regime for cesium charge states between 20+ and 32+. The charge state of 25+ was omitted in the plot because the corresponding mass-to-charge ratio is intensely dominated with $16O^{3+}$ current.

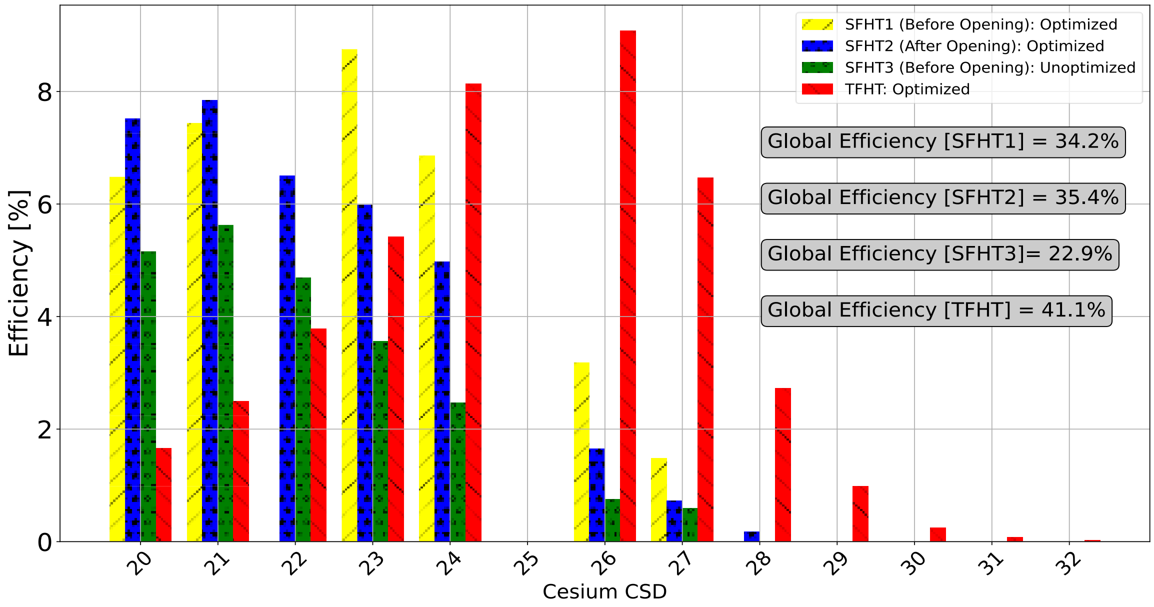

Figure 6.10: Comparison of the efficiency of the CSB under the single and two-frequencies heating regimes. For the SFHT1 and SFHT2, the rf frequency was launched at 14.5 GHz at a TWTA power of 350 W and optics optimized for Cs^{24+}, For the SFHT3, the rf frequency was launched at 14.45 GHz at a TWTA power of 300 W and optics optimized for Cs^{18+}, and for the TFHT, the rf frequencies were launched into the plasma at 14.0631 GHz and 14.3536 GHz at a TWTA power of 300 W and 46 W. Optics were optimized for Cs^{28+} under the TFH regime.

The plot also compares the efficiency of the cesium before and after opening the CSB. It is important to know that the two-frequency heating was implemented after opening the CSB for magnetic field measurements. As seen in the plot under the single frequency heating regime, before opening the CSB and before optimizing the CSB (green bars), Cs^{21+} has the highest efficiency of approximately 5.6 %, while before opening the CSB and after optimizing the CSB (yellow bars), the Cs charge state with the maximum efficiency approximately 8.8 % shifted to 23+ but after opening the CSB the Cs charge state with the highest efficiency approximately 7.8 % shifted back to Cs^{21+}. Thus, it can be concluded that under the single-frequency heating of the CSB, the Cs charge state with the maximum efficiency that can be produced lies between 21+ and 23+. However, with the two-frequency heating of the ECRIS CSB plasma, the Cs charge state with the highest efficiency shifted from around 21+ and 23+ to a higher charge state which could either be 25+ or 26+. Because of the inability to measure the efficiency of Cs^{25+}, it is assumed that the efficiency shifted to Cs^{26+} with approximately 9.1 % efficiency. In addition to the shift in the peak of the efficiency distribution, the maximum charge state of Cs that can be produced under the SFHT regime is 28+ with an efficiency of $0.2\ \%$, but the maximum charge state that can be produced shifted to 32+ with an efficiency of 0.02 % under the TFHT, and as seen the two-frequency heating has the maximum global efficiency of $41.1\ \%$ of all the regimes considered. The global efficiency could be higher than $41.1\ \%$ if the efficiency for Cs^{25+} were known. The combined improvement of the efficiency and the shift in the maximum charge state that can be produced in the CSB under the TFHT regime can be attributed to the increase in the average energy of the ECR plasma electrons because of the additional resonance zone created where the plasma electrons were additionally heated, increase in the plasma density within the innermost resonance zone and increase in the ion confinement time.

6.7.4 Efficiency of Uranium-238 Injected from the TRIUMF ISAC Target Station: SFHT vs.TFHT

With the advanced performance of the CSB, it was used for the first time to deliver a highly charged $^{238}U^{27+}$ beam to the TRIUMF's Ion Trap for Atomic and Nuclear Science (TITAN) experiment. The online TRIUMF ISAC target station produced the singly charged uranium beam. The combined experience gained from operating the CSB using TRANSOPTR and systematic investigation were employed to tune the injection optics from quadrupole Q5, the injection system, the ECR plasma, the extraction system and the extraction optics up to Faraday cup FC16A.

Before general tuning of the CSB and the corresponding optics, it was set to about $8\ V$ less than the bias voltage of the target ion source, which was $10\ kV$. On the Faraday cup FC5 (see Figure 4.10) at the injection region of the CSB, the singly charged uranium beam intensity was about $2.6\ nA$. The first thing that was done was to measure the beam's emittance using the quadrupole scan technique (QST) by scanning quadrupole Q5 and recording the beam profile on profile monitor RPM5. Figure 6.11 shows the almost converging phase space ellipse of the uranium beam at the entrance of quadrupole Q5. The 4RMS emittance and the Twiss parameters of the beam at the entrance of Q5 were measured to be $\varepsilon = (85.6 \pm 5.8)\ mm - mrad$, $\alpha = -0.076 \pm 0.021$, $\beta\ = (183 \pm 12)\ cm$ and $\gamma = (0.0055 \pm 0.0004)\ cm^{-1}$.

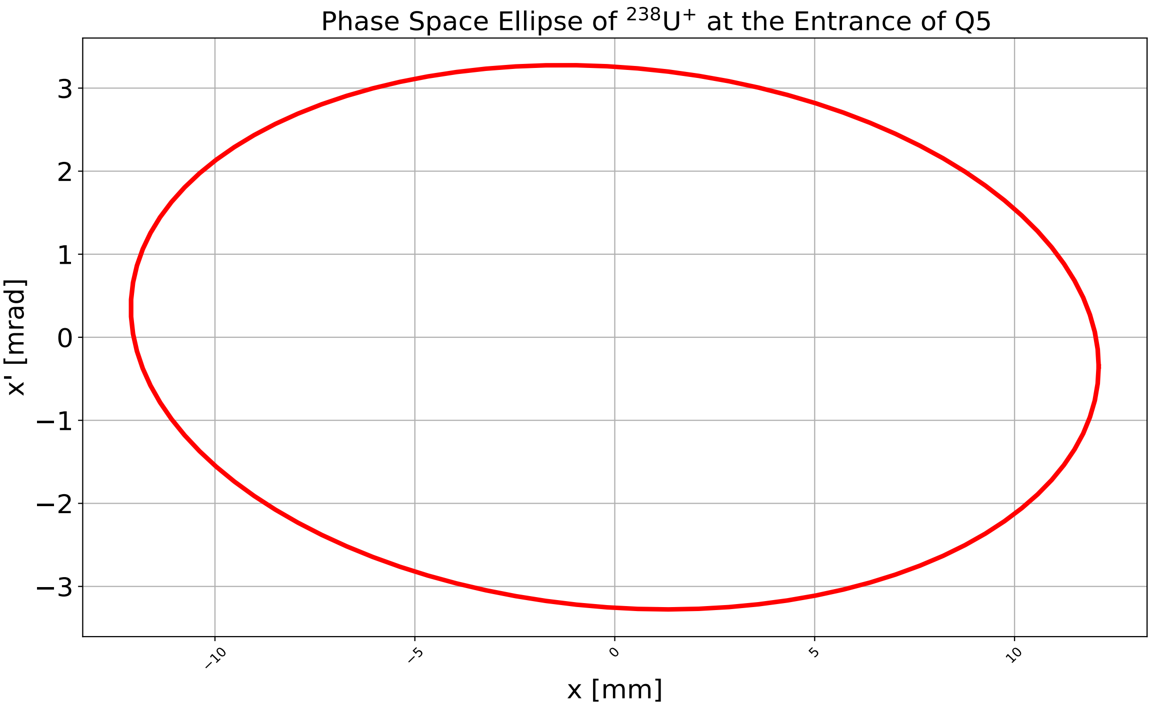

Figure 6.11: Phase space ellipse of ^{238}U^{+} in $x - x'$ plane at the entrance of Q5. The emittance and the Twiss parameters were measured using the quadrupole scan technique at an energy of Q*10 keV.

The emittance and the Twiss parameters were imported into the TRANSOPTR, and the optics tunes were calculated. The beam optics were physically set to the calculated values, and the CSB plasma, the extraction system and optics were tuned for the production, extraction and transportation of ^{238}U^{27+}. After systematic tuning of the charge state booster and the adjacent optics, frequency1 = $14\ GHz$ at TWTA power = $300\ W$, frequency2 = $14.5\ GHz$ at TWTA power = $46\ W$, extraction voltage = $2.65\ kV$, gas valve voltage = $6.7\ V$ (helium support gas) magnetic fields distribution at $I_{inj} = 1200\ A$, $I_{mid} = 264\ A$ and $I_{ext} = 793\ A$ were found to produce highest efficiency of $27+$ on Faraday cup FC16A. To compare the efficiency of the uranium beam under the two-frequency heating with the efficiency under the single-frequency heating, one of the signal generators was switched off, and the second one was set to an rf frequency of $14.5\ GHz$ and TWTA power of $350\ W$, all other parameters were kept constant. The mass separator (see Figure 4.16) was scanned, and the spectrum of the CSB with and without injecting singly charged uranium ion was measured for single-frequency heating and two-frequency heating. The mass spectra under the two regimes are shown in Figures 6.12 and 6.13 for the mass-to-charge ratio (A/Q) between 6.0 and 14.0. In the plots, the spectral without uranium is red, and the spectral with uranium is blue. The peaks of the uranium charge states are indicated with the black text arrows, while the rest are from background ions.

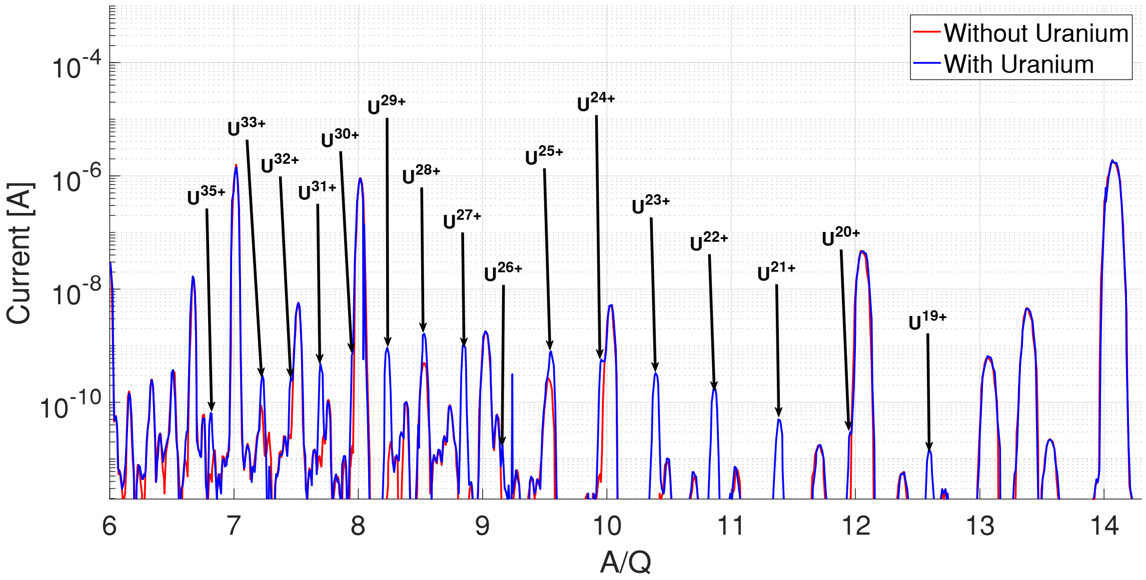

Figure 6.12: Mass spectrum of the CSB with and without uranium under SFHT. The rf frequency was launched at 14.5 GHz and a TWTA power of 350 W. The optics were optimized for the extraction of U^{27+}. The entrance and exit slits of the magnetic dipole were set to 5 mm, 5 mm and 3 mm.

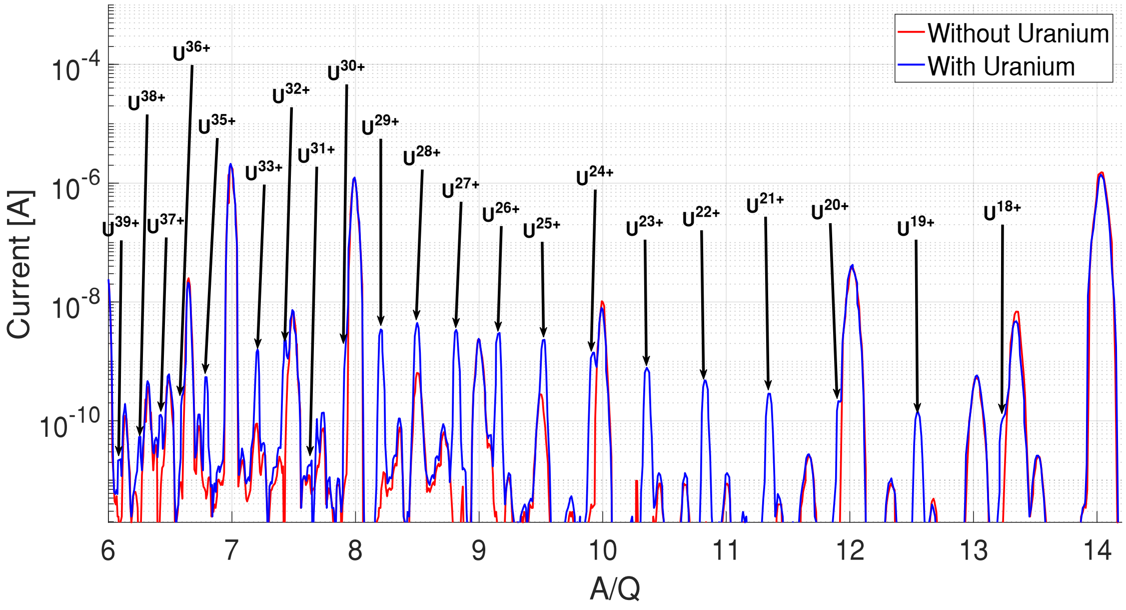

Figure 6.13: Mass spectrum of the CSB with and without uranium under TFHT. The rf frequencies were launched at 14 and 14.5 GHz and TWTA of 300 and 46 W. The optics were optimized for the extraction of U^{27+}. The entrance and exit slits of the magnetic dipole were set to 5 mm, 5 mm and 3 mm.

Using Equations 5.1 and 5.2, the single charge state efficiency and the global efficiency of the uranium were calculated by extracting the intensity of the uranium charge states that can be determined from Figures 6.13 (SFH of the CSB) and 6.14 (TFH of the CSB).

Figure 6.15 compares the efficiency of uranium under the two heating regimes. The blue plot is the efficiency under SFHT, while the red plot is the efficiency under TFHT. No information was recorded for 17+ and 34+ because the corresponding A/q is dominated by $^{14}N^{+}$ and $^{14}N^{7+}$, as can be seen in the mass spectrum in Figures 6.13 and 6.14. Also, because of the spark in the high voltage bias of the CSB during the mass spectrum scan, the intensity of U^{26+} dropped under the SFHT, and the intensity of U^{31+} dropped under the TFHT. The reduction in the intensity can be seen in Figures 6.13 and 6.14.

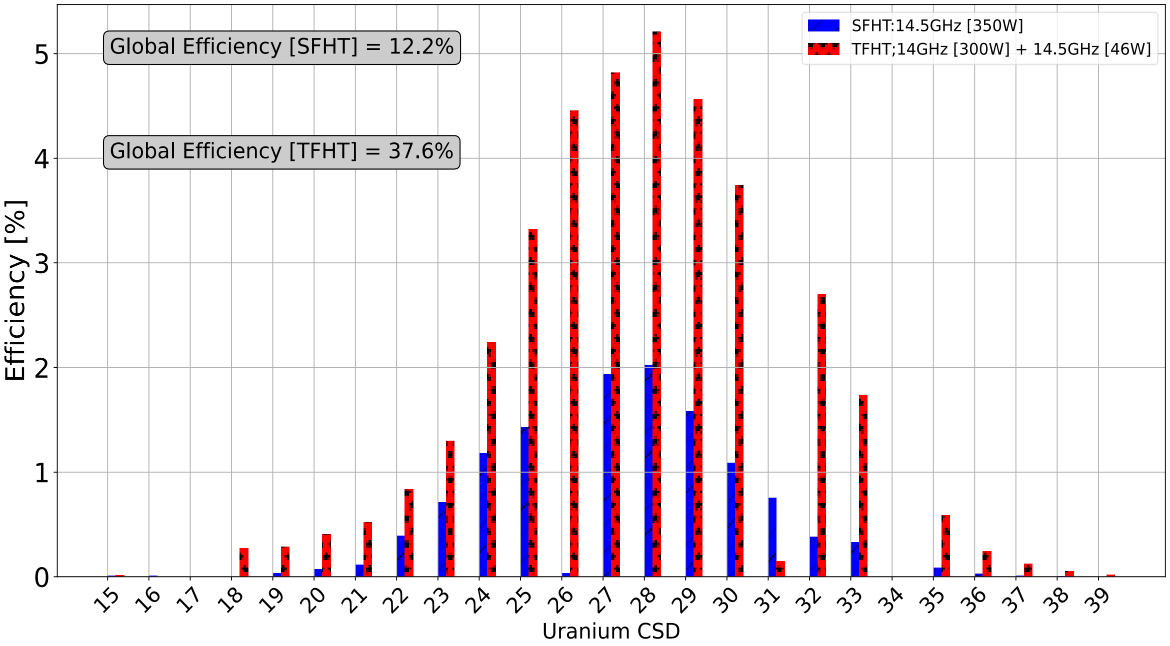

Figure 6.14: Efficiency of uranium under SFHT and TFHT regimes. Global efficiency is the summation of all the charge states that can be measured. For the SFHT, the rf frequency was launched at 14.5 GHz and a TWTA power of 350 W and the optics was optimized for the extraction of U^{27+}. For the TFHT, the rf frequencies were launched at 14 GHz and 14.5 GHz and TWTA of 300 W and 46 W and the optics were optimized for the extraction of U^{27+}.

With the single-frequency heating of the ECRIS CSB, the maximum charge state of uranium that can be detected is 36+ with an efficiency of 0.03 %. However, with the two-frequency heating, the maximum charge state that can be detected shifted to 39+ with an efficiency of 0.02 %. Furthermore, the charge state with the maximum efficiency is 28+ under both heating regimes, but the efficiency is about 2.0 % under the SFHT and about 5.2 % under the TFHT, which is about 2.6 times greater than the SFHT. Also, by summing up all the efficiencies, the global efficiency under the TFHT is about 38 %, while the global efficiency under the SFHT is about 12 %, as shown in Figure 6.15. Even though the global efficiencies for both single-frequency heating (SFH) and two-frequency heating (TFH) will be higher than the values reported if the efficiencies of the missing charges states were known, regardless, it is seen that the global efficiency under the TFH of the CSB is more than a factor of 3 greater than the global efficiency under the SFH of the ECRIS CSB plasma.

Chapter 7 – Summary and Outlook

7.1 Summary

In Rare Isotope Beam (RIB) facilities using the ISOL method, exotic isotopes are extracted as singly charged ions from the target-ion source station where they are produced. The radioactive isotopes must undergo a charge breeding process to an n+ state to match the limit in the mass-to-charge ratio (A/q) of the post-accelerator for nuclear physics experiments. The study and development of charge breeding techniques play a prominent role in optimizing the post-acceleration of intense and exotic beams. High charge states, i.e., relatively low A/Q ratios, allow for compact ion accelerators and higher final beam energies in combination with superconducting LINAC structures. Therefore, this advanced post-acceleration scheme has been chosen by TRIUMF for the ISAC facility. With the construction of the ISAC I facility, a 14.5 GHz PHOENIX ECRIS booster from Pantechnik was installed for the charge breeding of the radioactive ions. After many years of operation, improving operational performance using modern modelling and techniques became mandatory. The two-frequency heating technique was implemented on the ECRIS CSB so that more highly charged ions could be produced and delivered to the experiments in the TRIUMF ISAC facility. The initial setback was that the TRIUMF CSB was not designed to accommodate two separate waveguides to implement the two-frequency heating technique as it is conventionally implemented in other facilities worldwide. However, the setback was overcome by implementing the superior technique using a single waveguide. In addition to the two-frequency heating of the booster, the injection and the extraction optics, as well as the injection and the extraction systems of the CSB, were optimized for the first time, and the overall improvements led to a significantly increased efficiency and operational performance of the booster.

Furthermore, for accurate modelling of the CSB extraction system in IGUN and beam envelope in TRANSOPTR, the magnetic field distributions of the CSB, both radial and axial, were mapped and compared with OPERA simulation for benchmarking. The OPERA modelling and field mapping provides up-to-date information about the magnet system of the CSB. Furthermore, the results of the magnetic field measurements revealed a discrepancy in the control settings of the power supply of the CSB solenoid coils, which could be fixed. The discrepancy was identified after comparing the mapped magnetic fields with the OPERA modelling.

From the results discussed in Chapters 5 and 6, it can be summarized that optimization of the injection optics improved the injection efficiency of the cesium and uranium singly charged ions, partly contributing to the increase in the intensities and efficiencies of the highly charged ions that are extracted. Besides, the increase in the efficiency of cesium and uranium charge states reported is largely influenced by the implementation of the two-frequency heating of the ECR plasma of the CSB. The TFH created an additional resonance surface in the plasma core where the electrons were efficiently heated. In addition to the increase in the electron energy as a result of the second resonance surface, the electron density and the ion confinement time were also increased; this is evident in the shift of the peak of the charge state distribution to a higher state, most especially in cesium charge breeding results. Because of the increase in the electron population at the plasma core due to the additional resonance zone, a negative potential dip is created, and ions are electrostatically attracted to the plasma core by the potential. The negative potential allows improved confinement of the ions while they are bombarded by the energetic electrons and get ionized to higher charge states, and upon extraction, the ions have a small size and hence lower emittance since they were produced at the position that is closer to the plasma core. Also, a planar plasma meniscus could be achieved by systematically optimizing the extraction system of the CSB through the variation of the extraction field.

In conclusion, with the overall improvement of the CSB, the total emittance of the extracted ions from the CSB reduced to $80.6\,mm - mrad$ from $117.8\,mm - mrad,$ the maximum charge state of cesium that can be detected shifted from 28+ to 32+, the maximum charge state of uranium shifted from 36+ to 39+. The global efficiency of Cs charge states between 20+ and 31+ increased from 23 % to 41 %, while that of uranium between 15+ and 39+ increased from 12 % to 38 %.

With the overall improvement of the CSB, a highly charged uranium ion beam was successfully delivered to the TRIUMF’s Ion Trap for Atomic and Nuclear Science (TITAN) to investigate a radioactive molecule involving uranium and Fluorine. Singly charged uranium ions were injected into the CSB online from the TRIUMF target ion source station.

7.2 Outlook

The Electron Cyclotron Resonance Ion Source is a powerful device that produces highly charged ions in heavy ion accelerator facilities. With the single-frequency heating technique (SFHT), a restricted parameter space is available for the user of such an ion source to produce a desired charged state and intensity. Implementing the two-frequency heating technique (TFHT) further increases the number of parameters that can be tuned and optimized for operational performance. The additional parameters include frequency and phase shift tuning. The effect of frequency tuning has been described as beneficial in [65] and the effect of shifting the phase between the two applied frequencies has also been shown to be beneficial in [64]. As presented and discussed in the two-frequency heating chapter, it was only possible to tune the CSB between the electromagnetic wave frequency of $14\,GHz$ and $14.5\,GHz$ because the dummy load used to terminate the magic tee power combiner was designed for that frequency range. The dummy load was borrowed to complete this thesis project in a reasonable time. Due to massive supply chain issues, the contracted companies significantly delayed the original component for more than a year. When this RF component finally arrives, further tuning of the CSB will be conducted over a wide frequency bandwidth to optimize the ECRIS CSB further. The phase shift tuning of the electromagnetic waves could not be performed due to time restrictions and the availability of the charge state booster; however, an experimental campaign is planned to systematically optimize all the parameters associated with the electromagnetic heating of the ECR plasma to improve the performance overall and position the charge state booster in a state that is capable of producing higher charge state with higher intensity with and reduced beam emittance that can be delivered to the experiments in the ISAC facility of TRIUMF.

Furthermore, as presented in Chapter 6, the efficiency of the Electron Cyclotron Resonance Ion Source Charge State Booster (ECRIS CSB) does not only depend on the conditioning of the plasma. The injection and extraction system of the CSB must be properly designed and optimized. The extraction system of the TRIUMF CSB has been changed twice and optimized for the extraction of highly charged ions with the best beam quality, which can theoretically be achieved. The corresponding beamline and injection system are also well understood. Using the TRANSOPTR design code, a useful tune can easily be calculated and used in real-time to transport singly charged ions into and extract highly charged ions from the CSB up to the experimental stations. An issue on the injection side of the CSB that needs to be addressed is that the CSB was originally designed with an asymmetry in the magnetic field at the injection region, making beam injection into the CSB problematic, especially for light ions. The magnetic field asymmetry is due to the wide gap in the injection soft iron plug of the CSB to allow access of the waveguide and support gas pipes to the CSB. The dimension of the gap is about $60\,mm$ wide, $71\,mm$ high and $144\,mm$ long. Figure 7.1 shows the gap in the injection soft iron plug of the CSB modelled in OPERA.

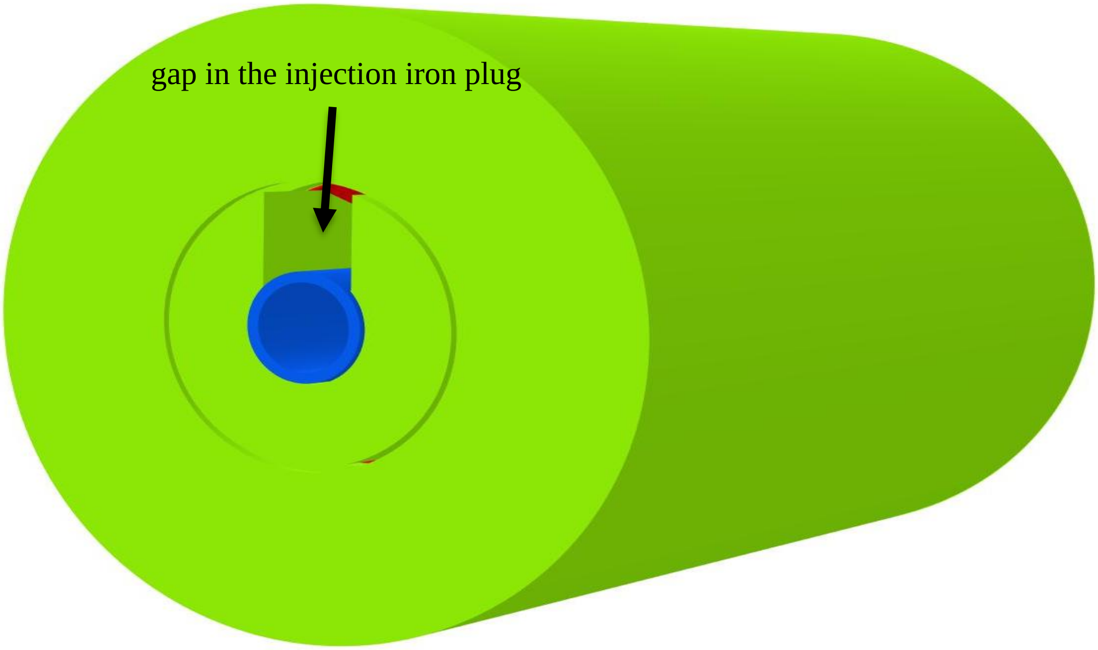

Figure 7.1: TRIUMF ECRIS CSB OPERA model showing the gap in the injection soft iron plug. The gap was created in the iron to feed through the waveguide into the plasma chamber.

Assuming the electrical potential of the CSB is OFF and only the magnetic field is ON, the effect of the asymmetric magnetic field in the injection region is due to the gap in the injection soft iron plug on the trajectories of the injected ions was investigated. This was achieved by tracking the trajectories of injected singly charged ions along the longitudinal direction of the CSB. A $10\,keV$ singly charged cesium ion beam of $10\,nA$ with $5\,mm$ in size was injected into the CSB from the left at $-400\,mm$ with respect to the geometrical center of the model. Meanwhile, in the absence of no magnetic asymmetry, the injected ions should travel to the right covering a total length of $1000\,mm$ along the axis into the CSB. The injected beam was assumed to have no diverging angle, a characteristic that can easily be achieved at the entrance of the CSB. Figure 7.2 shows the trajectory tracking of the ions with the CSB geometry sliced in the plane parallel to the YZ plane.

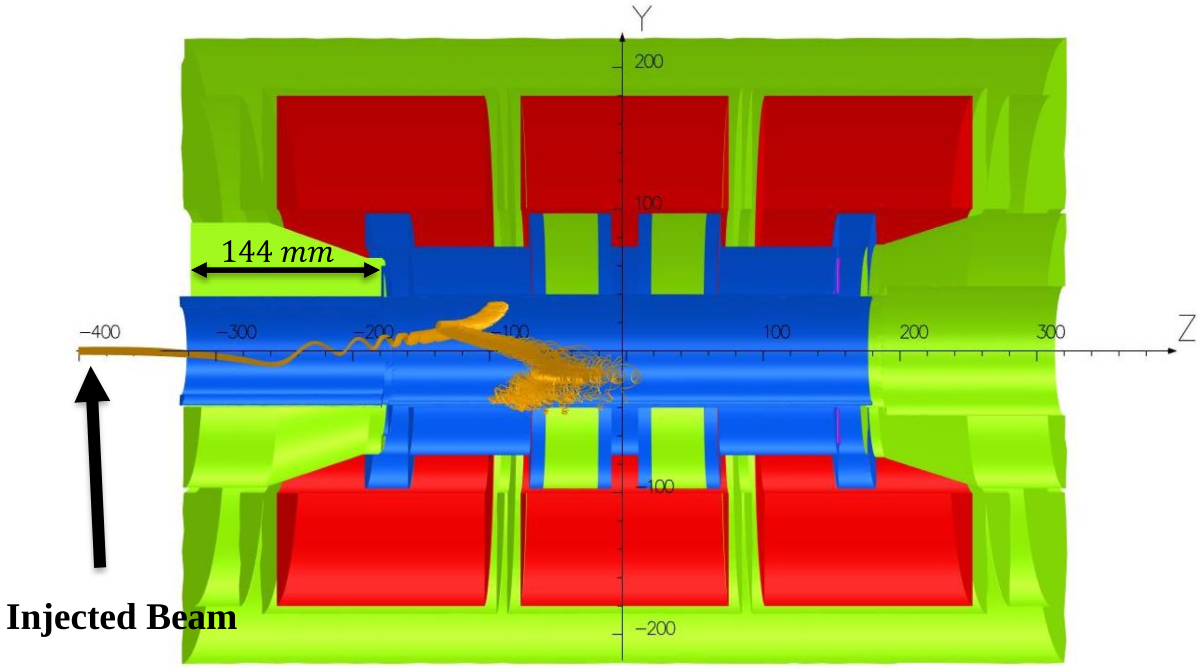

Figure 7.2: Modelling of the trajectories of singly charged cesium ion beam into the CSB with the gap in the injection soft iron assuming only magnetic field is present in the CSB. The beam was launched at an energy of Q*10 keV. The space charge of the plasma is not included in the simulation.

As seen, the injected ions do not have a straight trajectory as they travel into the CSB; rather, they are deflected and directed toward the vacuum chamber and eventually lost to the chamber wall. The deflection of the trajectories of the ions is caused by the asymmetric magnetic field, which has a strong dipole component at the injection region of the CSB created by the cut in the injection soft iron plug. This simulation confirmed the scrape-off observed on the injection electrode (IE2) of the CSB when it was opened for the magnetic field mapping, as shown in Figure 7.3.

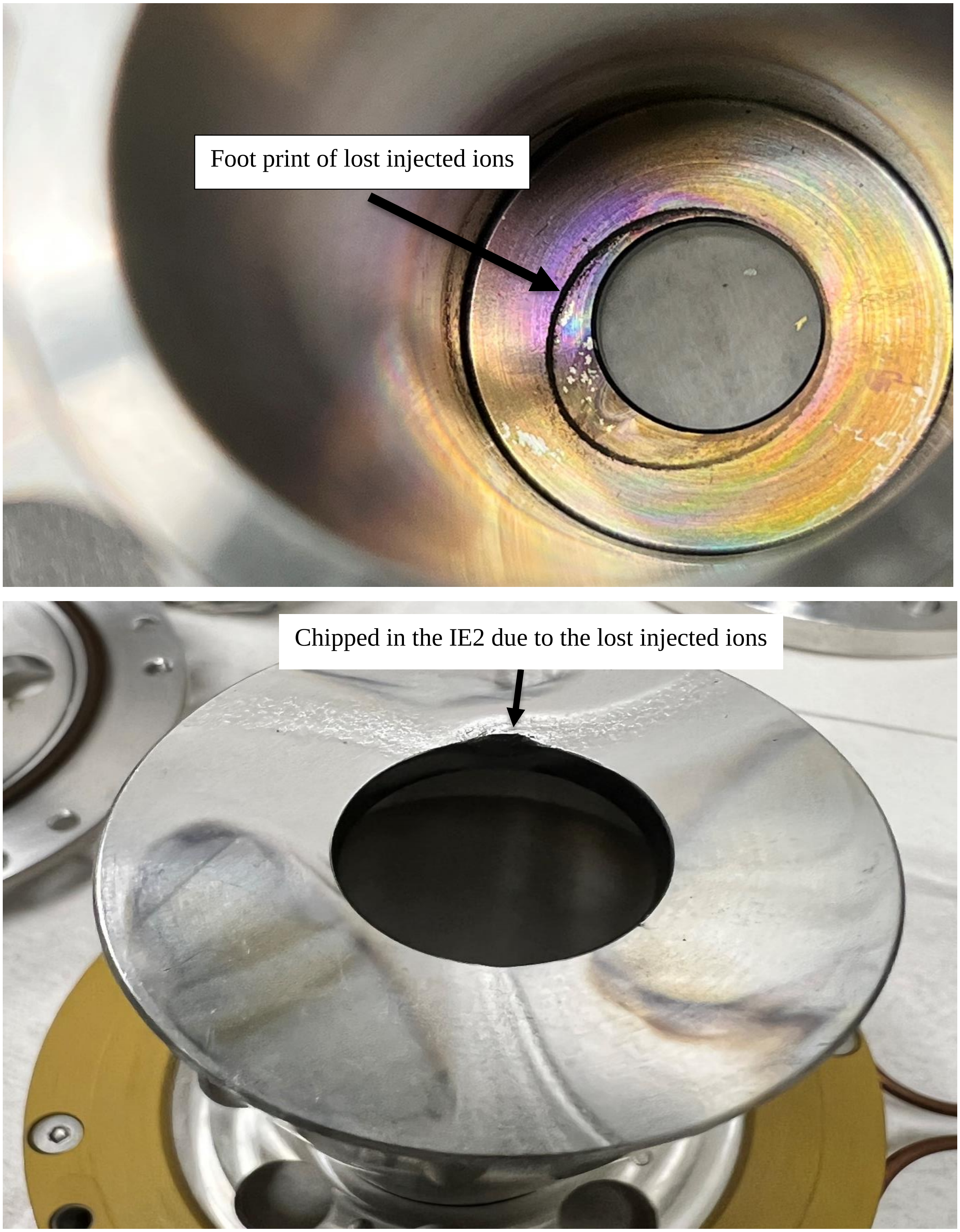

Figure 7.3: Footprint of the lost injected ions on the second injection electrode due to the magnetic field asymmetry as a result of the gap in the injection soft iron.

To better understand the effect of the opening in the injection soft iron plug, another geometry of the CSB was modelled in OPERA without the gap in the injection plug. Figure 7.4 shows the trajectory of the same beam as in Figure 7.2.

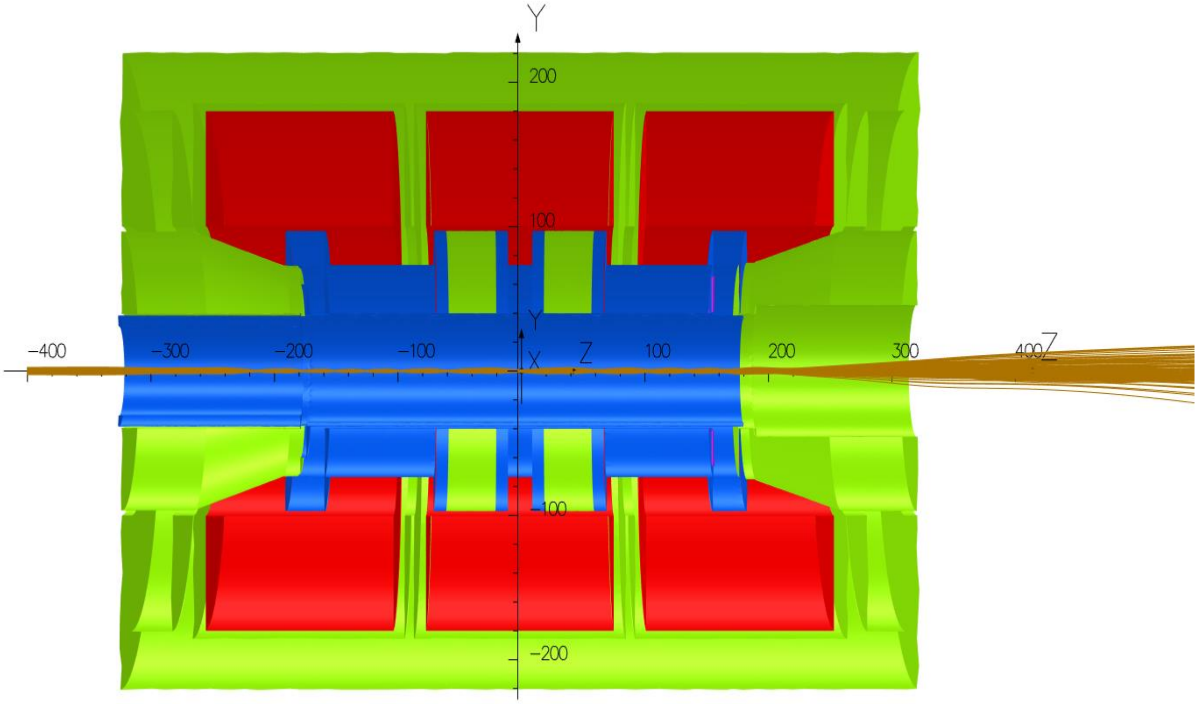

Figure 7.4: Modelling of the trajectories of singly charged cesium ion beam into the CSB without the gap in the injection soft iron assuming only magnetic field is present in the CSB. The beam was launched at an energy of Q*10 keV. The space charge of the plasma is not included in the simulation.

In the absence of asymmetry in the magnetic field due to the missing part in the injection side iron plug, the injected ions travel in a straight line through the CSB without experiencing any deflection in their trajectories. However, in the presence of plasma, the injected ions will eventually be captured and charged-bred before being extracted as highly charged ions on the right. These simulations demonstrated the flaws in the design of the PHOENIX ECRIS charge state booster, and it is important to fix the wide angle cut in the injection soft iron plug to enhance the performance of the CSB further. Because no matter how much the injection beamline, the extraction beamline and the plasma are optimized, if the injected ions do not make it into the CSB, the efficiency of the CSB would always be below the theoretically expected value.

Furthermore, the extraction diagnostics of the CSB, such as the RPM12 and RPM14, must be exchanged, and the entire beam optics must be properly aligned. Figure 7.5 shows the screenshot of the RPM12 wire scanner with the beam's profile coming out of the CSB with the extraction system optimized for $12.784\ Q * keV, 55\ \mu A$ beam. The $x -$ profile is on the left, and $y -$ profile is on the right of the picture.

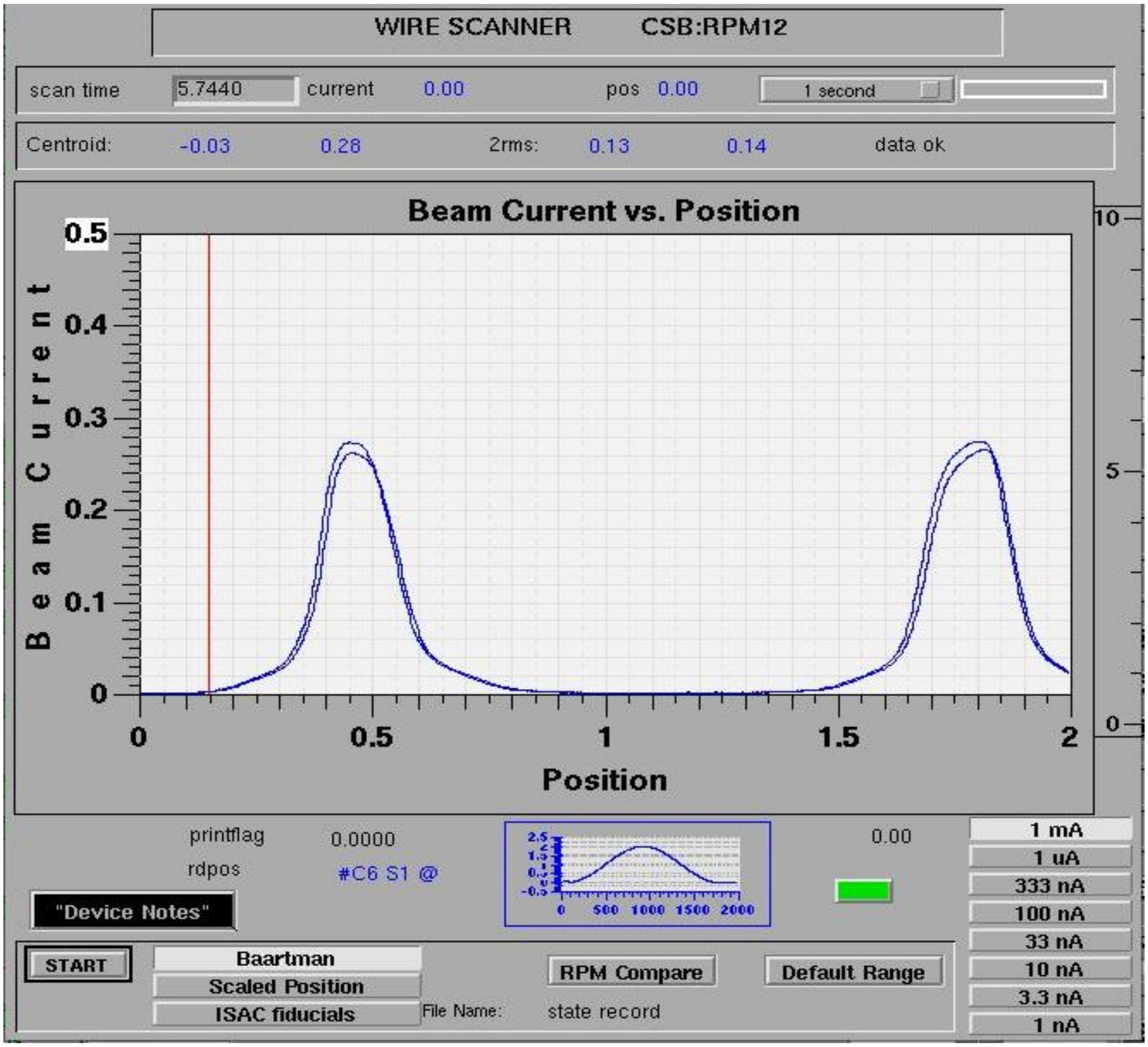

WIRE SCANNER CSB:RPM12

scan time 5.7440 current 0.00 pos 0.00

Centroid: -0.03 0.28 2rms: 0.13 0.14 data ok

printflag 0.0000

rdpos #C6 S1 @

0.00

File Name: state record

Figure 7.5: Measured beam distribution of the total extracted current from the CSB with RPM12. The left profile is in the x-direction and the right profile is in the y-direction.

As seen, the wire scanner is not well aligned with the extraction system of the CSB or vice versa, and the edge of the $y -$ profile is cut off, suggesting misalignment in the beamline. Furthermore, Figure 7.6 shows the beam profile taken with the RPM14 located downstream of quadrupole Q14. The x and y directions are the same as in Figure 7.5. The profile monitor is usually used with Q14 to perform the quadrupole scan technique (QST) for the emittance of the total beam extracted from the CSB. Meanwhile, one of the requirements to perform QST is having a beam intensity that is greater than or equal to zero, but RPM14, as shown in Figure 7.6, produces profiles with negative intensity values, and the negative values vary with the voltage scan of quadrupole Q14 making it difficult to measure the emittance of the CSB accurately. The source of the negative signal may be from the electronics of the wire scanner since the negative signal is not present in the RPM12 data, which is located before RPM14.

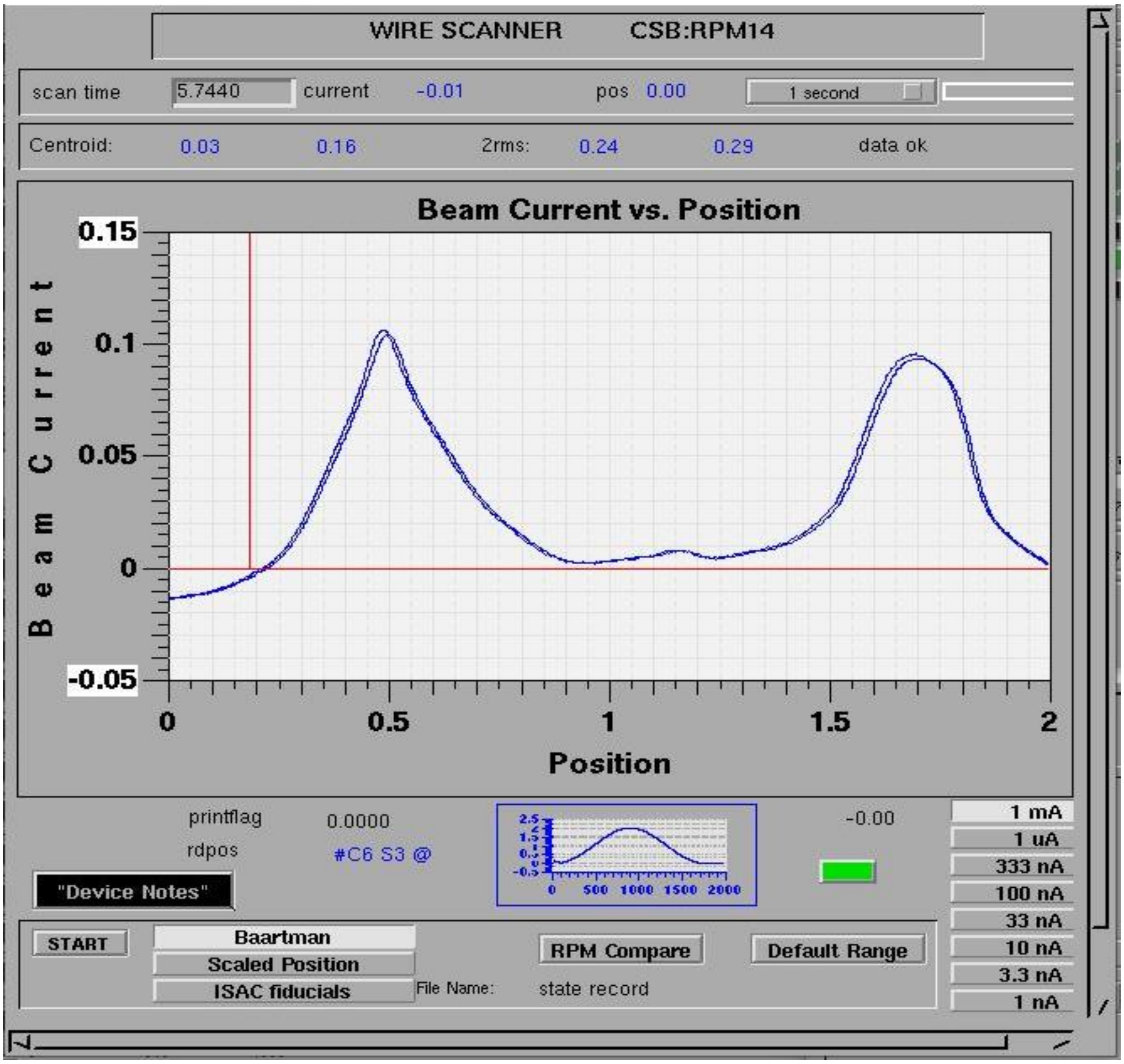
WIRE SCANNER CSB:RPM14

scan time 5.7440 current -0.01 pos 0.00

Centroid: 0.03 0.16 2rms: 0.24 0.29 data ok

printflag 0.0000

rdpos #C6 S3 @

File Name: state record

Figure 7.6: Measured beam distribution of the total extracted current from the CSB with RPM14. The left profile is in the x-direction and the right profile is in the y-direction.

However, to accurately describe the extraction system of the CSB in IGUN simulation, the RPM12 directly at the exit of the CSB should be exchanged with a Faraday cup to properly quantify the total extracted current from the charge state booster. Also, the profile monitor RPM12 or RPM14 should be relocated between Q12 and Q13 to efficiently and accurately measure the total emittance of the CSB.

In addition, the sparking of the CSB high voltage bias that has been observed during operation is currently under investigation. The cause of the sparking is suspected to be the improper positioning of the insulators between the injection electrodes of the CSB.

Finally, there is a suspicion of internal vacuum leaks that materialized after the opening of the CSB. This is evident in the mass spectrum of the CSB before and after the opening intervention, as shown in Figure 7.7. Before opening the CSB, the intensity of $^{14}\mathrm{N}^{+}$ was around 0.2 uA but increased to about 2 uA After opening the CSB, the intensity of $^{14}\mathrm{N}^{2+}$ was around 0.5 uA before but increased to about 1.6 uA after opening the CSB. With the higher density of background ions, the efficiency of the CSB and composition of the extracted ion beam can be highly impacted.

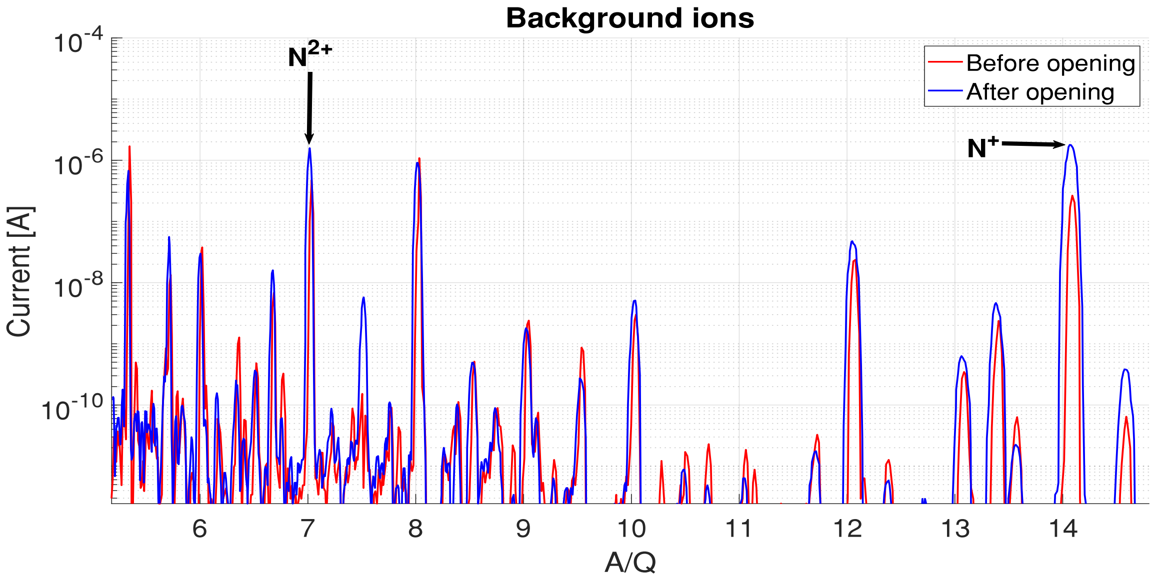

Figure 7.7: Comparison between the mass spectrum of the CSB before and after opening the CSB for magnetic field mapping.

Meanwhile, several leak tests have been conducted to identify the source of the leaks with no success. However, routine maintenance has been scheduled to open the CSB again and check the O-ring seal between the plasma electrode and the vacuum chamber. It is expected that the

CSB will reach a global efficiency of close to 95 %, as it has already been demonstrated in [50] after all the factors presented have been addressed.

Bibliography

[1] M. Wiescher, J. Görres, E. Uberseder, G. Imbriani, and M. Pignatari, “The Cold and Hot CNO Cycles,” *Annual Review of Nuclear and Particle Science*, vol. 60, no. 1, pp. 381–404, 2010, doi: 10.1146/annurev.nucl.012809.104505.

[2] O. Kester, F. Wenander, and R. Becker, “Charge breeding of stable and radioactive ion beams with EBIS/T devices,” *J Phys Conf Ser*, vol. 2, pp. 107–116, 2004, doi: 10.1088/1742-6596/2/1/014.

[3] R. Vondrasek, “On-line Charge Breeding using ECRIS and EBIS,” *Nucl Instrum Methods Phys Res B*, vol. 376, pp. 1–8, 2015, doi: 10.1016/j.nimb.2015.11.043.

[4] F. A. Maldonado Millan, “Comprehensive Ionization Model Development for the FEBIAD Ion Source and Its Application for TRIUMF’s Radioactive Ion Beam Program,” Ph.D. Thesis, University of Victoria, BC, Victoria, 2022.

[5] J. Lassen, P. Bricault, M. Dombsky, J. P. Lavoie, C. Geppert, and K. Wendt, “Resonant Ionization Laser Ion Source Project at TRIUMF,” in *Hyperfine Interactions*, 2005. doi: 10.1007/s10751-005-9212-2.

[6] J. Dilling, R. Krücken, and L. Merminga, “ISAC and ARIEL: The TRIUMF radioactive beam facilities and the scientific program,” in *ISAC and ARIEL: The TRIUMF Radioactive Beam Facilities and the Scientific Program*, 2014, p. 113. doi: 10.1007/978-94-007-7963-1.

[7] TRIUMF, “ISAC Facility Layout.” http://www.triumf.ca/research-program/research-facilities/isac-facilities (accessed Jul. 29, 2018).

[8] A. O. Nier and T. R. Roberts, “The Determination of Atomic Mass Doublets by Means of a Mass Spectrometer,” *Physical Review*, vol. 81, no. 4, pp. 507–510, Feb. 1951, doi: 10.1103/PhysRev.81.507.

[9] B. Herrmannsfeldt, G. Herrmannsfeldt, R. Becker, and J. G. Becker, “IGUN.” http://www.egun-igun.com/ (accessed Feb. 02, 2020).

[10] R. Becker and W. B. Herrmannsfeldt, “IGUN - A program for the simulation of positive ion extraction including magnetic fields,” *Review of Scientific Instruments*, vol. 63, no. 4, pp. 2756–2758, 1992, doi: 10.1063/1.1142795.

[11] OPERA, "ELECTROMAGNETIC AND ELECTROMECHANICAL SIMULATION," 2021. https://www.3ds.com/products-services/simulia/products/opera/ (accessed Apr. 04, 2021).

[12] E. A. Heighway and R. M. Hutcheon, "Transoptr — A second order beam transport design code with optimization and constraints," *Nuclear Instruments and Methods in Physics Research*, vol. 187, no. 1, pp. 89–95, Aug. 1981, doi: 10.1016/0029-554X(81)90474-2.

[13] R. Baartman, "TRANSOPTR: Changes since 1984," Vancouver, 2016. Technical Report: TRI-BN-16-06.

[14] R. Baartman, "TRANSOPTR Manual." 2022. [Online]. Available: http://lin12.triumf.ca/text/design_notes/transoptr-manual.xml

[15] F. Chen, "Introduction to Plasma Physics and Controlled Fusion," 2nd ed.Plenum Press, New York, 2006, p. 3.

[16] P. Debye and E. Huckel, "The Theory of Electrolytes I. The Lowering of the Freezing Point and Related Occurrences," *Physikalische Zeitschrift*, vol. 24, pp. 185–206, 1923, Accessed: Jan. 25, 2021. [Online]. Available: http://ci.nii.ac.jp/naid/10029454771/en/

[17] Z. Q. Xie and C. M. Lyneis, "Plasma Potentials and Performance of the Advanced Electron Cyclotron Resonance Ion Source," *Review of Scientific Instruments*, vol. 65, no. 9, pp. 2947–2952, 1994, doi: 10.1063/1.1144583.

[18] S. Gammino, G. Ciavola, L. G. Celona, D. Mascali, and F. Maimone, "Numerical simulations of the ECR heating with waves of different frequency in electron cyclotron resonance ion sources," *IEEE Transactions on Plasma Science*, vol. 36, no. 4 PART 2, pp. 1552–1568, 2008, doi: 10.1109/TPS.2008.927288.

[19] K. S. Golovanivsky, V. D. Dougar-Jabon, and D. V. Reznikov, "Proposed Physical Model for Very Hot Electron Shell Structures in Electron Cyclotron Resonance Driven Plasmas," *Phys Rev E*, vol. 52, no. 3, pp. 2969–2973, 1995, doi: 10.1103/PhysRevE.52.2969.

[20] W. Lotz, "Electron-Impact Ionization Cross-Sections and Ionization Rate Coefficients for Atoms and Ions," *Astrophys J Suppl Ser*, vol. 14, p. 207, May 1967, doi: 10.1086/190154.

[21] I. Brown, “The Physics and Technology of Ion Sources,” I. Brown, Ed., 2nd ed.California: WILEY-VCH, 2003, pp. 203–215.

[22] A. Müller and E. Salzborn, “Scaling of cross sections for multiple electron transfer to highly charged ions colliding with atoms and molecules,” *Phys Lett A*, vol. 62, no. 6, pp. 391–394, 1977, doi: 10.1016/0375-9601(77)90672-7.

[23] R. Bardet, P. Briand, L. Dupas, C. Gormezano, and G. Melin, “Hot-Electron-Plasma Accumulation in the Circe Mirror Experiment,” *Nuclear Fusion*, vol. 15, no. 5, pp. 865–873, Oct. 1975, doi: 10.1088/0029-5515/15/5/016.

[24] WikiHelper2134, “Magnetic Bottle.” https://commons.wikimedia.org/wiki/File:Fields_in_magnetic_bottles.jpg (accessed Apr. 04, 2021).

[25] R. J. Goldston and P. H. Rutherford, “Introduction to Plasma Physics,” 1st ed.Bristol and Philadelphia: The Institute of Physics Publishing, 1995, pp. 165–171.

[26] N. Krall and A. Trivelpiece, “Principles of Plasma Physics,” 1st ed.San Francisco: McGraw-Hill Book Company, 1986, p. 294.

[27] C. D. Child, “Discharge from Hot CaO,” *Physical Review (Series I)*, vol. 32, no. 5, pp. 492–511, 1911, doi: 10.1103/PhysRevSeriesI.32.492.

[28] I. Langmuir and K. T. Compton, “Electrical Discharges in Gases Part II. Fundamental Phenomena in Electrical Discharges,” *Rev Mod Phys*, vol. 3, no. 2, pp. 191–257, 1931, doi: 10.1103/RevModPhys.3.191.

[29] I. H. Hutchinson, “Principles of Plasma Diagnostics,” 2nd ed.Cambridge University Press, United Kingdom, 2002, pp. 104–111.

[30] D. G. Swanson, “Plasma Waves,” 2nd ed.Bristol and Philadelphia: Institute of Physics Publishing, 2003, pp. 302–305.

[31] H. Wollnik, *Optics of Charged Particles*, 1st ed. Orlando: Academic Press Inc., 1987.

[32] K. Wille, “The Physics of Particle Accelerator,” 1st ed.New York: Oxford University Press, 2000, pp. 44–132.

[33] R. Baartman, “Electrostatic Bender Fields, Optics, Aberrations, with Application to the Proton EDM Ring,” Vancouver, BC, 2013. Technical Report: TRI-BN-13-08.

[34] R. Baartman, “Electrostatic Bender Optics,” Vancouver, BC, 2013. Technical Report: TRI-DN-05-7.

[35] F. J. Sacherer, “RMS Envelope Equation with Space Charge,” *IEEE Trans Nucl Sci*, pp. 1105–1107, 1971.

[36] A. T. Green, “Implementation of Quadrupole-Scan Emittance Measurement At Fermilab’s Advanced Superconducting Test Accelerator (ASTA),” in *Proceedings of IPAC2015*, 2015, pp. 669–671. doi: 10.18429/JACoW-IPAC2015-MOPMA052.

[37] C. Limborg, S. Gierman, and J. Power, “A Modified Quadscan Technique for Emittance Measurement of Space Charge Dominated Beams,” in *Proceedings of the IEEE Particle Accelerator Conference*, 2003, pp. 2667–2669. doi: 10.1109/pac.2003.1289224.

[38] E. Prat and M. Aiba, “Four-Dimensional Transverse Beam Matrix Measurement Using the Multiple-Quadrupole Scan technique,” *Physical Review Special Topics - Accelerators and Beams*, vol. 17, no. 5, pp. 1–9, May 2014, doi: 10.1103/PhysRevSTAB.17.052801.

[39] S. Y. Lee, “Accelerator physics, third edition,” in *Accelerator Physics, Third Edition*, World Scientific Publishing Co., 2011, p. 62. doi: 10.1142/8335.

[40] P. Tenenbaum, “Emittance Measurements in CTF-2 Drive Beam,” Feb. 1997. Technical Report: CLIC-NOTE-326.

[41] M. Reiser, “Theory and Design of Charged Particle Beams,” in *Linear Beam Optics with Space Charge*, 2nd ed.Maryland: Wiley-VCH, 2008, pp. 163–264.

[42] F. Ames, R. Baartman, P. Bricault, and K. Jayamanna, “Commissioning of the ECRIS Charge State Breeder at TRIUMF,” in *Proceedings of ECRIS*, Grenoble, France, 2010, pp. 178–180. doi: INIS-FR--13-0058.

[43] TRIUMF, “TRIUMF CSB Components Drawing,” *2018*. TRIUMF Design Office, Vancouver.

[44] D. Wutte, M. A. Leitner, C. M. Lyneis, C. E. Taylor, and Z. Q. Xie, “Design Study of the Extraction System of the 3rd Generation ECR Ion Source,” 2009, pp. 384–395. doi: 10.1063/1.58959.

[45] D. Wutte, M. A. Leitner, and C. M. Lyneis, “Emittance Measurements for High Charge State Ion Beams Extracted from the AECR-U Ion Source,” in *Physica Scripta T*, 2001, pp. 247–249. doi: 10.1238/physica.topical.092a00247.

[46] F. Ames, R. Baartman, P. Bricault, K. Jayamanna, and A. Mjøs, "Operation of an ECRIS Charge State Breeder At TRIUMF," in *Proceedings of ECRIS2012, Sydney, Australia,* 2012, pp. 163–166.

[47] A. S. Gilmour, "Klystrons, Traveling Wave Tubes, Magnetrons, Crossed-Field Amplifiers, and Gyrotrons," Artech House, 2011, pp. 3–4.

[48] F. Ames, M. Marchetto, A. Mjøs, and A. C. Morton, "Charge state breeding experiences and plans at TRIUMF," *Review of Scientific Instruments*, vol. 87, no. 2, pp. 1–4, 2016, doi: 10.1063/1.4932317.

[49] J. Adegun, F. Ames, and O. Kester, "Improvement of the Efficiency and Beam Quality of the TRIUMF Charge State Booster," *J Phys Conf Ser*, vol. 2244, no. 012067, pp. 1–5, 2022, doi: 10.1088/1742-6596/2244/1/012067.

[50] J. Angot, M. Baylac, M. Luntinen, M. Migliore, O. Tarvainen, and T. Thuillier, "Recent developments and results of the LPSC PHOENIX type ECR charge breeder," in *Journal of Physics: Conference Series*, Apr. 2022, p. 3. doi: 10.1088/1742-6596/2244/1/012063.

[51] R. Becker and O. Kester, "Acceleration of Heavy Ions Generated by ECRIS and EBIS," in *Proceedings of HIAT*, Venice, Italy, 2009, pp. 143–146.

[52] S. Bliman, R. Geller, B. Jacquot, and C. Jacquot, "A high-intensity ECR stripped ion source," *IEEE Trans Nucl Sci*, vol. 19, no. 2, pp. 200–203, 1972, doi: 10.1109/TNS.1972.4326655.

[53] R. Vondrasek *et al.*, "ECRIS Operation with Multiple Frequencies," in *AIP Conference Proceedings*, 2005, pp. 31–34. doi: 10.1063/1.1893362.

[54] S. C. Jeong *et al.*, "KEKCB-18 GHz ECR Charge Breeder at TRIAC," *Nucl Instrum Methods Phys Res B*, vol. 266, no. 19–20, pp. 4411–4414, 2008, doi: 10.1016/j.nimb.2008.05.072.

[55] Z. Q. Xie, "State of the Art of ECR ion sources," *Proceedings of the IEEE Particle Accelerator Conference*, vol. 3, pp. 2662–2666, 1998, doi: 10.1109/pac.1997.752725.

[56] A. G. Drentje, A. Kitagawa, T. Uchida, R. Rácz, and S. Biri, "Experiments with biased side electrodes in Electron Cyclotron Resonance Ion Sources," in *Review of Scientific Instruments*, 2014, pp. 1–5. doi: 10.1063/1.4827309.

[57] A. G. Drentje, “The ECR ion source and associated equipment at the KVI,” *Nuclear Inst. and Methods in Physics Research, B,* vol. 9, no. 4, pp. 526–528, Jul. 1985, doi: 10.1016/0168-583X(85)90360-X.

[58] O. Tarvainen, P. Suominen, and H. Koivisto, “Effect of the Gas Mixing Technique on the Production Efficiency of Ion Beams Extracted From an Electron Cyclotron Resonance Ion Source,” *Nucl Instrum Methods Phys Res B,* vol. 217, no. 1, pp. 136–142, 2004, doi: 10.1016/j.nimb.2003.08.045.

[59] R. Vondrasek, A. Levand, R. Pardo, G. Savard, and R. Scott, “Charge breeding results and future prospects with electron cyclotron resonance ion source and electron beam ion source,” *Review of Scientific Instruments*, vol. 83, no. 2, 2012, doi: 10.1063/1.3673629.

[60] J. Adegun, F. Ames, and O. Kester, “Systematic Investigation of the TRIUMF Electron Cyclotron Resonance Ion Source Charge State Booster,” in *Canadian Association of Physicists*, Hamilton, ON, 2022.

[61] ANSYS, “HFSS,” 2019. https://www.ansys.com/products/electronics/ansys-hfss (accessed Jan. 24, 2019).

[62] J. Adegun, “University of Victoria Ph.D. Candidacy Report,” Victoria, BC, 2019.

[63] J. Adegun, F. Ames, and O. Kester, “Improvement of the Efficiency of the TRIUMF Charge State Booster (CSB),” *JACoW,* vol. ECRIS2020, pp. 160–163, 2022, doi: 10.18429/JACoW-ECRIS2020-WEZZO04.

[64] R. Rácz *et al.*, “Effect of the Two-Close-Frequency Heating to the Extracted Ion Beam and to the X-ray Flux Emitted by the ECR plasma,” in *Journal of Instrumentation*, 2018, p. 3. doi: 10.1088/1748-0221/13/12/C12012.

[65] L. Thierry *et al.*, “Fine Frequency Tuning of the Phoenix Charge Breeder Used As a Probe for ECRIS Plasmas,” in *International Workshop on ECR Ion Sources*, 2010, pp. 184–187.

Appendix

The optimized TRANSOPTR input files for both the injection and extraction optics, IGUN input files, OPERA files, Quadrupole Scan technique Python codes for emittance measurement, and mapped magnetic field are stored on TRIUMF SharePoint which can be found in Relevant Simulation files from Joseph Adegun's PhD Thesis. Please note that a TRIUMF ID is required to access the folder.

A. TRANSOPTR Files

Refer to [14] and https://gitlab.triumf.ca/beamphys/transoptr on how to install, run and perform optimization in TRANSOPTR on Windows and the UNIX operating system. Previously, instruction on how to run TRANSOPTR on Windows OS was not available but with the help of Thomas Planche, I developed a comprehensive step-by-step on how to install it on Windows OS.

1 For the injection optics, four input files that must be in the same folder are required to run the files – data.dat, sy.f, fort.58, and fort.2. Fort.58 contains the generalized electric field map of the injection system of the CSB, while fort.2 contains the magnetic field for a defined current on the CSB solenoid coil. The current file corresponds to when 1050A/200A/762A are set on the CSB solenoid coils. If the settings are changed, a new fort.2 must be created to replace the old one.

2 For the extraction optics, only three input files are required and they must also be in the same folder. They are data.dat, sy.f and fort.2. Fort.2 contains the magnetic field of the CSB mapped and imported into TRANSOPTR. The current file corresponds to 1050A/200A/762 A setting on the CSB solenoid coils

B. IGUN Files

To simulate the extraction system of the cesium test ion source (CTIS) and the extraction system of the CSB, only one input file is needed for each simulation. The input file contains the geometry of the extraction system to be simulated. In particular, since the extraction system of the CSB is located in the strong magnetic field of the ECR, the input file also contains the imported mapped magnetic field of the CSB. The current mapping corresponds to 1050A/200A/762 A settings on the CSB solenoid coils. If a new current value is set on the solenoid coils and an extraction system simulation is required, the &INPUT3 of the input file for the CSB IGUN file must be updated accordingly. Please refer to the IGUN manual for more information.

1 For CTIS extraction system simulation, the input file is named TRICTIS.IN
2 For the CSB extraction system, the input file is named ECRISCSB.IN. The other file in the folder is named ECRISCSB2.IN allows the simulation of the plasma electrode and half of the puller electrode for the magnification of the plasma meniscus.

C. OPERA Files

This folder contains the geometry of the CSB modelled and simulated in OPERA. There are three subfolders in this directory, each subfolder contains the geometry and the solution of the simulation.

1 Electric Potential Only: This contains the modelling of the complete electric potential of the CSB including the injection and the extraction systems. The boundary condition currently defined on the electrodes in the Voltage_distribution (type – Opera-3d Modeller Data File) are injection systems: IE1 = 8884 V, IE2 = 12484 V, CSB Bias voltage: HV = 12784 V, and the extraction system: PE (same as the CSB bias voltage), EE = 9471 V. The solution of the modelling is named Voltage_distribution_solution (type- Opera-3d Database). Please note that installation of OPERA is required to load and view the solution.
2 Magnetic field and Electric field: This folder contains the modelling of the CSB by combining both the electric and magnetic fields of the CSB.
3 Magnetic field only: This folder contains the modelling of the total magnetic field of the CSB including the hexapole permanent magnet.

D. CSB Mapped Magnetic Field Results

This folder contains the results of the magnetic field mapping of the CSB and all the relevant information about the setup of the magnetic mapper. For more information about the mapper, please talk to Marco Marchetto at TRIUMF.

E. Python Codes

At the moment, a UNIX-based computer such as Mac Book or LINUX is required to run the Python code for emittance measurement. For example, to scan quadrupole Q5 to measure the emittance of the CTIS, two separate Python codes are required, (the same applies to other quadrupole scans). The first code which was partly written by Spencer Kiy and modified by me is required to be run in a Python virtual environment. This code was specifically written to scan Quadrupole Q5. It accepts the start value and end value of the voltage of Q5 to scan through. It is named quad5_scan.py. The second Python code which was largely written by me is required to retrieve the data saved by the previous code, extract the data, perform fitting, plot graphs and print the emittance and the Twiss parameters. It contains the geometrical parameters and transfer matrices of the optics required for the emittance measurement. The second file is named rpm5_QST_data_processor.py. It does not require a Python virtual environment. It accepts the measure_id of the data saved from running the first code and input. The outputs are the plots of rpm raw data, rpm processed data, the QST parabolic curve with modelled fitted on the measurement, Phase space ellipses of the beam and a print-out of the Emittance, the Twiss parameters, cross-correlation, xmax and xprime max. In general, the same applies to the scanning of quadrupoles Q14 and Q16. Please note that to use the codes for scanning and processing other QST data, the content of the quad_scan.py and the QST_data_processor.py must be edited accordingly. In conclusion, the Python codes in this folder can only scan and process data from Q5 and rpm5, Q12 and rpm 14, Q14 and rpm14 and Q16 and rpm16.